



The University of  
**Nottingham**

UNITED KINGDOM • CHINA • MALAYSIA

Faculty of Engineering

Mechanical, Materials and Manufacturing Research Division

Department of Mechanical Engineering

The University of Nottingham Malaysia Campus

EXPLOITATION OF ZnO/Fe<sub>3</sub>O<sub>4</sub> AND TiO<sub>2</sub>/Fe<sub>3</sub>O<sub>4</sub> NANOCOMPOSITES ON THE  
DEGRADATION OF ORGANIC COMPOUNDS

By

TAN THIAN KHOON

Thesis Submitted to the School of Graduate Studies,  
The University of Nottingham Malaysia Campus, in Fulfilment of the Partial  
Requirements for  
the Degree of Doctor of Philosophy in Mechanical Engineering

Aug 2018

## **Abstract**

Water is the main sources for all living beings. However, with the vast development and advancement of technology, water resources have been seriously contaminated by industries effluent, especially organic dyes. Various methods have been implemented to achieve certain level of acceptable cleanliness. Current most efficient and cost effective process is the photocatalytic process using highly photoreactive ZnO and TiO<sub>2</sub> semiconductors. However, separation of the semiconductor powder arises at the end of the decomposition process. Therefore, there have been many researches trying to dope magnetic material into the semiconductor to make it easily separable and cost effective by just applying a magnetic field. However, most of the preparations require various recalcitrant and toxicant precursor chemicals as well as high sintering temperature. In light of these, this study has tried to use simple method of preparation and followed by a significantly moderate sintering temperature. The ZnO/Fe<sub>3</sub>O<sub>4</sub> and TiO<sub>2</sub>/Fe<sub>3</sub>O<sub>4</sub> nanocomposite materials have been successfully prepared by simple mechanical mixing and sintered at significantly moderate temperature of 300 and 350 °C, respectively. Besides, the prepared nanocomposite exhibit remarkable photocatalytic decomposition on few chosen dyes.

The XRD results indicated a good crystallinity with the standard for both nanocomposites. The SEM and TEM results showed ZnO/Fe<sub>3</sub>O<sub>4</sub> nanocomposite was square-like and elongated in shape, while it was mostly

spherical for TiO<sub>2</sub>/Fe<sub>3</sub>O<sub>4</sub> nanocomposite. VSM measurements showed that both nanocomposites exhibit ferromagnetism, while ZnO and TiO<sub>2</sub> are diamagnetism in nature. Both nanocomposites able to completely decomposed the MB dye. All the photocatalytic measurements show that the photodegradation processes are following the pseudo-first-order kinetics. Both nanocomposites were successfully magnetically separated from the decomposed solution by using a 0.60 T permanent magnet. A 9.0wt% loading of ZnO/Fe<sub>3</sub>O<sub>4</sub> nanocomposite with 10wt% doped Fe<sub>3</sub>O<sub>4</sub> and sintered at 300 °C was able to completely decomposed MB in 30 minutes (99.9%) with kinetic constant of 0.242 min<sup>-1</sup>. On the other hand, TiO<sub>2</sub>/Fe<sub>3</sub>O<sub>4</sub> nanocomposite with 1wt% doped Fe<sub>3</sub>O<sub>4</sub> sintered at 350 °C and at optimum loading of 3wt% was able to decompose 98.7% of MB in 60 minutes with kinetic constant of 0.0729 min<sup>-1</sup>.

The repeatability experiments were conducted and the results indicated that there was a minor deactivation (~1.08%) after the second and third run. This shows that both nanocomposites were photocatalytically stable and reusable for wider application on organic dyes decomposition. The effect of the intrinsic properties for the chosen organic dyes, such as their azo groups, benzene groups, molecular weight and absorbance, in relation to their rate of decomposition were evaluated in the last part of this study. The results show that the degradation rate is linearly proportional to the number of azo groups, the number of benzene groups, the molecular weight and inversely proportional to the absorbance of the dye's solution.

## **Acknowledgements**

First and foremost I would like to convey my deepest gratitude to my friendly and patient supervisor, Professor Khiew Poi Sim, for being my guidance and advisor whilst at the same time allowing me the atmosphere to work on my own. One simply could not wish for a better or friendlier supervisor. He has immensely supported me throughout my research work and patiently corrected my work. Special thanks also to my lovely and cheerful co-supervisor, Dr. Michelle Tan, for her insightful advice and encouragement during this study.

I am thankful and grateful to Professor Dino Isa for his support in terms of laboratory facilities. My special thanks to laboratory officers, Mr. Andrew Yakin Sinit, Mr. Ahmad Fareez Mohd Rawi, Ms. Filzah Mohd Fauzi, Ms. Khairani Hasuna Jaapar and administration officers, Ms. Yogeswary Arumugam and Ms. Siti Zaharatul Asyiqin Mohammed Mokhtar for their help in technical assistance and time lent.

My special thanks and gratitude also go to Dr. Chiu Wee Siong and Dr. Chia Chin Hua for their instant support and assistance in sample characterization which without them this study will not be possible. I am grateful to the staffs at the Electron Microscopy Unit (UKM) for their assistance in the electron microscopy characterization.

I am grateful with the smooth running of this study and am deeply thankful for the financial support from Ministry of Science, Technology and Innovation (Malaysia) for the Fundamental Research Grant Scheme (FRGS) in supporting various needs of this research and Faculty of Engineering on the scholarship conferred to me.

I would also like to acknowledge the immense impact and support that my family has given me, including my parents, elder brother and two younger sisters. They have always been encouraging with their very best wishes. I am grateful and thankful to my wife, Niu Kim Sua, for her patience and understanding. She was always there with lots of encouragement and moral support through my ups and downs.

<b><u>Table of Contents</u></b>	<b><u>Page</u></b>
Abstract_____	ii
Acknowledgement_____	iv
Table of Contents_____	vi
List of Figures_____	x
List of Tables_____	xx
List of Abbreviations_____	xxii
Chapter 1: Introduction_____	1
1.1 Introduction	1
1.2 Rationale and Novelty of the Study	10
1.3 Objectives of the Study	11
1.4 Thesis Organisation	12
Chapter 2: Background Studies_____	15
2.1 Introduction	15
2.2 The Influence of Nanostructured Materials	18
2.3 Principles of Photocatalyst	24
2.3.1 Photocatalyst Reaction	26
2.3.2 Understanding on Solid Band	28
2.3.3 Band Gap Excitation	32
2.3.4 Electron Hole Recombination	34
2.4 Zinc Oxide Photocatalyst	35
2.4.1 Introduction	35
2.4.2 Crystal Structures of Zinc Oxide	37
2.5 Titanium Dioxide Photocatalyst	41
2.5.1 Introduction	41
2.5.2 Crystal Structures of Titanium Dioxide	42
2.6 Iron Oxide Photocatalyst	44
2.6.1 Introduction	44
2.6.2 Crystal Structures of Iron Oxide (Fe <sub>3</sub> O <sub>4</sub> )	45
2.7 Influence of Parameters on the Photocatalytic Performance	46
2.7.1 Photocatalyst Loading	47
2.7.2 Organic Concentration	48
2.7.3 Effect of pH	50
2.7.4 Effect of Light Intensity	52
2.7.5 Effect of Temperature	55
2.7.6 Effect of Morphologies	57
2.8 Modified Photocatalyst	60
2.8.1 Effect of Doping on Photocatalytic Activity	61
2.8.2 Surface Modifications	63

2.8.3	Sensitization in Photocatalytic System	66
2.8.3.1	Polymer Hybridization	66
2.8.3.2	Coupled Semiconductor	68
2.8.3.3	Organic Dye Sensitized Photocatalyst	70
2.9	Dyes as Wastewater Effluent	72
Chapter 3: Experimental Preparations_____		79
3.1	Introduction	79
3.2	Materials	79
3.2.1	Raw Materials	79
3.2.2	Preparation of the Magnetic Nanocomposite Materials	81
3.3	Photodegradation Study	84
3.4	Characterization	87
3.4.1	X-Ray Diffraction	87
3.4.2	Scanning Electron Microscope	93
3.4.3	Transmission Electron Microscope	97
3.4.4	Surface Area Analysis	102
3.5	Photocatalytic Performance Investigation	104
3.5.1	Photodegradation Measurement	104
3.5.2	Photocatalysis Kinetic Analysis	110
Chapter 4: Characterization of Zinc Oxide and Titanium Dioxide and Iron (II,III) Oxide Photocatalysts and Degradation Study of Three Organic Dyes (MB, PR & MO)_____		113
4.1	Introduction	113
4.2	Experimental Results	116
4.2.1	X-Ray Deffractometry (XRD)	116
4.2.2	Field Emission Scanning Electron Microscopy (FESEM)	120
4.2.3	Transmission Electron Microscopy (TEM)	122
4.2.4	Brunauer-Emmett-Teller Surface Area Analysis (BET)	125
4.2.5	Energy Dispersive X-Ray Spectroscopy (EDX)	126
4.2.6	Photocatalytic Analysis Using UV Visible Spectrophotscopy	129
4.2.6.1	Photodecomposition Study on the Organic Dye Solution without the Presence of Photocatalytic Material	129
4.2.6.2	Effect of Photocatalyst Loading	136
4.2.6.3	Effect of Initial Dye Concentration	147
4.2.6.4	Effect of Irradiation Duration on the Three Dyes by the ZnO, TiO <sub>2</sub> and Fe <sub>3</sub> O <sub>4</sub> Photocatalysts	174
4.3	Summary	184
Chapter 5: Zinc Oxide/Iron Oxide Nanocomposite_____		186
5.1	Introduction	186
5.2	Background Study	187
5.3	Results and Discussions	190
5.3.1	Different Sintering Temperature	190
5.3.2	Different Weight Percent of Fe <sub>3</sub> O <sub>4</sub>	199

5.3.3	Transmission Electron Microscopy (TEM)	208
5.3.4	Photocatalytic Analysis for Different Loading of ZnO/Fe <sub>3</sub> O <sub>4</sub>	210
5.3.5	Photocatalytic Study on the Effect of Sintering Temperature with ZnO/Fe <sub>3</sub> O <sub>4</sub> Nanocomposite Material	214
5.3.6	Photocatalytic Study on the Effect of Different wt% Fe <sub>3</sub> O <sub>4</sub> Doped into the ZnO/Fe <sub>3</sub> O <sub>4</sub> Nanocomposite Material	217
5.3.7	Vibrating Sample Magnetometry Analysis (VSM)	221
5.3.8	Magnetic Separation	222
5.3.9	Repeatability Analysis	224
5.4	Summary	227
Chapter 6: Fabrication of Titanium Dioxide/Iron Oxide Nanocomposite		228
6.1	Introduction	228
6.2	Background Study	228
6.3	Results and Discussions	230
6.3.1	Morphology and Crystalline Structure of the Nanocomposite with Different Sintering Temperature	230
6.3.2	Morphology and Crystalline Structure of the Nanocomposite Doped with Different Weight Percent of Fe <sub>3</sub> O <sub>4</sub>	239
6.3.3	Transmission Electron Microscopy (TEM)	247
6.3.4	Photocatalytic Study for Different Loading of TiO <sub>2</sub> /Fe <sub>3</sub> O <sub>4</sub>	249
6.3.5	Photocatalytic Study for Different Sintering Temperature	252
6.3.6	Photocatalytic Study for Different wt% of Fe <sub>3</sub> O <sub>4</sub>	255
6.3.7	Vibrating Sample Magnetometry Analysis (VSM)	259
6.3.8	Magnetic Separation Analysis	260
6.3.9	Repeatability Analysis	262
6.4	Summary	265
Chapter 7: Photodecomposition of Few Dyes by ZnO/Fe <sub>3</sub> O <sub>4</sub> Nanocomposite		266
7.1	Introduction	266
7.2	Background Study	267
7.3	Results and Discussions	270
7.3.1	Effect of Azo Functional Group on the Photodegradation Rate	271
7.3.2	Effect of Benzene Group on the Photodegradation Rate	274
7.3.3	Effect of Molecular Mass on the Photodegradation Rate	276
7.3.4	Effect of Absorbance on the Photodegradation Rate	278
7.4	Summary	280
Chapter 8: Conclusions		281
8.1	Conclusions	281
8.2	Future Recommendation	286



## **LIST OF FIGURES**

- Figure 2.1 Schematic representation of the top-down and bottom-up processes and their relationship to biological processes and structures\_\_\_\_\_ 21
- Figure 2.2 Schematic representation of the variation of yield stress as a function of grain size in microcrystalline, ultrafine crystalline and nanocrystalline metals and alloys.  $\langle d \rangle$  is average grain size and  $k, \sigma_0$  are constants\_\_\_\_\_ 23
- Figure 2.3 The photocatalytic process of oxide semiconductor\_ 28
- Figure 2.4 Electron energy level diagram for a progressively larger linear chain of atoms showing the broadening of molecular orbitals into energy bands for a one-dimensional solid\_\_\_\_\_ 30
- Figure 2.5 Band gap energy diagram\_\_\_\_\_ 31
- Figure 2.6 The conduction and valence band positions of selected metal oxide semiconductors\_\_\_\_\_ 33
- Figure 2.7 Photoexcitation of semiconductor resulted in charge separation/oxidation/reduction/recombination\_\_\_\_\_ 35
- Figure 2.8 The hexagonal wurtzite structures of ZnO. O atoms are shown as large white spheres, Zn atoms as smaller black spheres. One unit cell is outlined for clarity\_\_\_\_\_ 39
- Figure 2.9 The rock salt (left) and zincblende (right) phases of ZnO. O atoms are shown as large white spheres, Zn atoms as smaller black spheres. One unit cell is outlined for clarity\_\_ 40

Figure 2.10	The anatase, rutile and brookite structures of TiO <sub>2</sub> . O atoms are shown as large red spheres, Ti atoms as smaller blue spheres_____	43
Figure 2.11	Spinel crystal structure of Fe <sub>3</sub> O <sub>4</sub> . The green atoms are Fe <sup>2+</sup> , brown atoms are Fe <sup>3+</sup> and white atoms are oxygen_	46
Figure 2.12	Heterogeneous photocatalytic reaction rate vs solar irradiance____	54
Figure 2.13	Doping semiconductor photocatalyst: $h\nu_1$ : pure photocatalyst; $h\nu_2$ : metal-doped photocatalyst; $h\nu_3$ : nonmetal-doped photocatalyst_____	62
Figure 2.14	Schematic diagram for surface modification of TiO <sub>2</sub> loaded with platinum_____	64
Figure 2.15	Sensitization mechanism for polymer hybridization under UV light (a) and Vis light (b) irradiation_____	68
Figure 2.16	Sensitization mechanism for combined semiconductor photocatalyst_____	70
Figure 2.17	Sensitization mechanism for dye sensitized photocatalyst _____	71
Figure 3.1	Flowchart of mechanically prepared ZnO/Fe <sub>3</sub> O <sub>4</sub> and TiO <sub>2</sub> /Fe <sub>3</sub> O <sub>4</sub> nanocomposites_____	82
Figure 3.2	Different wt% of ZnO/Fe <sub>3</sub> O <sub>4</sub> powders after mechanical mixing. (a) 20 wt% of Fe <sub>3</sub> O <sub>4</sub> ; (b) 1 wt% of Fe <sub>3</sub> O <sub>4</sub> _____	83
Figure 3.3	Schematic diagram of the experimental set up_____	85

Figure 3.4	Illustration of X-rays scattered by atoms in an ordered lattice interfere constructively in directions given by Bragg's law _____	89
Figure 3.5	XRD patterns for three TiO <sub>2</sub> samples treated at different temperature_____	92
Figure 3.6	Images of an electron gun and a LaB <sub>6</sub> filament_____	94
Figure 3.7	Schematic diagram of the layout of a scanning electron microscope_____	96
Figure 3.8	Differentiating between a solid ball ( <i>left</i> ) and a hollow sphere ( <i>right</i> ) in a transmission electron microscope_____	98
Figure 3.9	(a) Overhead view of a grid, showing the mesh. (b) Side view of a carbon coated grid showing the relative position of the carbon film to the grid and sample_____	100
Figure 3.10	Schematic diagram of a layout of an analytical transmission electron microscope_____	101
Figure 3.11	Specific area and dispersion are important characteristic properties of a supported catalyst_____	102
Figure 3.12	Eight different concentration of the MB dye solutions in vials_____	107
Figure 3.13	UV vis absorption spectra for different concentrations of MB dye solutions_____	108
Figure 3.14	The dyes absorbance versus their concentrations____	109
Figure 4.1	X-ray diffraction pattern of ZnO (i), TiO <sub>2</sub> (ii) and Fe <sub>3</sub> O <sub>4</sub> (iii) nanoparticle photocatalysts_____	117

Figure 4.2	FESEM picture of ZnO (A), TiO <sub>2</sub> (B) and Fe <sub>3</sub> O <sub>4</sub> (C) nanopowder photocatalysts_____	121
Figure 4.3	TEM picture of ZnO (A), TiO <sub>2</sub> (B) and Fe <sub>3</sub> O <sub>4</sub> (C) nanoparticle photocatalysts_____	123
Figure 4.4	Particle size distribution histogram for ZnO (A), TiO <sub>2</sub> (B) and Fe <sub>3</sub> O <sub>4</sub> (C) nanoparticles_____	124
Figure 4.5	Energy dispersive X-ray spectroscopy (EDX) for ZnO (A), TiO <sub>2</sub> (B) and Fe <sub>3</sub> O <sub>4</sub> (C) nanoparticles _____	127
Figure 4.6	Time variation of UV-vis absorption spectra of 12.0 ppm MB without photocatalyst under UV irradiation_____	131
Figure 4.7	Time variation of UV-vis absorption spectra of different concentration of MB without photocatalyst under UV irradiation _____	131
Figure 4.8	Time variation of UV-vis absorption spectra of 48.0 ppm PR without photocatalyst under UV irradiation_____	133
Figure 4.9	Time variation of UV-vis absorption spectra of different concentration of PR without photocatalyst under UV irradiation _____	133
Figure 4.10	Time variation of UV-vis absorption spectra of 32.0 ppm MO without photocatalyst under UV irradiation_____	135
Figure 4.11	Time variation of UV-vis absorption spectra of different concentration of MO without photocatalyst under UV irradiation__	135

Figure 4.12	Percentage degradation of MB (12.0 ppm) with different loading of ZnO photocatalyst_____	137
Figure 4.13	Percentage degradation of MB (12.0 ppm) with different loading of TiO <sub>2</sub> photocatalyst_____	138
Figure 4.14	Absorbance and Percentage degradation of MB (12.0 ppm) with different loading of Fe <sub>3</sub> O <sub>4</sub> photocatalyst_____	140
Figure 4.15	First-order kinetics on the effect of MB degradation with different loading of ZnO photocatalyst_____	142
Figure 4.16	First-order kinetics on the effect of MB degradation with different loading of TiO <sub>2</sub> photocatalyst_____	143
Figure 4.17	First-order kinetics on the effect of MB degradation with different loading of Fe <sub>3</sub> O <sub>4</sub> photocatalyst_____	144
Figure 4.18	Kinetic constant, <i>K</i> , of MB (12.0 ppm) with different loading of ZnO photocatalyst_____	146
Figure 4.19	Kinetic constant, <i>K</i> , of MB (12.0 ppm) with different loading of TiO <sub>2</sub> photocatalyst_____	146
Figure 4.20	Kinetic constant, <i>K</i> , of MB (12.0 ppm) with different loading of Fe <sub>3</sub> O <sub>4</sub> photocatalyst_____	147
Figure 4.21	UV-vis absorption spectra for different concentration of PR without photocatalyst_____	149
Figure 4.22	Absorbance versus concentration for PR dye _____	149
Figure 4.23	UV-vis absorption spectra for different concentration of MO without photocatalyst_____	150
Figure 4.24	Absorbance versus concentration for MO dye _____	150

Figure 4.25	Percentage degradation with different concentration of MB for ZnO, TiO <sub>2</sub> and Fe <sub>3</sub> O <sub>4</sub> photocatalyst_____	153
Figure 4.26	First-order kinetics on the effect of initial concentration of MB for ZnO, TiO <sub>2</sub> and Fe <sub>3</sub> O <sub>4</sub> photocatalyst_____	155
Figure 4.27	Kinetic constant, K, on the effect of initial concentration of MB for ZnO, TiO <sub>2</sub> and Fe <sub>3</sub> O <sub>4</sub> photocatalyst_____	157
Figure 4.28	Percentage degradation with different concentration of PR for ZnO, TiO <sub>2</sub> and Fe <sub>3</sub> O <sub>4</sub> photocatalyst_____	160
Figure 4.29	First-order kinetics on the effect of initial concentration of PR for ZnO, TiO <sub>2</sub> and Fe <sub>3</sub> O <sub>4</sub> photocatalyst_____	163
Figure 4.30	Kinetic constant, K, on the effect of initial concentration of PR by ZnO, TiO <sub>2</sub> and Fe <sub>3</sub> O <sub>4</sub> photocatalyst_____	165
Figure 4.31	Percentage degradation with different concentration of MO for ZnO, TiO <sub>2</sub> and TiO <sub>2</sub> photocatalyst_____	168
Figure 4.32	First-order kinetics on the effect of initial concentration of MO for ZnO, TiO <sub>2</sub> and Fe <sub>3</sub> O <sub>4</sub> photocatalyst_____	171
Figure 4.33	Kinetic constant, K, on the effect of initial concentration of MO for ZnO, TiO <sub>2</sub> and Fe <sub>3</sub> O <sub>4</sub> photocatalyst _____	173
Figure 4.34	Degradation of 12.0 ppm MB for ZnO (2.5wt%), TiO <sub>2</sub> (3.0wt%) and Fe <sub>3</sub> O <sub>4</sub> (3.0wt%) with the respective irradiation duration _____	176
Figure 4.35	Degradation of 16.0 ppm PR for ZnO, TiO <sub>2</sub> and Fe <sub>3</sub> O <sub>4</sub> for the respective irradiation duration_____	179

Figure 4.36	Degradation of 16.0 ppm MO for ZnO, TiO <sub>2</sub> and Fe <sub>3</sub> O <sub>4</sub> for the respective irradiation duration_____	182
Figure 5.1	FESEM microstructures for 20 wt% doped Fe <sub>3</sub> O <sub>4</sub> of ZnO/Fe <sub>3</sub> O <sub>4</sub> nanocomposites with different sintering temperature (200, 250, 300, 350, 400 and 450 °C)_____	192
Figure 5.2	XRD for ZnO/Fe <sub>3</sub> O <sub>4</sub> nanocomposites with different sintering temperature (200, 250, 300, 350, 400 and 450 °C)_	194
Figure 5.3	Energy dispersive X-ray spectroscopy (EDX) for different sintering temperature for ZnO/Fe <sub>3</sub> O <sub>4</sub> nanocomposites	196
Figure 5.4	FESEM microstructures for ZnO/Fe <sub>3</sub> O <sub>4</sub> nanocomposites with different wt% of Fe <sub>3</sub> O <sub>4</sub> (20, 15, 12, 10, 5 and 1wt%)	200
Figure 5.5	XRD for ZnO/Fe <sub>3</sub> O <sub>4</sub> nanocomposites with different wt% of Fe <sub>3</sub> O <sub>4</sub> (20, 15, 12, 10, 5 and 1wt%) sintered at 300 °C____	203
Figure 5.6	Energy dispersive X-ray spectroscopy (EDX) for different wt% of Fe <sub>3</sub> O <sub>4</sub> for ZnO/Fe <sub>3</sub> O <sub>4</sub> nanocomposites_____	205
Figure 5.7	TEM micrograph and Particle size distribution histogram for ZnO/Fe <sub>3</sub> O <sub>4</sub> nanocomposites_____	209
Figure 5.8	Percentage degradation of MB by different loading of ZnO/Fe <sub>3</sub> O <sub>4</sub> nanocomposites_____	211
Figure 5.9	Degradation rate for MB by different loading of ZnO/Fe <sub>3</sub> O <sub>4</sub> nanocomposites_____	212
Figure 5.10	Degradation rate of MB by different loading of ZnO/Fe <sub>3</sub> O <sub>4</sub> nanocomposites_____	213

Figure 5.11 Percentage degradation of MB for 20 wt% doped Fe <sub>3</sub> O <sub>4</sub> of ZnO/Fe <sub>3</sub> O <sub>4</sub> nanocomposites with different sintering temperatures.	214
Figure 5.12 First-order kinetics for the degradation of MB with different sintering temperature for ZnO/Fe <sub>3</sub> O <sub>4</sub> nanocomposites	215
Figure 5.13 Kinetic constant for ZnO/Fe <sub>3</sub> O <sub>4</sub> samples with different sintering temperature	216
Figure 5.14 Percentage degradation of MB for samples with different wt% of Fe <sub>3</sub> O <sub>4</sub> doped into ZnO/Fe <sub>3</sub> O <sub>4</sub> nanocomposite	218
Figure 5.15 Degradation rate of MB for samples with different wt% of Fe <sub>3</sub> O <sub>4</sub> doped into ZnO/Fe <sub>3</sub> O <sub>4</sub> nanocomposites	219
Figure 5.16 Kinetic constant for ZnO/Fe <sub>3</sub> O <sub>4</sub> samples with different wt% of doped Fe <sub>3</sub> O <sub>4</sub> nanoparticles	220
Figure 5.17 Hysteresis loop for ZnO and 10 wt% doped Fe <sub>3</sub> O <sub>4</sub> sintered at 300 °C of ZnO/Fe <sub>3</sub> O <sub>4</sub> (ZnF) nanoparticles	222
Figure 5.18 Separation of ZnO/Fe <sub>3</sub> O <sub>4</sub> nanocomposites in degraded MB dye solution by applying a magnetic field with a 0.6 T magnet	224
Figure 5.19 Repeatability experiment for ZnO/Fe <sub>3</sub> O <sub>4</sub> nanocomposites	226
Figure 6.1 FESEM microstructures for TiO <sub>2</sub> /Fe <sub>3</sub> O <sub>4</sub> nanocomposites for different sintering temperature (200, 250, 300, 350, 400 and 450 °C)	232

Figure 6.2	XRD for $\text{TiO}_2/\text{Fe}_3\text{O}_4$ nanocomposites for different sintering temperature (200, 250, 300, 350, 400 and 450 °C)_	234
Figure 6.3	Energy dispersive X-ray spectroscopy (EDX) for different sintering temperature for $\text{TiO}_2/\text{Fe}_3\text{O}_4$ nanocomposites	236
Figure 6.4	FESEM microstructures for $\text{TiO}_2/\text{Fe}_3\text{O}_4$ nanocomposites for different wt% of $\text{Fe}_3\text{O}_4$ (20, 15, 12, 10, 5 and 1wt%)	240
Figure 6.5	XRD for $\text{TiO}_2/\text{Fe}_3\text{O}_4$ nanocomposites for different wt% of $\text{Fe}_3\text{O}_4$ (20, 15, 12, 10, 5 and 1wt%)_____	242
Figure 6.6	Energy dispersive X-ray spectroscopy (EDX) for different wt% of $\text{Fe}_3\text{O}_4$ for $\text{TiO}_2/\text{Fe}_3\text{O}_4$ nanocomposites_____	244
Figure 6.7	TEM micrograph and Particle size distribution histogram for $\text{TiO}_2/\text{Fe}_3\text{O}_4$ nanocomposites_____	248
Figure 6.8	Percentage degradation and degradation rate of MB by different loading of $\text{TiO}_2/\text{Fe}_3\text{O}_4$ nanocomposite_____	250
Figure 6.9	Kinetic constant of MB by different loading of $\text{TiO}_2/\text{Fe}_3\text{O}_4$ nanocomposite_____	252
Figure 6.10	Percentage degradation of MB by $\text{TiO}_2/\text{Fe}_3\text{O}_4$ nanocomposite at different sintering temperature_____	253
Figure 6.11	First order kinetic of MB by different sintering temperature of $\text{TiO}_2/\text{Fe}_3\text{O}_4$ nanocomposite_____	254
Figure 6.12	Kinetic constant of MB by different sintering temperature of $\text{TiO}_2/\text{Fe}_3\text{O}_4$ nanocomposite_____	255
Figure 6.13	Percentage degradation of MB by different substitution of $\text{Fe}_3\text{O}_4$ into $\text{TiO}_2/\text{Fe}_3\text{O}_4$ nanocomposite_____	256

Figure 6.14	Degradation rate of MB by different addition of Fe <sub>3</sub> O <sub>4</sub> into TiO <sub>2</sub> /Fe <sub>3</sub> O <sub>4</sub> nanocomposite_____	257
Figure 6.15	Kinetic constant of MB by different substitution of Fe <sub>3</sub> O <sub>4</sub> into TiO <sub>2</sub> /Fe <sub>3</sub> O <sub>4</sub> nanocomposite_____	258
Figure 6.16	Hysteresis loop for TiO <sub>2</sub> (TiO <sub>2</sub> ) and TiO <sub>2</sub> /Fe <sub>3</sub> O <sub>4</sub> (TiF) nanocomposite powders_____	260
Figure 6.17	Separation of TiO <sub>2</sub> /Fe <sub>3</sub> O <sub>4</sub> powder in degraded MB dye solution by applying a magnetic field _____	262
Figure 6.18	Repeatability analysis of TiO <sub>2</sub> /Fe <sub>3</sub> O <sub>4</sub> nanocomposites	264
Figure 7.1	The kinetic constant and azo functional group of five dyes under decomposition of ZnO/Fe <sub>3</sub> O <sub>4</sub> composites nanoparticles	273
Figure 7.2	The kinetic constant and benzene functional group of five dyes under decomposition of ZnO/Fe <sub>3</sub> O <sub>4</sub> composites nanoparticles _____	275
Figure 7.3	The kinetic constant and molecular mass of five dyes under decomposition of ZnO/Fe <sub>3</sub> O <sub>4</sub> composites nanoparticles	277
Figure 7.4	The kinetic constant and absorbance of five dyes under decomposition of ZnO/Fe <sub>3</sub> O <sub>4</sub> composites nanoparticles	279
Figure 7.5	The kinetic constant of five dyes with various operational parameters under decomposition of ZnO/Fe <sub>3</sub> O <sub>4</sub> composites nanoparticles_____	280

## **LIST OF TABLES**

Table 1.1	Summary of advantages and disadvantages of common AOP technologies_____	7
Table 2.1	The Redox potential of a number of oxidants_____	25
Table 2.2	List of Dyes and their properties_____	74
Table 4.1	Crystallite size for different peaks and average crystallite size for ZnO, TiO <sub>2</sub> and Fe <sub>3</sub> O <sub>4</sub> nanoparticles_____	119
Table 4.2	BET data for ZnO, TiO <sub>2</sub> and Fe <sub>3</sub> O <sub>4</sub> nanoparticles_____	126
Table 4.3	EDX data of ZnO, TiO <sub>2</sub> and Fe <sub>3</sub> O <sub>4</sub> nanoparticles_____	128
Table 4.4	Kinetic constants for MB, PR and MO dye with ZnO, TiO <sub>2</sub> and Fe <sub>3</sub> O <sub>4</sub> photocatalysts_____	183
Table 5.1	BET data for different sintering temperature for ZnO/Fe <sub>3</sub> O <sub>4</sub> nanocomposites_____	195
Table 5.2	EDX data for different sintering temperature of ZnO/Fe <sub>3</sub> O <sub>4</sub> nanocomposites_____	197
Table 5.3	BET data for different wt% of Fe <sub>3</sub> O <sub>4</sub> for ZnO/Fe <sub>3</sub> O <sub>4</sub> nanocomposites_____	204
Table 5.4	EDX data for different wt% of Fe <sub>3</sub> O <sub>4</sub> of ZnO/Fe <sub>3</sub> O <sub>4</sub> nanocomposites_____	206
Table 6.1	BET data for different sintering temperature for TiO <sub>2</sub> /Fe <sub>3</sub> O <sub>4</sub> nanocomposites_____	235
Table 6.2	EDX data for different sintering temperature of TiO <sub>2</sub> /Fe <sub>3</sub> O <sub>4</sub> nanocomposites_____	237

Table 6.3	BET data for different wt% of Fe <sub>3</sub> O <sub>4</sub> for TiO <sub>2</sub> /Fe <sub>3</sub> O <sub>4</sub> nanocomposites_____	243
Table 6.4	EDX data for different wt% of Fe <sub>3</sub> O <sub>4</sub> of TiO <sub>2</sub> /Fe <sub>3</sub> O <sub>4</sub> nanocomposites_____	245

## **LIST OF ABBREVIATION**

AOP	Advanced oxidation process
CB	Conduction band
CO <sub>2</sub>	Carbon dioxide
E <sub>g</sub>	Energy gap
EHP	Electron hole pair
FESEM	Field emission scanning electron microscopy
Fe <sub>3</sub> O <sub>4</sub>	Iron (II,III) oxide (magnetite)
FP	Final product
H <sub>2</sub> O	Water
LH	Langmuir–Hinshelwood (model)
MB	Methylene blue
MO	Methyl orange
MOS	Metal oxide semiconductor
O <sub>3</sub>	Ozone
PR	Phenol red
SACNT	Superaligned carbon nanotube
SEM	Scanning electron microscopy
T	[Tesla]
TEM	Transmission electron microscopy
TiO <sub>2</sub>	Titanium dioxide
US	Ultrasound
UV	Ultraviolet

VB	Valence band
VSM	Vibrating sample magnetometry
XRD	X-Ray Diffraction
ZnO	Zinc oxide

## **CHAPTER 1**

### **Introduction**

#### **1.1 Introduction**

Organic compounds such as dyes from textiles, paper, printing, cosmetics and other industries are the main source of environmental contamination. Contaminations by these non-biodegradable effluents such as organic dyes and heavy metal ions into ground water system face a serious environmental threat to the environment and human health, due to the released of toxic and carcinogenic substances they possess (Kansal, Singh, & Sud, 2007; T. F. Shen et al., 2009). For example, the widely used methyl orange in printing, paper, textiles, pharmaceutical and food industries has been proved fatal and could induce cancers in human (Chung, Stevens, & Cerniglia, 1992).

There are many potential conventional treatment methods being implemented to remove such contaminated wastewater like adsorption, coagulation and flocculation, however each having limitations and are non-destructive (Maliyekkal, Lisha, & Pradeep, 2010). These, however, are not the most effective and best ways to process them, which include poor removal of color and trace organic compounds, since they are just merely converted the dyes from liquidize phase into the solid phase, which require

additional treatment and may add into different kinds of pollution and toxic by-products (Padmanabhan et al., 2006).

Another conventional methods used in water purification are sedimentation, filtration and chemical & membrane technologies. However, these methods involve high operating costs and could also generate secondary pollutants into the water system (Gaya & Abdullah, 2008). Nonetheless, most common and widely used disinfection process is chlorination. Similarly, disinfection by-products generated from chlorination are mutagenic and carcinogenic to human health (Matilainen & Sillanpaa, 2010).

There is a report on conventional wastewater treatment which proved to be mostly unsuccessful for removing textile dyes from wastewater stream due to the resilient and stability of these pollutants (Forgacs, Cserhati, & Oros, 2004). Huge amount of textile dyes are resistant to chemical and biological degradation. Therefore, the aforementioned processes have various limitations in efficacy to totally decompose dyes contaminated effluents discharge from industries sewage system (Schwarzenbach, Egli, Hofstetter, von Gunten, & Wehrli, 2010).

In light of these, advanced oxidation processes (AOPs) have seen as an alternative and potential method that may improve the overall removal of the toxicity of various types of recalcitrant water pollutants. Among the

highly utilized in AOPs is the ultraviolet (UV)-assisted processes by employing hydroxyl radicals ( $\cdot\text{OH}$ ) which have been shown to be very effective in decolorization of textile dye effluents (Bansal & Sud, 2011). There are several methods for generating  $\cdot\text{OH}$  radicals, e.g. Fenton-based processes (Babuponnusami & Muthukumar, 2014), UV-based processes (Baffoun, El Ghali, & Hachani, 2017), ozone based processes (Saileshkumar Singh, Seth, Tabe, & Yang, 2015) and photocatalytic processes (Ahmad et al., 2013).

Therefore, highly effective and promising tool among the AOPs in the light of substituting the traditional wastewater treatment system is the photocatalysis by semiconductor materials such as  $\text{TiO}_2$ ,  $\text{SiO}_2$ ,  $\text{ZnO}$ ,  $\text{Fe}_2\text{O}_3$ ,  $\text{CdS}$ ,  $\text{ZnS}$ , etc. AOPs are based on the utilization of the highly powerful and non-selective oxidant  $\cdot\text{OH}$  radicals for oxidation/degradation processes. In addition, under natural water conditions,  $\cdot\text{OH}$  radical is very easy to produce as well as ubiquitous in nature. Oxidation can be understood as, for inorganic compounds, to the removal of electrons to produce higher oxidation state, e.g.  $\text{Fe}^{2+}$  to  $\text{Fe}^{3+}$ , and for organic compounds, to the production of oxygenated compounds (Rizzo, Meric, Guida, Kassinos, & Belgiorno, 2009).

Currently, these semiconductor oxides are the most favourable photocatalyst in air and water purification system because of their nano-scale sizes and high photocatalytic efficiency, such as  $\text{TiO}_2$  and  $\text{ZnO}$  nanoparticles (Fujishima, Rao, & Tryk, 2000; J. Kaur & Singhal, 2014). For  $\text{TiO}_2$

photocatalyst, anatase phase is the most preferable material for the photocatalytic process due to its high photosensitivity, non-toxicity, large band gap and stability (Dette et al., 2014; Tudose & Sucheai, 2016). With the high band gap ( $E_g \sim 3.2$  eV), it is excited only by the UV light ( $\lambda \sim 388$  nm) irradiation and limits the use of sunlight or visible light (Grabowska, 2016; Seriani, Pinilla, & Crespo, 2015). Despite those positive attributes, there are few drawbacks with  $\text{TiO}_2$  photocatalyst. The first one is the instant recombination between the charge carrier which occurs within nanoseconds (Linsebigler, Lu, & Yates, 1995), and the second drawback is the band edge absorption threshold does not allow the utilization across the visible light irradiation (Seriani et al., 2015).

On the other hand, the use of ZnO as a photocatalyst as compared to  $\text{TiO}_2$ , has grown quite substantially, to be an alternative photocatalyst due to its low cost, high stability and possesses almost similar band gap energy compared to  $\text{TiO}_2$ . Thus, it can absorb over a larger fraction of UV spectrum. ZnO photocatalyst has wide band gap energy (3.37 eV) and a large exciton binding energy (60 meV) at room temperature (Han et al., 2012). ZnO is also biocompatible, biodegradable and biosafe for medical and environmental applications (Zhang et al., 2014).

Although traditional process has been a very effective and environmentally safe method in separating the organic substances from the contaminated wastewater effluent, however additional step is required to

separate the photocatalytic substance from the treated wastewater. This has brought in an additional cost in the treatment of the wastewater which causes many industries feel reluctant to apply this method in their treatment plant.

Most of the photocatalytic processes are in the slurry-type systems. However, the challenge is to create an economically reliable technology to separate the solid-liquid photocatalytic system after treatment since the photocatalytic particles tend to be fine powders. Expensive post-treatment separation methods are often needed to recover the catalyst. As a result, researchers have studied ways to increase the size of the catalyst particle so that they are easier to filter or better to pack into a fixed column, and have investigated methods to incorporate the magnetic properties of the catalyst particle so that they can easily be recovered (Beydoun, Amal, Low, & McEvoy, 2000; F. Chen, Xie, Zhao, & Lu, 2001). Many researchers have attempted to immobilize TiO<sub>2</sub> on solid surfaces such as silica, glass and carbon fibers, woven fiber cloth, and ceramic materials (Pirkanniemi & Sillanpää, 2002). Various preparation methods have been used to combine the catalyst with mesoporous silica to develop new catalytic functions for the materials (Mohseni, 2005; Reddy, Davydov, & Smirniotis, 2003). Nevertheless, it does not seem to be easy to replicate and exceed the photocatalytic performance of slurry-type systems which use pure and well-crystallized high-surface TiO<sub>2</sub> particles such as the commercially available P25 (Dalrymple, Yeh, & Trotz, 2007).

Therefore, in view of the obstacles discussed previously, this study has been carried out to apply an effective and novel approach, as well as cost minimization, in solving this processing stage, that is by adding a magnetic property to the photocatalyst. This will allow the photocatalyst to be separated and collected easily and directly by just applying a magnetic field to the system. Besides, the collected materials could be reused for subsequent cycle and still achieve almost the same efficiency. In this context, incorporation of iron oxide nanoparticle to the photocatalyst material seems a promising approach. The superparamagnetic Fe<sub>3</sub>O<sub>4</sub> nanoparticles exhibit optimal magnetic properties and with essential functionality, may contribute to higher adsorption efficiency, and easy and rapid separation of the adsorbent from solution could be achieved by just applying a magnetic field (Sarika Singh, Barick, & Bahadur, 2013). Table 1.1 illustrates the advantages the disadvantages of the most common advanced photocatalytic processes.

Table 1.1 Summary of advantages and disadvantages of common AOP technologies (Cesaro, Naddeo, & Belgiorno, 2013).

<b>AOP</b>	<b>ADVANTAGES</b>	<b>DISADVANTAGES</b>
<b>O<sub>3</sub></b>	<ul style="list-style-type: none"> <li>- Strong oxidizing power with a short reaction time.</li> <li>- No chemicals added to the water.</li> <li>- Can eliminate a wide spectrum of contaminants.</li> </ul>	<ul style="list-style-type: none"> <li>- There is a higher equipment and operational cost.</li> <li>- System may require pretreatment.</li> <li>- Energy and cost intensive.</li> <li>- Potential fire hazards and toxicity issues associated with ozone generation.</li> </ul>
<b>O<sub>3</sub> - UV</b>	<ul style="list-style-type: none"> <li>- High efficiency in water treatment.</li> <li>- More effective than O<sub>3</sub> or UV.</li> <li>- More efficient at generating •OH radicals than H<sub>2</sub>O<sub>2</sub>/UV process for equal oxidant concentrations.</li> <li>- Disinfection supplementary.</li> </ul>	<ul style="list-style-type: none"> <li>- More energy intensive than single processes.</li> <li>- Potential bromate formation.</li> <li>- Turbidity can interfere with UV light penetration.</li> <li>- Ozone diffusion can result in mass transfer limitations.</li> <li>- Potential increase in trihalomethane (THM) and nine haloacetic acid (HAA<sub>9</sub>) formation when combined with pre and/or post-chlorination.</li> </ul>

<p><b>H<sub>2</sub>O<sub>2</sub> – UV</b></p>	<ul style="list-style-type: none"> <li>- UV irradiation can serve as disinfectant.</li> <li>- Existing of full-scale drinking water treatment.</li> </ul>	<ul style="list-style-type: none"> <li>- Turbidity can interfere with UV light penetration.</li> <li>- Less stoichiometry efficient at generating •OH radicals than O<sub>3</sub>/UV process.</li> </ul>
<p><b>O<sub>3</sub> – H<sub>2</sub>O<sub>2</sub></b></p>	<ul style="list-style-type: none"> <li>- High efficiency in water treatment.</li> <li>- More effective than O<sub>3</sub> or UV.</li> <li>- Established technology for remediation applications.</li> <li>- Disinfection supplementary.</li> </ul>	<ul style="list-style-type: none"> <li>- Potential for bromate formation.</li> <li>- May require treatment of excess H<sub>2</sub>O<sub>2</sub> due to potential for microbial growth.</li> <li>- Energy and cost intensive process.</li> </ul>
<p><b>TiO<sub>2</sub> - UV</b></p>	<ul style="list-style-type: none"> <li>- Can be performed at higher (300 – 380 nm) wavelengths than other UV oxidation processes.</li> </ul>	<ul style="list-style-type: none"> <li>- Pre-treatment necessary to avoid fouling of the TiO<sub>2</sub> catalyst.</li> <li>- If TiO<sub>2</sub> is added as a slurry, then a separation step is required.</li> <li>- Potential for rapid loss of TiO<sub>2</sub> activity, requiring catalyst on-site storage or regeneration method.</li> </ul>

<p><b>Ultrasound (US)</b></p>	<ul style="list-style-type: none"> <li>- Versatile design with low maintenance.</li> <li>- Interesting upgrade applications.</li> <li>- Degradation of chemicals pollutants.</li> <li>- Economical treatment of small volumes.</li> </ul>	<ul style="list-style-type: none"> <li>- Design criteria still developing.</li> <li>- Increase of the water turbidity.</li> <li>- Energy consuming technology.</li> <li>- Ultrasound probe erosion issues; increase consumption.</li> <li>- Long sonication time.</li> </ul>
<p><b>Fe<sup>2+</sup> - H<sub>2</sub>O<sub>2</sub></b></p>	<ul style="list-style-type: none"> <li>- Not as energy intensive as compared to AOPs that utilize O<sub>3</sub> or UV.</li> </ul>	<ul style="list-style-type: none"> <li>- No-full scale applications exist.</li> <li>- Requires iron extraction system; higher cost.</li> <li>- Very low pH (&lt;2.5) is required to keep the iron in solution.</li> <li>- pH adjustment will increase operation and maintenance costs.</li> </ul>

## **1.2 Rationale and Novelty of the Study**

From the above discussion thus arise the rationale of the current study. One of the most effective tools among the advanced oxidation water treatment processes is the *in situ* photodegradation of water pollutants using photocatalyst nanomaterial, which are ZnO and TiO<sub>2</sub> semiconductors. The photocatalytic process is attributed to its stability, non-toxic, low cost and suitability towards solar spectrum. Although the details mechanism in the photocatalytic process is very complex and the pathway is not yet very clear, very extensive study is going on in this field. Besides, the ability of these photocatalysts to carry the magnetic properties without compromising their photocatalytic properties is the main rationale of producing a magnetic photocatalyst which can be easily magnetically separated from the solutions after the degradation process has been taken place. This again brought another advantage as no additional waste will be produced or generated during purification processes. This is because the magnetic photocatalyst can be easily separated by applying magnetic field after the treatment process. The regenerated photocatalyst material can then be subjected for subsequent batch of photodegradation process. The recyclability of the photocatalyst material from an aqueous system is particularly promising for large scale commercial application.

Albeit there have been many studies on the magnetic photocatalysts (Chiu et al., 2010; J. Wang et al., 2016), most of the methods used are

adopting various incalcitrant chemicals and sintered at highly pronounced temperature (S.-E. Kim et al., 2016). The chemical agents like *n*-hexane, APTMS and glycerol are unfriendly organic materials to the environment (Hou et al., 2015). In addition, few of the preparation temperature was as high as 700 °C (Deraz & Alarifi, 2012). Therefore, the novelty of this study is twofold, that is to prepare the sample in a mechanically simple method and sinter at a moderate temperature. These novelties would tremendously contribute to broader applications and it may also be further refined to their need and requirement.

### **1.3 Objectives of the Study**

The objectives of current study are to:

- i) prepare and characterize magnetic photocatalysts of ZnO/Fe<sub>3</sub>O<sub>4</sub> and TiO<sub>2</sub>/Fe<sub>3</sub>O<sub>4</sub>.
- ii) characterize and evaluate the ZnO/Fe<sub>3</sub>O<sub>4</sub> and TiO<sub>2</sub>/Fe<sub>3</sub>O<sub>4</sub> magnetic photocatalysts by FESEM, TEM, XRD, and BET.
- iii) investigate the photodecomposition efficiency of ZnO/Fe<sub>3</sub>O<sub>4</sub> and TiO<sub>2</sub>/Fe<sub>3</sub>O<sub>4</sub> on organic dyes under various experimental condition

such as catalyst loading, Fe<sub>3</sub>O<sub>4</sub> substitution and sintering temperature.

- iv) study the photodegradation effect and kinetic study of these photocatalysts on the wider range of organic dyes characteristics, such as their azo groups, benzene groups, molecular weight and absorbance.

#### **1.4 Thesis Framework**

This thesis has been organized into eight chapters.

Chapter 1 is a brief introduction on the general problems faced by few implementations on water purification. In addition, all processes related to AOPs were tabled with their advantages and disadvantages. The rationale and objectives of this study were also mentioned.

Chapter 2 provides a comprehensive review of background studies on the principle of photocatalyst, types of photocatalyst, photocatalytic optimization and effect of different parameters on the photocatalytic efficiency.

Chapter 3 describes the experimental procedures in detailed for the entire study. First part provides the material used while the second part indicates the preparation of the magnetic nanocomposites. The third part explains in detail characterization used in the experiments.

Chapter 4 serves the characterization results for all the three purchased powder, ZnO, TiO<sub>2</sub> and Fe<sub>3</sub>O<sub>4</sub>. In addition, it also provides detailed photocatalytic experimental results on the photodecomposition of MB dye, followed by few results on MO and PR dyes.

Chapter 5 presents the characterization for the ZnO/Fe<sub>3</sub>O<sub>4</sub> nanocomposite. Moreover, it also includes the optimization properties, such as photocatalyst loading, sintering temperature and different weight percent of doped Fe<sub>3</sub>O<sub>4</sub>, in the photodecomposition of MB dye.

Chapter 6 provides the characterization for the TiO<sub>2</sub>/Fe<sub>3</sub>O<sub>4</sub> nanocomposite. On the other hand, it also describes the photodecomposition of MB dye under the optimization properties of the nanocomposite, such as photocatalyst loading, sintering temperature and different weight percent of doped Fe<sub>3</sub>O<sub>4</sub>.

Chapter 7 highlights the photodecomposition of the ZnO/Fe<sub>3</sub>O<sub>4</sub> nanocomposite with reference to properties of few chosen dyes, such

as their azo groups, benzene groups, molecular weight and absorbance, in relation to their rate of decomposition.

Chapter 8 concludes the work done in the study and provides propositions for further studies and improvement.

## **CHAPTER 2**

### **Background Studies**

#### **2.1 Introduction**

Water is one of the most essential resources on Earth that helps in various daily activities. These activities can be as simple as household chores, and others are like commercial, institution, agricultural and the most severe are industries, which consumed more than one-third of Earth's accessible renewable freshwater (Schwarzenbach et al., 2010). As a result from these daily activities, all sorts of wastes are produced and being released into the stream, as well as into the air. Those liquid waste, called wastewater, will assimilate with surface water and/or stormwater, and finally with groundwater. It was estimated about 300 million tons of synthetic compounds being used by industries and 140 million tons of fertilizers and several million tons of pesticides being applied by agriculture, annually (Schwarzenbach et al., 2010). Besides, naturally occurred geological elements, such as arsenic-enriched geothermal waters, has also contributed to the amount of arsenic in surface water. Untreated wastewater, or even surface water, may contain various pathogenic microorganisms, nutrients, as well as toxic compounds that may potentially be harmful, mutagenic or carcinogenic. Therefore, immediate or subsequent handling of these wastewater through proper treatment, high efficiency treatment technology,

is necessary before disposal into the stream to secure a healthy and safety freshwater system.

With the rapid growth of various industries and population, the requirement for clean water demand has inadvertently surfaced. About 15% of the world's population lives in areas under water intensification. It is due to intense development that changed the face of the land, especially for agriculture, electric power source and settlements adjacent to the water bodies (Palmer, 2010). In addition, volume of clean water being contaminated keep on increasing due to the continuous discharge of micropollutants and contaminants into the stream (Schwarzenbach et al., 2010).

One alternative option to offset more clean water resources is the possible reuse of treated municipal wastewater from treatment plants for agricultural and industrial activity. However for commercial usage, associated handling processes, like suspended solid, health-treat coliform, and soluble refractory organic compounds, are very tedious and very expensive to treat (Schwarzenbach et al., 2010). Another option currently available, like adsorption and coagulation, are just transferring the pollutants into another phases of constituents, without completely destroy them, or transform them into safer elements (Padmanabhan et al., 2006). One commonly used conventional methods are sedimentation, filtration, and chemical and membrane technologies. However, this methods could easily escalate the

operating cost and generate secondary pollutants that are highly toxic to the environment (Gaya & Abdullah, 2008). In addition, another widely used disinfection process is the chlorination. However, similar problem arises, that is disinfection by-products generated from chlorination are mutagenic and carcinogenic to human health (Schwarzenbach et al., 2010).

Another commonly used method for wastewater treatment is the oxidation processes. One of the available and feasible choices is biological oxidation. However, biodegradation is uneconomical as it is very slow and produces unpredictable results due to high concentrated waste and toxic pollutants. On the other hand, physical techniques such as adsorption on activated carbon, reverse osmosis and incineration can be used for water treatment. These, however, also not as good since they are nondestructive and even produce dangerous and toxic secondary. This requires additional treatment which are expensive to operate (Zangeneh, Zinatizadeh, Habibi, Akia, & Isa, 2015). On top of that, chemical methods, too have been very expensive due to requirement of high dosage chemicals and production of large quantity of sludge (Schwarzenbach et al., 2010). Therefore, wastewater treatment using conventional methods are facing various obstacles and difficulties. In view of these, better and more efficient treatments in reducing and completely terminate such contaminants should be developed. One of the increasing interests is based on the generation of very reactive and oxidizing capability free radicals due to their high oxidant power (Zangeneh et al., 2015). This is the innovative water treatment

technologies due to the rapid development in research and development in the field of "Advanced Oxidation Processes (AOPs)". AOPs has been a promising and emerging alternative technology due to its novel and economical feature, as it is based on the *in-situ* generation of highly reactive transitory species (i.e.  $\text{H}_2\text{O}_2$ ,  $\text{OH}\cdot$ ,  $\text{O}_2^{\cdot-}$ ) for mineralization of organic compounds, water pathogens and disinfection by-products (Schwarzenbach et al., 2010). As mentioned earlier, there are many ways in producing these free radicals, especially  $\cdot\text{OH}$  radicals, such as Fenton-based processes, UV-based processes, ozone-based processes and photocatalytic processes. Among these AOPs, an escalating alternative in treating wastewater effluents is heterogeneous photocatalysis employing semiconductor catalysts such as  $\text{TiO}_2$ ,  $\text{ZnO}$ ,  $\text{Fe}_2\text{O}_3$ ,  $\text{CdS}$ ,  $\text{GaP}$  and  $\text{ZnS}$ . This is because it demonstrates strong degradation efficiency on various organic pollutants by transforming them into intermediate compounds and finally mineralized them into innocuous carbon dioxide and water (Robinson, McMullan, Marchant, & Nigam, 2001; Venkatachalam, Palanichamy, & Murugesan, 2007).

## **2.2 The Influence of Nanostructured Materials**

The term nanotechnology has been extensively used and applied to various materials and systems that show significant improvement in the physical, chemical properties and processes as a result of the limited dimension of each constituent particles or molecules. It is the science of the

fabrication of novel materials, devices and systems through manipulation of the molecular and atomic dimensions at the nanoscale level. The significant behavior is due to the structural features linkage between the single atom and bulk materials, in the size of 1 to 100 nm (Zhu et al., 2011), displaying physical attributes substantially different from those atoms or bulks materials. Therefore, with reduction in the spatial dimension or the confinement of particles in their crystal structure, has significantly changes the physicochemical properties of the nanostructured materials and its systems (X. Shen, Liang, Zhai, & Ning, 2013). Therefore, nanomaterials advancement has been widely applied into commercial usage such as catalyst, semiconductors, microelectronics, cosmetics, pharmaceuticals, energy storage and corrosion resistant coatings (Farre, Gajda-Schranz, Kantiani, & Barcelo, 2009).

Current development in the research of nanostructured materials is reviewed as one of the most advanced and interdisciplinary field of research in physics, chemistry, engineering and bioscience (Porter & Youtie, 2009). The microstructure and properties of nanostructured materials and systems are designed and fabricated through mechanical, chemical or biological growth, shaping or assembling, as well as on the processing route. With this flexible approaches and assembling ideas, it is of utmost importance to select the most suitable technique for preparation of nanomaterials with desired properties and property combinations. There are two famous approaches in achieving this, as shown in Figure 2.1. The first is the bottom-up approach

that fabricates the substances or devices at the atomic or molecular level. Bottom-up processes includes many different techniques which are based on liquid or gas phase processes, and effectively encompass chemical synthesis and/or the highly controlled deposition and growth of materials. The processes are such as vapour phase deposition method, plasma-assisted deposition processes, molecular beam epitaxy (MBE) and metallorganic vapour phase epitaxy (MOVPE), liquid phase methods, colloidal methods, sol-gel methods and electrodeposition. Classically, wet chemical processes such as precipitation and sol-gel have been employed to obtain nanoparticles, however, with the disadvantage of severe agglomeration. The electrodeposition under oxidizing conditions (EDOC) process was developed to synthesize nanocrystalline oxides with improved properties as compared to oxides obtained by precipitation and sol-gel routes (Kelsall, Hamley, & Geoghegan, 2006). In this process, as well as other related processes, it showed that the microstructure, the morphology, the size and size distribution, the agglomeration, the elemental distribution and surfaces modification can be controlled (Kelsall et al., 2006). The next method is the top-down approach which is etching or milling of smaller structures from larger ones. The initiation of this approach is by using materials with conventional crystalline microstructures, typically metals and alloys, and involves the removal or reformation of atoms to create the desired structure, such as milling, lithographic processes and machining (Kelsall et al., 2006). This recrystallization of the material leads to finer and finer grain sizes and under certain processing condition to nanostructured materials. The

advantage of these approaches is the fact that bulk nanostructured materials with theoretical density can be prepared. An alternative to obtain theoretical dense materials is the pulsed electrodeposition method developed by El-Sherik and Erb (1995) which yields nanocrystalline strips, however, only with thicknesses of several hundred microns (El-Sherik & Erb, 1995; K. S. Kumar, Van Swygenhoven, & Suresh, 2003).

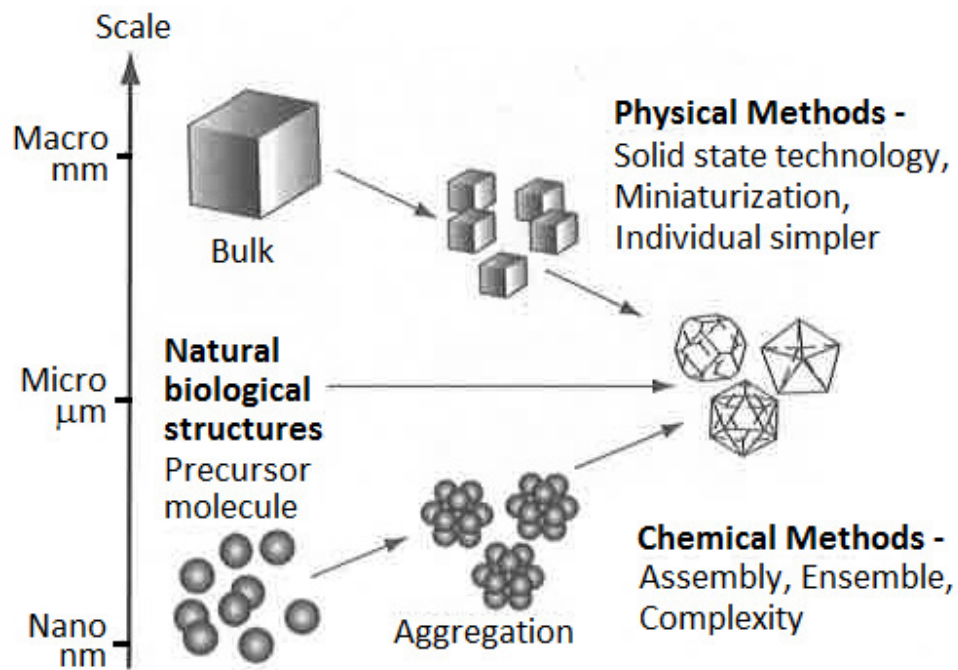


Figure 2.1 Schematic representation of the top-down and bottom-up processes and their relationship to biological processes and structures (Kelsall et al., 2006).

The influence of the nanoscale systems will be directly related to the energy band structure which can indirectly lead to changes in the associated atomic structure of the systems. Besides, many properties are continuously

modified as a function of system size. Often these are appealing extrinsic properties which depend on the exact size and shape of the specimens, such as ultra-high yield and fracture strengths, changes in elongation and toughness, superior wear resistance, and the promise of enhanced superplastic formability at lower temperatures and faster strain rates (K. S. Kumar et al., 2003). Other properties depend critically on the microstructure of the materials, for example the strengthening with grain refinement has been closely rationalized to Hall-Petch mechanism for yield strength, as can be seen in Figure 2.2 (Kelsall et al., 2006; K. S. Kumar et al., 2003).

As the microstructure is refined from micron to nanometer size, it is clearly seen that the microstructure gained more pronounced yield strength. Further refinement of the grain seems, in many cases, the yield strength peaks at the average grain size on the order of 10 nm. By going over this grain size can cause weakening of the metal. However, the causes of the underlying mechanisms are not well understood even though many experimental evidences resulted in similar unusual deformation (K. S. Kumar et al., 2003).

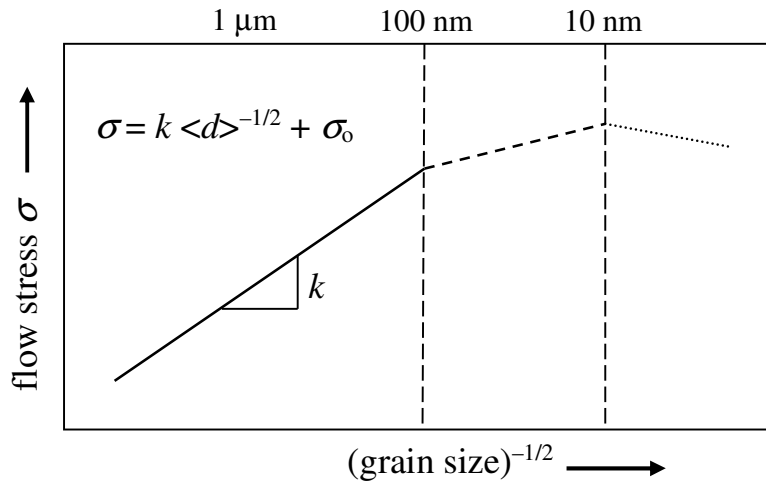


Figure 2.2 Schematic representation of the variation of yield stress as a function of grain size in microcrystalline, ultrafine crystalline and nanocrystalline metals and alloys.  $\langle d \rangle$  is average grain size and  $k$ ,  $\sigma_0$  are constants (K. S. Kumar et al., 2003).

Intrinsic materials properties, such as resistivity, should be independent of specimen size, however, even many of the intrinsic properties of matter at the nanoscale are not necessarily predictable from those observed at the larger scales. This is because totally new phenomena can emerge, such as quantum size confinement leading to changes in electronic structure; the presence of wave-like transport processes, and the predominance of interfacial effects. This effect is generally termed as quantum confinement, results in variation in the system total energy, the system structure, structural properties, thermal properties, chemical properties, mechanical properties, magnetic properties, optical properties,

electronic properties and finally the behavior of whole biological systems (Kelsall et al., 2006).

### **2.3 Principles of Photocatalysis**

Photocatalysis is a photochemical reaction using a catalyst under light (UV/Sunlight) irradiation. By principle, the catalyst participates and accelerates in the chemical reaction but itself remain unaltered at the end of the reaction which reacts according to the characteristics of semiconductors to decompose organic pollutants (Dalrymple et al., 2007). Photocatalytic process is an advantages technology over others due to its efficiency, environmentally friendly and cost effective AOPs. It leaves neither residual waste nor transferring them into other phase. This process runs under ambient conditions with atmospheric oxygen and solar light as its oxidant and light source, respectively, and generally leads to complete mineralization of organic pollutants into CO<sub>2</sub> and H<sub>2</sub>O (Zhan, Zhou, Fu, & Zhen, 2011).

Basically, AOPs are based on the generation of a very reactive oxidizing agent such as hydroxyl radicals (OH•). Table 2.1 lists various oxidants with their redox potential, with reference to the normal hydrogen electrode (NHE). This OH• radicals able to oxidize a wide varieties of organic matters in water very quickly due to its non-selectivity characteristic (Ibhadon & Fitzpatrick, 2013). Current photocatalytic processes applied in

the wastewater treatment are heterogeneous photocatalysts. They are called as such because they present in two different phases, liquid and solid phases. Heterogeneous photocatalysts are using various oxides ( $\text{TiO}_2$ ,  $\text{ZnO}$ ,  $\text{CeO}_2$ ,  $\text{ZrO}_2$ ,  $\text{WO}_3$ ,  $\text{Fe}_2\text{O}_3$ , etc.) and sulfides ( $\text{CdS}$ ,  $\text{ZnS}$ , etc.) semiconductors (Lee, Nam, Kim, & Boo, 2012).

Table 2.1 The Redox potential of a number of oxidants (Grote, 2012).

<b>Oxidant</b>	<b>Redox potential, V vs NHE</b>
Fluorine, $\text{F}_2$	3.06
Hydroxide radical, $\text{HO}\bullet$	2.80
Oxygen radical, $\text{O}\bullet$	2.42
Ozone, $\text{O}_3$	2.08
Hydroperoxyl radical, $\text{HO}_2\bullet$	1.70
Hydrogen peroxide, $\text{H}_2\text{O}_2$	1.78
Potassium permanganate, $\text{KMn}_4$	1.67
Hypochlorous, $\text{HOCl}$	1.49
Chlorine, $\text{Cl}_2$	1.36
Chlorine dioxide, $\text{ClO}_2$	1.27
Oxygen, $\text{O}_2$	1.23

Among the most extensively studied photocatalysts is titanium dioxide ( $\text{TiO}_2$ ). This is due to its multiple and strong characteristics such as high photocatalytic activity, photostability, biologically and chemically stable, low

energy consumption, low operation temperature, suitable flat band potential, insoluble in water and exhibiting undesirable by-products formation. On the other hand, zinc oxide (ZnO) has also been found to be a suitable photocatalyst in many applications as it also exhibits the above characteristics as TiO<sub>2</sub> does, if not all. Besides having similar band gap energy with TiO<sub>2</sub>, the biggest advantage of manipulating ZnO photocatalyst instead of TiO<sub>2</sub> is its ability to adsorb over a larger fraction of UV spectrum with the corresponding threshold of 425 nm (Hunge, 2017). The photocatalytic activity of a semiconductor depends greatly on its surfaces and structural properties, such as surface area, porosity, band gap energy, particle size distribution and crystal composition. Particle size of a semiconductor photocatalyst is important as it determines the photocatalyst surface area because most interactions in heterogeneous photocatalyst takes place on the surface. The specific surface area will increase as the particle size decreases thus increase the active sites for the photochemical activity to take place.

### *2.3.1 Photocatalyst Reaction*

Briefly, photocatalytic process by metal oxide semiconductor (MOS), e.g. wide band gap energy like ZnO and TiO<sub>2</sub>, takes place upon the UV irradiation with energy equal or higher than the band gap energy,  $E_g$ . An electron ( $e^-$ ) and hole ( $h^+$ ) pair is generated upon irradiation where valence

band (VB) electrons are promoted to the conduction band (CB) leaving a hole behind (1). These electron-hole pairs (EHPs) can either recombine (2) or interact separately with other molecules. The holes at the oxide semiconductor valence band can oxidize adsorbed water or hydroxide ions to produce  $\cdot\text{OH}$  radicals (3) & (4).

On the other hand, electron in the conduction band on the catalyst surface can reduce molecular oxygen to superoxide anion (5). This radical may be protonated to form the hydroperoxyl radical ( $\text{HO}_2\cdot$ ) and subsequently form hydrogen peroxide (6) or organic peroxides ( $\text{R}_{\text{org}}\text{-OO}\cdot$ ) in the presence of organic scavengers (7). The  $\cdot\text{OH}$  radical is a powerful oxidizing agent that attaches to organic compounds ( $\text{R}_{\text{org}}$ ) and consequently intermediates are formed (8). These intermediates react with  $\cdot\text{OH}$  radicals to produce final products (FP), such as  $\text{CO}_2$ ,  $\text{H}_2\text{O}$  and weak acid (9) (Shinde, Shinde, Bhosale, & Rajpure, 2011). A brief mechanism of the photocatalysis process is depicted in Figure 2.3.



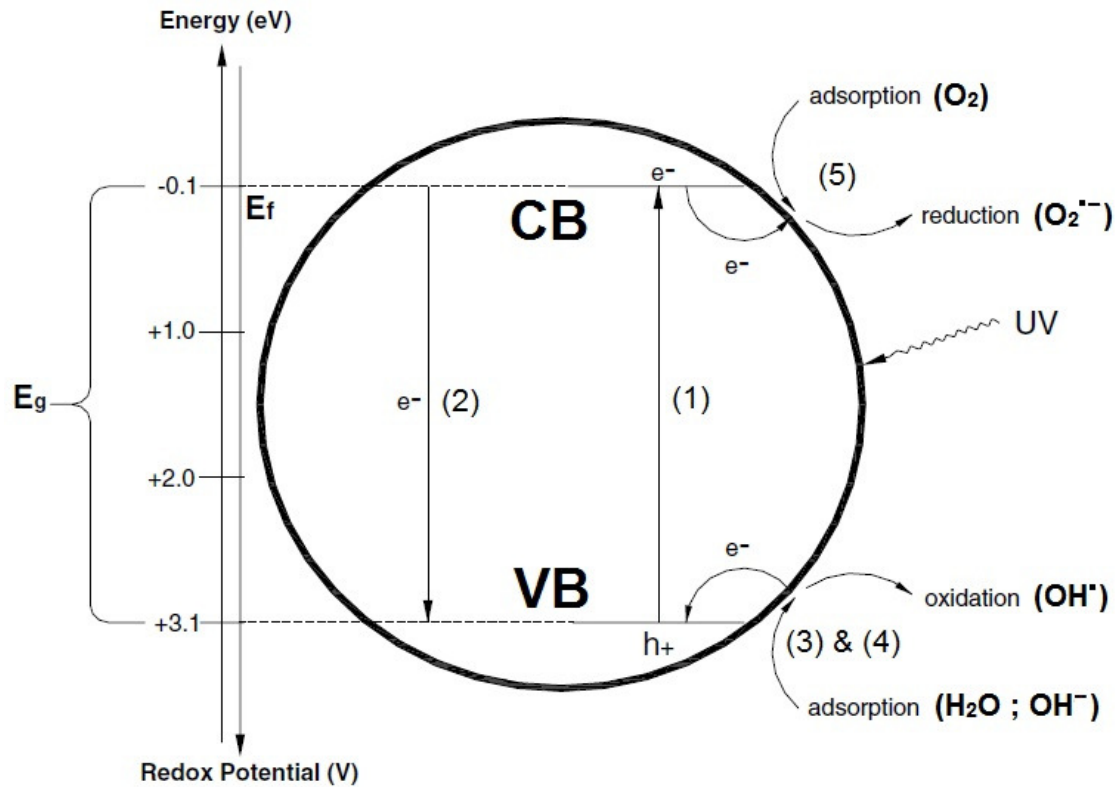


Figure 2.3: The photocatalytic process of oxide semiconductor (Dalrymple et al., 2007).

### 2.3.2 Understanding on Solid Band

Single and isolated atom has discrete energy levels with a single degeneracy (atomic orbital). Excitingly, when two atoms placed close to each other, the molecule formed has two molecular energy levels. Consequently, the resultant energy level of the molecule has a double

degeneracy (molecular orbitals). These molecular energy levels are formed by the wavefunctions of the electrons in the outermost shells, the valence electrons; which eventually overlap in space as atoms become progressively closer together. Although most of the electrons remain localized in association to a particular atom, nevertheless, those outer electrons will naturally involve in bonding with neighboring atoms. Upon bonding, the well-defined outer electron states of individual atom will overlap with those of neighboring atoms and become broadened into energy bands. Therefore, when a cluster of  $N$  atoms is produced, the outermost unfilled as well as core electronic energy levels get perturbed and broadened in the form of bands with degeneracy  $N$  (S. C. Singh, Zeng, Guo, Gopal, & Cai, 2012).

Naturally, with significantly large values of  $N$ , these  $N$  degenerate subenergy levels (sub-bands) inside the bands are so close to each other that electrons can easily transit between them even below room temperature, and therefore can be considered as single band. If there is  $n$  electronic energy levels in each atomic entity, and  $N$  such atoms make a single nanoparticle, the resultant particle has  $n$  energy bands and each band consists of  $N$  sub-bands. The highest occupied energy band is called the valence band ( $VB$ ), while the lowest unoccupied band is termed as the conduction band ( $CB$ ). The difference in energy between the top of a valence band and the bottom of the conduction band is termed as band gap ( $E_g$ ) energy (S. C. Singh et al., 2012), as shown in Figure 2.4.

In monoatomic systems such as particles of Si, Ag, Au, and so on, the outermost filled/partially filled (3p orbital in Si) atomic orbitals of  $N$  atoms get linearly combined to produce valence bands with  $N$  sublevels. Similarly, a conduction band with  $N$  sublevels is made by a linear combination of the first vacant atomic orbital (4s orbital for Si) of  $N$  constructing atoms. In diatomic semiconductor nanomaterials such as CdSe or HgS, the occupied molecular orbitals are made of a linear combination of atomic orbitals of the negatively charged anions (e.g.,  $\text{Se}^-$ ,  $\text{S}^-$ ), while the unoccupied molecular orbitals are made of atomic orbitals of the metallic cations ( $\text{Cd}^{++}$ ,  $\text{Hg}^{++}$ , etc.). There are a number of occupied and unoccupied molecular orbitals. The highest occupied molecular orbital (HOMO) serves as the valence band, while the lowest unoccupied molecular orbital (LUMO) is the conduction band (S. C. Singh et al., 2012).

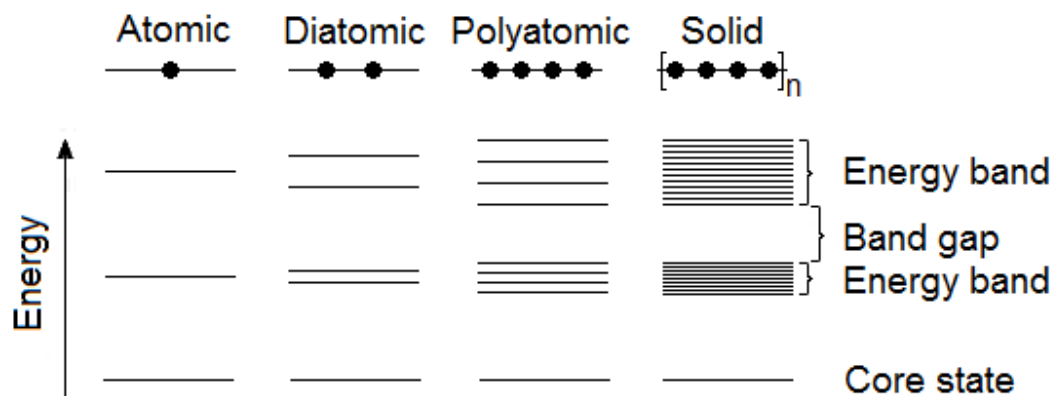


Figure 2.4 Electron energy level diagram for a progressively larger linear chain of atoms showing the broadening of molecular orbitals into energy bands for a one-dimensional solid (Kelsall et al., 2006).

The bands are not flat, but have several hills and valleys on their surfaces. If one or more of the hills of the valence band lie below the valleys of the conduction band, the materials are called direct band gap semiconductors; otherwise, they are indirect band gap semiconductors, as shown in Figure 2.5. Oxides of zinc, titanium, copper, and so on, are direct band gap semiconductors, while Si nanoparticles, GaP, and so on, are indirect (S. C. Singh et al., 2012).

Semiconductors have band gap energies in between metals ( $E_g = 0$ ) and insulators ( $E_g \geq 5.0$  eV). Semiconductors with band gap energies between 0.1 and  $\approx 2.5$  eV (such as InAs, GaAs, GaP, etc.) are assigned as narrow band gap semiconductors, while those with higher ranges than this are wide band semiconductors (ZnO, TiO<sub>2</sub>, and CuO) (S. C. Singh et al., 2012).

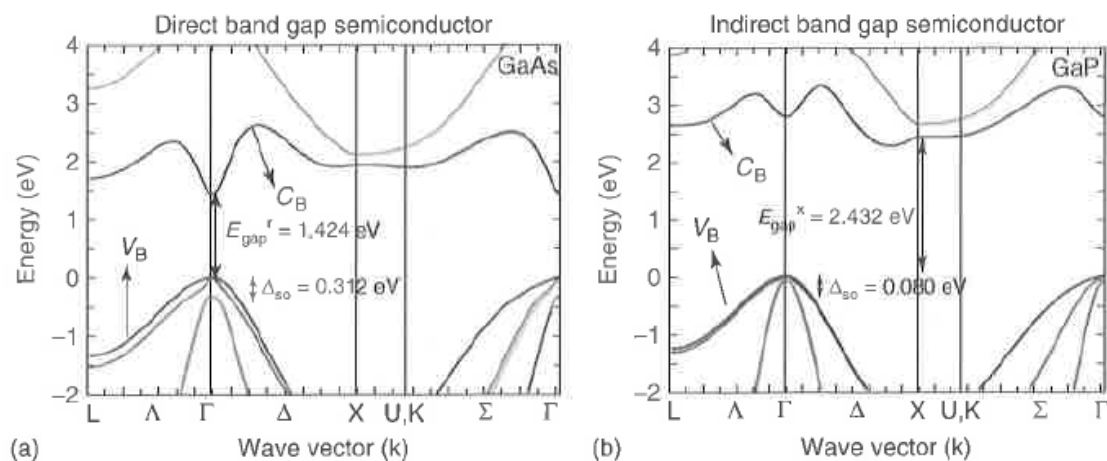


Figure 2.5 Band gap energy diagram (S. C. Singh et al., 2012).

Nanomaterials made of single element are known as monoatomic (Ag, Au, Pt, Si, Ge, etc.), those with two elements are termed diatomic (metal-oxide, metal-carbide, metal-nitride, metal-sulfide, metal-selenide, etc.), those made of three elements are triatomic (InGaAs, InGaP, ZnCdS, etc.), and those having more than three are called polyatomic (biological materials, organic nanoparticles, perovskite, etc.) (Grabowska, 2016) nanoparticles.

### *2.3.3 Band Gap Excitation*

Photocatalytic process operates quite simple and easy to understand. Just as a well-known photosynthesis by plants, it is an example of photocatalysis in nature where chlorophyll serves as the photocatalyst, while photocatalysis is a chemical reaction induced by photoirradiation in the presence of a catalyst. This catalyst assists the chemical reactions without itself being consumed or transformed.

The catalytic mechanism follows the fundamental principle that the electrons at the valence band transit to the conduction band by absorbing photons when the incident light energy is equal or greater than the band gap of the semiconductor and hence leave holes at the valence band (J. Chen, Cen, Xu, & Li, 2015). Visible light has longer wavelength as compared to UV light. Longer wavelength light source able to photo-excite smaller band gap semiconductor material.

Different semiconductors exhibit different band gap widths and band positions, as shown in Figure 2.6, so the hole and electron pairs generated in situ have different oxidation and reduction potentials (J. Chen et al., 2015).

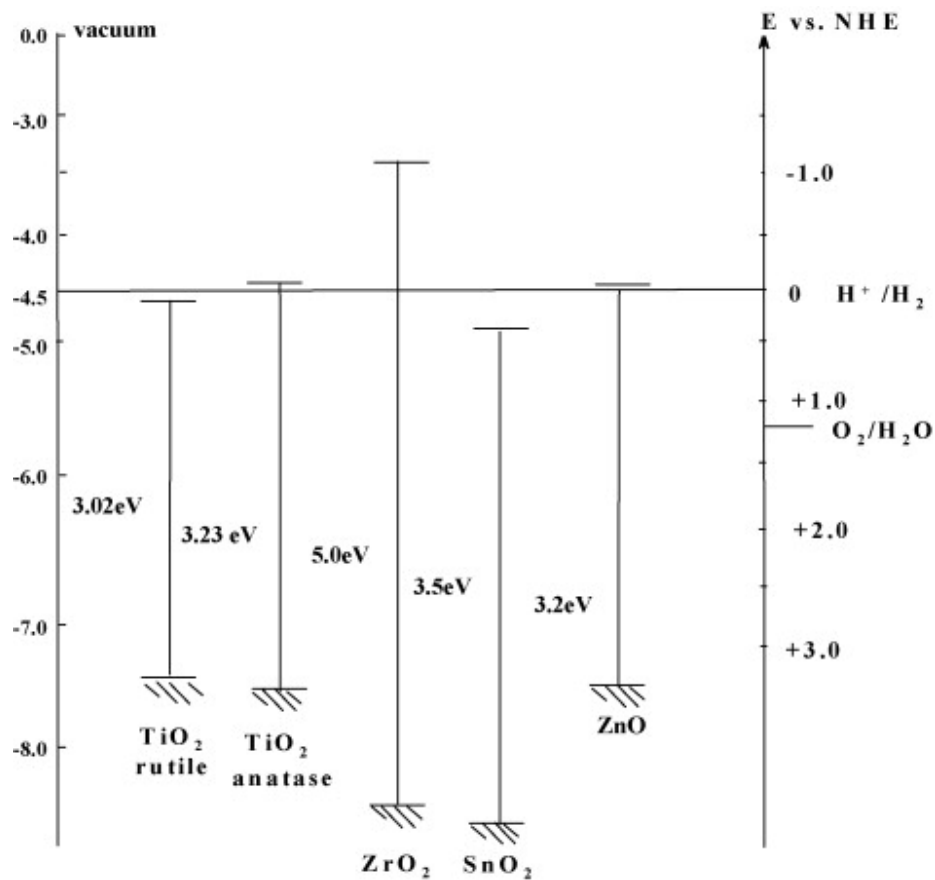


Figure 2.6 The conduction and valence band positions of selected metal oxide semiconductors (Gaya & Abdullah, 2008).

#### 2.3.4 Electron Hole Recombination

Initially when the photocatalytic material is irradiated by appropriate light spectrum with energy greater than the bandgap of photocatalyst, electron-hole pairs (EHPs) will be created, as electron in valence band (VB) excites into conduction band (CB). These EHPs will diffuse to the surface of the semiconductor to allow for reaction to take place, that is the electron ( $e^-$ ) and hole ( $h^+$ ) reduce and oxidise chemical species, respectively. However, there will be some short lived pairs that will recombine during the diffusion period, such as recombination in the bulk (B), as shown in Figure 2.7. On the other hand, while EHPs diffuses to the surface, they may recombine with each other, recombination near the surface (S), or being caught in pores, such as vacancies or defects. When the EHPs reach the surface, they then can carry out the reduction or oxidation processes instantaneously with the organic contaminants which are in contact with the photocatalyst surface.

The recombination of hole and electron pairs often occurs during the migration of the carrier ( $e^-$  &  $h^+$ ) migrate to the surface of the catalyst, which lowers the photocatalytic efficiency (J. Chen et al., 2015). Several methods have been reported to enhance the separation efficiency of EHPs, such as taking a photocatalyst supported on graphene with a large surface area (Q. Xiang, Yu, & Jaroniec, 2012; M. Q. Yang, Zhang, Pagliaro, & Xu, 2014), or to make full use of a precious metal material with strong electron conductivity

like Pt that could accelerate the photogenerated charge transfer (J. Chen et al., 2015).

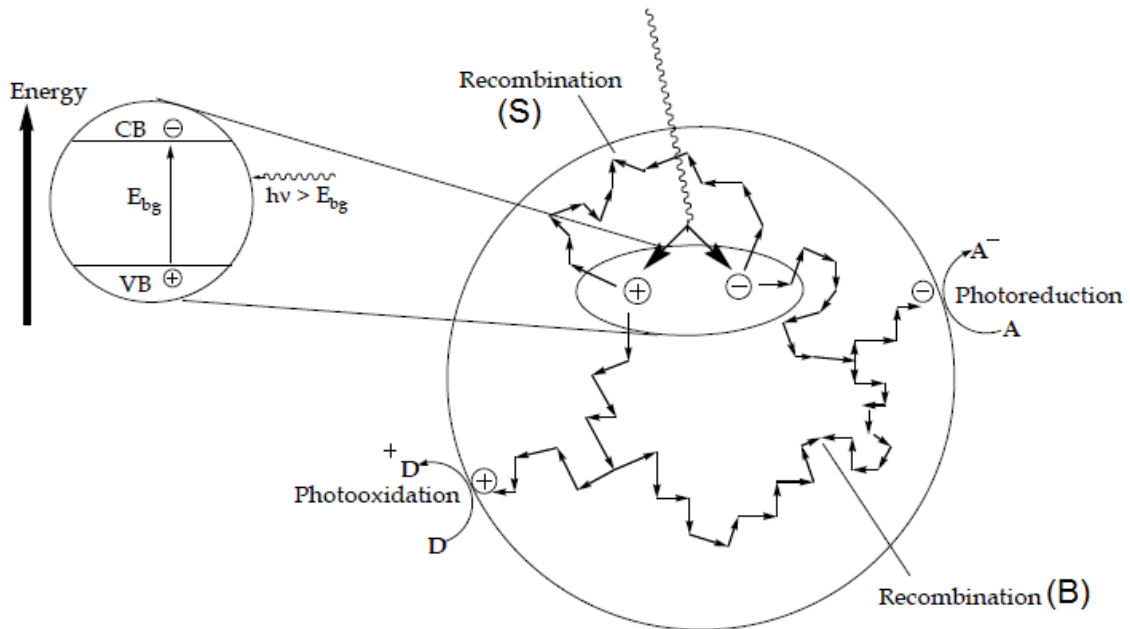


Figure 2.7 Photoexcitation of semiconductor resulted in charge separation/oxidation/reduction/recombination (Malik Mohibbul Haque, Bahnemann, & Muneer, 2012).

## 2.4 Zinc Oxide Photocatalyst

### 2.4.1 Introduction

Lately, ZnO photocatalyst has been considered as an efficient and promising catalyst in the environmentally related wastewater purification system due to its remarkable characteristics, such as wide band gap, strong oxidative catalyst, and significantly large binding energy (Janotti & Van de

Walle, 2009; Kołodziejczak-Radzimska & Jesionowski, 2014). It is environmentally friendly as it adapts well with a wide range of day to day applications. Besides, it does not bring any negative impact to human health, as well as to the environment (Schmidt-Mende & MacManus-Driscoll, 2007). ZnO has a band gap and binding energy of 3.2 eV and 60 meV, respectively, at room temperature (Janotti & Van de Walle, 2009; Kołodziejczak-Radzimska & Jesionowski, 2014).

In addition, the advancement of growth technologies in fabrication has always been possible to scrutinize ZnO to the nanoscale level by modifying and improving its electrical, optical and magnetic properties toward the required specification and capacity (Schmidt-Mende & MacManus-Driscoll, 2007; Shrama, Saurakhiya, Barthwal, Kumar, & Sharma, 2014). With such beneficial and significant characteristics, ZnO has been introduced and used in varistors, rubber and paint industries, fertilizers, cosmetics and catalytic processes (Iglesias-Jueza, Kubackaa, Colónb, & Fernández-García, 2013; Kołodziejczak-Radzimska & Jesionowski, 2014).

Recently, ZnO has been among the most focused semiconductor photocatalysts due to its ability to photodegrade and completely mineralize a broad range of recalcitrant wastewater effluents (Bansal & Sud, 2011; Navarro, Fenoll, Vela, Ruiz, & Navarro, 2009). On the other hand, ZnO has shown compatible capabilities as TiO<sub>2</sub> due to its close proximity band gap energy with the later. Besides, ZnO material itself is relatively cheaper than

TiO<sub>2</sub> which give the former an advantage in the application of large scale wastewater treatment system (Y. Xia, Wang, Chen, Zhou, & Xiang, 2016). Its wide band gap has been the greatest advantage as compared to other semiconductor metal oxides as it able to absorb larger amount of light quanta with the wider range of solar spectrum (Behnajady, Modirshahla, & Hamzavi, 2006).

ZnO is very stable chemically, thermally and also under high energy radiation. ZnO has good electro-optical properties and high electrochemical stability (Rajendran et al., 2016). The recombination of generated electron and hole pairs in ZnO would produce UV/blue light (López et al., 2017). Thus, ZnO has been used for short wavelength optoelectronics such as UV/blue light emitter application (J. G. Lu et al., 2006).

#### *2.4.2 Crystal Structures of Zinc Oxide*

In fact, ZnO exists as white powder or white hexagonal crystal known as zinc white. ZnO is mostly available as in bulk single crystals in wurtzite crystalline structure (Reynolds, Look, Jogai, & Collins, 2001). In addition, ZnO is odourless and insoluble in water (Jagadish & Pearton, 2006).

ZnO has three different allomorphic crystal structures, namely wurtzite, rocksalt and zinc blende structures. The wurtzite structure is the

most common structure due to its thermodynamically stable as compared to the other two structures. Nonetheless, the rarest structure among them is the rocksalt structure as it needs a very high pressure to be produced (Özgür et al., 2005; Z. L. Wang, 2004).

At ambient temperature and pressure, ZnO exists as hexagonal wurtzite crystal structure with the values of its two lattice parameters,  $a$  and  $c$  as 0.3296 nm and 0.52065 nm, respectively (Baruah & Dutta, 2009). This ZnO hexagonal wurtzite space group structure belongs to the P6<sub>3</sub>mc space group (Jagadish & Pearton, 2006). Figure 2.8 exhibits the wurtzite whereas Figure 2.9 depicts the rock salt and zinc blende structures of ZnO.

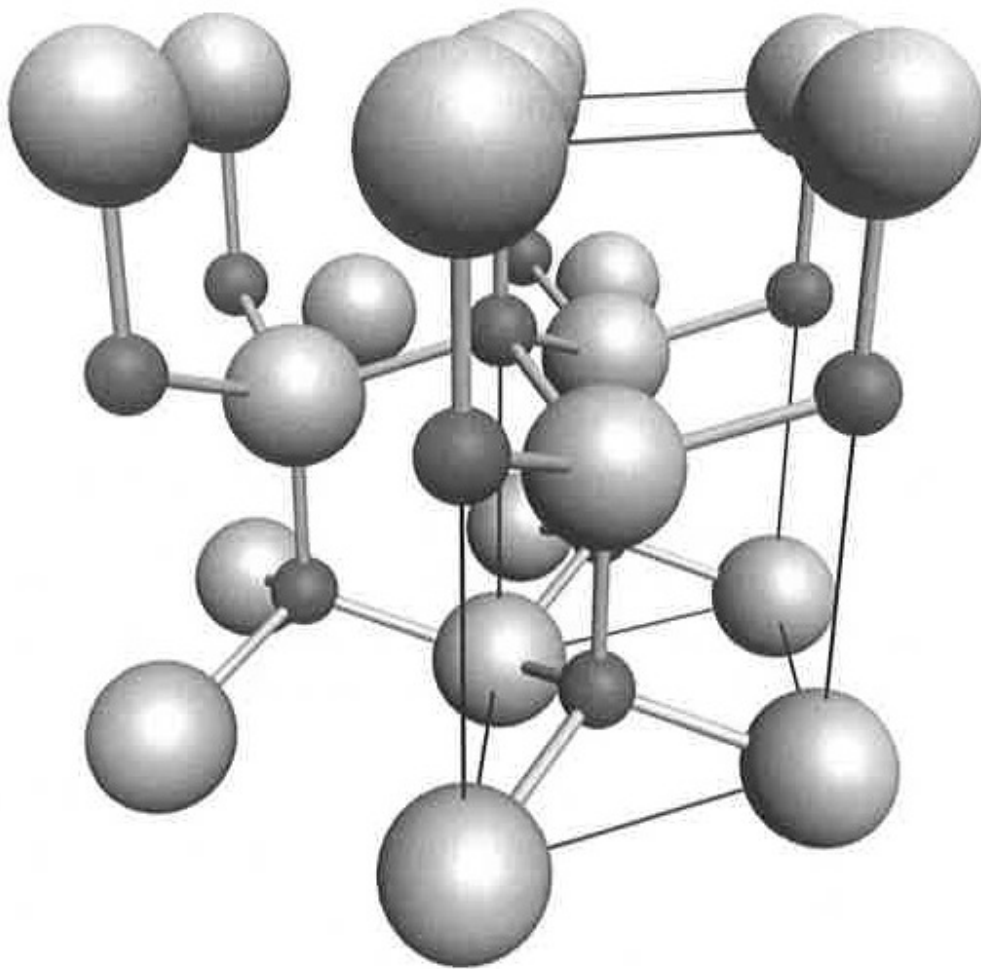


Figure 2.8 The hexagonal wurtzite structures of ZnO. O atoms are shown as large white spheres, Zn atoms as smaller black spheres. One unit cell is outlined for clarity (Jagadish & Pearton, 2006).

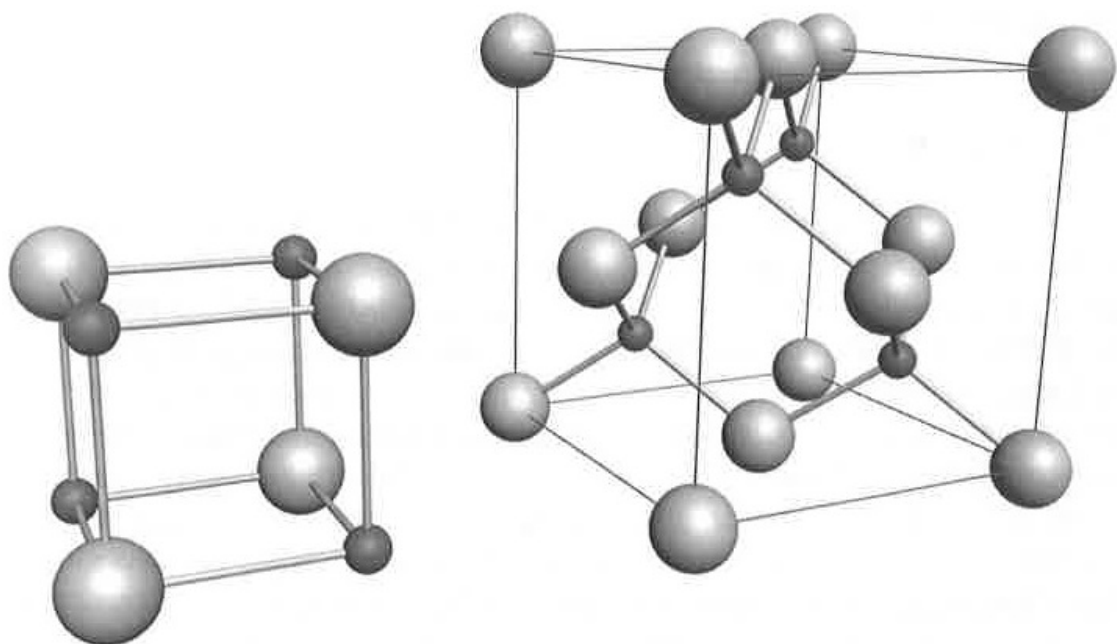


Figure 2.9 The rock salt (left) and zincblende (right) phases of ZnO. O atoms are shown as large white spheres, Zn atoms as smaller black spheres. One unit cell is outlined for clarity (Jagadish & Pearton, 2006).

## **2.5 Titanium Dioxide Photocatalyst**

### *2.5.1 Introduction*

TiO<sub>2</sub> or titania has appeared to be one of the promising semiconductors in the application of AOPs photocatalytic system due to its chemically and biologically inert, photocatalytically stable, and relatively good in physical, electrical and optical properties (Akpan & Hameed, 2009). TiO<sub>2</sub> is an efficient, cost effective and eco-friendly that able to completely degrade organic pollutants (M. Wang, Ioccozia, Sun, Lin, & Lin, 2014). TiO<sub>2</sub> able to degrade various azo dyes such as Acid Red 18, Methyl Orange, and Reactive Red 198 (S. Kaur & Singh, 2007; Y. Wang, 2000). The use of TiO<sub>2</sub> has also been shown good results in detoxification of water samples loaded with molecules like anilines, alcohols, and organochlorides (Chatterjee & Dasgupta, 2005; X. R. Xu, Li, & Gu, 2006).

In a typical experiment, the powdery photocatalyst is mixed with the solution and exposed to light, of appropriate wavelength, to cause the degradation of the contaminants to take place. The solution with the suspended catalyst is irradiated for certain period of time to allow a complete degradation (Patchaiyappan, SaranSuja, & Devipriya, 2016).

### *2.5.2 Crystal Structures of Titanium Dioxide*

TiO<sub>2</sub> is an allomorphic material in nature which exists in three forms, namely rutile, anatase and brookite. The predominant forms are rutile and anatase. However, rutile is energetically more stable as compared to anatase due to its symmetrical crystal structure (Akimov, Neukirch, & Prezhdo, 2013). Anatase and brookite are the two phases that irreversibly transform into rutile upon heating. Brookite is rarely found in significant amount; therefore, pure anatase and rutile as well as their transition phases are usually studied. Besides, brookite is known to be less photoactive than anatase (Shibata et al., 2004) and least study phase of TiO<sub>2</sub>. It exhibits quite similar characteristics as rutile and has a band gap of roughly 3.4 eV (Koelsch, Cassaignon, Guillemoles, & Jolivet, 2002).

In addition, a phase equilibrium does not exist for the rutile-anatase transformation; therefore, no specific temperature can be assigned to their phase transition, which depends on parameters such as synthesis method, reaction atmosphere, impurity content, particle size and oxygen vacancy concentrations within the TiO<sub>2</sub> lattice (Gennari & Pasquevich, 1998).

Crystalline phases of both anatase and rutile are characterized by the tetragonal crystal system with the differences lies in the assembly of their octahedral chains. In rutile crystal structure, each Ti atom has an octahedral O coordination, with each O in a trigonal-planar coordination with 3

neighboring Ti atoms, as shown in Figure 2.10 (Akimov et al., 2013). These that causes them to differ in their particle morphology and consequently in chemical and physical properties. The differences are surface charge separation and recombination, surface area, photoproducted radicals, formation of intermediates, role of crystal faces, and adsorption of water and hydroxyl groups (X. Shen et al., 2013).

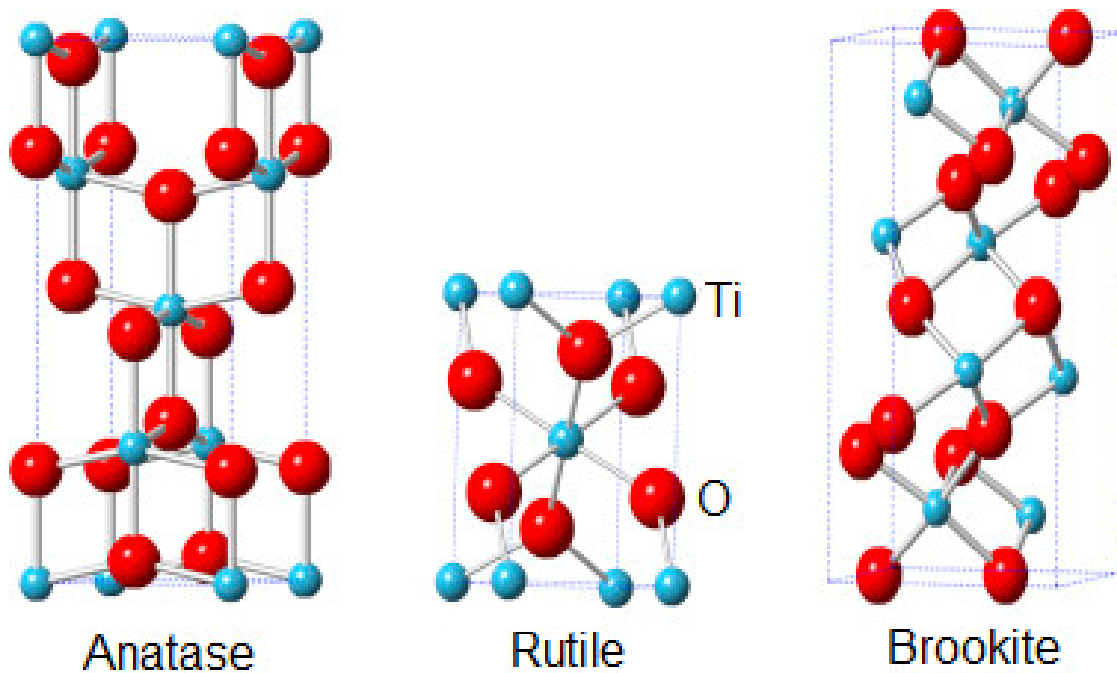


Figure 2.10 The anatase, rutile and brookite structures of  $\text{TiO}_2$ . O atoms are shown as large red spheres, Ti atoms as smaller blue spheres (Etacheri, Di Valentin, Schneider, Bahnemann, & Pillai, 2015).

It is due to these cumulative differences that favour anatase form of TiO<sub>2</sub> towards the application of photocatalytic systems. Besides, there have been many studies showing anatase advantages over rutile, such as the larger band gap, longer period for recombination, and larger surface area as the particle size decreases (Luttrell et al., 2014).

## **2.6 Iron Oxide Nanoparticle**

### *2.6.1 Introduction*

Magnetically related technology provides a convenient approach to remove and recycle magnetic nanoparticles or nanocomposites by applying external magnetic field in aqueous system (Dewi, Sutanto, Fisli, & Wardiyati, 2016). Therefore, magnetism is a unique property that could be applied into water purification system to assist in reducing organic recalcitrant in contaminated water. Combinations between adsorption and magnetic separation have been extensively studied in the field of water treatment and purification (Mahdavian & Mirrahimi, 2010). The capability of iron oxide in removing contaminants from polluted water has been demonstrated in the laboratory as well as at the field tests (Girginova et al., 2010; White, Stackhouse, & Holcombe, 2009). In addition, iron oxide nanoparticles has strong adsorption capability, low cost, very stable and easily separated (Carabante, Grahn, Holmgren, Hedlund, & Kumpiene, 2009; Fan et al., 2012; Hu, Chen, & Lo, 2005).

### 2.6.2 Crystal Structures of Iron Oxide ( $Fe_3O_4$ )

Iron oxides exist in many forms in nature, few of which includes hematite ( $\alpha$ - $Fe_2O_3$ ), maghemite ( $\gamma$ - $Fe_2O_3$ ), and magnetite ( $Fe_3O_4$ ). Among these common forms of Iron oxides,  $\alpha$ - $Fe_2O_3$  has the corundum structure whereas the other two have the cubic structure (Chan & Ellis, 2004; J. Lu et al., 2006).

Magnetite has cubic inverse spinel structure with a space group of  $Fd\bar{3}m$ . The unit cell of  $Fe_3O_4$  has 32  $O^{2-}$  ions with regular cubic close packed along the [110] direction with lattice constant  $a = 0.839$ . The crystal structure of  $Fe_3O_4$  consists of two different iron sites, which include tetrahedral sites and octahedral sites that are occupied by Fe(III) and both Fe(II) and Fe(III), respectively (C. Yang, Wu, & Hou, 2011). The spinel crystal structure for  $Fe_3O_4$  is shown in Figure 2.11.

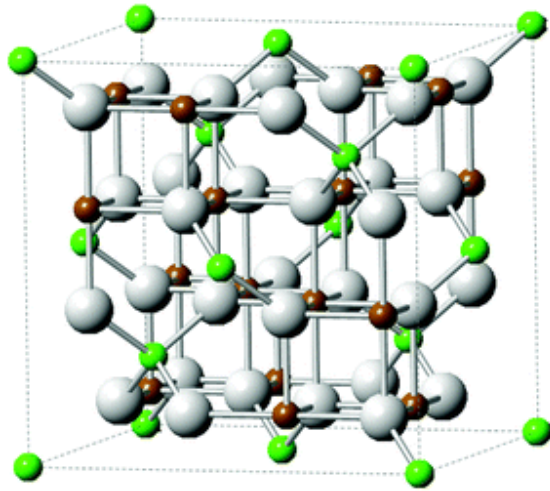


Figure 2.11 Spinel crystal structure of  $\text{Fe}_3\text{O}_4$ . The green atoms are  $\text{Fe}^{2+}$ , brown atoms are  $\text{Fe}^{3+}$  and white atoms are oxygen (C. Yang et al., 2011).

## **2.7 Influence of Parameters on the Photocatalytic Performance**

There are many factors that affect the efficiency and reliability of the semiconductor photocatalyst during the photocatalytic reaction processes, such as physical and structural properties of the semiconductor or experimental aspects. The physical and structural properties can be attributed to surface area, particle size distribution, porosity, band gap and surface hydroxyl density (S. Ahmed, Rasul, Martens, Brown, & Hashib, 2010), whereas experimental aspects are generally influenced by the loading of the photocatalyst, initial concentration of the reactant, light wavelength, light intensity, irradiation time, pH, and temperature (Zangeneh et al., 2015). The details elucidation for few of the variables is presented in the following sections.

### *2.7.1 Photocatalyst Loading*

It is well understood that the catalyst loading is one of the important parameters when designing a photoreactor, especially for an aqueous system. Many studies have shown that regardless of the photoreactor systems, there is always be an optimum value for the catalyst loading. For example, as being reported by Chen and Ray on the same catalyst (Degussa P25), a wide range of optimal catalyst loadings (0.15 to 8 g/L) were obtained for different configuration of the photoreactor systems (D. Chen & Ray, 1999).

As in the common chemical interaction, the rate initially increases with the increased of the catalyst loading until it reached an optimum concentration. These results were well understood that by increasing the catalyst loading, the total surface area for reaction increases, therefore enhance the total active sites for the reaction to take place on the catalyst surface. As a consequence, there will be a significant improved in the number of hydroxyl and superoxide radicals that greatly accelerates the degradation of the organic contaminants (Byrne, Eggins, Brown, McKinney, & Rouse, 1998; Mazzarino, Piccinini, & Spinelli, 1999).

As more catalyst was added into the solution, it will gradually act as screening effects and light scattering to UV light penetration. It is due to the

increase of the solution turbidity thus increases the opacity of the suspension and greatly affects the light penetration into the solution (Kositzi, Poullos, Samara, Tsatsaroni, & Darakas, 2007; Mazzarino et al., 1999; Mrowetz & Selli, 2006). In addition, overloaded with catalyst creates agglomeration between catalyst particles which leads to significant drop to the total surface area and will significantly lowered the light and contaminants absorption, therefore reduced the photocatalytic efficiency (Chatzitakis et al., 2008; Hayat, Gondal, Khaled, Ahmed, & Shemsi, 2011; Lu et al., 2009). As a consequence, the number of available photoreactive sites decreases, and therefore contributes to the dropping of the degradation rate. Nonetheless, a study found that the optimum catalyst dosage can be achieved by improving the intensity of the light source. It is found that optimum value of the catalyst loading is higher with the increasing of the light intensity (D. Chen & Ray, 1999).

### *2.7.2 Organic Concentration*

Generally, photocatalytic reactions take place on the surface of photocatalyst. The degree of organic contaminants concentration in aqueous solutions provides significant impact to the rate of degradation of a photocatalyst. The adsorption of reactants on the surface of photocatalyst and the amount of photons arrived at the catalyst surface to photogenerate •OH radicals are very important for achieving high yield photocatalytic

process (Mahalakshmi, Arabindoo, Palanichamy, & Murugesan, 2007; Wu, Gao, Tu, Chen, & Zhang, 2010).

It is well understood that with the increase of the contaminants concentration, it will cause the degradation rate to drop after certain concentration limit. This is due to the increase of the amount of the target contaminants that are adsorbed on the catalyst surface. Nonetheless, light penetration into the solution will also be affected. Therefore, higher initial concentration will reduce the amount of photons that successfully arrived at the surface of the catalyst (Rabindranathan, Devipriya, & Yesodharan, 2003; Sirtori, Altvater, de Freitas, & Peralta-Zamora, 2006). On the other hand, only the amount of contaminant adsorbed on the surface of the photocatalyst will contribute to the photocatalytic process and not those in the bulk of the solution (Mahalakshmi et al., 2007; Rabindranathan et al., 2003). As more are adsorbed, the demand for oxidizing and reducing species for degradation process also increase. Since other factors, like catalyst loading, light intensity and irradiation period, are fixed, therefore the number of active sites available on the catalyst surface remains constant. As a result, the available amounts of the  $\bullet\text{OH}$  radicals are limited and the adsorption of hydroxyl ions to generate more subsequent  $\bullet\text{OH}$  radicals is significantly reduced.

In the study reported by Guettai and co-researchers, photocatalytic degradation decreased from 100 to less than 70% when the initial

concentration of methyl orange (MO) increases from 5 to 75 mg/L (Guettaï & Amar, 2005). As a result, the available amounts of the •OH radicals are limited when the dye molecules are significantly increased. On the other hand, the light rays have been intercepted by high concentration of contaminants before the photons able to reach the catalyst surface. Hence, the amount of radicals produced in the system is reduced and this retarded the photodecomposition efficiency (Rabindranathan et al., 2003).

### *2.7.3 Effect of pH*

Organic wastewater, especially those discharged from industries, may not be neutral and come with varied pH. Therefore solution pH has to be taken seriously when handling the photocatalytic water system since it critically influence the surface charge properties of the photocatalyst particles thus significantly contributes to the photocatalytic process, such as the reaction rate (Malik M. Haque, Muneer, & Bahnemann, 2006).

This could be seen as an electrostatic interaction between charged TiO<sub>2</sub> particles and the contaminants. Therefore, this highly affects the adsorption process since photocatalytic reactions are said to be surface reactions (Litter, 1999). The characteristics of the surface charge are greatly influenced by the medium pH, which significantly affect the absorption and desorption processes of the photocatalyst surface (Piscopo, Robert, & Weber, 2001).

TiO<sub>2</sub> particles are amphoteric in nature; therefore changes in solution pH affect its surface charge which causes its surface to react differently towards contaminants (Dalrymple et al., 2007; S. Kumar & Davis, 1997).

In addition, the photodegradation rates are also influenced by the solution pH due to the dispersion stability of the catalyst (Dyk & Heyns, 1998). In a report, the pH for an aqueous dispersion of TiO<sub>2</sub>, in the absence of additional solutes, is found to be at pH 6.8. This shows that by irradiating the dispersions will cause the formation of positive charges on the photocatalyst surfaces and resulted in acidic medium (Parks, 1965). In another study when acid/base titrations was applied on the TiO<sub>2</sub> particles with regards to the surface-bound hydroxyl groups, it concluded that only at pH 5 most of the surface hydroxyl groups exist in an uncharged form (Bahnemann, 1993).

For example, at low pH, the photogenerated holes (h<sup>+</sup>) are the predominant oxidizing species, whereas at neutral and higher pH, •OH radicals play the important role in oxidizing the organic contaminants (Shifu & Gengyu, 2005). In an acidic solution (pH < 2.0), the amount of hydroxyl production is greatly affected by hydroxyl radical scavenging like proton ions (Lucas & Peres, 2006). As an example, when solution pH is higher, the number of hydroxyl ions on the surface increases which leads to an increase in the degradation of methylene blue (Dyk & Heyns, 1998). This clearly proves that whilst at higher pHs, there were abundance of hydroxyl anions,

which facilitate photogeneration of  $\bullet\text{OH}$  radicals and subsequently accelerate photodegradation process (Mohamed, Mkhaliid, Baeissa, & Al-Rayyani, 2012).

On the contrary, it has to be aware that also at high pH,  $\bullet\text{OH}$  radicals are rapidly scavenged due to abundance of hydroxyl ions which inhibits its reaction with the organic contaminants (Davis & Huang, 1989). On the other hand, the decrease in the photocatalytic degradation at lower pH (acidic), is due to dissolution of photocatalytic material. For example, in a study reported by Mohamed et al. (2012) on ZnO nanomaterial, they found that at pH of 7.5, there was no trace of  $\text{Zn}^{2+}$ , but at pH 5.2 and 2.5, the amount of  $\text{Zn}^{2+}$  was significantly increased to 365 and 430  $\text{mg}\cdot\text{L}^{-1}$ , respectively (Mohamed et al., 2012). Besides, solution pH seriously affects the positions of conduction and valence bands in semiconductor materials (Beranek, 2011; Y. Xu & Schoonen, 2000). As reported by Litter (1999), the flatband potential decreases by 59 mV per pH unit as provided by Nernstian pH dependence. This is greatly affected the continuation of the subsequent redox reactions by electrons and holes (Litter, 1999).

#### *2.7.4 Effect of Light Intensity*

As explained earlier, to initiate a photocatalyst process, the light source has to be at certain wavelength or higher. However, at a given wavelength, the amount of light photon absorb by the semiconductor

photocatalyst will also depend on the intensity of the light source. Light intensity has been one of an important factor influencing the rate of photodegradation because light irradiation supplies certain amount of photons required for the electron transfer from the valence band to the conduction band of the semiconductor photocatalyst. With higher amount of radiations reaching the surface of the catalyst, more •OH radicals are produced, and hence increased the rate of photodegradation (Behnajady et al., 2006; Mahalakshmi et al., 2007; Shafaei, Nikazar, & Arami, 2010).

This shows that light intensity greatly determine the rate for the photocatalyst to be initiated and the photoreaction of electron-hole formation (Cassano & Alfano, 2000). Therefore, it translates the importance of designing a photoreactor in making sure light irradiated onto the system is at its highest intensity to compliment with the high cost of artificial illuminator and solar concentrators (Shafaei et al., 2010).

Practically, the profiles for the reaction rate in heterogeneous photocatalysis are proportional to the number of incoming photons on the surface of the solid photocatalyst. In low solar irradiance, the performance is almost linear. Above certain intensity, the reaction rate becomes proportional to the square root of the solar irradiance, depending upon the reaction conditions, such as photocatalyst, organic contaminant, photoreactor design, etc. (Spasiano, Marotta, Malato, Fernandez-Ibañez, & Di Somma, 2015). The reaction rates are briefly depicted in Figure 2.12.

A study by Chen and Ray, and other researchers, found that the proportionality of the degradation rates are highly depend on the light intensity, such as  $I^{0.5}$  and  $I^{1.0}$  at high and low intensity, respectively (D. Chen & Ray, 1999; Turchi & Ollis, 1990). It has been found by Herrmann (1999) that the reaction rate reacts differently away from  $25 \text{ mW}\cdot\text{cm}^{-2}$ . The reaction rate was proportional to light intensity below that value, but varied to square-root ( $I^{0.5}$ ) dependency above it (Jean-Marie Herrmann, 1999).

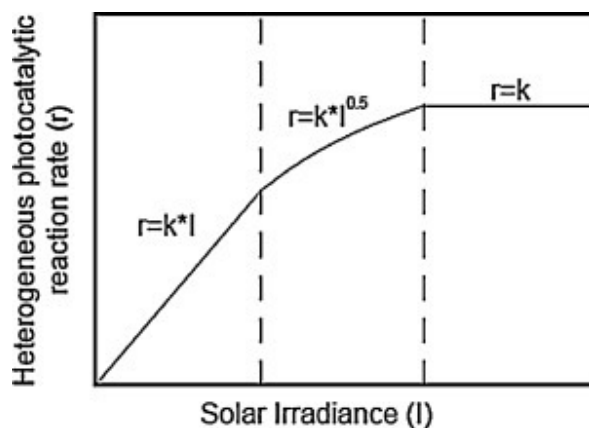


Figure 2.12 Heterogeneous photocatalytic reaction rate vs solar irradiance (Spasiano et al., 2015).

On another  $\text{TiO}_2$  photocatalyst experiment on the degradation of dichloroacetic acid (DCA), in oxygen-saturated solutions, degradation rates were linearly related to the light intensity (below  $1.2 \times 10^{-6} \text{ mol photons L}^{-1} \text{ s}^{-1}$ ) at solutions pH of 2.6, 7, and 11. However, the rate of degradation was, surprisingly, proportional to the square root of the light intensity at pH 5 (Bahnemann, 1993).

On the other hand, when the distance of UV light sources was changing, the intensity of the UV light changed. The reaction pathway does not affected either by the nature or form of the light source. The only dependent of the photocatalyst on the light is the photocatalytic reaction rate of the radiation absorption (Gaya & Abdullah, 2008).

Besides, it has also been shown that too much light irradiation can bring adverse effect and promote faster electron-hole recombination (Litter, 1999), thus competing with the formation of  $\bullet\text{OH}$  radicals (Beydoun et al., 2000; Halmann, 1996). With even higher intensity, the degradation rate is no longer depends on the radiation received. The rate remains constant although the radiation increases. This could be due to the limitation of the mass transfer within the reaction, which could be due to the lack of electron scavengers, i.e.  $\text{O}_2$ , or lack of organic molecules in the proximity of the photocatalyst surfaces (Gogate & Pandit, 2004; Silva, Nouli, Xekoukoulotakis, & Mantzavinos, 2007).

#### *2.7.5 Effect of Temperature*

One of the special characters of photocatalytic process is it able to operate at ambient temperature and atmospheric pressure. As has been

reported by Malato et al. (2003), the optimum operating temperature for photocatalytic process is in the range of 20-80 °C (Malato et al., 2003).

The temperature is found not playing an important role in the overall process of photocatalytic degradation. The main reason is that the low activation energy of photocatalytic reactions (5-20 kJ/mol) if compared with the ordinary thermal reactions (D. Chen & Ray, 1999). For example, the thermal activation energy ( $kT = 0.026$  eV at 25 °C) for TiO<sub>2</sub> photocatalyst is too low as compared to its band gap energy ( $E_g = 3.0$  eV), therefore, the heterogeneous photocatalysis is not very temperature sensitive (Kositzi et al., 2007).

On the other hand, it has also been shown that solution temperature may contribute some impact to the photodegradation rate of the organic contaminants. Although the semiconductor photocatalysis is usually not temperature dependent, an increase in temperature may enhanced the degradation rate of the organic contaminants, however it may cause reduction of the adsorptive capacities of the reactant species and dissolved oxygen, which significantly reduced the photodegradation rate (Chatzitakis et al., 2008; Gaya & Abdullah, 2008; Jean-Marie Herrmann, 1999; Kositzi et al., 2007).

However, if the medium temperature is too high, the adsorption capability of the photocatalyst will be reduced as well as the superficial

reaction of other reagents due to spontaneous exothermic phenomenon of the adsorption processes. In addition, the concentration of dissolved oxygen will drop to a point that contribute to electron-hole recombination (J. -M. Herrmann, 2005; Mozia, Tomaszewska, & Morawski, 2005)(Mozia et al. 2005, Herrmann 2005). Of course, in the usual photocatalytic process, when the temperature of the medium increases, an increasing number of the electron-hole recombination would be observed (Al-Ekabi & Mayo, 1985).

#### *2.7.6 Effect of Morphologies*

With the advancement of current technology and great interest in the photocatalytic study, researchers have developed various synthesis methods to obtain unique and varieties nanostructured ZnO to improve the photodegradation efficiency. The nanostructured ZnO can exists in various morphologies that are very much different from its bulk appearance such as nanowires, nanorods, nanobelts, nanosheets, nanotetrapods, nanoflowers and nanospiral disk (Lai, Meng, & Yu, 2010; Saravanan, Shankar, Prakash, Narayanan, & Stephen, 2011).

The advantage of nanostructured ZnO is higher surface area. A study performed by Assi et al. (2015) on the ZnO nanorods for the degradation of methylene blue found that nanorods with higher surface area shows better

photodegradation efficiency as compared to the lower surface area nanorods (Assi, Mohammadi, Manuchehri, & Walker, 2015).

Generally, a high surface area gives an advantage to a catalyst process since it provides better interaction and wider active sites per unit area, therefore higher results could be achieved (Abrahams, Davidson, & Morrison, 1985). As a comparison, TiO<sub>2</sub> anatase was said to contribute higher activity as compared to rutile due to its higher surface area (Bacsa & Kiwi, 1998).

It is well known that the size of particles contributes to the amount of surface area for the photocatalytic activity to take place. Thus, the smaller the particle size, the bigger the surface area, therefore the expected activity is higher. This translates that with the increase of the surface area, it equate that the number of active sites per unit area also increases, therefore improved the adsorbability of recalcitrant organics on the catalyst surface (N. Xu et al., 1999). However, there is a lower limit for the particle size of the catalyst (10 nm), where other factors have to be considered as quantum size effects starts to dominate (Bahnemann, 1993).

In general, there have been many reports on TiO<sub>2</sub> crystal phases claiming that anatase is more active than rutile (Bacsa & Kiwi, 1998; Chhabra, Pillai, Mishra, Morrone, & Shah, 1995). One of the reports proposed that the most outstanding characteristics which shows anatase

performed better in the photocatalytic activity as compared to rutile is the degree of hydroxylation (Surender, Fotou, & Pratsinis, 1998). They reported that anatase surface was highly hydroxylated while rutile possessed very scarce superficial hydroxyl groups.

In another study on the ratios between anatase and rutile with crystallite size, it is found that the photocatalytic reaction was more effective with larger crystallite size. Larger crystallite size is due to longer migration distances existed for the photoproducted electrons and holes, which reduced the probability of electron hole recombination. In addition, lower degradation rates with rutile as compared to anatase was attributed to the more positive conduction band of rutile, which retarded the reduction of oxygen (Tanaka, Capule, & Hisanaga, 1991).

Although many reports mentioning anatase possess better photocatalytic performance, however pure anatase may not be the best catalyst as counter reported by other researchers. There are many reports suggested an addition of rutile into anatase might be the best combination (Bacsa & Kiwi, 1998). They believed that with the presence of rutile, the photocatalytic activity was enhanced with the appearance of mesoporosity and wider pore size distribution.

In addition, photocatalytic activity is governed by the recombination rate between electrons and holes and the interfacial electron transfer rate.

These rates are related to variations of the surface area, existence of structural defects in the crystalline, impurities or density of hydroxyl groups on the photocatalyst surface. These factors would influence the adsorption behavior of a pollutant or degradation intermediates and the life time and recombination rate of EHPs (Qamar, Saquib, & Muneer, 2005).

## **2.8 Modified Photocatalyst**

Semiconductor oxides used in photocatalytic system may come from various oxides which possess different positions of conduction and valence band and hence all oxides exhibit various band gap energies, as shown earlier in Figure 2.6. For photocatalytic process to take place, light irradiation is required to photogenerate the EHPs. However, to photoexcite electron requires certain wavelength of light source due to the constraint of band gap energy for the particular semiconductor oxide. For example, band gap of titania is about 3.2 eV which requires the irradiation of UV light with wavelength below 380 nm, which account for approximately 4% of the intensity of the solar radiation, to initiate photocatalytic process. This therefore limits the utilization of visible light which occupies a large part of the solar light (Grabowska, 2016; Rattanakam & Supothina, 2009). Nonetheless, photogenerated EHPs are the main source of the photoactivity. However, the quick recombination of these photogenerated EHPs is the major drawback for the efficiency of the semiconductor photocatalysis that lower

the quantum yield as well as energy wasting (Li et al. 2006; Lu et al. 2011). In light of these, ways to improve the efficiency of photocatalytic process are important subject of study to exploit the full potential of the semiconductor photocatalyst. Recently, there have been modifications being applied on the semiconductor oxide for the utilisation of the light source and an improvement of photocatalytic efficiency (Quanjun Xiang, Yua, & Wong, 2011). These modifications can be grouped as doping, surface modification and sensitization of semiconductor oxide (Zangeneh et al., 2015).

### *2.8.1 Effects of Doping on Photocatalytic Activity*

Since photogenerated EHPs are the main source of photocatalytic system, thus recombination process should be inhibited to achieve better photocatalytic efficiency. Therefore, doping has been considered as one of the prominent development in reducing EHPs recombination as well as in utilizing wider range of the solar light (Ansari et al., 2012). Different dopants may have different effects on the photoactivity of the semiconductor such as concentration and nature of the dopant, synthesis method and operating conditions (Zangeneh et al., 2015). Schematic diagram for semiconductor doped with metal and nonmetal as compared to pure oxide is shown in Figure 2.13. Therefore, with the capability of controlling the system by avoiding or lowering the EHPs recombination, the production of hydroxyl radicals and

superoxides species will increase enormously and hence significantly improves the photocatalytic process (Kato et al., 2005).

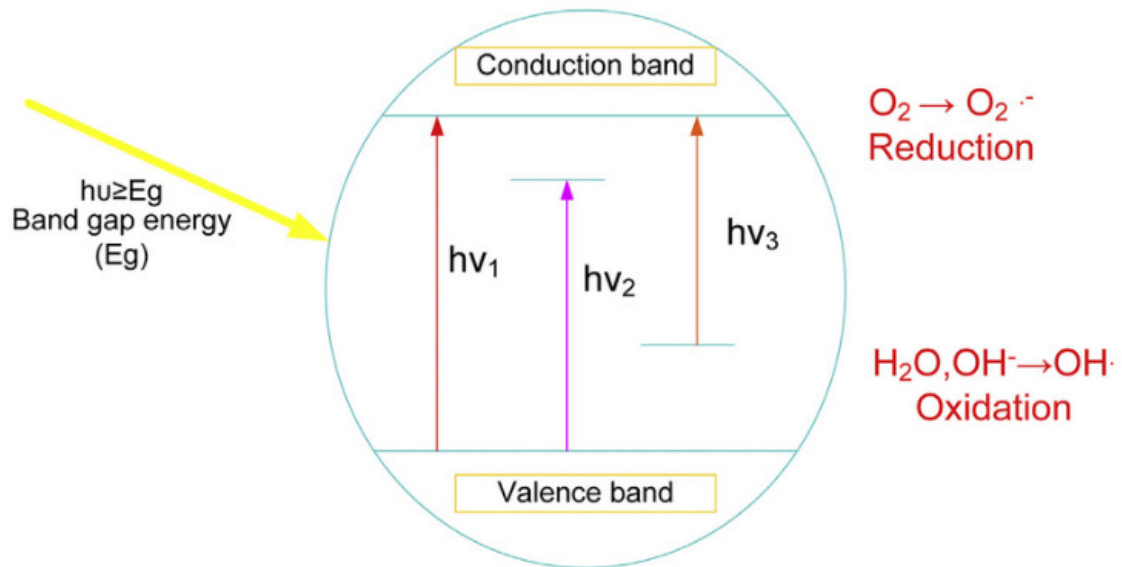


Figure 2.13: Doping semiconductor photocatalyst:  $h\nu_1$ : pure photocatalyst;  $h\nu_2$ : metal-doped photocatalyst;  $h\nu_3$ : nonmetal-doped photocatalyst (Zangeneh et al., 2015).

Photocatalyst doped with metals such as Cr, Mo, and Fe significantly improve photocatalytic activity due to the enhancement of the EHPs photogeneration and adsorption of organic pollutants (Ansari et al., 2012; Xuemin Li, Guo, & He, 2013). Silver (Ag), gold (Au) and platinum (Pt) doped photocatalyst able to facilitates electron-hole separation and promote the interfacial electron transfer process, that is enhance the electron-hole separation by acting as electron traps. In addition, it extends the light absorption into the visible range and enhance surface electron excitation by

plasmon resonances excited by visible light (Begum, Gogoi, & Bora, 2017; Hosseini, Abdolhosseini Sarsari, Kameli, & Salamati, 2015; S. Kim, Hwang, & Choi, 2005; R. Liu, Wang, Wang, Yu, & Yu, 2012; Mohammed Harshulkhan, Janaki, Velraj, Sakthi Ganapthy, & Nagarajan, 2016; Padikkaparambil, Narayanan, Yaakob, Viswanathan, & Tasirin, 2013; Santos et al., 2015). Nevertheless, these doping also modify the surface properties of photocatalysts (Santos et al., 2015).

In another occasion, most of the non-metal doped photocatalysts are active under the visible light, such as doping with nitrogen (Cheng, Yu, Xing, & Yang, 2016), iodine (G. Liu et al., 2011), Chlorine (Long, Cai, Chen, & Xu, 2007), fluoride (Tan, Wong, & Mohamed, 2011), sulfur (C. Wang et al., 2014), phosphorous (Gopal et al., 2012) and carbon (Palanivelu, Im, & Lee, 2007) activate and functionalize the photocatalytic process under visible light (Mohammed Harshulkhan et al., 2016). However, higher reaction rate has to be pursued for practical application since the photocatalytic efficiency of such nonmetal and anion doped photocatalyst under visible light is much lower than that under UV light (Islam, Nagpure, Kim, & Rankin, 2017).

### *2.8.2 Surface Modifications*

In search of better performances of semiconductor photocatalysts, much attention has been focused on the visible light source utilization (due to

wide band gap) and EHPs trapping. This could be achieved through organic, metal or oxide modification on the semiconductor surface. The organic modification approaches is based on the chemical reaction of phenolic hydroxyl group of organic compounds, such as salicylic and binaphthol, with hydroxyls (OH) group in the photocatalyst follows by chemical adsorption of dye molecules on the photocatalyst surface, as shown in Figure 2.14 (Ikeda, Abe, Torimoto, & Ohtani, 2003). The photocatalytic process is going through interfacial electron transfer caused by charge injection into the conduction band of the photocatalyst at sub-band gap excitation (Chatterjee & Mahata, 2001). As a consequence, the modification photocatalyst will have higher absorption capacity through a wider range by effectively utilise the visible light source (Tan et al., 2011).

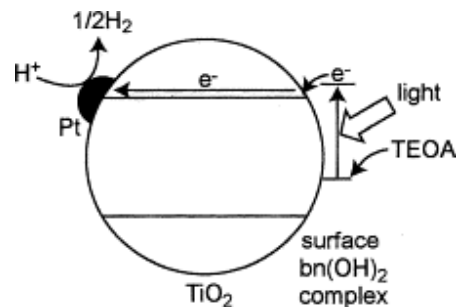


Figure 2.14: Schematic diagram for surface modification of TiO<sub>2</sub> loaded with platinum (Ikeda et al., 2003).

As reported by Libanori et al. (2009) and co-researchers, the superficially modified semiconductor photocatalyst (TiO<sub>2</sub>) by depositing high-

dielectric oxides, such as  $Y_2O_3$  and  $Al_2O_3$  on the  $TiO_2$  surface produces coating of insulating modifying surface by forming an intermediate phase such as titanates. Optimum modifier amount of 0.8% (w/w) with  $Y_2O_3$  modification was found to show the highest photodegradation rate for Rhodamine B under visible light irradiation. They were suggesting that higher performance of the surface-modified nanoparticles might be due to the synergistic effect in electron capture through improved absorption rates and generation of high energy barrier (Libanori, Giraldi, Longo, Leite, & Ribeiro, 2009).

In a phosphate modified photocatalyst for degradation of 4-chlorophenol (4CP) under UV irradiation, the result shows better performance than non-modified photocatalyst. This was due to its inhibition of the contaminant absorption for direct oxidation hole pathway, which enhance the separation of photogenerated hole and electron by negative electrostatic field formed by the surface anion, and hence can force the formation of free hydroxyl radical (Gopal et al., 2012). Another significant improvement on the photocatalytic activity is by depositing noble metals, such as platinum or gold on the semiconductor nanoparticles. This is because noble metal acts as a sink for photoinduced charge carriers, increase the interfacial charge transfer processes and hence inhibits electron recombination (L. M. Ahmed, Ivanova, Hussein, & Bahnemann, 2014; S. Kim et al., 2005).

From the above discussion, it is worth mentioned that surface modification on the photocatalyst particles may enhanced the

photocatalytic systems in a few ways, such as inhibit charge recombination, expand the wavelength response range and control the selectivity or yield of a particular product (Gopal et al., 2012).

### *2.8.3 Sensitization in Photocatalytic System*

Photocatalysis sensitization is viewed as the bridging between the sensitizer and semiconductor photocatalyst. The implementation of the sensitizer is to potentially induce photoexcited EHPs with high mobility by simultaneously injecting electrons into the conduction band of the semiconductor and efficiently absorbs larger proportion of sunlight. This photocatalysis sensitization could be categorized as polymer hybridization, sensitization by narrow band gap semiconductor and dye sensitization (Zangeneh et al., 2015).

#### *2.8.3.1 Polymer Hybridization*

Lately, conjugated polymers have been extensively applied to hybridize with photocatalyst nanoparticles due to their ability to improve the photocatalytic response as compared to the bare photocatalyst nanoparticles in aqueous medium (Chowdhury, Paul, & Chattopadhyay, 2005). Common conjugated polymers such as polyaniline (Xingwei Li, Wang, Li, & Lu, 2004), polythiophene (S. Xu et al., 2012), polypyrrole and polyvinyl alcohol (Luo, Li,

Wang, Wang, & An, 2011) are promising materials to be used as photosensitive and charge mobilization components, due to their excellent properties such as narrow and easy to control band gap, easy chemical modification, high charge carriers mobilization, very stable and low cost. In addition, polymer/photocatalyst hybrid materials provide very promising application in degrading organic contaminants under both UV light and visible light irradiation (Luo et al., 2011; S. Xu et al., 2012).

Under the UV light irradiation, the separations of photoinduced EHPs are effectively enhanced due to capability of conjugated polymers in the mobilization of photoinduced holes. Whereas under visible light irradiation, the hybrid polymers are excited to produce EHPs and the induced electrons are injected into the conduction band of the photocatalyst. The electron acceptors such as oxygen adsorbing on the photocatalyst surface will react with those electrons to generate oxidative species, such as hydroxyl radicals and superoxide radicals (Qiu et al., 2008; S. Xu et al., 2012). The schematic mechanism for the polymer hybridization under UV light and visible light irradiation is shown in Figure 2.15.

However, there is an adverse effect on the conjugated polymers themselves since they are organic too, thus they may be decomposed by those oxidative species together with the organic contaminants during the process. Therefore, further studies on the effectiveness of the conjugated

polymer/photocatalyst composites are very important after the polymer was partially oxidized (S. Q. Wang, Liu, & Zhu, 2011).

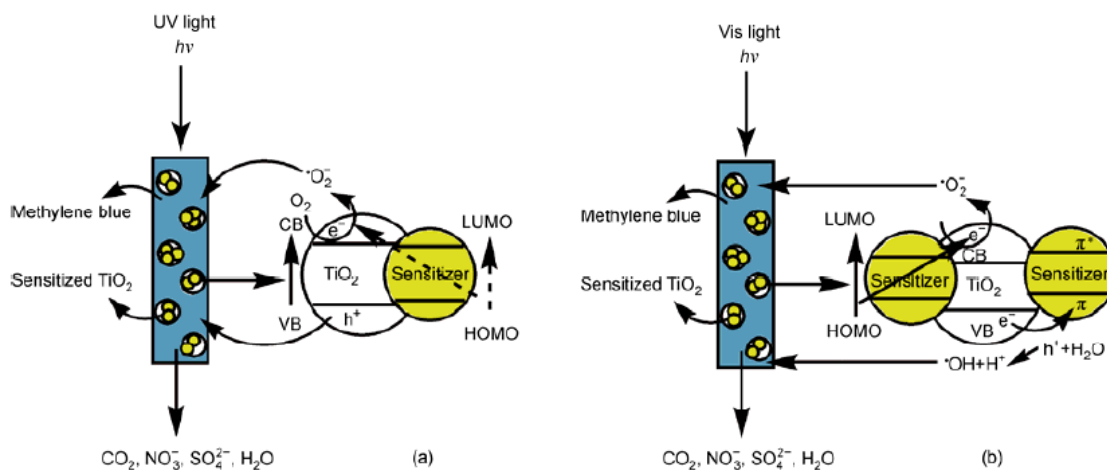


Figure 2.15: Sensitization mechanism for polymer hybridization under UV light (a) and Vis light (b) irradiation (P. Liu, Zhang, Cao, & Xue, 2012).

### 2.8.3.2 Coupled Semiconductor

One of the significant methods to simultaneously enhance the photoexcited EHPs by reducing the recombination of electron hole (Serpone, Maruthamuthu, Pichat, Pelizzetti, & Hidaka, 1995) and efficiently absorbed larger portion of the sunlight is by combining different types of semiconductor photocatalysts (Fujii, Ohtaki, Eguchi, & Arai, 1997). Various coupling system have been applied in photodegradation of organic contaminants, such as CdS/TiO<sub>2</sub> (Kannaiyan et al., 2010), CuO/ZnO (Sathishkumar, Sweena, Wu, & Anandan, 2011), Ag<sub>2</sub>S/ZnO (Subash, Krishnakumar, Pandiyan, Swaminathan, & Shanthi, 2012), CeO<sub>2</sub>/ZnO

(Lamba, Umar, Mehta, & Kansal, 2015), SnO<sub>2</sub>/ZnO (Uddin et al., 2012), Fe<sub>3</sub>O<sub>4</sub>/ZnO (J. Xia, Wang, Liu, & Su, 2011), WO<sub>3</sub>/TiO<sub>2</sub> (Leghari, Sajjad, Chen, & Zhang, 2011) and TiO<sub>2</sub>/ZnO (Pant et al., 2012).

The highest photodegradation efficiency among the studied coupling system is the graphene oxide coupled with ZnO, in the degradation of Methylene Blue with irradiation time of only 40 minutes. Besides, in the degradation of Rhodamine B (RhB), the percentage of decolourization increased at least twice as much when applied to coupled photocatalyst such as (ZnO/CeO<sub>2</sub>)-β-CD (Velusamy & Lakshmi, 2017), CeO<sub>2</sub>/ZnO/TiO<sub>2</sub> (Prabhu, Viswanathan, Jothivenkatachalam, & Jeganathan, 2014) and Bi<sub>2</sub>O<sub>3</sub>/ZnO (Y. Yang et al., 2014).

The advantages of coupled photocatalysts as compared to individual photocatalyst were the induced of an efficient charge separation and enhanced of photostability (Ghugal, Umare, & Sasikala, 2015). The measured lifetimes for the composite as compared to single photocatalyst are 590 ps and 470 ps, respectively, whereas the photostability measurements showed only a small dropped from 99% to 84% for up to 6 cycles of photocatalytic reactions. Sensitization mechanism for the coupled semiconductor photocatalyst is shown in Figure 2.16.

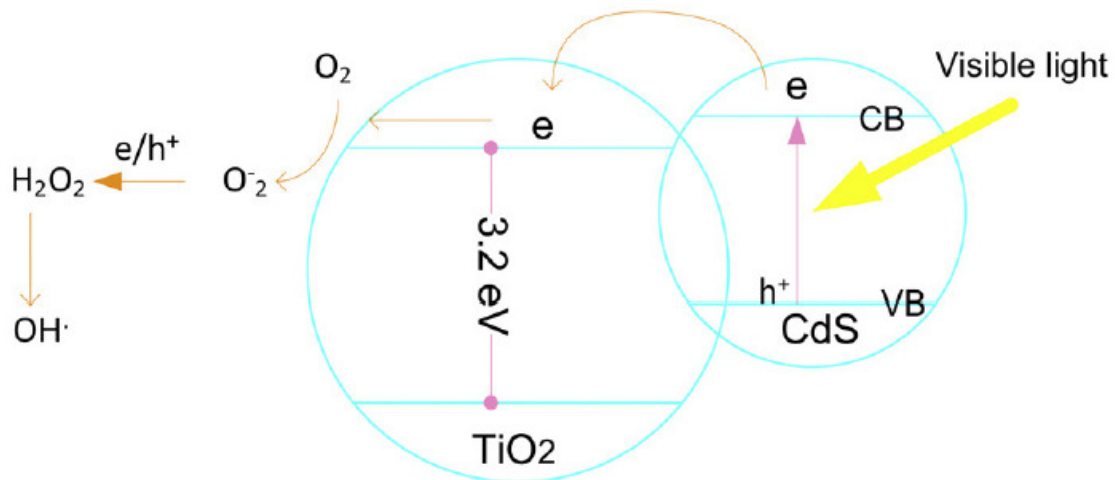


Figure 2.16: Sensitization mechanism for combined semiconductor photocatalyst (Zangeneh et al., 2015).

### 2.8.3.3 Organic Dye Sensitized Photocatalyst

In the dye sensitized photocatalyst, the dye act as a bridging molecule to the photocatalyst. Upon irradiation with visible light, the sensitizer is photoexcited to produce EHPs and then the electrons are injected into the conduction band of the semiconductor. The process continues to react with the absorb oxygen on the semiconductor surface that generates hydroxyl radicals and superoxide radicals (Zangeneh et al., 2015). There are two types of organic dye sensitized photocatalysts. The first one was based on the physical or chemical adsorption of dye molecules on the photocatalyst surface and the second was a construction of dye sensitized photocatalysts (Chatterjee & Mahata, 2001).

It has been recognized that dye sensitizing semiconductor involves three consecutive processes, namely dye sensitizer adsorbs onto the surface of photocatalyst. Next, the adsorbed dye is excited by visible light, and finally, high mobility electrons from the excited dye are injected into the photocatalyst conduction band (L. Song et al., 2007; S. Song et al., 2011). It has to make known that the dyes are easily dissolved in the medium during the photocatalytic process as the physical adsorption of the dyes on the photocatalytic surface is not so firm. Therefore, in overcoming this, a costly synthesization with chemical bonding between dye and photocatalyst can be applied (Zangeneh et al., 2015). Simple sensitization mechanism for the dye sensitized photocatalyst is shown in Figure 2.17.

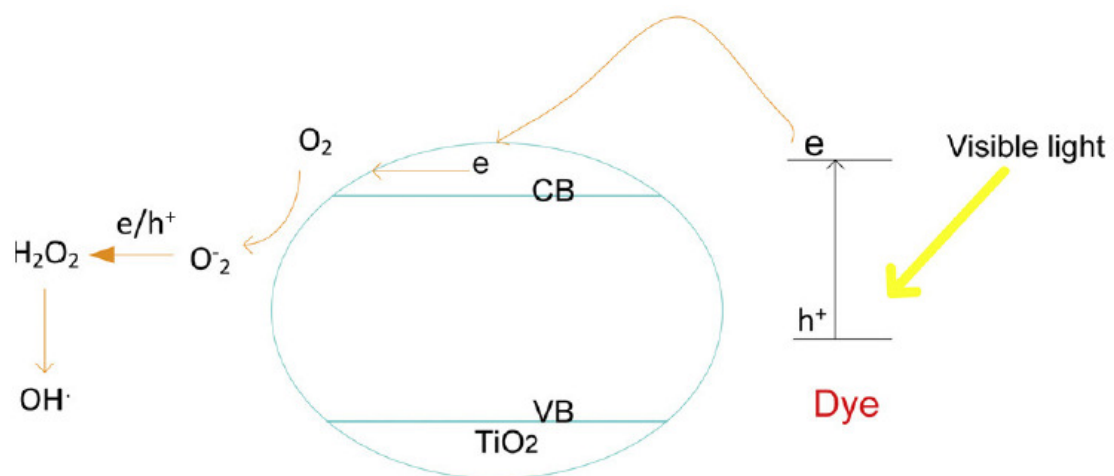


Figure 2.17: Sensitization mechanism for dye sensitized photocatalyst (Zangeneh et al., 2015).

In one of the dye sensitized photocatalyst, a photocatalyst has been chemically prepared with tolylene-2,4-diisocyanate (TDI) dye with TDI as a

bridging molecule. This dye modification photocatalyst has shown strong adsorption in visible light region and increased in the Methylene Blue adsorption capacity, therefore resulting in significant increase in its photocatalytic activity as compared to bare photocatalyst (Zangeneh et al., 2015).

## **2.9 Dyes as Wastewater Effluent**

There have been plenty of industries such as textiles, leather, plastic, paper and food, using dyes in their product. There are several ways commercial dyes can be classified, in term of structure, colour and application methods. They are most favourably on application, due to the complexities of the colour nomenclature from the chemical structure system. Besides, dyes also classified based on their particle charge upon dissolution in aqueous application medium such as cationic (all basic dyes), anionic (direct, acid, and reactive dyes), and non-ionic (dispersed dyes) (Yagub, Sen, Afroze, & Ang, 2014).

Dyes is 'coloured' due to the presence of a substance called chromophore in them, which are basically ionizing and aromatic compound showing affinities towards the substrates. One characteristic of dye is that the dyes must get completely or at least partially soluble in which it is being put into. Therefore, it is generally applied in an aqueous solution.

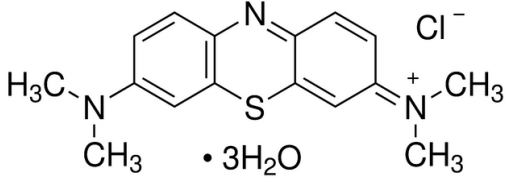
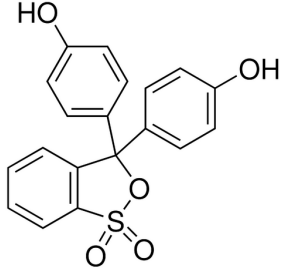
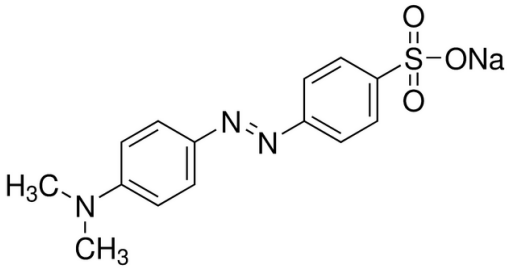
Dyes may also require a mordant or a reagent such as alumina or tannic acid, to improve the fastness of the dye on the material on which it is applied. There are similar categories applicable to dyes as well as other chemicals too. Therefore, certain kind of dyes can be toxic, carcinogenic or mutagenic and can pose as a hazard to health.

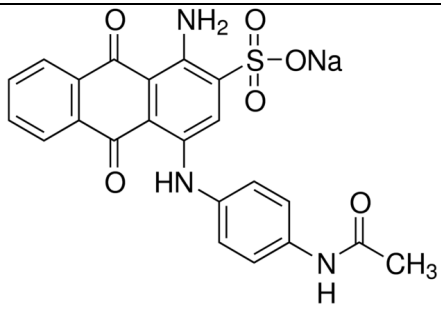
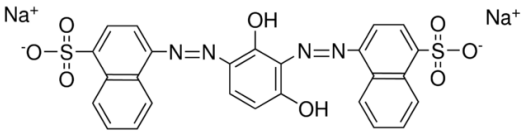
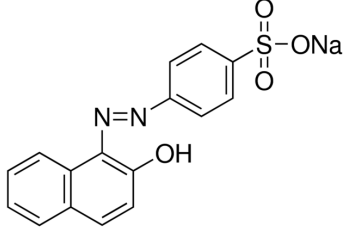
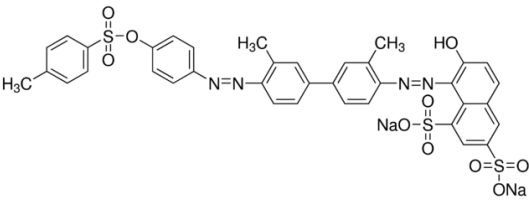
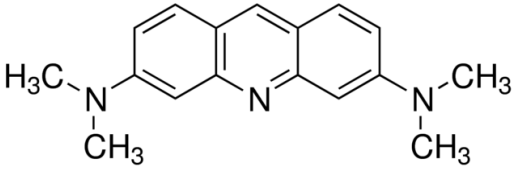
Dyes with aryl rings have delocalised electron systems. These structures responsible for the absorption of electromagnetic radiation of varying wavelengths, based upon the energy of the electron clouds. It is actually because of this reason that chromophores do not make dyes coloured. Rather it makes the dyes proficient in their ability to absorb radiation. Chromophores acts by making energy changes in the delocalised electron cloud of the dye. This alteration invariably results in the compound absorbing radiation within the visible range of colours. Human eyes detect this absorption, and responds to it. In another possibility, if the electrons are removed from the electron cloud, it may result in loss of colour. To conclude chromophores are the atomic configurations which has delocalised electrons. Generally they are represented as carbon, nitrogen, oxygen and sulphur. They can have alternate single and double bonds.

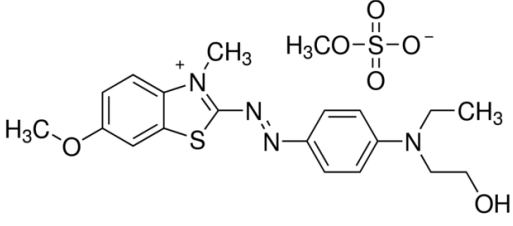
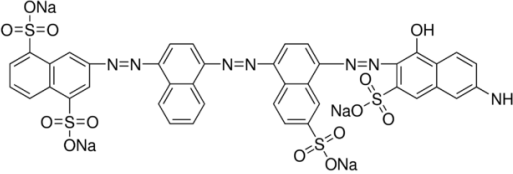
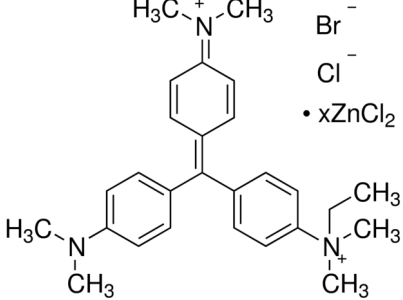
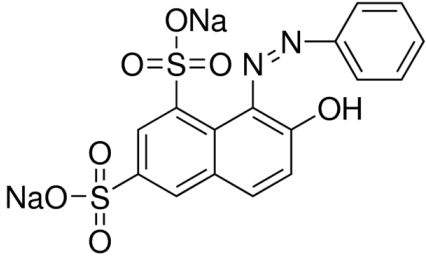
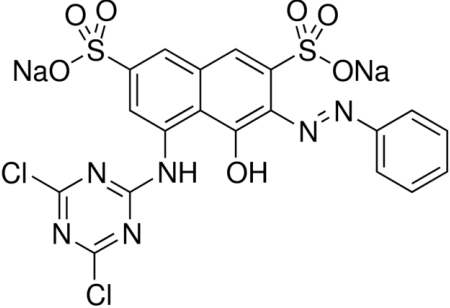
Most synthetic dyes are made from coal-tar derivatives, which is a highly complicated technical operation and constantly changing. There is variation in the manners in which fibers respond to dyes. Sometimes, the same fibers do not produce a full range of colors with a particular type of

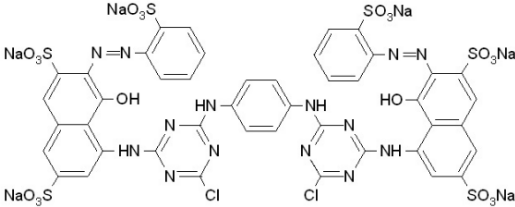
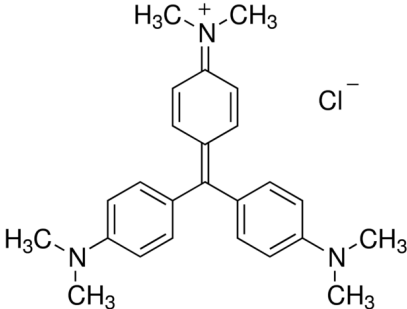
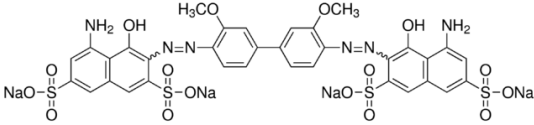
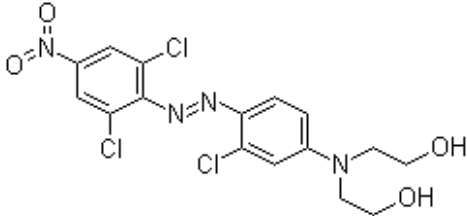
dye. By using triazine as a bridge link in dye molecule, a wide range of chromophore with excellent fastness can be selected (Kusic, Koprivanac, & Bozic, 2013). The properties of each dye were obtained from Sigma Aldrich safety data sheet (SDS) and are listed in Table 2.2 below.

Table 2.2 List of Dyes and their properties (Sigma Aldrich SDS)

<b>Dyes</b>	<b>Empirical Formula; Molecular Weight; Absorption Max. (<math>\lambda_{\max}</math>)</b>	<b>Structure</b>
Methylene blue (C.I. 52015)	$C_{16}H_{18}N_3SCl \cdot 3H_2O$ $M_w = 373.90 \text{ g/mol}$ $\lambda_{\max} = 665 \text{ nm}$	
Phenol Red	$C_{19}H_{14}O_5S$ $M_w = 354.38 \text{ g/mol}$ $\lambda_{\max} = 435 \text{ nm}$	
Methyl Orange (C.I. 13025)	$C_{14}H_{14}N_3NaO_3S$ $M_w = 327.33 \text{ g/mol}$ $\lambda_{\max} = 465 \text{ nm}$	

<p>Acid Blue 40 (C.I. 62125)</p>	<p><math>C_{22}H_{16}N_3NaO_6S</math> <math>M_w = 473.43 \text{ g/mol}</math> <math>\lambda_{\max} = 621 \text{ nm}</math></p>	
<p>Acid Brown 14 (C.I. 20195)</p>	<p><math>C_{26}H_{16}N_4Na_2O_8S_2</math> <math>M_w = 622.55 \text{ g/mol}</math> <math>\lambda_{\max} = 467 \text{ nm}</math></p>	
<p>Acid Orange 7 (C.I. 15510)</p>	<p><math>C_{16}H_{11}N_2NaO_4S</math> <math>M_w = 350.32 \text{ g/mol}</math> <math>\lambda_{\max} = 488 \text{ nm}</math></p>	
<p>Acid Red 114 (C.I. 23635)</p>	<p><math>C_{37}H_{28}N_4Na_2O_{10}S_3</math> <math>M_w = 830.81 \text{ g/mol}</math> <math>\lambda_{\max} = 525 \text{ nm}</math></p>	
<p>Acridine Orange (C.I. 46005)</p>	<p><math>C_{17}H_{20}N_3</math> <math>M_w = 438.09 \text{ g/mol}</math> <math>\lambda_{\max} = 495 \text{ nm}</math></p>	

<p>Basic Blue 41 (C.I. 11105)</p>	<p><math>C_{20}H_{26}N_4O_6S_2</math> <math>M_w = 482.57 \text{ g/mol}</math> <math>\lambda_{\max} = 608 \text{ nm}</math></p>	
<p>Direct Blue 71 (C.I. 34140)</p>	<p><math>C_{40}H_{27}N_7O_{13}S_4 \cdot Na_4</math> <math>M_w = 1029.88 \text{ g/mol}</math> <math>\lambda_{\max} = 587 \text{ nm}</math></p>	
<p>Methyl Green (C.I. 42585)</p>	<p><math>C_{27}H_{35}Cl_2N_3 \cdot ZnCl_2</math> <math>M_w = 608.78 \text{ g/mol}</math> <math>\lambda_{\max} = 630 \text{ nm}</math></p>	
<p>Orange G (C.I. 16230)</p>	<p><math>C_{16}H_{10}N_2Na_2O_7S_2</math> <math>M_w = 452.37 \text{ g/mol}</math> <math>\lambda_{\max} = 475 \text{ nm}</math></p>	
<p>Procion Red MX-5B (C.I. Reactive Red 2)</p>	<p><math>C_{19}H_{10}Cl_2N_6Na_2O_7S_2</math> <math>M_w = 615.33 \text{ g/mol}</math> <math>\lambda_{\max} = 538 \text{ nm}</math></p>	

<p>Reactive Red 120 (C.I. 292775)</p>	<p><math>C_{44}H_{24}Cl_2N_{14}Na_6O_{20}S_6</math> <math>M_w = 1469.98 \text{ g/mol}</math> <math>\lambda_{max} = 512 \text{ nm}</math></p>	
<p>Basic Violet 3 (C.I. 42555)</p>	<p><math>C_{25}H_{30}ClN_3</math> <math>M_w = 407.98 \text{ g/mol}</math> <math>\lambda_{max} = 588 \text{ nm}</math></p>	
<p>Direct Blue 15 (C.I. 24400)</p>	<p><math>C_{34}H_{24}N_6Na_4O_{16}S_4</math> <math>M_w = 992.80 \text{ g/mol}</math> <math>\lambda_{max} = 600 \text{ nm}</math></p>	
<p>Disperse Brown 1 (C.I. 11152)</p>	<p><math>C_{16}H_{15}Cl_3N_4O_4</math> <math>M_w = 433.67 \text{ g/mol}</math> <math>\lambda_{max} = 586 \text{ nm}</math></p>	

In the earlier part of the photodegradation study, three type of dyes, namely methylene blue (MB), phenol red (PR) and methyl orange (MO) were investigated together with the three metal oxides, ZnO, TiO<sub>2</sub> and Fe<sub>3</sub>O<sub>4</sub> nanoparticles photocatalysts. These dyes were chosen as the organic

compound since they are complex organic substances which contain a significant amount of various functional groups and are well dissolved in water. In the photocatalytic degradation study for the ZnO/Fe<sub>3</sub>O<sub>4</sub> and TiO<sub>2</sub>/Fe<sub>3</sub>O<sub>4</sub> nanocomposites, MB dye will be used as the model dye.

Last part of this photocatalytic study will be using 5 sample dyes, that have been randomly picked, to study different properties possessed by these dyes, such as the number of azo groups, number of benzene groups, molecular weight and UV-visible absorbance, in relation to their rate of decomposition by the ZnO/Fe<sub>3</sub>O<sub>4</sub> nanocomposites materials. These dyes are Reactive Red 120 (RR120), Disperse Blue 15 (DB15), Acid Brown 14 (AB14), Orange G (OG) and Acid Orange 7 (AO7).

## **CHAPTER 3**

### **Experimental Preparations**

#### **3.1 Introduction**

This chapter provides detailed description of the whole experimental works and procedures implemented throughout the study. First part gives the raw materials used in this study. The second part provides the flow of the main steps taken in characterizing and experimenting for the raw powder as well as the prepared nanocomposites samples. Next, the raw and prepared samples are sent for characterization. Finally, those samples are used to evaluate their photocatalytic efficiency on the particular dyes.

#### **3.2 Materials**

##### **3.2.1 Raw Materials**

Zinc oxide (ZnO, R & M Chemicals, U.K.), titanium dioxide (TiO<sub>2</sub>, R & M Chemicals, U.K.) and iron oxide (Fe<sub>3</sub>O<sub>4</sub>, System, ChemPur) purchased are of analytical grades and used without any modification.

The dyes chemical include: methylene blue ( $C_{16}H_{18}N_3SCl \cdot 3H_2O$ ;  $M_w=373.90$  g/mol), phenol red ( $C_{19}H_{14}O_5S$ ;  $M_w=354.38$  g/mol), methyl orange ( $C_{14}H_{14}N_3NaO_3S$ ;  $M_w=327.33$  g/mol), acridine orange ( $C_{17}H_{20}ClN_3$ ;  $M_w=438.09$  g/mol) and methyl green ( $C_{27}H_{35}Cl_2N_3 \cdot ZnCl_2$ ;  $M_w=608.78$  g/mol) were purchased from R & M Chemicals, UK. Acid blue 40 ( $C_{22}H_{16}N_3NaO_6S$ ;  $M_w=473.43$  g/mol), acid brown 14 ( $C_{26}H_{16}N_4Na_2O_8S_2$ ;  $M_w=622.55$  g/mol), acid red 114 ( $C_{37}H_{28}N_4Na_2O_{10}S_3$ ;  $M_w=830.81$  g/mol), basic blue 41 ( $C_{20}H_{26}N_4O_6S_2$ ;  $M_w=482.57$  g/mol), direct blue 71 ( $C_{40}H_{27}N_7O_{13}S_4 \cdot Na_4$ ;  $M_w=1029.88$  g/mol), procion red MX-5B ( $C_{19}H_{10}Cl_2N_6Na_2O_7S_2$ ;  $M_w=615.33$  g/mol), reactive red 120 ( $C_{44}H_{24}Cl_2N_{14}Na_6O_{20}S_6$ ;  $M_w=1469.98$  g/mol), basic violet 3 ( $C_{25}H_{30}ClN_3$ ;  $M_w=407.98$  g/mol), direct blue 15 ( $C_{34}H_{24}N_6Na_4O_{16}S_4$ ;  $M_w=992.80$  g/mol), and disperse brown 1 ( $C_{16}H_{16}Cl_2N_4O_4$ ;  $M_w=399.24$  g/mol) were purchased from Sigma-Aldrich. Acid orange 7 ( $C_{16}H_{11}N_2NaO_4S$ ;  $M_w=350.32$  g/mol) and orange G ( $C_{16}H_{10}N_2Na_2O_7S_2$ ;  $M_w=452.37$  g/mol) were purchased from Friendemann Schmidt. All the chemical products were used as received without any further purification. The deionised water obtained from Favorit Water Distiller (Favorit Water Still W4L; conductivity of 3-4  $\mu S/cm$  and resistivity of 0.25-0.30  $M\Omega \cdot cm$ ) was used to prepare all the aqueous solutions. In preparation of solutions of different pH, the acid and base precursor materials that used were sulfuric acid ( $H_2SO_4$ ) and sodium hydroxide (NaOH), respectively.

### **3.2.2 Preparation of the Magnetic Nanocomposite Material**

The first part of the experiment was to determine the amount of catalyst loading that will contribute to the optimum degradation of organic dye. Therefore, the photocatalysts nanopowders were prepared in a series of catalyst loading, in the range of 1.0 to 10.0 wt% and 1.0 to 6.0 wt% for ZnO and TiO<sub>2</sub> photocatalysts samples, respectively. In every photocatalytic test, 0.20 g of different catalyst loading will be capped and mixed with 3.0 ml of organic dyes.

Figure 3.1 shows the flowchart in the preparation for the ZnO/Fe<sub>3</sub>O<sub>4</sub> and TiO<sub>2</sub>/Fe<sub>3</sub>O<sub>4</sub> magnetic nanocomposites photocatalyst materials. Firstly, ZnO and TiO<sub>2</sub> nanopowders were prepared in few vials followed by weighing of the iron oxide (Fe<sub>3</sub>O<sub>4</sub>) nanopowders. In order to evaluate the effect of the magnetic nanomaterial on the photocatalytic properties, ZnO/Fe<sub>3</sub>O<sub>4</sub> and TiO<sub>2</sub>/Fe<sub>3</sub>O<sub>4</sub> nanocomposites samples doped with different weight percentage (wt%) of Fe<sub>3</sub>O<sub>4</sub> were prepared, in a series of 1, 5, 10, 12, 15 and 20 wt%. These nanocomposites powders were mechanically mixed in a porcelain bowl for about 15 to 20 minutes. Figure 3.2 shows the ready mixed nanocomposites powders for ZnO/Fe<sub>3</sub>O<sub>4</sub> with different wt% of doped Fe<sub>3</sub>O<sub>4</sub> before calcination.

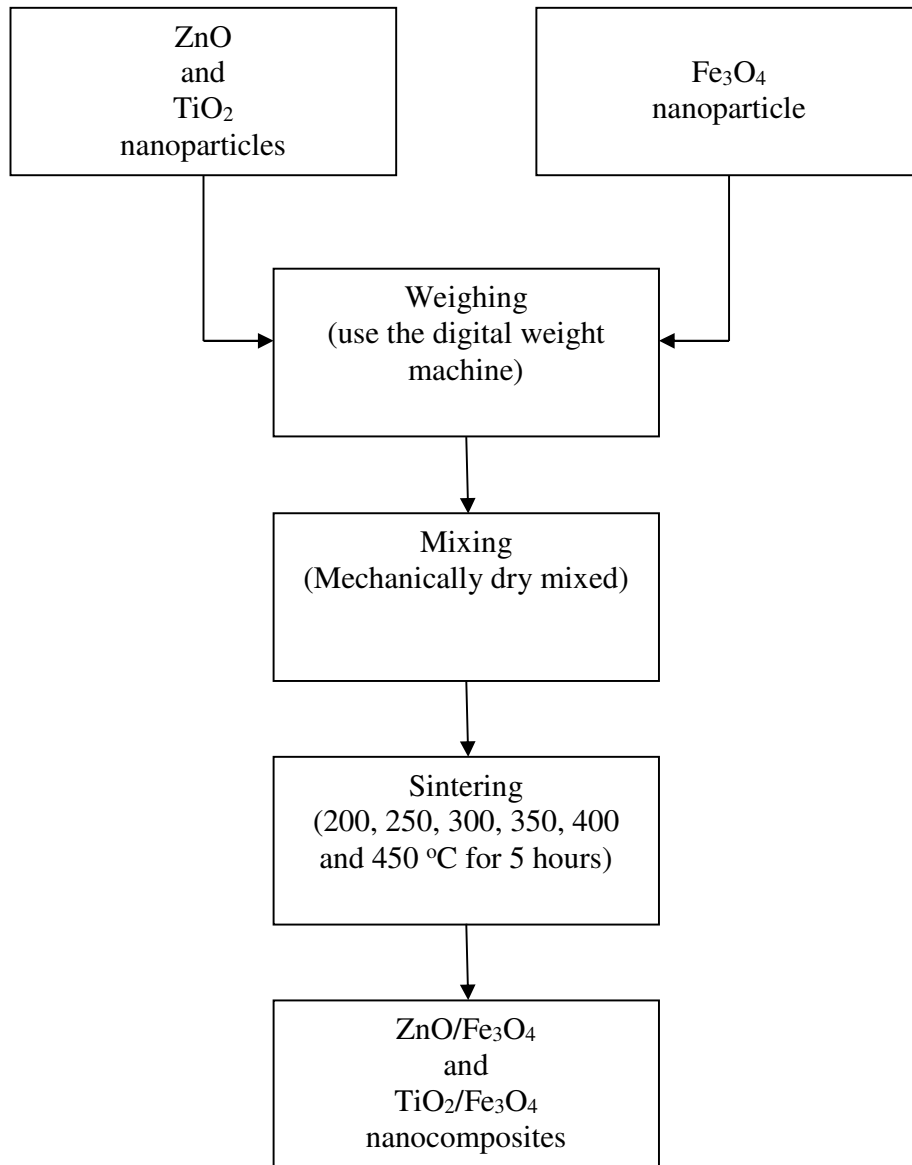


Figure 3.1 Flowchart of mechanically prepared ZnO/Fe<sub>3</sub>O<sub>4</sub> and TiO<sub>2</sub>/Fe<sub>3</sub>O<sub>4</sub> nanocomposites.



Figure 3.2: Different wt% of ZnO/Fe<sub>3</sub>O<sub>4</sub> powders after mechanical mixing. (a) 20 wt% of Fe<sub>3</sub>O<sub>4</sub>; (b) 1 wt% of Fe<sub>3</sub>O<sub>4</sub>.

Each series of the ready mixed nanocomposites powders were then sintered in the muffle furnace (Carbolite, ELF 11/6) at different sintering temperature (200, 250, 300, 350, 400 and 450 °C) for a duration of 5 hours. The heating rate adopted was fixed at 20 C° per minute. After sintering, all powders were physically grinded by using the micro spatula before kept in the vials. These nanocomposites samples were ready to be used for the photocatalytic process experiments. This is a simple method of low temperature powder mixing technique which has been used to prepare mixed oxide catalyst material (Bridgwater 2012, Ramezani and Neitzert 2012).

### **3.3 Photodegradation Study**

The aqueous solutions of the organic dyes were prepared in test tubes and the studies of its photocatalytic degradation were carried out in aqueous immobilized mode and slurry type experiment. This method was chosen due to its simple apparatus requirement, in agreement with several researchers whom reported significant degradation has taken place on the organic compound in aqueous immobilised mode (Augugliaro, Litter et al. 2006).

Before the degradation processes, the individual photocatalyst powder and the nanocomposites powder were premixed with distilled water in beakers and vials to obtain different concentration of the catalysts loading, that is between 0.50 wt% to 10.0 wt%. In addition, the organic dyes, such as MB, PR and MO, were also premixed by adding the weighted dyes powder (or solution) with distilled water to obtain the desired concentration, in the range of 2.00 ppm to 64.0 ppm depending on the dyes. MB dye was used as the model organic dye in few experiments. After that, 3.00 ml of organic dye solutions were added with 0.20 g (0.20 mL) of premixed photocatalyst of different concentrations. These mixtures were allowed to be in the dark for about 30 minutes to allow the establishment of adsorption/desorption equilibrium between the dye molecules and the surface of the photocatalyst (Kaur and Singhal 2014). They were then shifted and placed under UV light irradiation for various durations, with 10 minutes interval, to allow the degradation process to take place. The photocatalytic degradation was

carried out in the UV chamber (Uvitec Cambridge ultraviolet crosslinker, CL-508.G, with 5 of 8 W tube bulbs) equipped with five UV tube each producing light source of 254 nm wavelength, as shown in Figure 3.3.

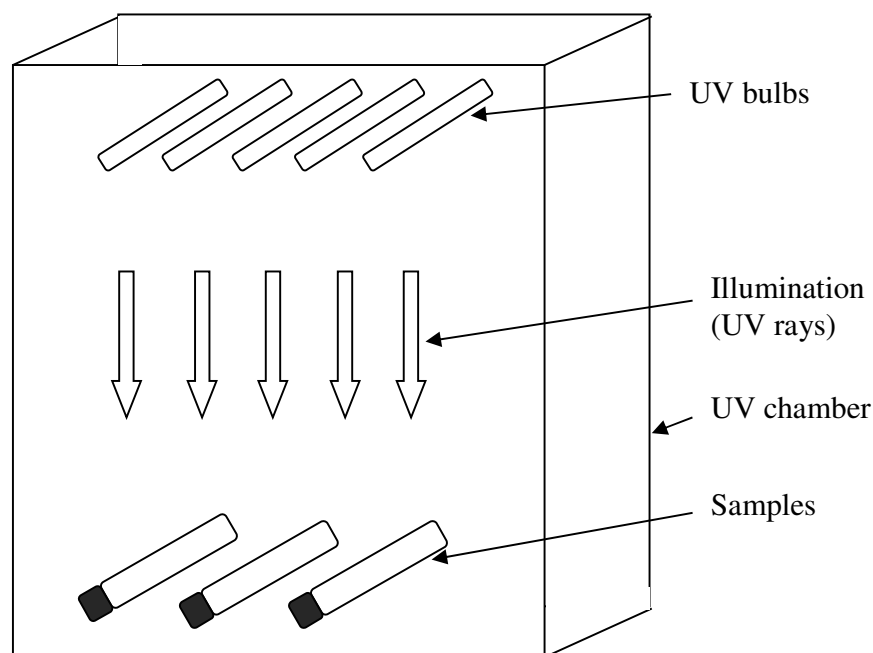


Figure 3.3: Schematic diagram of the experimental set up.

After the irradiation, each individual photocatalyst sample will be placed into the centrifuge (Kubota Tabletop Centrifuge 2420) to remove the photocatalyst before analysis whereas the nanocomposite sample was applied with magnetic field to separate the photocatalysts from the organic dye solutions. A 2 mL aliquot was taken from the solutions at regular time intervals to measure the absorption spectra of the dyes, and subsequently determine the percentage degradation of each dye. The first aliquot was withdrawn from the solutions right after the dark absorption/desorption

equilibrium period to determine the first absorbance spectrum ( $A_0$ ) of the dye, which represents the initial concentration ( $C_0$ ) of the dye.

The photocatalytic performance efficiency of the nanocomposite photocatalyst materials were evaluated by measuring the absorption spectra of the dyes in aqueous solutions using a UV-Visible Spectrophotometer (Varian, Cary 50) detector with scan rate of 120 nm/min for wavelength range from 200 nm to 800 nm. The degradation was studied by observing at the changes of the absorption maximum of the organic dye used. Throughout the investigations, various types of sample solutions were examined, such as dyes concentrations, irradiation duration and photocatalyst loading.

In the final part of this study, 5 sample dyes, Reactive Red 120 (RR120), Disperse Blue 15 (DB15), Acid Brown 14 (AB14), Orange G (OG) and Acid Orange 7 (AO7), have been randomly picked for the study of the photodecomposition processes by the ZnO/Fe<sub>3</sub>O<sub>4</sub> nanocomposites materials. All dyes were similarly prepared, with all dyes having similar concentration, and 3 ml of each dye was placed in individual vial. The ZnO/Fe<sub>3</sub>O<sub>4</sub> nanocomposite was then added into the each dye solutions. The properties such as the number of azo groups, benzene groups, molecular weight and absorbance, in relation to their rate of decomposition were studied.

### **3.4 Characterization**

The raw and prepared nanocomposites samples were sent for particle size and microstructures measurements. The microstructures of the samples were studied by using field emission scanning electron microscopy (FESEM) from FEI, Quanta 400 SE/SEM, coupled with energy dispersive X-ray analyser (EDX) and a high resolution transmission electron microscope (TEM) from LEO 912AB equipped with energy filter. TEM sample was obtained from a suspension of nanocomposites then was sonicated before it was dispensed onto a 300-mesh carbon-coated copper grid and then evaporated the solvent. The crystal structures were characterised by using X-ray diffraction (XRD) by using PANalytical, US, X'Pert Pro Powder employing a scanning rate of 0.20 degree per second through the  $2\theta$  range of  $10^\circ$  to  $80^\circ$  with Cu-K $\alpha$  radiation. The specific surface area was determined on the basis of BET instrument using Micromeritics, ASAP 2020 V3.01 H. The sample was degassed for 2 hrs at 250 °C prior to the N<sub>2</sub> adsorption analysis.

#### **3.4.1 X-Ray Diffraction**

In the study of materials, it is common to use X-ray diffraction (XRD) to determine the bulk structure and composition of heterogeneous photocatalysts with crystalline structure. X-ray diffraction is the elastic scattering of energetic X-ray photons by atoms in a periodic lattice. The

scattered monochromatic X-rays that are in phase produce constructive interference.

The XRD analysis is the identification of the lattice planes that produce peaks at their corresponding angular positions  $2\theta$ , through the derivation of lattice spacing by using the Bragg's law (Niemantsverdriet 2007):

$$2d \sin \theta = n\lambda; \quad n = 1, 2, \dots \quad [3.1]$$

where:

$n$  is the integer for the order of the reflection;

$\lambda$  is the wavelength of the X-rays;

$d$  is the distance between two lattice planes;

$\theta$  is the angle between the incoming X-rays and the normal to the reflecting lattice plane.

Although XRD analysis is typically limited to the identification of a number of specific lattice planes, the characteristic patterns associated with individual solids make XRD quite useful for the identification of bulk crystalline or composite materials. An illustration of X-rays diffraction by crystal planes is shown in Figure 3.4.

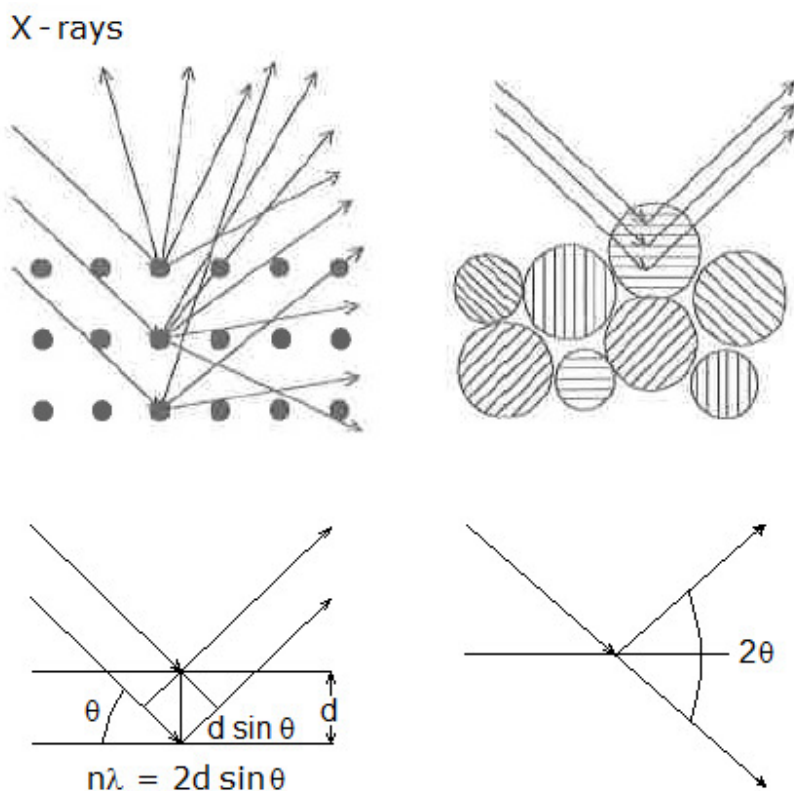


Figure 3.4 Illustration of X-rays scattered by atoms in an ordered lattice interfere constructively in directions given by Bragg's law (Niemantsverdriet 2007).

Thus, XRD is very useful in the identification of bulk crystalline components of solid photocatalysts because of its ability to give the corresponding lattice spacings which produce the characteristic patterns associated with individual solid. The X-ray diffraction pattern of a powdered sample is measured with a stationary X-ray source (usually Cu-K $\alpha$ ) and a moveable detector, which scans the intensity of the diffracted radiation as a function of the angle  $2\theta$  between the incoming and the diffracted beams. In

addition, this method also able to identify any impurity phases, if they exist in the sample powder.

Besides, XRD also able to estimate the average crystallite or grain size of photocatalysts. Although XRD assist in phase recognition, it has one limitation, namely that clear diffraction peaks are only observed when the sample possesses sufficiently long range order. However, this limitation is a clear advantage since the width (or rather the shape) of diffraction peaks provides information on the dimensions of the reflecting planes. The diffraction lines are very narrow if it is perfect crystals, but the line is broadening when incomplete destructive interference in scattering directions where the X-rays are out of phase.

For sample with sufficiently long-range order, the XRD peaks are intense and sharp, whereas for crystallite sizes below about 100 nm, the peaks become broader due to incomplete destructive interference in scattering directions. X-ray diffraction pattern with 2.4 and 1.1 wt% Pd in two silica-supported palladium catalysts showing a line broadening at the (111) and (200) reflections where the average particle size are found to be 4.2 and 2.5 nm, respectively (Niemantsverdriet 2007). The average crystallite/grain size  $D$ , can be estimated by applying the Debye-Scherrer equation (Singh, Zeng et al. 2012):

$$D = \frac{K\lambda}{\beta \cos\theta} \quad [3.2]$$

where

$K$  is the shape factor (has typical value of about 0.90);

$\lambda$  is the X-ray wavelength (e.g. Cu-K $_{\alpha}$  line);

$\beta$  is the measured width (in radian) of a diffraction line at half-maximum at position of diffraction angle  $2\theta$ ; normally called FWHM.

$\theta$  is the angle between the beam and the normal on the reflecting plane.

The Scherrer equation is limited to nanoscale particles (Singh, Zeng et al. 2012). It is not applicable to grains larger than about 100 nm, which precludes those observed in most metallographic and ceramographic microstructures. The width of the diffracted X-ray peak would solely give particle size, if contribution from inhomogeneous strain and instrumental effect into the line width is zero; otherwise, size calculated using the Scherrer equation has a larger value than the actual particle size (Singh, Zeng et al. 2012).

Another example of the application of the equation above, for the characterization of anatase TiO $_2$  photocatalysts is shown in Figure 3.5. Zhang et al. (1998) was using the line width of the (101) diffraction peak at 25.4° to determine the average grain sizes of samples which were treated at different temperatures; a significant growth in particle size was clearly observed for sample sintered at higher temperatures (Zhang, Wang et al. 1998).

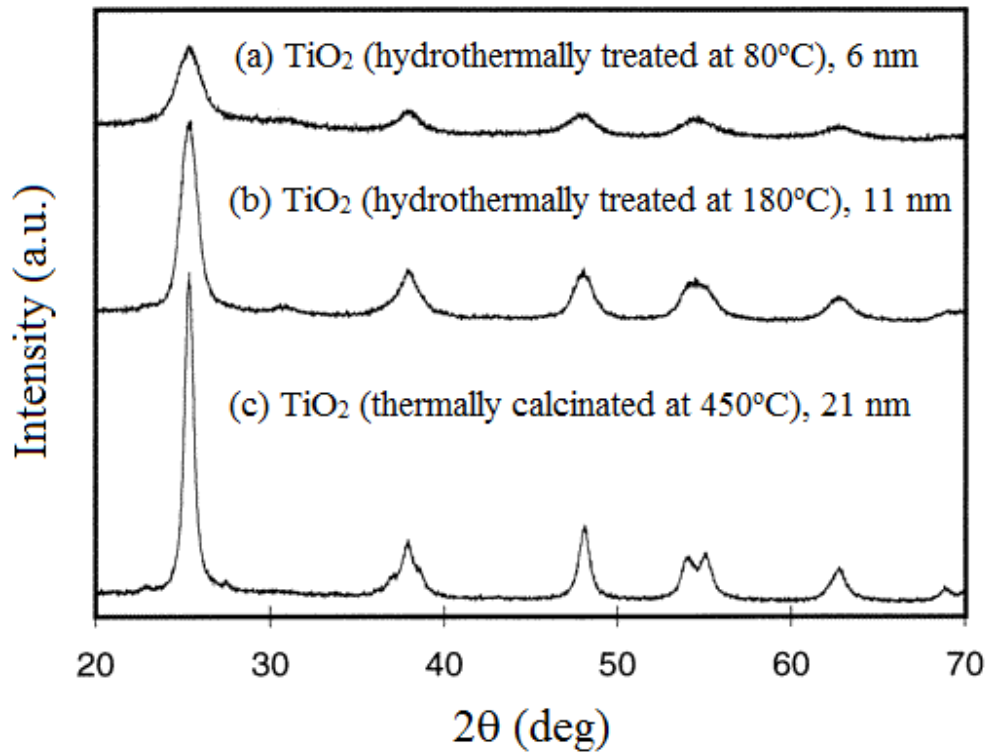


Figure 3.5 XRD patterns for three TiO<sub>2</sub> samples treated at different temperature (Zhang, Wang et al. 1998).

On the other hand, by using smaller wavelengths and when the diffraction lines shift to lower angle, the line broadening is reduced. Thus, by using Mo K $\alpha$  X-rays (17.44 keV;  $\lambda \approx 0.07$  nm), one can obtain diffraction patterns from smaller particles than with Cu K $\alpha$  radiation (8.04 keV;  $\lambda \approx 0.15$  nm) (Niemantsverdriet 2007).

In this study, the photocatalysts powder were characterised by using PANalytical, US, X'Pert Pro Powder employing a scanning rate of 0.20 degree per second through the  $2\theta$  range of  $10^\circ$  to  $80^\circ$  with  $\text{Cu-K}_\alpha$  radiation. The measurement was done in reflection mode ( $\text{Cu-K}_\alpha$  radiation with  $\text{Ge}(220)$  monochromator). After the scanning, the completed XRD pattern for the particular sample was compared and matched to the published standard patterns in the literature. This matching will be able to identify the crystal structures present in the sample as well as any impurities that existed.

### ***3.4.2 Scanning Electron Microscope***

The scanning electron microscope (SEM) is one of the most useful tools for imaging surface and subsurface microstructure. The accelerating voltage is usually between 1 and 30 keV. The electron gun usually consists of a tungsten or lanthanum hexaboride ( $\text{LaB}_6$ ) filament, as shown in Figure 3.6, however field emission guns (FEGs) are becoming increasingly necessary for imaging nanostructures at high resolution. The lower voltages can be used with high-brightness  $\text{LaB}_6$  and FEG sources and they are often employed to increase surface detail and obviate sample charging in non-conducting or poorly conducting samples.

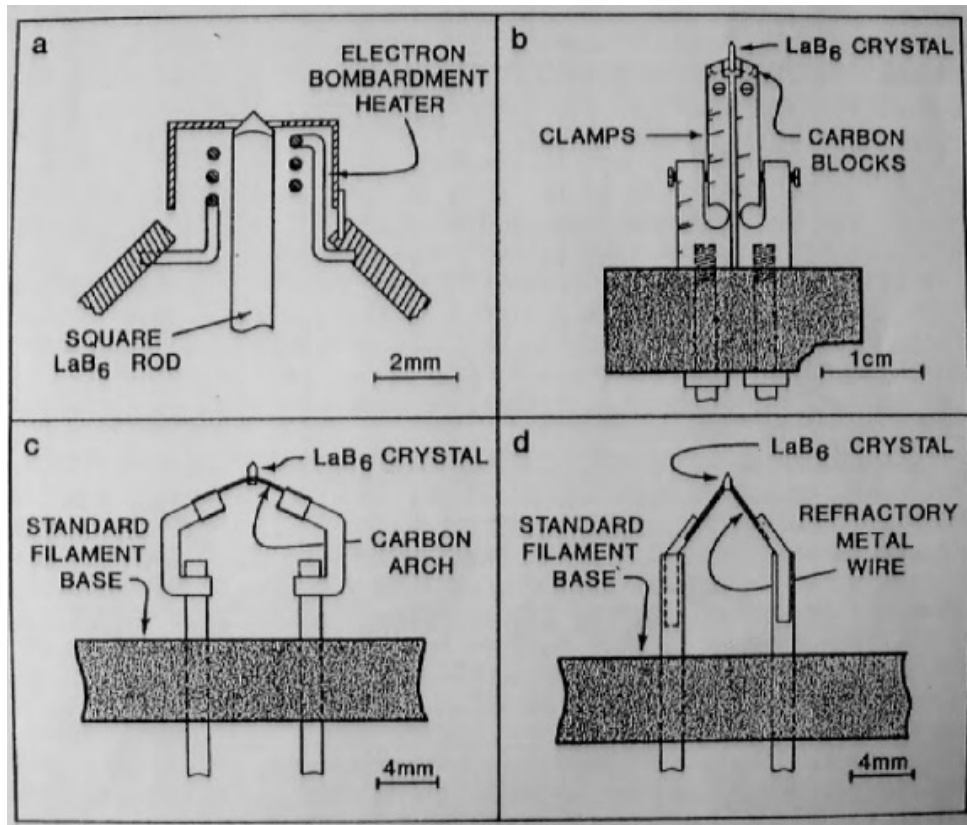


Figure 3.6 Images of an electron gun and a LaB<sub>6</sub> filament (Yoshimura 2007).

Usually, two or more condenser lenses are used to demagnify the crossover produced by the gun, while the objective lens focuses the electron probe onto the specimen so that the final probe diameter lies between 2 and 10 nm. The objective aperture limits the angular spread,  $\alpha$ , of the electrons. The focused beam is scanned across the specimen surface in a two-dimensional raster, with the beam passing through the optic axis at the objective lens; meanwhile, an appropriate detector monitors the secondary electrons or other signal, such as backscattered electrons or X-rays, as they

are emitted from each point on the surface. Simultaneously, using the same scan generator, a beam is scanned across the recording monitor.

The intensity of each pixel on the monitor is controlled by the amplified output of the selected detector and is corresponding point on the specimen surface. The magnification is simply the ratio of the monitor raster size to the specimen raster size and, as in field ion microscopy, it involves no lens. Simple diagram of the SEM is shown in Figure 3.7.

Finally, to determine the elemental composition of the nanocomposites, they were examined by the energy dispersion X-ray analyser (EDX) that is attached to the FESEM instrument mentioned above. The analysis of EDX is based on the emission of an X-ray. An X-ray is emitted when an electron from an outer shell of an atom (e.g. the 2s shell) lowers its energy to fill the hole in a lower shell (e.g. the 1s shell). The detected signals are displayed as a spectrum of X-rays intensities versus their energies. The energies of the characteristic X-rays allow the elements making up the sample to be identified, while the intensities of the characteristic X-ray peaks allow the concentrations of the elements to be quantified (Razeghi 2009).

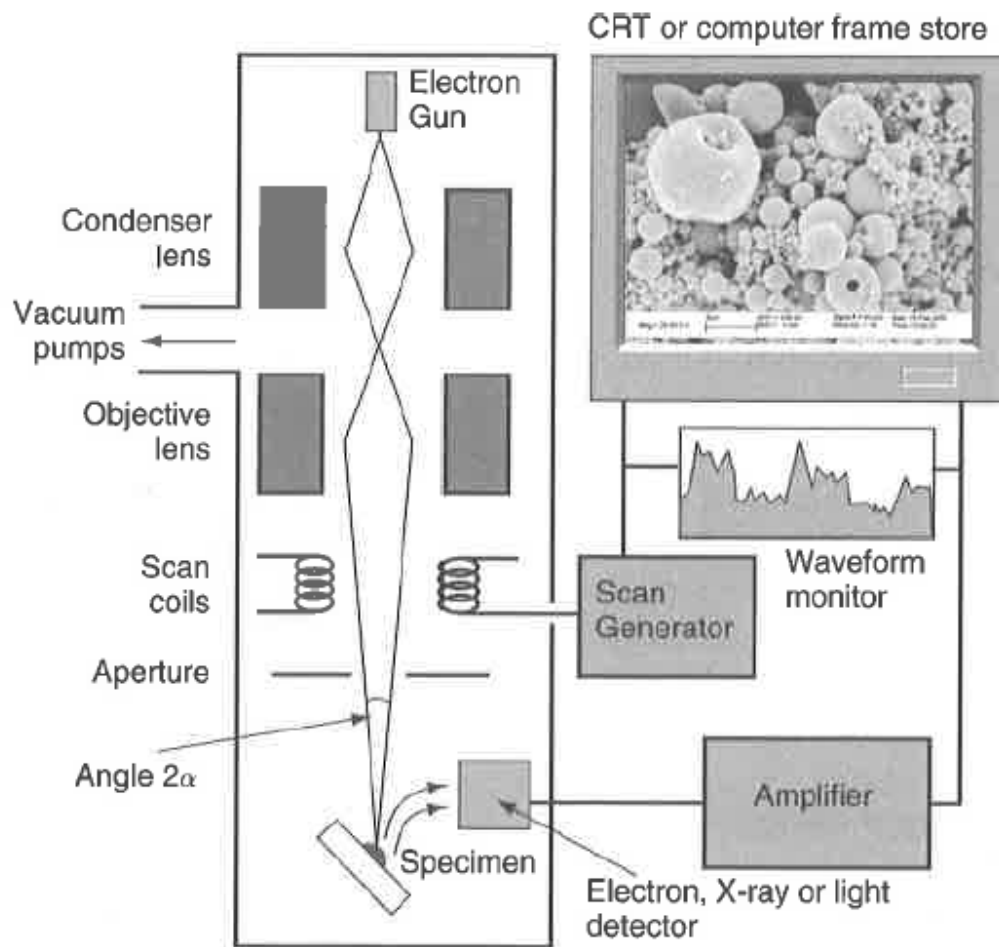


Figure 3.7 Schematic diagram of the layout of a scanning electron microscope (Kelsall, Hamley et al. 2006).

In this study, all the powder samples were characterized by field emission scanning electron microscopy (FESEM) from FEI, Quanta 400 SE/SEM. This instrument is coupled with energy dispersive X-ray analyser (EDX). After obtaining the results, the micrographs were analysed by

observing the dispersibility of all samples. In addition, porosity and agglomeration of the nanocomposites were also investigated.

### ***3.4.3 Transmission Electron Microscope***

A tool that effectively employed for imaging the internal microstructure of ultrathin specimens is transmission electron microscope. The electron gun is usually thermionic tungsten or LaB<sub>6</sub>, however FEGs are becoming increasingly common. The accelerating voltage is considerably higher than in an SEM and is typically 100-400 kV, although a number of specialist high-voltage instruments are designed to operate at 1 MV and above. The benefits of high voltage include increased imaging resolution, due to the decreased electron wavelength, and also increased penetration and thus the ability to study thicker samples. The scanned images are able to differentiate between solid and hollow sphere, as shown in Figure 3.8.

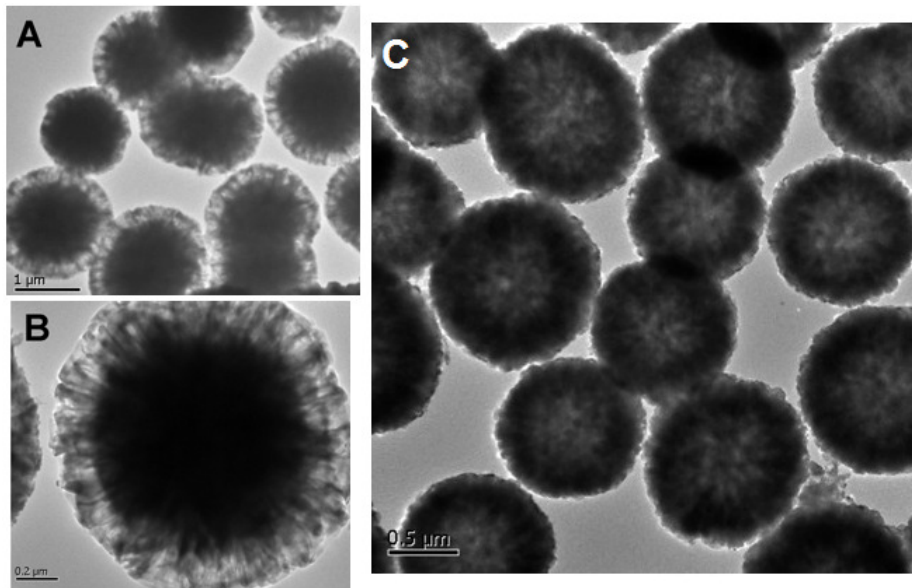


Figure 3.8 Differentiating between a solid ball (**A**, **B**) and a hollow sphere (**C**) in a transmission electron microscope (Yang and Zeng 2004).

Two or more condenser lenses demagnify the probe to typically 1 mm in diameter, although this can be reduced via use of a condenser-objective nanoprobe system. The condenser excitation controls the beam diameter and convergence. The first condenser (C1) controls the demagnification of the crossover (the spot size), whilst the second condenser (C2) controls the size and convergence of the probe at the specimen, and hence the area of the sample under illumination.

The specimen must be no more than a few hundred nanometers in thickness, and is usually in the form of a 3 mm diameter disc. The specimen is located between the pole pieces of the objective lens. The combination of

the objective lens and the projector lens system provides an overall magnification of around  $10^6$ . The selected area diffraction (SAD) aperture allows selection of a minimum samples are of  $\sim 0.1$ mm diameter for electron diffraction. Smaller areas (down to a few nanometres in diameter) can be selected using a focused probe rather than an aperture; this is convergent beam electron diffraction (CBED).

TEM specimens are normally in the form of an ultrathin disc, prepared by cutting, mechanical polishing or chemical dissolution, followed by electropolishing (for conducting materials), chemical polishing (for semiconductors and ceramics) or ion beam milling, including focused ion beam (FIB) machining. Powder may be ground and dispersed onto an amorphous support film on a 3.05 mm circular metal grid, as shown in Figure 3.9(a). Simple layout of an analytical TEM is shown in Figure 3.10.

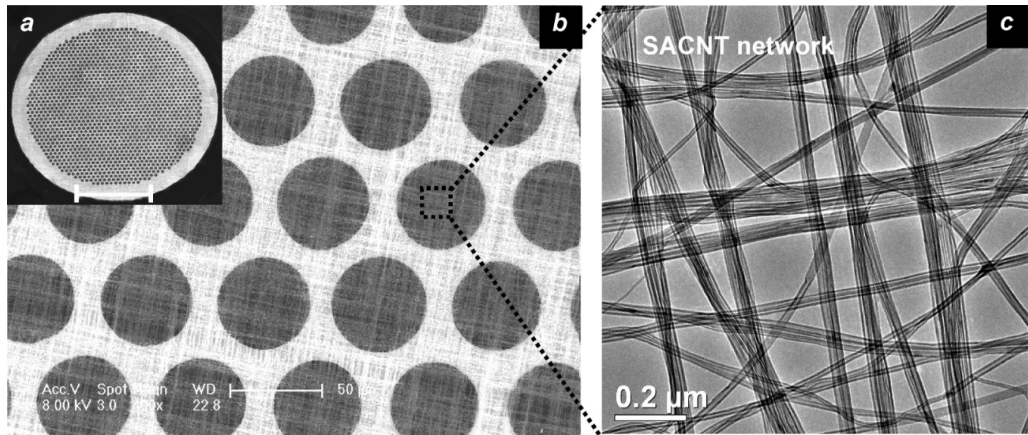


Figure 3.9 (a) Overhead Morphologies of a SACNT-grid. (a) A SEM full view image of a SACNT-grid (the scale bar represents 1 mm length). (b) Image of the SACNT gauze over the holes of the copper grid base (local magnification of panel a). (c) Image of the carbon nanotube gauze covering a hole showing a network morphology (local magnification of panel b) (Zhang, Feng et al. 2008).

In the current study, high resolution transmission electron microscope (TEM) from LEO 912AB was used for the characterization and particle size analysis. It is also equipped with energy filter. For the characterization, TEM sample was obtained from a suspension of nanocomposites and then was sonicated before it was dispensed onto a 300-mesh carbon-coated copper grid and then evaporated the solvent. At the point of obtaining the results, each micrograph was analyzed to examine their degree of agglomeration. Moreover, all the micrographs were also used to measure the average particle size of the nanocomposites.

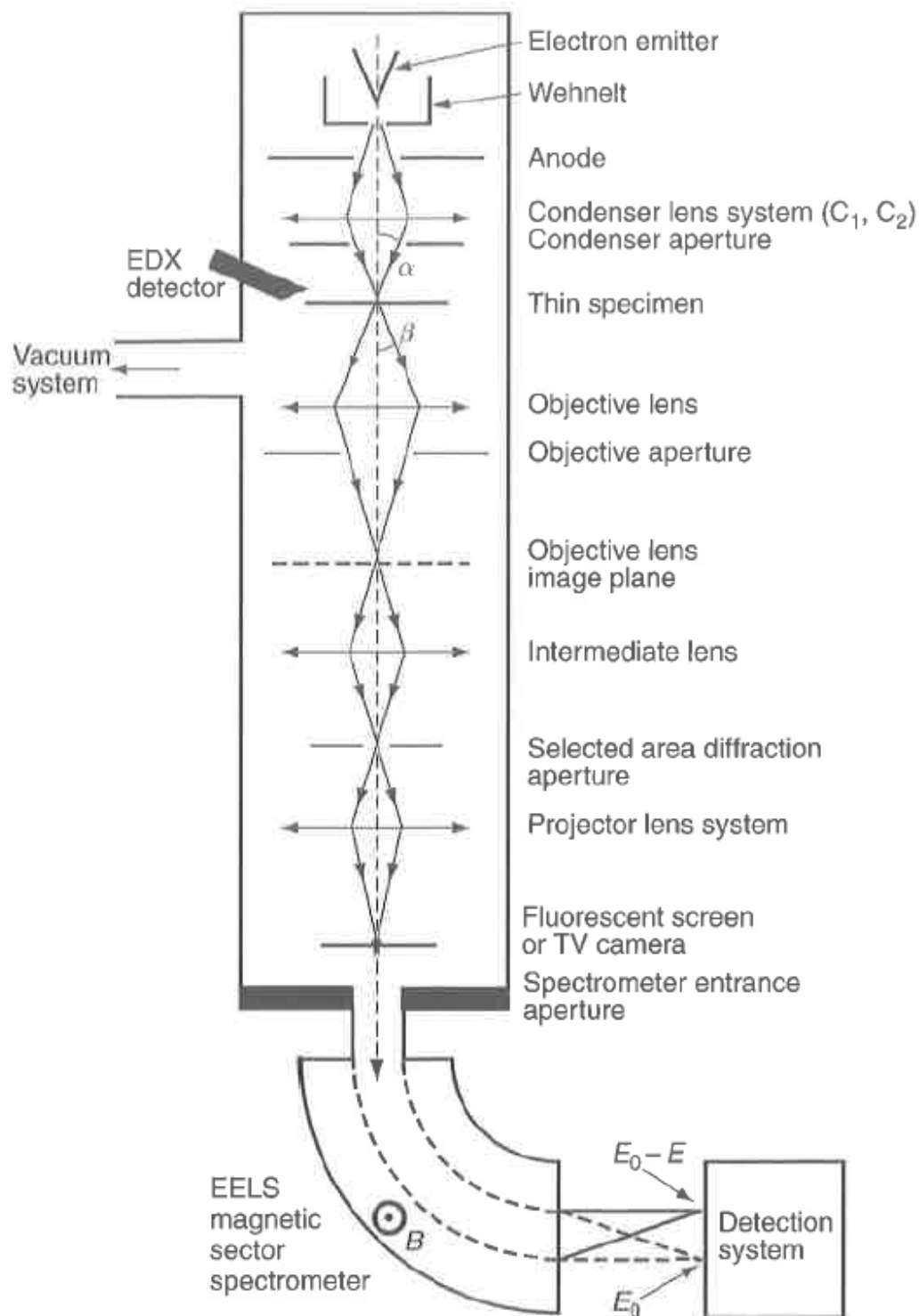


Figure 3.10 Schematic diagram of a layout of an analytical transmission electron microscope (Kelsall, Hamley et al. 2006).

### 3.4.4 Surface Area Analysis

When the size of a particle is getting smaller, its surface area will become increasingly significant. It is therefore very important to know how much of the material is exposed to the gas phase no matter whether it is unsupported catalysts or support materials. This property is expressed by the specific area, in units of  $\text{m}^2 \cdot \text{g}^{-1}$ , as shown in Figure 3.11. Typical supports such as silica and alumina have specific areas on the order of 200 to 300  $\text{m}^2 \cdot \text{g}^{-1}$ , while active carbons may have specific areas of up to 1000  $\text{m}^2 \cdot \text{g}^{-1}$  or more. Unsupported catalysts have much lower surface area, typically in the range of 1 to 50  $\text{m}^2 \cdot \text{g}^{-1}$  (Niemantsverdriet 2007).

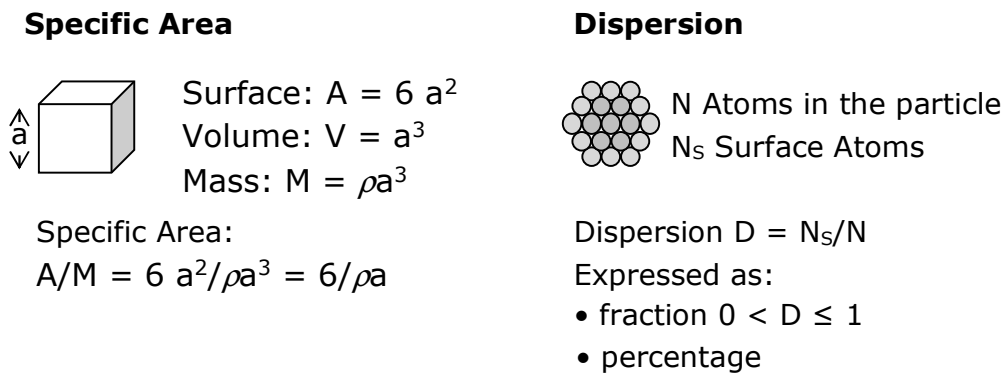


Figure 3.11 Specific area and dispersion are important characteristic properties of a supported catalyst (Niemantsverdriet 2007).

Surface areas are determined by physisorption. The most common procedure to determine surface area is to measure how much N<sub>2</sub> is adsorbed onto a certain amount of material. The uptake is measured at a constant low temperature, i.e., 80K, as a function of N<sub>2</sub> pressure, and is usually very well described by the Brunauer-Emmett-Teller (BET) isotherm. After determining the number of N<sub>2</sub> molecules that form a monolayer on the support, one obtains the total area by setting the area of a single N<sub>2</sub> molecule to 0.16 nm<sup>2</sup> (Niemantsverdriet 2007).

For particles on a support, dispersion is an important property and is straight-forwardly defined as the fraction of atoms in a particle located at the surface, as given in Figure 3.11. The dispersion is usually determined by chemisorption of a gas that adsorbs only on the supported particles, and not on the support. The most frequently used gas in the modelling of the adsorption in pores is nitrogen, N<sub>2</sub>. It is due to the nonpolar nature of the nitrogen molecules and it can be modelled as spherical shape. Moreover, the adsorption data for nitrogen are easily accessible in the literature (Nguyen and Do 1999). On the other hand, for metals, hydrogen or CO are the obvious choices. It is necessary to adopt a certain stoichiometry for the number of H-atoms or CO molecules that can be accommodated per surface atom in the particle (this is usually taken as one CO or H-atom per metal atom) (Niemantsverdriet 2007).

The specific surface area for all sample powder was determined by using the BET instrument using Micromeritics, ASAP 2020 V3.01 H. The sample was degassed for 2 hrs at 250 °C prior to the N<sub>2</sub> adsorption analysis. The results used in the analysis were BET specific surface area, pore size and pore volume. The results will provide better understanding on the photocatalytic capability of the nanocomposites.

### ***3.5 Photocatalytic Performance Investigation***

#### ***3.5.1 Photodegradation Measurement***

The photocatalytic experiments were conducted to investigate the photodegradation of organic compounds in aqueous suspension system. After the UV light irradiation for a certain time interval, each sample was applied with magnetic field (or by centrifugation for raw powders) to separate the suspensions of the photocatalyst nanoparticles from the dye solution. The concentration of the dye was measured by UV-vis spectrophotometer using Cary 50 (Varian) detector with a scan rate of 120 nm/min in the range of 200 nm to 800 nm.

The photodegradation of sample dyes were analysed with the UV-vis spectrophotometer to determine the absorbance ( $A$ ) of the dyes after each irradiation. The Beer-Lambert law governs the absorption of monochromatic

light that connects the decrease in intensity of the light with the optical path and the concentration of the absorbing species by an exponential equation (Kelsall, Hamley et al. 2006):

$$I = I_0 \exp \varepsilon l C \quad [3.3]$$

where

$I$  is the intensity of the monochromatic light after it passed through a cell of length  $l$ , containing a solution of concentration  $C$  of the absorbing species.

$I_0$  is the incident light intensity; and

$\varepsilon$  is the absorptivity, a constant characteristic of the absorbing material.

Transmission is probably one of the common forms that is generally used for high surface area samples and thin films due to little radiation is absorbed by a single monolayer. In the mode of transmission, the amount of absorbed radiation is characterized in terms of the transmittance given by (Kelsall, Hamley et al. 2006):

$$T = I/I_0 \quad [3.4]$$

or, the absorbance given by:

$$A = - \log T \quad [3.5]$$

In the condition where reflection and scattering are negligible, the transmittance is given by:

$$T = 10^{-\epsilon l C} = \exp(-\alpha l) \quad [3.6]$$

where the absorption coefficient,  $\alpha$ , is related to the absorptivity and concentration by:

$$\alpha = \ln 10 \epsilon C \quad [3.7]$$

Therefore, the absorbance of a solution is directly proportional to the concentration of the compound in the solution and the path length (Kelsall, Hamley et al. 2006):

$$A = \epsilon l C \quad [3.8]$$

where

$A$  is the absorbance (no units);

$\epsilon$  is the molar absorptivity ( $\text{L mol}^{-1}\text{cm}^{-1}$ );

$l$  is the path length of the sample solution in the cuvette (cm);

$C$  is the concentration of the compound in the solution ( $\text{mol L}^{-1}$ ).

The rate of degradation was studied in terms of changes of the absorption maximum at their absorption peak. Different organic materials

have specific absorption peak. In order to produce the absorbance calibration curve of the dye solution used as according to Beer-Lambert law, eight (8) aqueous solutions of different concentrations of the dyes were prepared, in the range of 2 – 16 ppm, as shown in Figure 3.12 for MB.



Figure 3.12 Eight different concentration of the MB dye solutions in vials.

It is very obvious that with increasing concentration, the color of the dye solution turns darker when under visual inspection, which subsequently will increase the light absorption significantly. The UV vis absorption spectra of the dyes were measured and the results is shown in Figure 3.13.

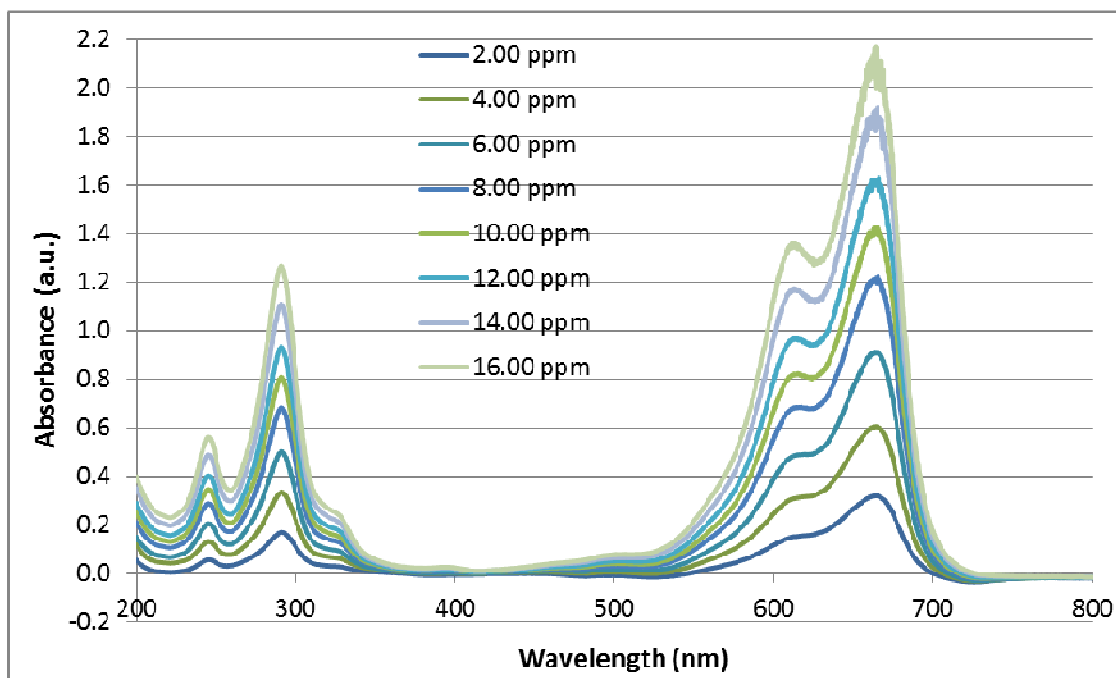


Figure 3.13 UV vis absorption spectra for different concentrations of MB dye solutions.

By taking the value of each dyes' absorbance at their maximum absorbance, the graph of the dyes absorbance versus their individual concentration were plot, as shown in Figure 3.14. The graph shows a straight line ( $R^2 = 0.9823$ ) and passing through the origin, which indicate good linear relationship between the absorbance and the concentration of the dyes, for concentration in the range of 2 – 16 ppm.

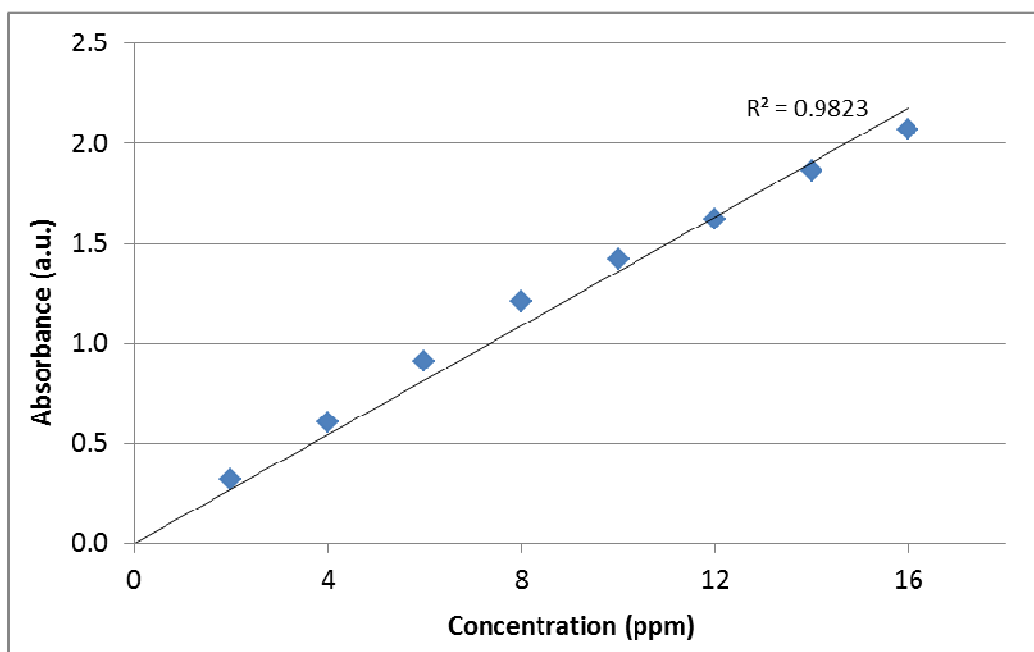


Figure 3.14 The dyes absorbance versus their concentrations.

With the above confirmation that the absorbance ( $A$ ) of the dyes is directly proportional to its concentration ( $C$ ), therefore, the following equation is valid to be used to calculate the photodegradation efficiency of the dyes. The percentage degradation was calculated from the initial and final absorption of the UV-vis experiments as follows:

$$\% \text{ Degradation} = \frac{C_o - C}{C_o} \times 100 = \frac{A_o - A}{A_o} \times 100 \quad [3.9]$$

where

$C_o$  and  $C$  are the initial and post-irradiation concentration of the dye, respectively;

$A_0$  and  $A$  are the initial and post-irradiation absorbance of the dye, respectively, as measured by the UV-vis spectrophotometer.

The degradation rate was studied by observing the changes of the absorption maximum of the particular organic dye. The monitored wavelength was 665 nm for MB, 435 nm for PR and 465 nm for MO. MB is used as the model organic dye in determining the optimum concentration and substitution for photodegradation process, as well as the appropriate sintering temperature to form the magnetic nanophotocatalyst material.

### ***3.5.2 Photocatalysis Kinetics Analysis***

There are few factors affecting the photocatalytic reaction rate and efficiency of photocatalytic processes, one of which is the adsorption of the substrate onto the surface of the catalyst. In the reactions, the organic contaminant is oxidized by the reactive oxygen species such as the hydroxyl  $\cdot\text{OH}$  and superoxide  $\text{O}_2^{\cdot-}$  radicals or by the photo-generated holes ( $\text{h}^+$ ) formed on the surface of the catalyst. The prerequisite mechanism for an efficient oxidation requires that the contaminant absorbs on the catalyst surface. The absorption and desorption process is characterized by the transfer of the reactants in the aqueous phase to the surface; adsorption of the reactants; reaction in the adsorbed phase; desorption of the products;

and removal of the products from the interface region (Dalrymple, Yeh et al. 2007).

Generally, researchers describe the adsorption and desorption process and reaction rate constant based on the associated Langmuir–Hinshelwood (L–H) model, which is represented as follows (Dalrymple, Yeh et al. 2007):

$$r = -\frac{dC}{dt} = k\left(\frac{KC}{1+KC}\right) \quad [3.10]$$

where  $r$  is the rate of photooxidation,  $k$  is the reaction rate constant,  $C$  is the concentration and  $K$  is the adsorption coefficient. The applicability of the equation depends on several assumptions, which include (i) the reaction system is in dynamic equilibrium; (ii) the reaction is surface mediated; (iii) the competition for the photocatalyst active surface sites by the intermediates and other reactive oxygen species is not limiting (Chong, Jin et al. 2010). When the organic contaminant concentration is very low, generally at mM ( $C \ll 1$ ), an apparent first-order rate constant could be expressed as follows:

$$r = -\frac{dC}{dt} = k_r C \quad [3.11]$$

where  $k_r$  ( $\text{min}^{-1}$ ) is the apparent first-order photocatalytic reaction rate constant. By some rearrangement and simple integration on equation (Eq.

3.11) yields the typical pseudo-first-order model that can be expressed as follows:

$$C(t) = C_o e^{-k_r t} \quad [3.12]$$

$$\ln \frac{C_o}{C} = k_r t \quad [3.13]$$

This rate constant is often determined by observing the relative aqueous concentration changes of the contaminant, as in equation (Eq. 3.9), as a function of time during experiments, that is  $\ln(C_o/C)$  versus  $t$ .

## **CHAPTER 4**

### **Characterization of Zinc Oxide, Titanium Dioxide and Iron (II,III) Oxide Photocatalysts and Degradation Study of Three Organic Dyes (MB, PR & MO)**

#### **4.1 Introduction**

In general, metal oxides can take a variety of structural geometries together with an electronic structure that can exhibit different characteristics, such as metallic, semiconductor and insulator. Therefore, they have emerged as a very important substance and contribute in many areas of physics, chemistry and materials science (Amini and Ashrafi 2016). Recently, metal oxides have gained enormous interest in heterogeneous photocatalysis due to its emerging applications toward environmental remediation and organic synthesis (Amini and Ashrafi 2016). Many researchers attempted to study photocatalytic activity of different metal oxides like SnO<sub>2</sub>, ZnO, ZrO<sub>2</sub>, CeO<sub>2</sub>, WO<sub>3</sub>, TiO<sub>2</sub>, In<sub>2</sub>O<sub>3</sub>, etc. (Talebian and Nilforoushan 2010, Leghari, Sajjad et al. 2011, Wang, Zhai et al. 2013, Faisal, Ibrahim et al. 2015).

Both ZnO and TiO<sub>2</sub> have been extensively used as photocatalyst which have become a promising environmental remediation technology, water photoelectrolysis and dye-sensitized solar cells, due to their low cost,

environmental friendly, nontoxicity, high chemical stability and excellent degradation for organic pollutants (Amini and Ashrafi 2016).

On the other hand, little is known about the use of iron oxide as a photocatalyst although there has been extensive investigation for the possible use in photoelectrolysis cells (Iwanski, Curran et al. 1981). However, in recent years many of the iron oxide nanoparticles have been synthesized and extensively investigated (Casbeer, Sharma et al. 2012, El Ghandour, Zidan et al. 2012). Although there are numerous conditions determining the effectiveness of this magnetic nanoparticles in wastewater treatment system, there are a number of studies have demonstrated the success of  $\text{Fe}_3\text{O}_4$  nanoparticles on the removal of heavy metals from contaminated water (Hou, Tian et al. 2015, Kim, Woo et al. 2016). Besides, this magnetic nanoparticle also showed a sustainable treatment process through reusing and still regaining the removal capacity in few treatment cycles (Chiu, Khiew et al. 2010, Wang, Yang et al. 2016).

In the present study, the photodegradation of the three type of dyes, namely methylene blue (MB), phenol red (PR) and methyl orange (MO) were investigated and the most optimum amount of loading for the three metal oxides, ZnO,  $\text{TiO}_2$  and  $\text{Fe}_3\text{O}_4$  nanoparticles photocatalysts, were evaluated. These dyes were chosen as the organic compound since they are complex organic substances which contain a significant amount of various functional groups and are well dissolved in water.

MB consists of dark green crystals or crystalline powder and has a bronze-like luster. Solution of MB in water or alcohol gives a deep blue color. MB dye is easy to monitor by simple techniques such as UV-visible spectroscopy at its maximum absorption wavelength (Nogueira, Castro et al. 2014), with its four main peaks at 665, 614, 293 and 247 nm (Kuan and Chan 2012). Besides, MB is one of the high consuming materials in the dye industry, as well as in environmental sciences to study the suitability of various materials for wastewater discoloration (Reza, Kurny et al. 2015). On the other hand, MB is used as a bacteriological stain and as an indicator. It inhibits Guanylate Cyclase, and has been used to treat cyanide poisoning and to lower levels of Methemoglobin.

On the other hand, PR is a weak organic acid and is a typical reversible pH-sensitive dye. It is used as red dye, pH indicator and diagnostic aid for determination of renal function. In addition, it is also applied in the studies of the gastrointestinal and other biological systems (Sochacka 2015). Finally, MO is a typical azo dye and generally used in the textile industry. It is very stable and is commonly used as the probe for evaluating photocatalysts, with its absorption maximum wavelength,  $\lambda_{\max}$ , at 466.5 nm (Hakamada, Hirashima et al. 2012). Besides, it is also used for the detection, identification, analysis of chemical, biological, or pathologic processes or conditions. It is also used in a chemical titration that is on the passage between acidity and alkalinity. The ZnO, TiO<sub>2</sub> and Fe<sub>3</sub>O<sub>4</sub> nanoparticles

photocatalysts were used in the investigation of the effects of different operational parameters on the decomposition of these dyes.

## **4.2 Experimental Results**

### *4.2.1 X-ray Deffractometry (XRD)*

Figure 4.1 shows the XRD characterization for ZnO, TiO<sub>2</sub> and Fe<sub>3</sub>O<sub>4</sub> nanoparticles. All these nanoparticles were used without any further treatment. As shown in Figure 4.1(i), through the  $2\theta$  values, for ZnO nanoparticles, the diffraction peaks which appeared at 31.79°, 34.44°, 36.27°, 47.54°, 56.65°, 62.90°, 66.38°, 67.95° and 69.10° reveal the diffraction planes (100), (002), (101), (102), (110), (103), (200), (112) and (201), respectively. These peaks are consistent with the database in JCPDS file (#79-0208), which are the standard peaks of the ZnO planes with a hexagonal wurtzite crystal structure (SG:  $P6_3mc$ ) (Saravanan, Mansoob Khan et al. 2015). The diffraction pattern also indicates high purity of the nanopowder as there was no other impurity peaks are observed. The XRD pattern shows fine broadening of peaks that indicating ultrafine nature of the crystallites powder.

For the TiO<sub>2</sub> nanoparticles XRD characterization, as shown in Figure 4.1(ii), the diffraction maximum appeared at 25.27°, 36.94°, 37.74°, 38.56°,

47.99°, 53.84°, 55.03°, 62.65°, 68.70°, 70.23° and 75.00° correspond to the (101), (103), (004), (112), (200), (105), (211), (118), (116), (220) and (215) diffraction planes, respectively. These  $2\theta$  values match the characteristic pattern of pure anatase phase of  $\text{TiO}_2$  tetragonal structure (SG:  $I4_1amd$ ), with no other crystalline byproducts, in agreement with the literatures JCPDS file #21-1272 (Adachi, Jiu et al. 2008, Liu, Chu et al. 2015).

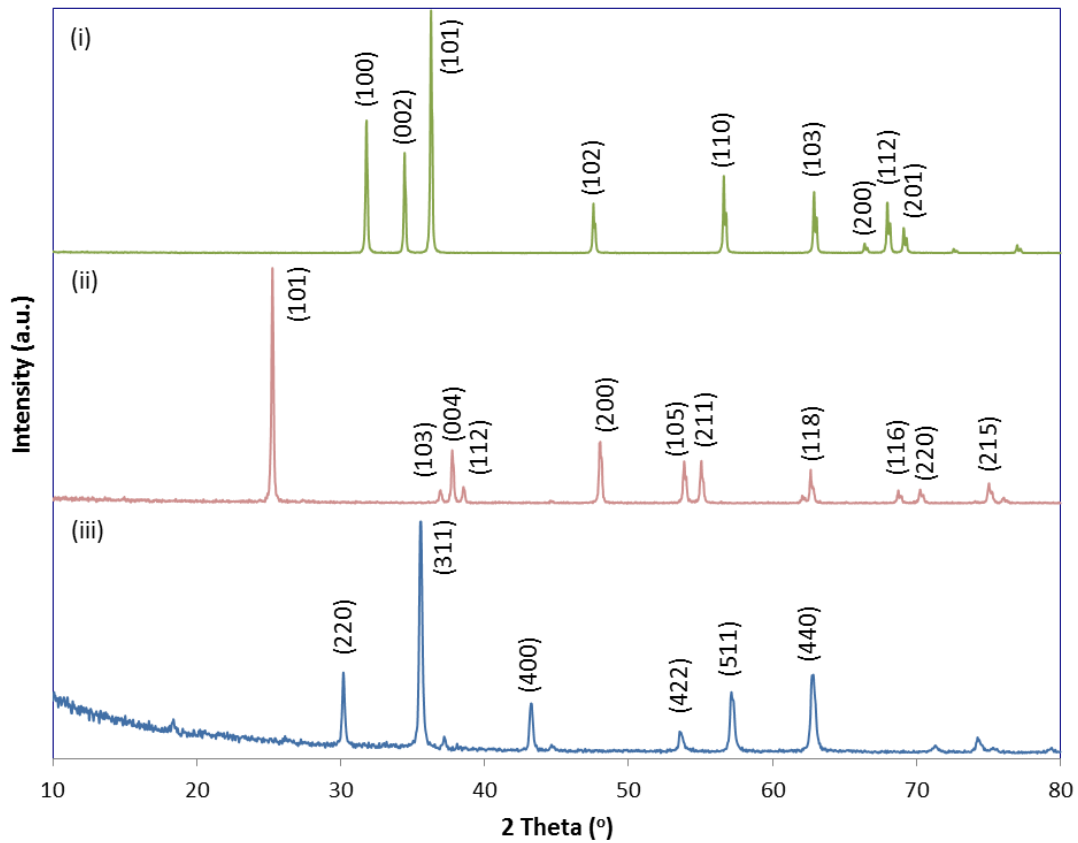


Figure 4.1: X-ray diffraction pattern of (i) ZnO, (ii)  $\text{TiO}_2$  and (iii)  $\text{Fe}_3\text{O}_4$  nanoparticle photocatalysts.

The XRD characterization for Fe<sub>3</sub>O<sub>4</sub> nanoparticles shows the diffraction peaks at 30.20°, 35.56°, 43.22°, 53.63°, 57.13° and 62.75° in correspondence to the diffraction planes (220), (311), (400), (422), (511) and (440), respectively. It can be seen that the diffraction peaks conform to the Fe<sub>3</sub>O<sub>4</sub> crystal of cubic spinel structure, consistent with literature JCPDS file #19-0629 (Wu, Shen et al. 2011).

It could also be learnt that the relatively wide half-peak breadth indicated a smaller crystalline size. These results, especially its purity, could be supported by the EDX analysis, which were discussed in section 4.2.5. On top of that, the average crystallite size of the samples also can be evaluated from Scherrer equation (Eq. 3.2). The average crystalline size of the ZnO, TiO<sub>2</sub> and Fe<sub>3</sub>O<sub>4</sub> oxides are (91 ± 12) nm, (117 ± 16) nm, and (62.1 ± 5.7) nm, respectively, as indicated in Table 4.1.

Table 4.1: Crystallite size for different peaks and average crystallite size for ZnO, TiO<sub>2</sub> and Fe<sub>3</sub>O<sub>4</sub> nanoparticles.

Sample	Peak	Crystallite Size (nm)	Average Crystallite Size (nm)
ZnO	(100)	108.2	91.1 ± 12.0
	(002)	108.9	
	(101)	91.26	
	(102)	142.1	
	(110)	73.87	
	(103)	50.83	
	(112)	62.74	
TiO <sub>2</sub>	(101)	106.6	117.4 ± 16.0
	(004)	78.56	
	(200)	142.4	
	(105)	145.9	
	(211)	146.6	
	(118)	60.91	
Fe <sub>3</sub> O <sub>4</sub>	(220)	80.83	62.12 ± 5.70
	(311)	65.57	
	(400)	67.15	
	(422)	43.72	
	(511)	50.78	
	(440)	52.24	

#### 4.2.2 Field Emission Scanning Electron Microscopy (FESEM)

Figure 4.2 shows the FESEM photos for morphologies of ZnO, TiO<sub>2</sub> and Fe<sub>3</sub>O<sub>4</sub> nanoparticles. All the three samples show no aggregation with a well disperse nanoparticle, and fairly homogeneous in size for TiO<sub>2</sub> and Fe<sub>3</sub>O<sub>4</sub>, while for ZnO nanoparticles with a slightly wider range of size distribution. The dimension of ZnO nanoparticles range from 48 to 778 nm and they are in irregular shapes with an average particle size of  $(166.8 \pm 9.4)$  nm. The SEM analysis for ZnO was similar to the study by Yassitepe et al. (2008), which the ZnO nanoparticles on plates that were sintered at 700 °C also showed irregular shapes and highly porous structure, while produced a relatively high surface area (Yassitepe, Yatmaz et al. 2008). The BET result for this ZnO plates was also quite similar to this study, as provided in section 4.2.4 (Table 4.2).

For the TiO<sub>2</sub> nanoparticles, they were spherical in shape. The size distribution and shape were quite uniform and well disperse. The spherical TiO<sub>2</sub> nanoparticles has a diameter in between 32 and 175 nm, with an average particle size of  $(80.2 \pm 1.7)$  nm. The morphology for the Fe<sub>3</sub>O<sub>4</sub> nanoparticles was quite similar to the TiO<sub>2</sub> nanoparticles with generally spherical in shape. However, the diameter of the Fe<sub>3</sub>O<sub>4</sub> nanoparticles was slightly larger than TiO<sub>2</sub> nanoparticles with the size range from 16 to 190 nm, with an average particle size of  $(64.5 \pm 2.3)$  nm.

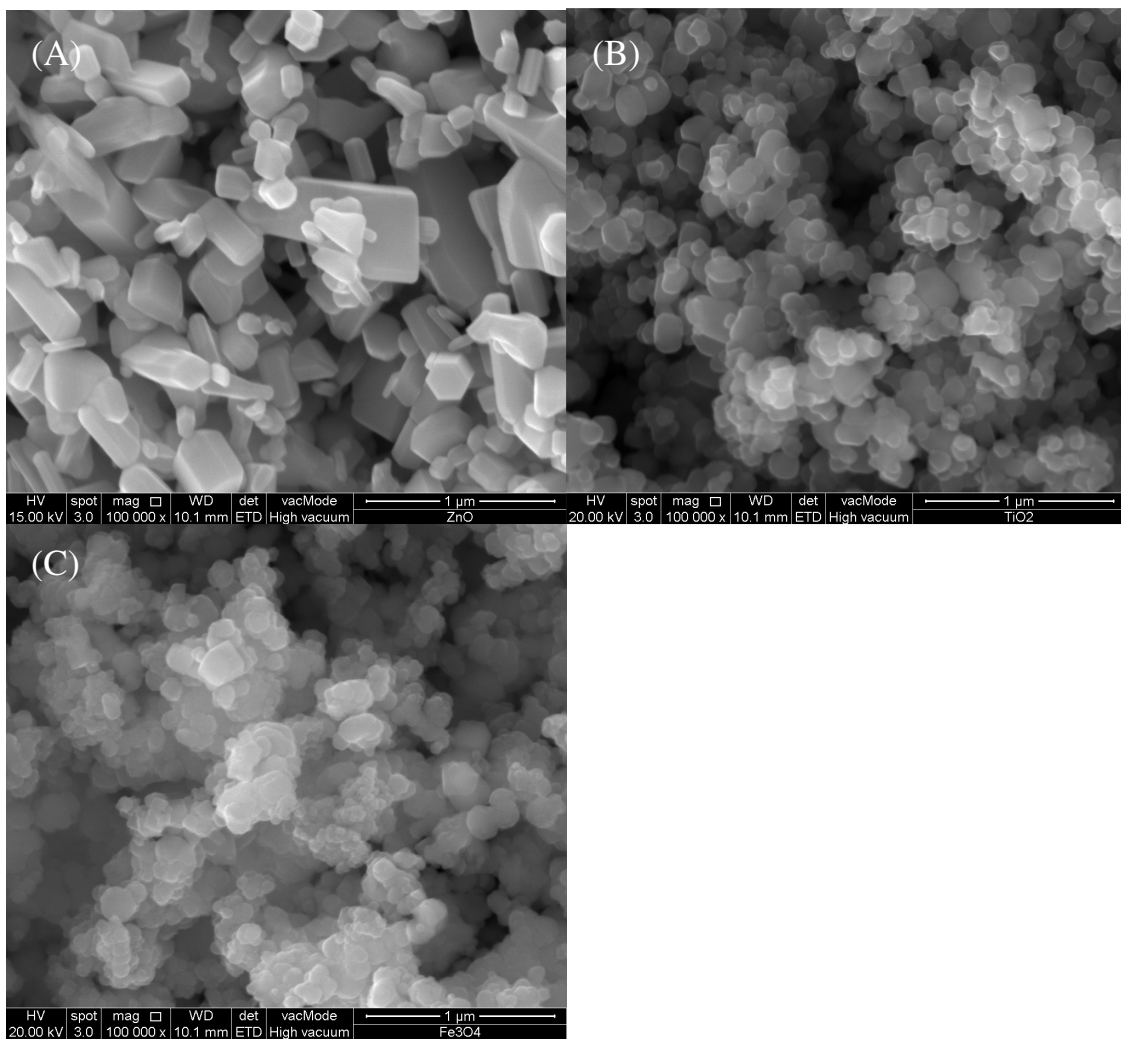


Figure 4.2: FESEM picture of (A) ZnO, (B) TiO<sub>2</sub> and (C) Fe<sub>3</sub>O<sub>4</sub> nanopowder photocatalysts.

### 4.2.3 Transmission Electron Microscopy (TEM)

TEM images in Figure 4.3 show the micrograph images of ZnO, TiO<sub>2</sub> and Fe<sub>3</sub>O<sub>4</sub> nanoparticles. The photo indicates that the metal oxide was well dispersed. The ZnO nanoparticles were irregular in shape with spherical to rod-like, as well as particle in blocks. It shows a wide particle size distribution with an average particle size of  $(93.2 \pm 4.6)$  nm. The details for the size distribution could be referred to the size distribution histogram, shown in Figure 4.4(A), which was obtained from the direct measurement from the transmission electron microscopy images. The average particle size was in approximate agreement with the crystallite size obtained from XRD.

The micrograph of TiO<sub>2</sub> nanoparticles (Figure 4.3(B)) shows that the metal oxide particles were generally spherical with few rod-like shape and fairly monodispersed. The particle size distribution was quite narrow as compared to the other two nanoparticles, as shown in Figure 4.4(B), with an average particle size of  $(80.0 \pm 3.9)$  nm. Figure 4.3(C) indicates the TEM characterization for the Fe<sub>3</sub>O<sub>4</sub> nanoparticles. The captured image showed that the oxide was uniformly dispersed throughout with the particles were globular in shape and quite evenly distributed in size. The average particle size is  $(64.0 \pm 4.6)$  nm, as measured directly from the micrograph with the histogram shown in Figure 4.4(C). This result was also in approximate agreement with the XRD result. These Fe<sub>3</sub>O<sub>4</sub> nanoparticles are slightly better than the magnetite nanoparticles reported by Nogueira et al. (2014), where

their TEM micrographs showed the nanoparticles were quite agglomerated. This would decrease the surface area and could affect the degradation capability of the nanoparticles (Nogueira, Castro et al. 2014).

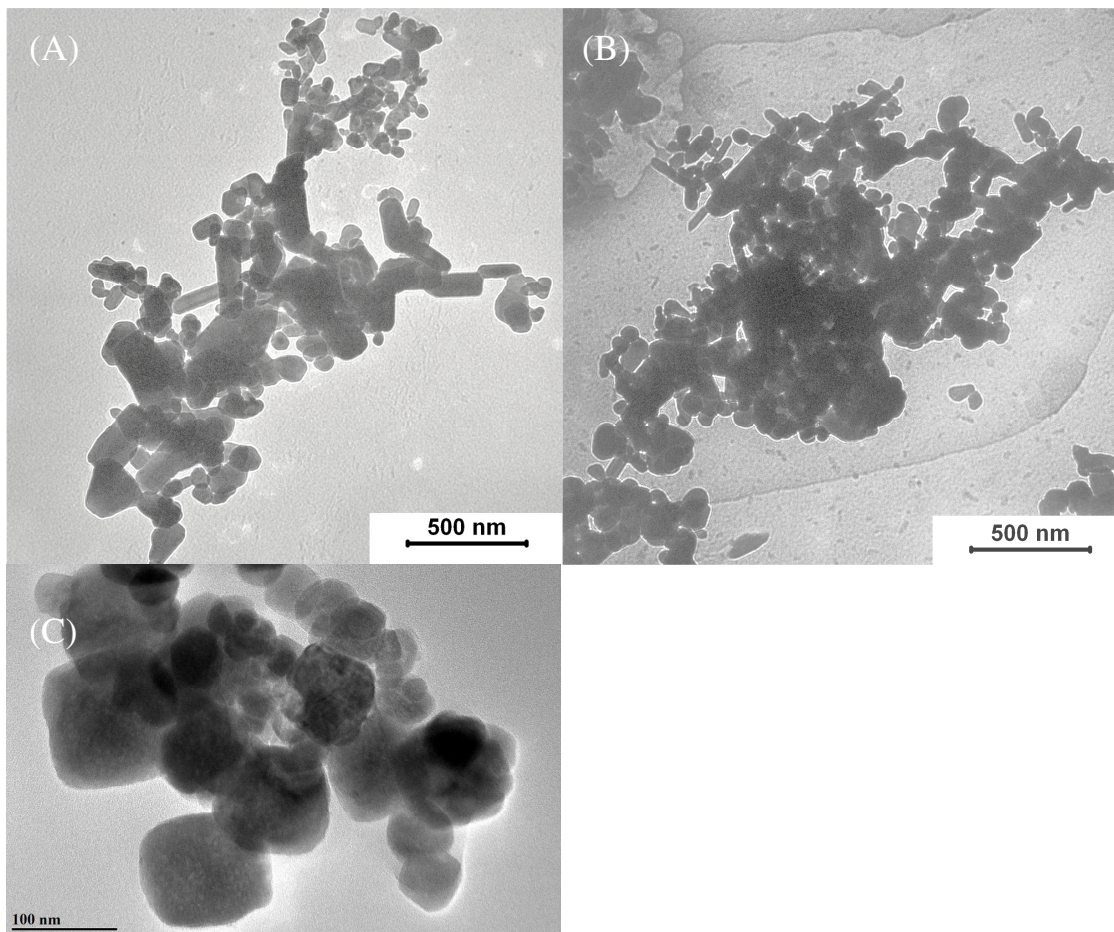


Figure 4.3: TEM picture of (A) ZnO, (B) TiO<sub>2</sub> and (C) Fe<sub>3</sub>O<sub>4</sub> nanoparticle photocatalysts.

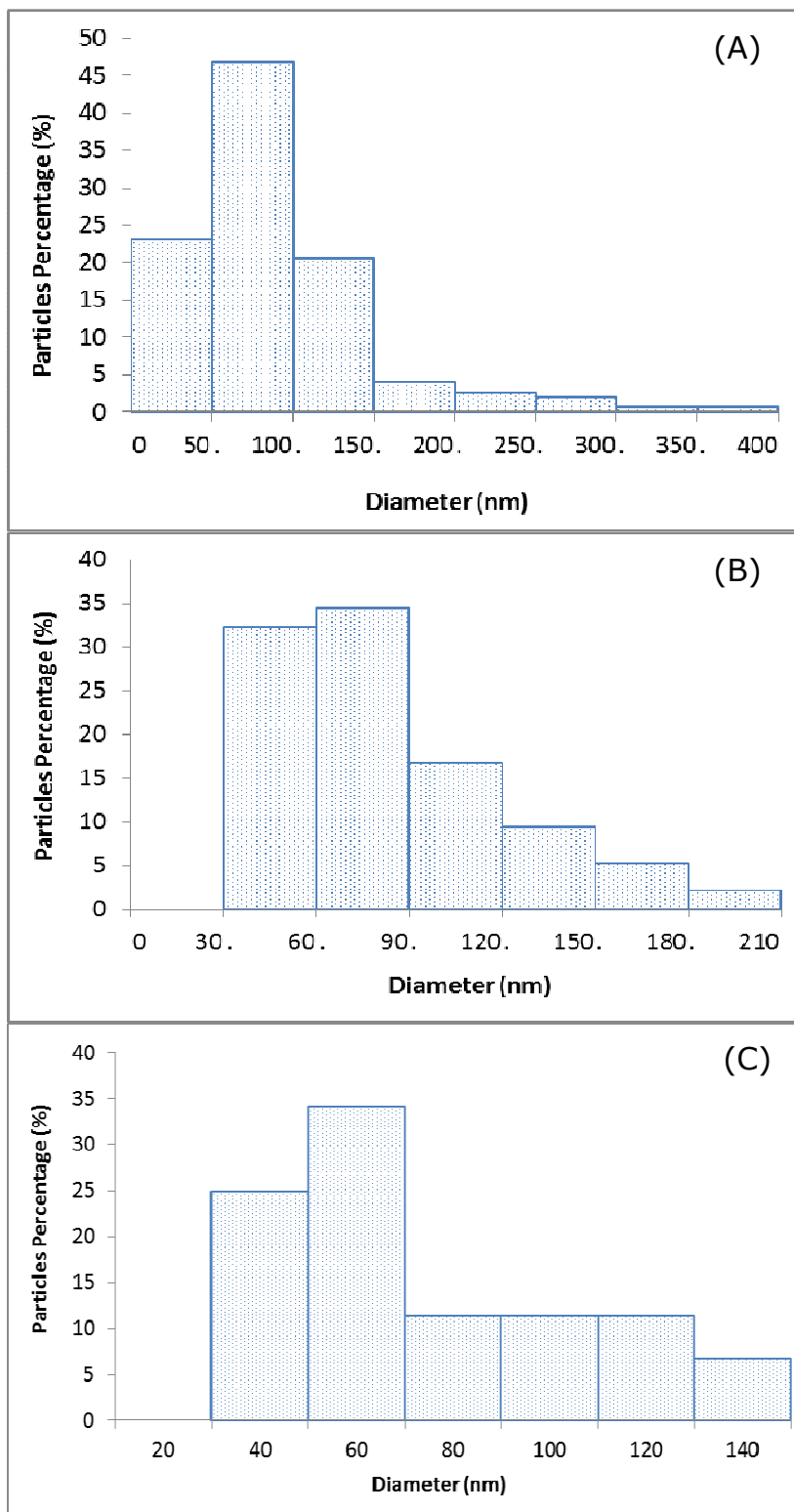


Figure 4.4: Particle size distribution histogram for (A) ZnO, (B) TiO<sub>2</sub> and (C) Fe<sub>3</sub>O<sub>4</sub> nanoparticles.

#### 4.2.4 Brunauer-Emmett-Teller Surface Area Analysis (BET)

The BET measurement for ZnO, TiO<sub>2</sub> and Fe<sub>3</sub>O<sub>4</sub> nanoparticles was given in Table 4.2. The BET surface area for ZnO, TiO<sub>2</sub> and Fe<sub>3</sub>O<sub>4</sub> were 2.406, 6.795 and 12.458 m<sup>2</sup>/g, respectively. The average pore size for ZnO was smaller than TiO<sub>2</sub> but larger than Fe<sub>3</sub>O<sub>4</sub>, which is 15.941 nm, whereas for TiO<sub>2</sub> and Fe<sub>3</sub>O<sub>4</sub> were 22.699 and 12.785 nm, respectively.

The measurement of pore volume for TiO<sub>2</sub> and Fe<sub>3</sub>O<sub>4</sub> showed quite similar values, which were 0.03856 and 0.03982 cm<sup>3</sup>/g, respectively. However, pore volume for ZnO was very much smaller as compared to other oxides, which recorded a value of merely 0.009590 cm<sup>3</sup>/g. The results clearly show that ZnO nanoparticles were having smaller surface area and pore volume if compared to the TiO<sub>2</sub> photocatalyst, which might impact its photodegradation capability. A report by Hakamada and his co-researchers on nanoporous metals showed that nanoporous Au exhibits effective catalytic degradation on methyl orange (MO) solution as compared to its counterpart, bulk Au which does not. They also show other nanoporous metals such as Pd and Ni which also exhibit the catalytic degradation properties (Hakamada, Hirashima et al. 2012).

Table 4.2: BET data for ZnO, TiO<sub>2</sub> and Fe<sub>3</sub>O<sub>4</sub> nanoparticles

Measurement Properties	ZnO	TiO <sub>2</sub>	Fe <sub>3</sub> O <sub>4</sub>
BET Surface Area (m <sup>2</sup> /g)	2.406	6.795	12.458
Pore Volume (cm <sup>3</sup> /g)	0.009720	0.04519	0.04367
Average Pore Size (nm)	16.156	26.606	14.023

#### 4.2.5 Energy Dispersive X-ray Spectroscopy (EDX)

Figure 4.5 shows the EDX spectrum for the ZnO, TiO<sub>2</sub> and Fe<sub>3</sub>O<sub>4</sub> nanoparticle photocatalysts. The atomic fraction of each materials elements, ZnO, TiO<sub>2</sub> and Fe<sub>3</sub>O<sub>4</sub>, were in close agreement with their chemical formulae, with the values (1:1.12), (1:2.96) and (1:1.52), respectively. The presence of each element for each respective spectrums strengthen the arguments on the purities of these nanoparticles (Hafez, Lan et al. 2010). The element C comes from the carbon tape that holding each nanoparticles, which was also reported in other study. The related EDX data is listed in Table 4.3. Together with the XRD analysis, it conforms that the samples are pure, single phase and nanocrystalline in nature.

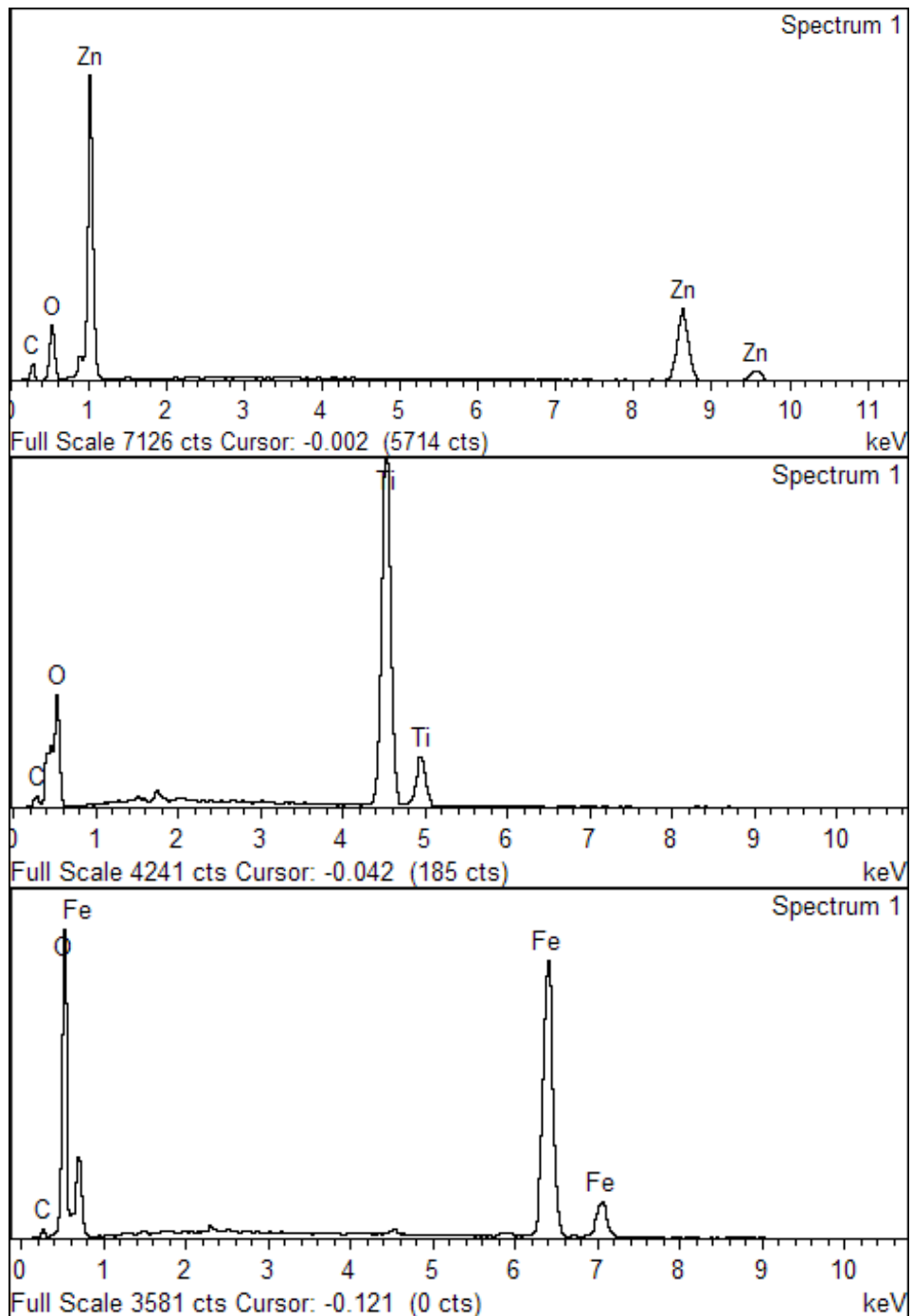


Figure 4.5: Energy dispersive X-ray spectroscopy (EDX) for (A) ZnO, (B) TiO<sub>2</sub> and (C) Fe<sub>3</sub>O<sub>4</sub> nanoparticles.

Table 4.3: EDX data of ZnO, TiO<sub>2</sub> and Fe<sub>3</sub>O<sub>4</sub> nanoparticles

Sample	Element	Weight percentage (wt%)	Atomic percentage (At%)
ZnO	C	4.88	14.35
	O	20.51	45.31
	Zn	74.61	40.34
	Total	100.00	100.00
TiO <sub>2</sub>	C	2.36	4.62
	O	48.52	71.28
	Ti	49.12	24.10
	Total	100.00	100.00
Fe <sub>3</sub> O <sub>4</sub>	C	3.92	9.35
	O	32.26	57.86
	Fe	63.82	32.79
	Total	100.00	100.00

#### *4.2.6 Photocatalytic Analysis using UV Visible Spectrophotometry (UV Vis)*

##### *4.2.6.1 Photodecomposition study on the organic dye solution without the presence of photocatalytic material*

Some organic dyes are very photostable and difficult to undergo photodecomposition even being irradiated with UV light for a long time, while certain dyes are self-degrading when exposed to direct UV light for a short period of time, without the presence of catalyst (Mekasuwandumrong, Pawinrat et al. 2010). Therefore, blank experiments were carried out to observe the effect of self-degradability of dyes under UV light in the absence of catalyst. The first blank experiment was conducted on the MB dye. The concentration of MB used for this observation was 12.0 ppm with solution volume of 3.0 ml. The sample was immediately measured with the UV-vis spectra to obtain the spectrum before being irradiated with UV light. The analysis was then continued for 60 minutes irradiation with 10 minutes irradiation for each interval. As shown in Figure 4.6, the UV-vis spectra measurement showed a gradual decrease as MB was irradiated with the UV light. The decreasing of the absorption peaks, which were observed at 665 nm, indicates that the organic compound in MB has been gradually degraded. The photodecomposition results clearly indicate that MB has gone through the photolysis or photodegrade when exposed to UV light, but very weak and insignificant. MB is a heterocyclic aromatic chemical compound, a model of thiazin dyes. It contains auxochromic alkylamine groups which plays an

important role in photocatalytic degradation. N-demethylation of MB occurs when part of the methyl groups degrade and hypsochromic shift occurs. Besides, the photolysis is very weak due to benzene ring and heteropolyaromatic linkage. (Tayade, Natarajan et al. 2009, Zuo, Du et al. 2014, Dariani, Esmaeili et al. 2016).

In addition, the blank observations were also being conducted on different concentration of MB which was also measured at absorption peak of 665 nm, as can be seen in Figure 4.7. From the graphs, it showed that although the concentration of the MB solutions were different, the degradation process that took place were all very minimal, as more than 70% of the organic dye still can be detected even after 60 minutes of intense UV irradiation. This indicates that MB is not able to go through photolysis and will harm the environment if release into the stream. Therefore, it requires additional treatment to completely decompose its organic compound before release into the river.

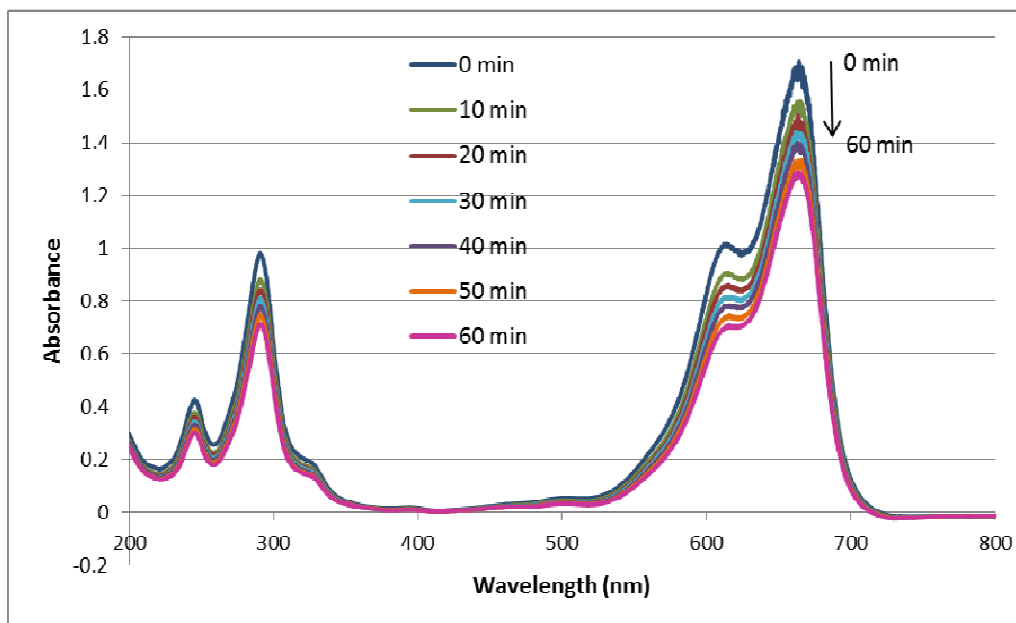


Figure 4.6: Time variation of UV-vis absorption spectra of 12.0 ppm MB without photocatalyst under UV irradiation.

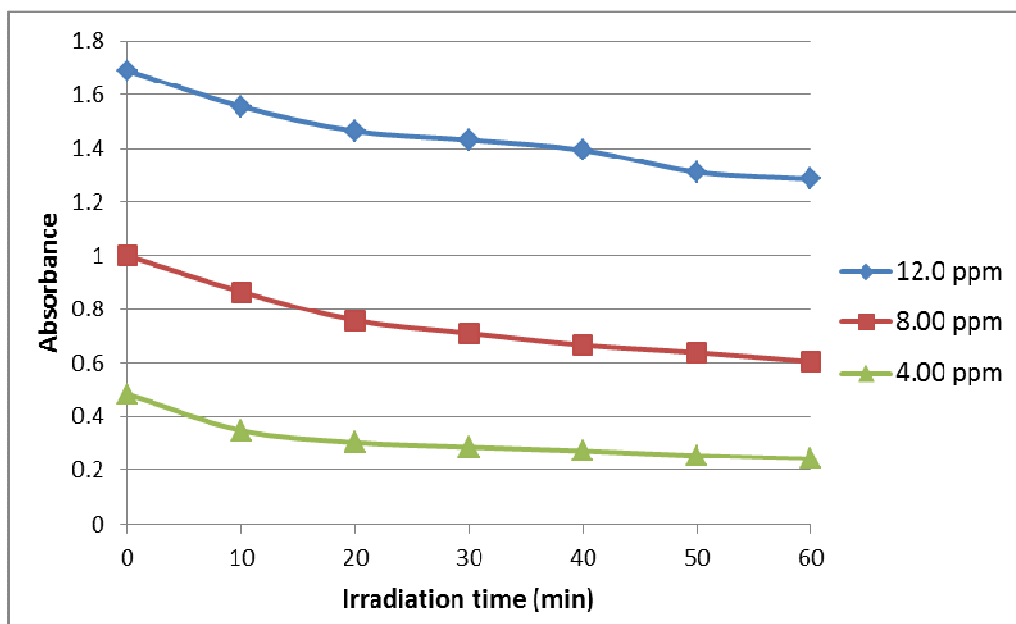


Figure 4.7: Time variation of UV-vis absorption spectra of different concentration of MB without photocatalyst under UV irradiation.

Similar investigation was conducted on phenol red (PR) solutions, with initial concentration of 48.0 ppm, without the presence of catalyst under direct illumination of UV light. This initial concentration was chosen since it provides the stable and optimum absorbance value. It was also irradiated in 10 minutes interval for 70 minutes to observe any degradation that might take place. However, as can be seen in Figure 4.8, there were insignificant changes observed for the duration of 70 minutes. Similar results were obtained for different concentration of PR solutions which was also measured at absorption peak of 435 nm, as shown in Figure 4.9, with no significant decrease in absorption maximum of the UV spectra could be observed. This shows that the organic compound in the PR solution is very photostable and difficult to undergo self-destruction mechanism even under intense UV light irradiation. This is supported by the previous study where PR that is mixed with Lauryl Sulfate Broth was found hard to be degraded under photo-irradiation if compared to other type of dyes (Rendina 1971). In solution, PR exists as a zwitterion structure and in polar form, with the sulfate group negatively charged and the ketone group carrying an additional proton. Therefore, it is quite photostable since it could accommodate itself by losing its proton when the pH solution increases.

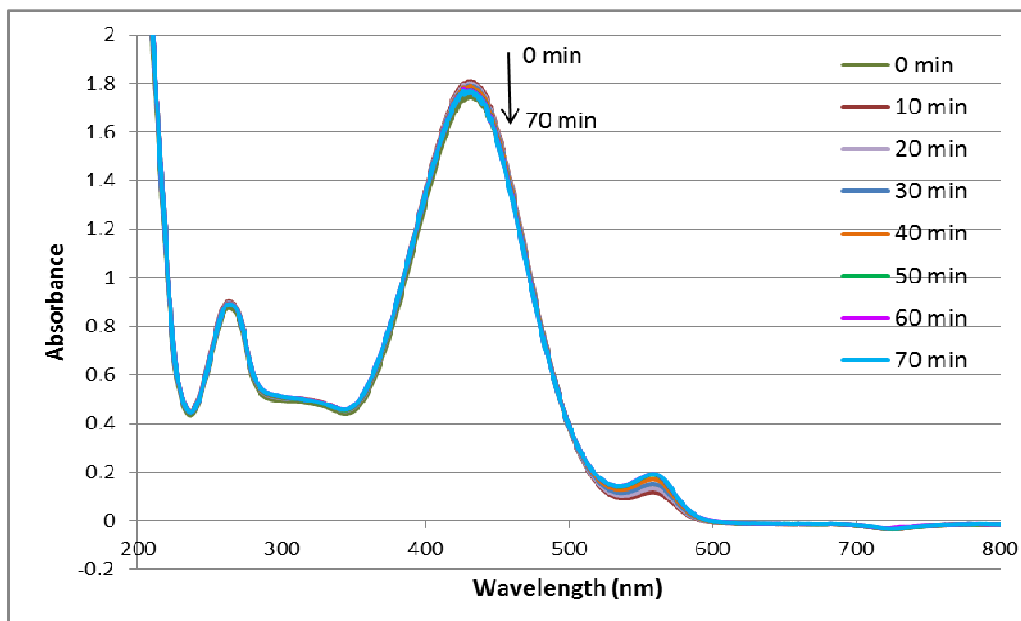


Figure 4.8: Time variation of UV-vis absorption spectra of 48.0 ppm PR without photocatalyst under UV irradiation.

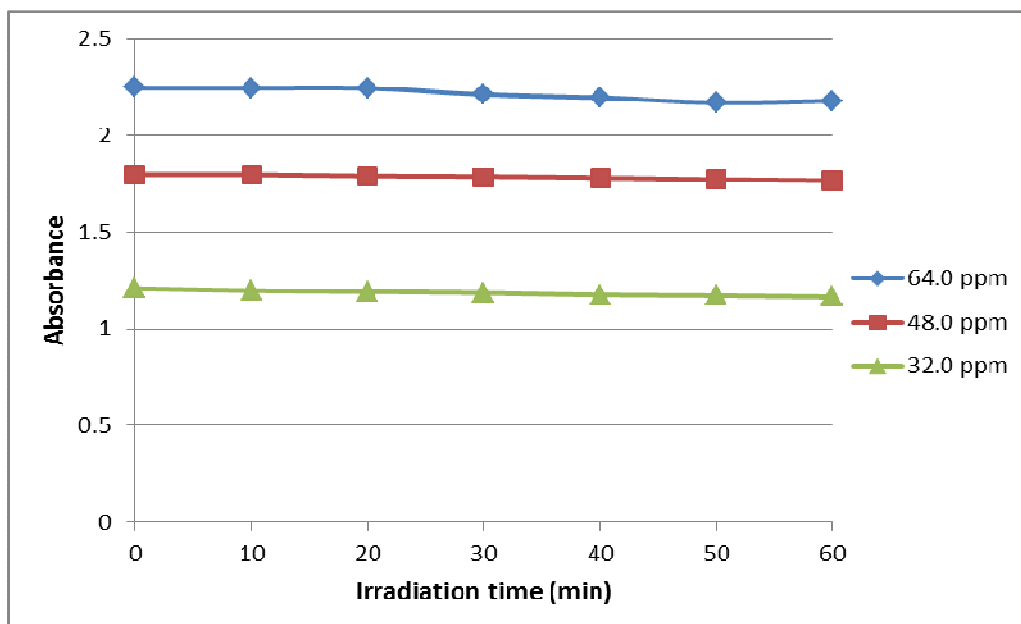


Figure 4.9: Time variation of UV-vis absorption spectra of different concentration of PR without photocatalyst under UV irradiation.

Similar investigation was conducted on the 32.0 ppm methyl orange (MO) solution by irradiating the sample under the UV light, together with the sample without the presence of the catalyst. The sample was irradiated for 60 minutes with 10 minutes interval to observe the photodegradation process. As can be observed in Figure 4.10, there were totally no degradation took place, even with different concentrations which was also measured at absorption peak of 465 nm, as shown in Figure 4.11. This showed that MO dye has a very photostable chemical structure, mainly due to its azo group (-N=N-). On the other hand, there is a report by Hakamada and his co-researchers, when they immersed the photocatalyst in the MO solution and placed them in the dark, no degradation has taken place (Hakamada, Hirashima et al. 2012).

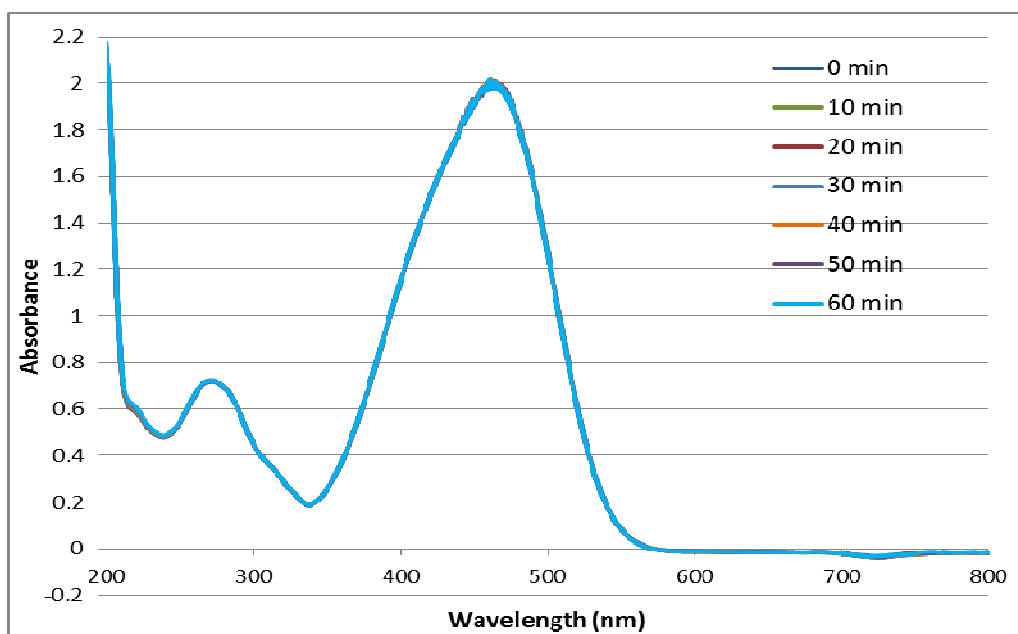


Figure 4.10: Time variation of UV-vis absorption spectra of 32.0 ppm MO without photocatalyst under UV irradiation.

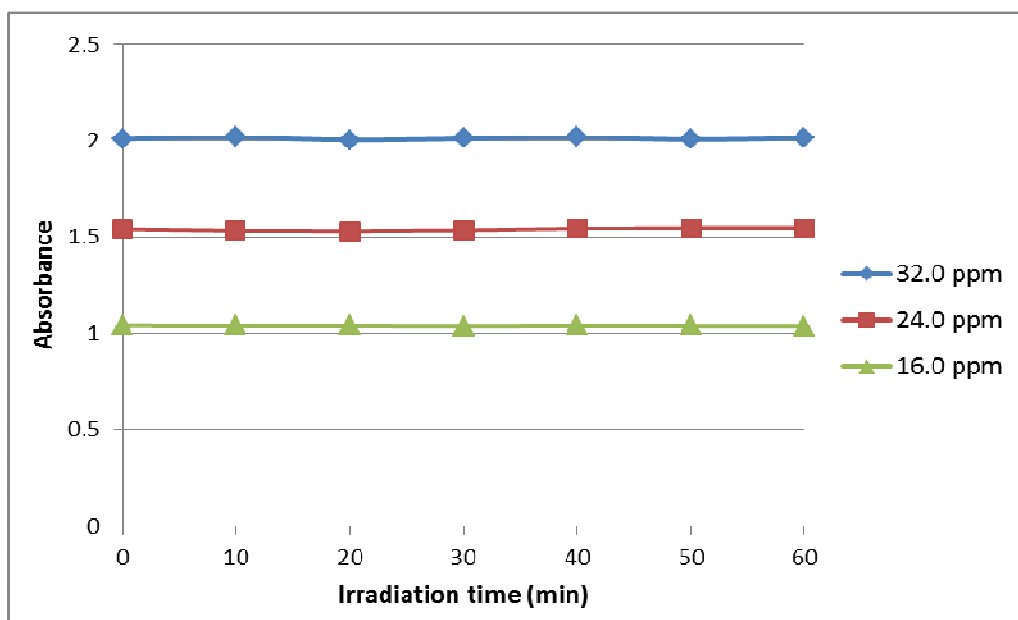


Figure 4.11: Time variation of UV-vis absorption spectra of different concentration of MO without photocatalyst under UV irradiation.

#### 4.2.6.2 *Effect of Photocatalyst Loading*

There have been many studies being focused on the effects of photocatalyst loading on the photocatalytic degradation of organic dyes in wastewaters (Sugiyana, Handajani et al. 2014, Regulska, Brus et al. 2016). The metal oxides photocatalyst materials that are used in the current study are ZnO, TiO<sub>2</sub> and Fe<sub>3</sub>O<sub>4</sub> nanoparticles. The sample dye used to determine the optimum value of loading for each photocatalyst was MB, with concentration of 12.0 ppm. The photocatalyst loading was varied from 0.50 to 3.50 wt% with an increment of 0.50 wt%, in order to study the photodegradation kinetic of the MB solutions.

Figure 4.12 shows the percentage degradation of 12.0 ppm MB with various loading of ZnO nanoparticles. Solution without ZnO photocatalyst showed quite slow degradation, with a linear like photodegradation with slightly more than 20% in 30 minutes irradiation, in agreement with the absorbance results shown in Figure 4.7. On the other hand, solutions with ZnO photocatalyst appeared to be significantly degraded with more than 60% degradation in just 10 minutes for all contents of catalyst loadings. The percentage of degradation also increased with the amount of catalyst added. These differences can be attributed to more catalyst surface area and photon light absorption that reached the surface of the catalyst (Yassitepe, Yatmaz et al. 2008). For the duration of 30 minutes, MB was degraded to more than 90% by the photocatalysts with all loadings. This shows that ZnO

nanoparticles is a very reactive photocatalytic material with superior photodecomposition capability (Behnajady, Modirshahla et al. 2006).

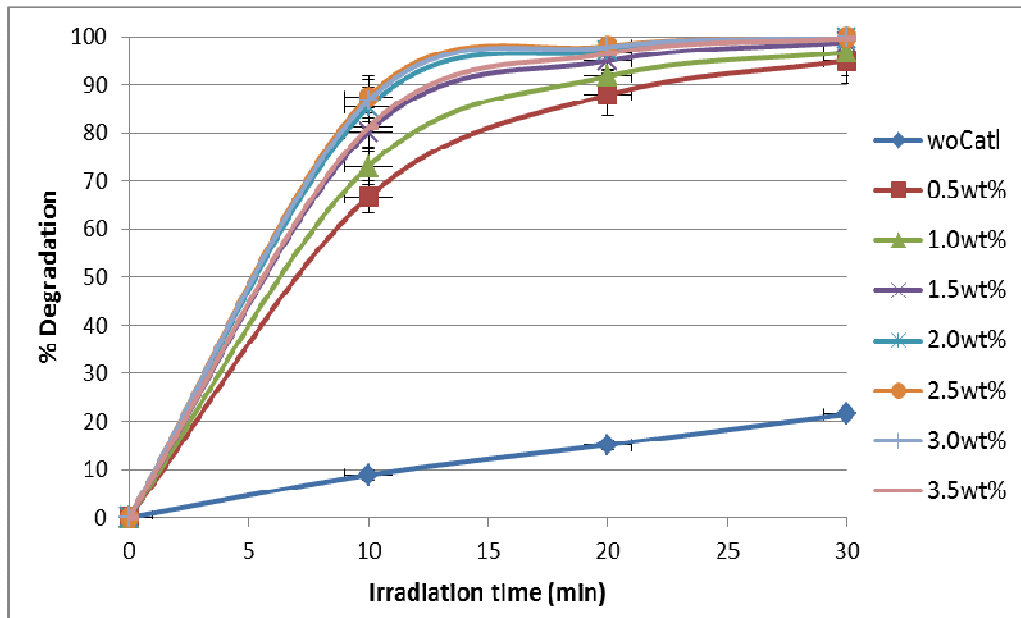


Figure 4.12: Percentage degradation of MB (12.0 ppm) with different loading of ZnO photocatalyst.

The photodegradation efficiency on the MB dye for the  $\text{TiO}_2$  photocatalyst also shows similar results. Solution without the  $\text{TiO}_2$  photocatalyst only shows a small percentage of degradation at the end of 60 minutes, just merely more than 20%, as shown in Figure 4.13. However, with the addition of  $\text{TiO}_2$  photocatalyst, the degradation was significantly increased. In just 20 minutes, all dye solutions with different amount of  $\text{TiO}_2$  loading were able to reach more than 50% of degradation and this value further increased to 90% after 60 minutes of UV irradiation. The significant enhancement of the degradation rate could be explained by the presence of

photocatalytic material that can induce the photodecomposition process at the surface of the material. Photocatalyst surface is the center for the production of hydroxyl radicals which can significantly decompose the organic dye (El-Kemary, El-Shamy et al. 2010).

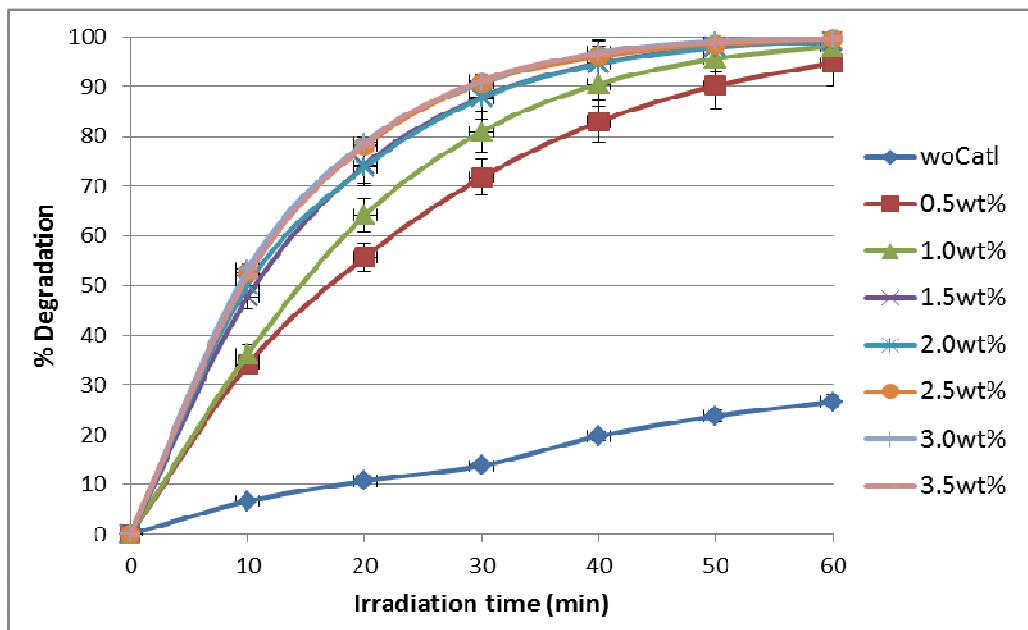


Figure 4.13: Percentage degradation of MB (12.0 ppm) with different loading of TiO<sub>2</sub> photocatalyst.

Similar experiment was conducted on the MB dye solution using iron oxide, Fe<sub>3</sub>O<sub>4</sub> as the photocatalytic material. This photocatalyst material did not show any photocatalytic capability if compared to the other two photocatalysts. As can be seen in Figure 4.14, the photodegradation of all the solutions with the Fe<sub>3</sub>O<sub>4</sub> photocatalyst were lower than the solution without the catalyst. Although the absorbance graph shows a gradual decreased for all photocatalyst loadings, however, the decreasing of the

absorbance values are believed to be caused by self-decomposition of the dye. This could be explained that the  $\text{Fe}_3\text{O}_4$  photocatalyst is not a good photocatalyst as compared to ZnO and  $\text{TiO}_2$  nanoparticles. As reported by Singh and his co-researchers (2013), the degradation of MB was negligible under the UV irradiation in the absence of photocatalyst, as well as in the presence of  $\text{Fe}_3\text{O}_4$  (Singh, Barick et al. 2013). There is also a report on its counterpart ( $\text{Fe}_2\text{O}_3$ ) that also exhibit negligible photocatalytic activity (Kormann, Bahnemann et al. 1989). Nonetheless,  $\text{Fe}_3\text{O}_4$  nanoparticles was generally used as a composite material with other photocatalyst materials, such as ZnO,  $\text{TiO}_2$  etc., due to its magnetic capabilities (Singh, Barick et al. 2013).

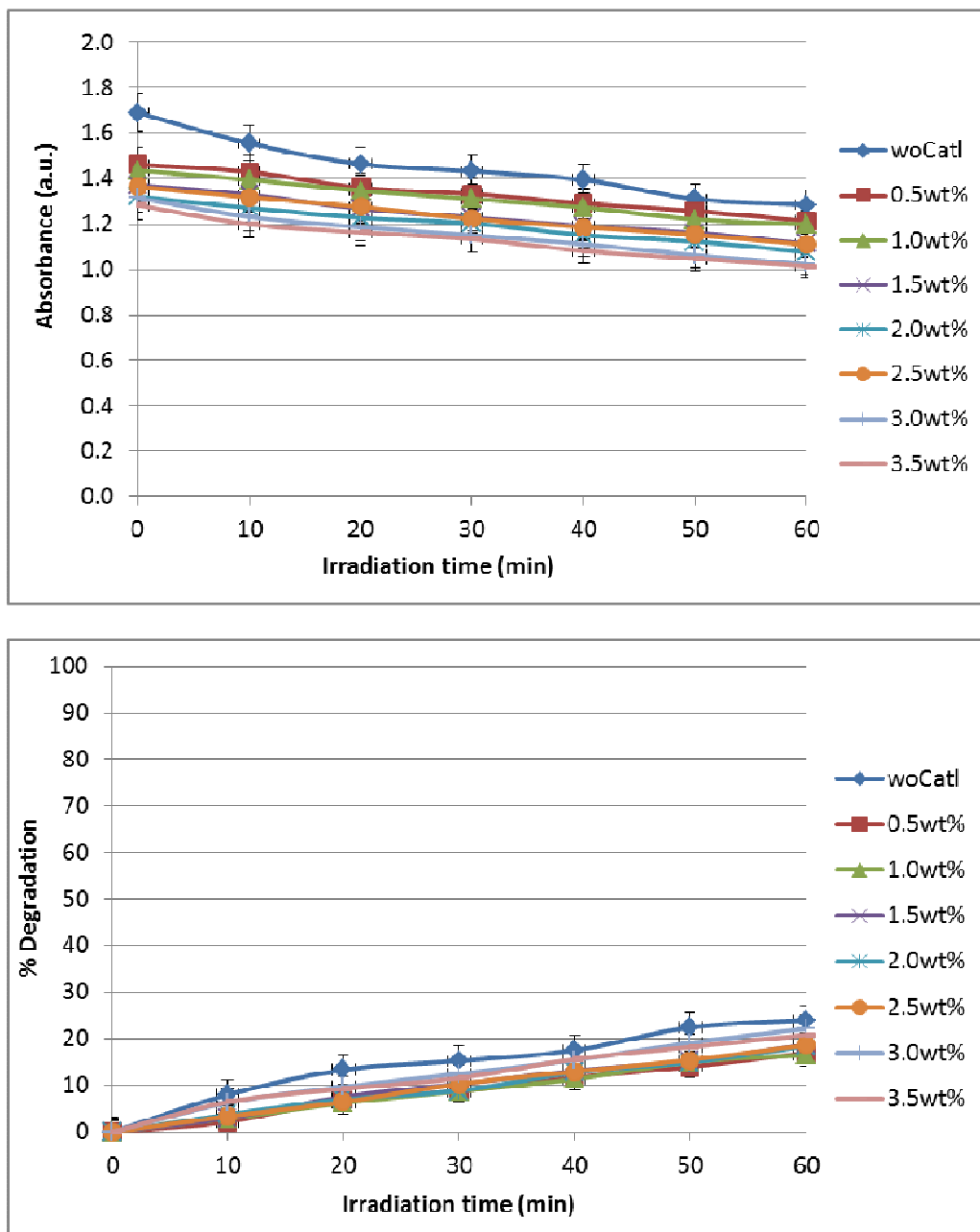


Figure 4.14: Absorbance and Percentage degradation of MB (12.0 ppm) with different loading of  $\text{Fe}_3\text{O}_4$  photocatalyst.

In obtaining better pictures on the optimum amount of each catalysts loading in the photodegradation processes of the MB solutions above, the

kinetics studies were performed. First-order kinetics study could easily convey the information of rate of the organic substance being degraded (Xie, Wang et al. 2011). The first-order kinetics results for the ZnO photocatalyst can be observed in Figure 4.15. It is obvious that the degradation rate was lowest for solution without catalyst, at  $0.0080 \text{ min}^{-1}$ . The degradation rate immediately improved with the addition of the ZnO photocatalyst, as the catalyst provides active radicals as well as interaction sites on its surface (Xu, Zhang et al. 2011). As the amount of catalyst increases, the photodegradation rate was improved too, but only until certain limit. The degradation rate increased until 2.5 wt% , $0.2221 \text{ min}^{-1}$ , of the catalyst loading, but dropped slightly with 3.0 wt%,  $0.2180 \text{ min}^{-1}$ , and further decreased when the catalyst loading was 3.5 wt%,  $0.1856 \text{ min}^{-1}$ . These could be explained that with the increase of the photocatalyst loading, the number of active sites increases which allowed more organic substances as well as active radicals to interact at the catalyst surfaces. However, when the amount of catalyst loading was further increased beyond the optimum level, i.e. 2.50 wt%, it will cause an adverse effect. The catalyst nanoparticles will block the photon light from reaching the other photocatalyst (Velmurugan and Swaminathan 2011). Therefore, the highest degradation rate only able to be achieved with the optimum amount of the photocatalyst loading, that is for this study is 2.50 wt%.

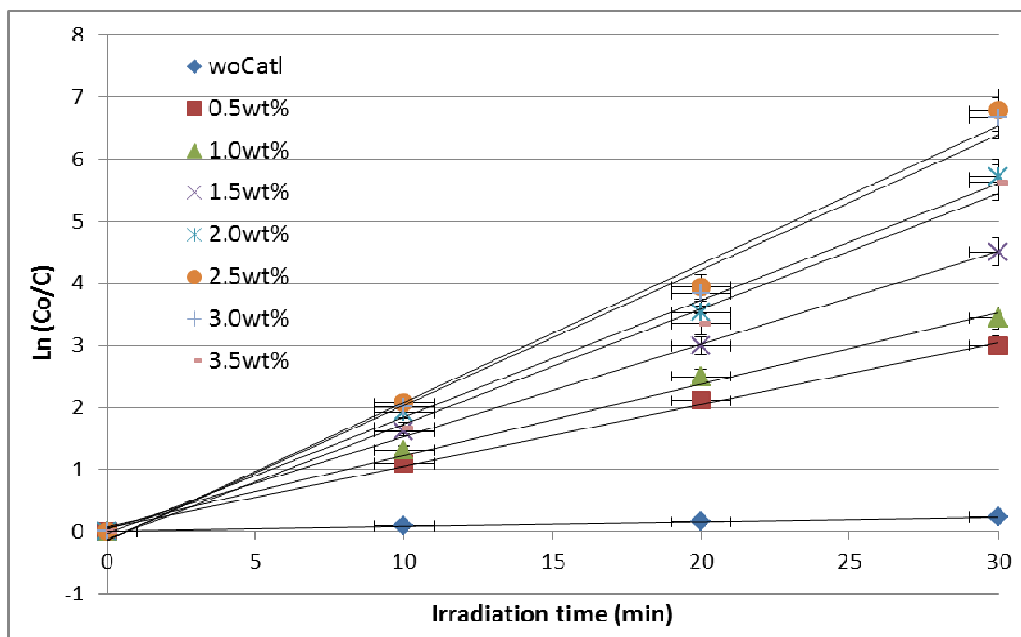


Figure 4.15: First-order kinetics on the effect of MB degradation with different loading of ZnO photocatalyst.

For the TiO<sub>2</sub> photocatalyst, as seen in Figure 4.16, similar pattern of degradation rate was observed as for the ZnO photocatalyst. The degradation rate was lowest (0.0051 min<sup>-1</sup>) when no catalyst was added and the degradation rates increased significantly (0.0487 min<sup>-1</sup> for 0.50 wt% loading) when the TiO<sub>2</sub> photocatalyst was present in the solutions. This could be similarly explained due to the presence of the active sites on the TiO<sub>2</sub> photocatalyst surfaces (Sher Shah, Park et al. 2012). The optimum loading for TiO<sub>2</sub> photocatalyst was achieved at 3.0 wt% with a slight dropped in photodegradation rate when the loading was increased to 3.5 wt%.

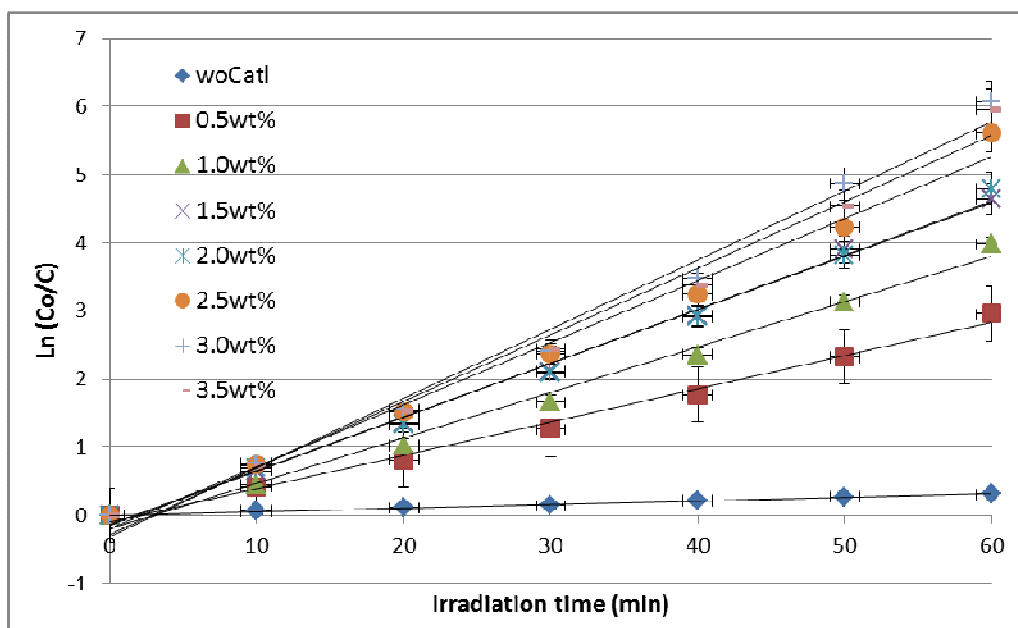


Figure 4.16: First-order kinetics on the effect of MB degradation with different loading of TiO<sub>2</sub> photocatalyst.

Figure 4.17 shows the first-order kinetics for the Fe<sub>3</sub>O<sub>4</sub> nanoparticles photocatalyst. It is clearly seen that the highest degradation rate was the solution without photocatalyst. It is very apparent that Fe<sub>3</sub>O<sub>4</sub> nanoparticles do not exhibit any interesting photocatalytic capability that able to enhance the photodegradation process. In contrary, the presence of Fe<sub>3</sub>O<sub>4</sub> nanoparticle with the organic dye solution shall distort the photodecomposition process, as it might cause hindrances of the UV photon to reach the organic dye molecule. At the same time, Fe<sub>3</sub>O<sub>4</sub> nanoparticle can serve as a competitor to absorb the photon energy which ultimately undergoes internal phonon scattering and do not contribute in the photodegradation process. This is in agreement with a report by Singh and

his co-researchers on  $\text{Fe}_3\text{O}_4$  which found that  $\text{Fe}_3\text{O}_4$  nanoparticles has insignificant photocatalytic capability (Singh, Barick et al. 2013).

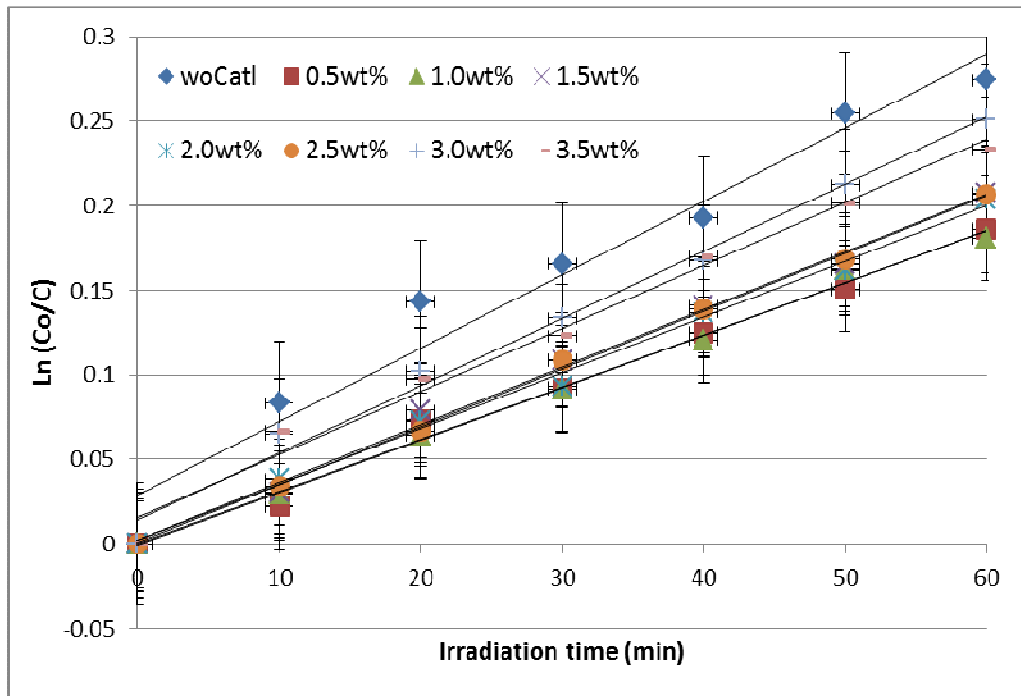


Figure 4.17: First-order kinetics on the effect of MB degradation with different loading of  $\text{Fe}_3\text{O}_4$  photocatalyst.

All the details for the values of the kinetic constant,  $k$  and coefficient of linear regression  $R^2$  are shown in Table 4.3. From the table, it shows that the optimum photocatalyst loading for the ZnO nanoparticle is 2.50 wt%, whereas for  $\text{TiO}_2$  and  $\text{Fe}_3\text{O}_4$  nanoparticles are similar, that is 3.00 wt%, with their degradation rates of 0.2221, 0.1012 and 0.0040  $\text{min}^{-1}$ , respectively. This could be resulted from the strong tendency for the  $\text{TiO}_2$  and  $\text{Fe}_3\text{O}_4$  photocatalysts to agglomerate during operation, due to its small particle size, followed by its large surface area to volume ratio and surface energy.

Particles agglomeration will critically affect particles size sustainability, surface area reduction and its reusable lifespan (Chong, Jin et al. 2010, Nogueira, Castro et al. 2014).

From these results, it can be summarized that the degradation rate for ZnO is the highest amongst all the three photocatalysts under the investigated condition. This shows that ZnO is one of the best photocatalyst material, which is consistent with the results reported in literature, that ZnO perform better than TiO<sub>2</sub> on certain organic contaminants, and significantly better than Fe<sub>3</sub>O<sub>4</sub> material (Bansal and Sud 2011).

Figure 4.18, 4.19, and 4.20 show the exact value of the kinetic constant for the degradation of 12.0 ppm MB by ZnO, TiO<sub>2</sub> and Fe<sub>3</sub>O<sub>4</sub> photocatalysts, respectively. These figures provide informative value on the optimum amount of loading that is required to photodegrade organic MB dye solution.

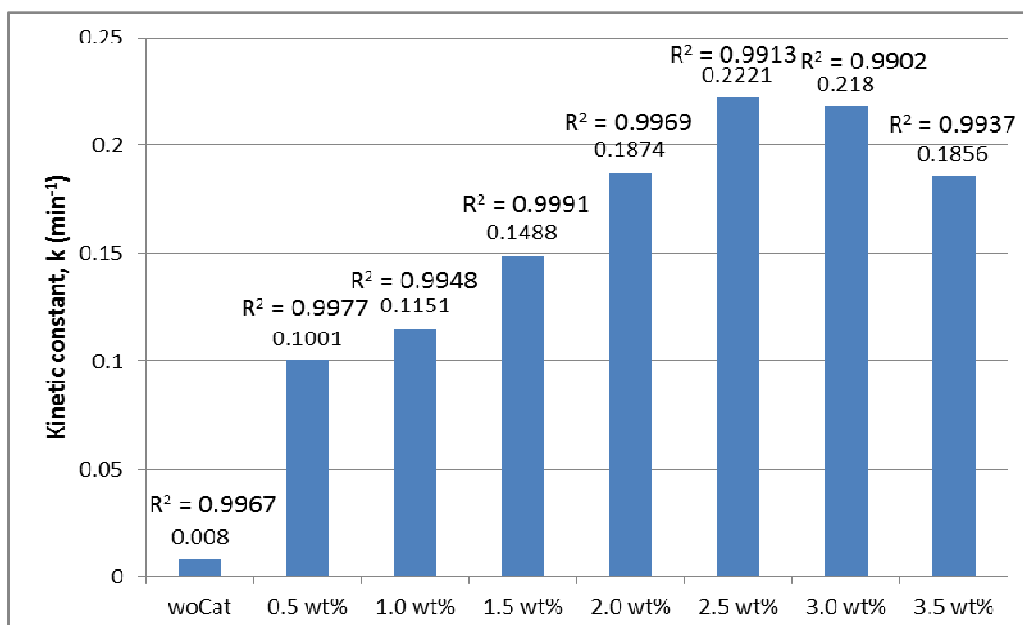


Figure 4.18: Kinetic constant,  $k$ , of MB (12.0 ppm) with different loading of ZnO photocatalyst.

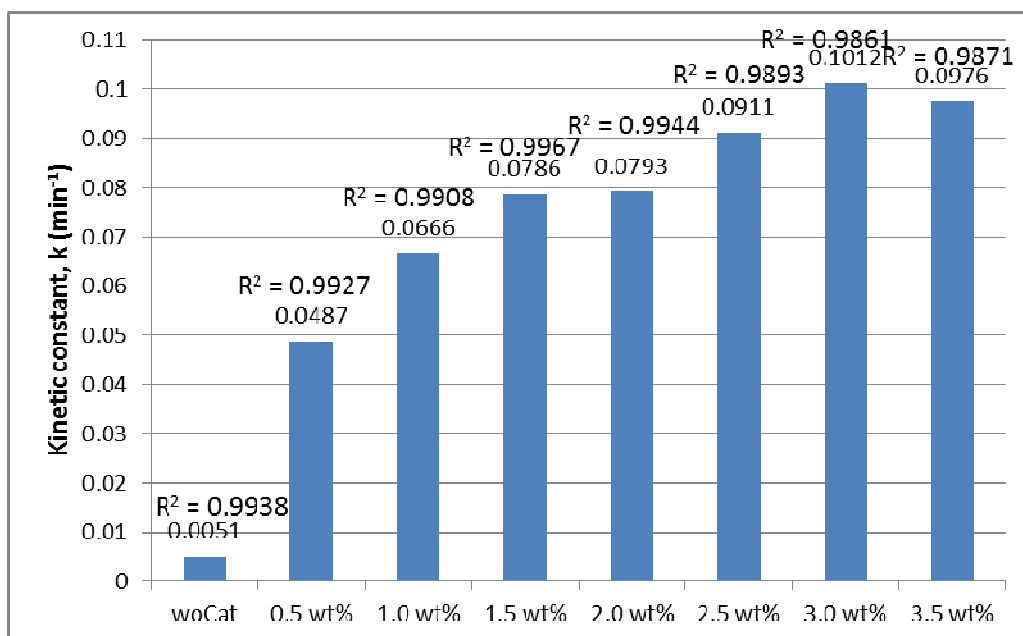


Figure 4.19: Kinetic constant,  $k$ , of MB (12.0 ppm) with different loading of  $\text{TiO}_2$  photocatalyst.

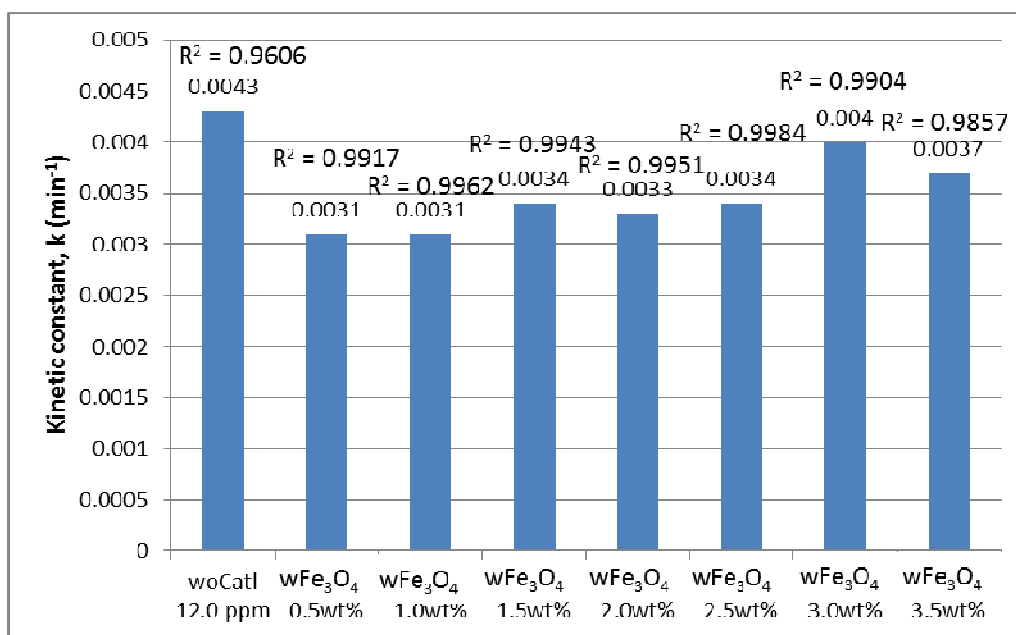


Figure 4.20: Kinetic constant,  $k$ , of MB (12.0 ppm) with different loading of  $\text{Fe}_3\text{O}_4$  photocatalyst.

#### 4.2.6.3 Effect of Initial Dye Concentration

Dyes at different concentration contain different amount of organic chemicals in the compound. Therefore, the degradation rate will be much depends on the response of the organic chemicals compound in the solutions to the UV light irradiation. In investigating this effect, the samples of dyes used were methylene blue (MB), phenol red (PR) and methyl orange (MO). Before the degradation experiments were conducted, different concentrations of solutions (MB, PR and MO) were prepared to determine the relationship

between the absorbance and concentration by using the UV-vis spectrophotometer.

The absorbance versus wavelength for different concentration of MB, PR and MO solutions are shown in Figure 3.12, 4.21 and 4.23, respectively. Absorption maxima for MB, PR and MO are at 665, 435 and 465 nm, respectively. It can be seen that with the increased of the dye concentration, the absorbance value of the peak increases. This could be explained due to the increasing amount of the organic chemicals substance that present in these dye solutions, thus more photons were being absorbed (Collard, El Hajj et al. 2014). By using these results, absorbance value for absorption maxima for each concentration was recorded and the absorbance versus concentration for all dyes, MB, PR and MO were drawn, as seen in Figure 3.13, 4.22 and 4.24, respectively. All figures show good linearity between absorbance and concentration with high correlation coefficient of 0.9823 for MB, 0.9968 for PR and 0.9939 for MO dye. This was in agreement with the Beer's Law, equation (3.2), which states that the absorbance is linearly correlated with the concentration of the solution.

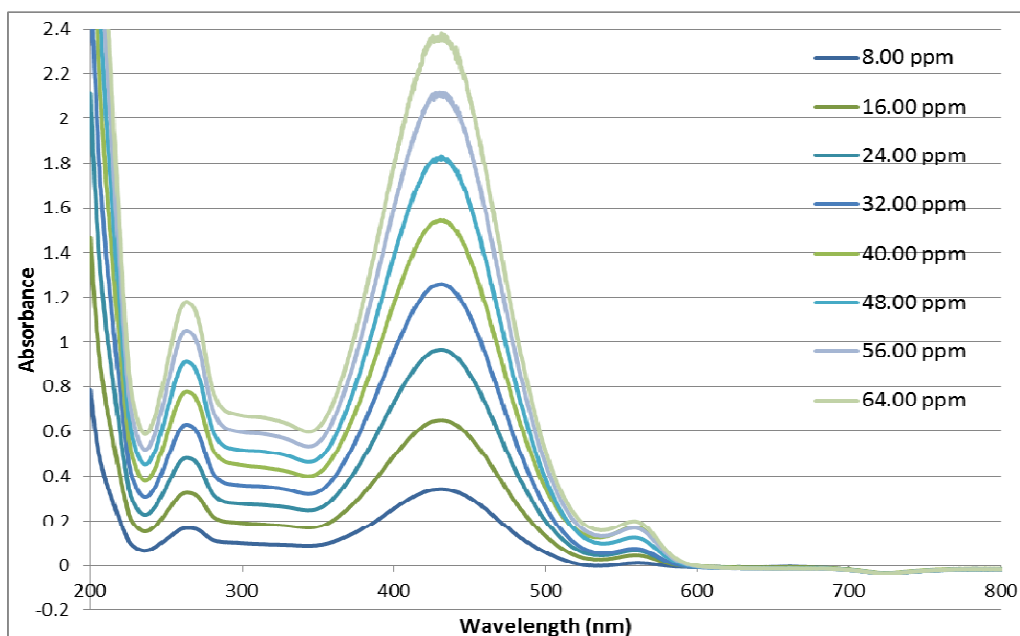


Figure 4.21: UV-vis absorption spectra for different concentration of PR without photocatalyst.

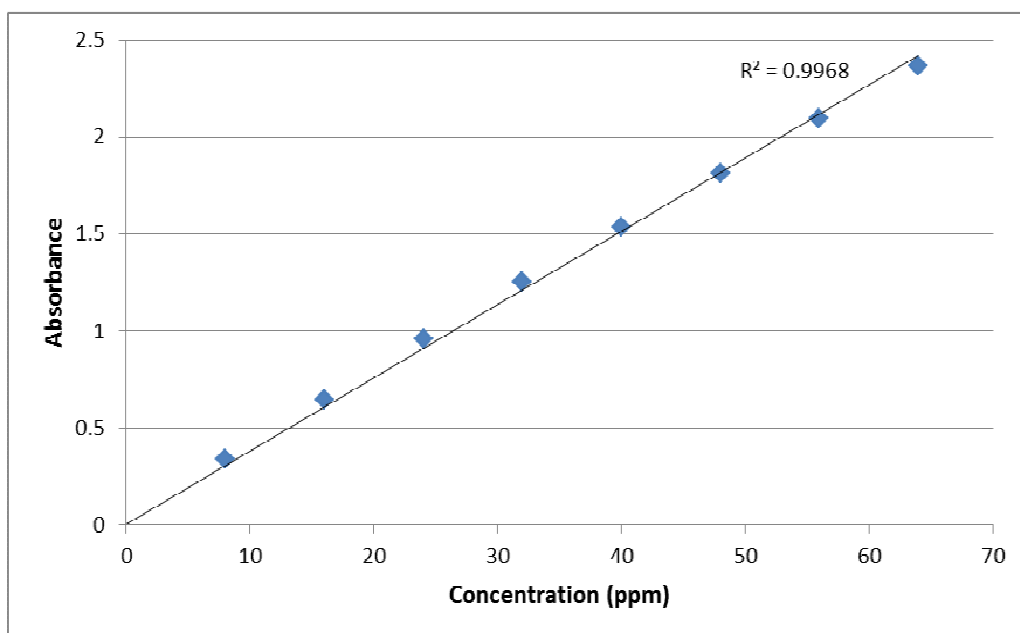


Figure 4.22: Absorbance versus concentration for PR dye.

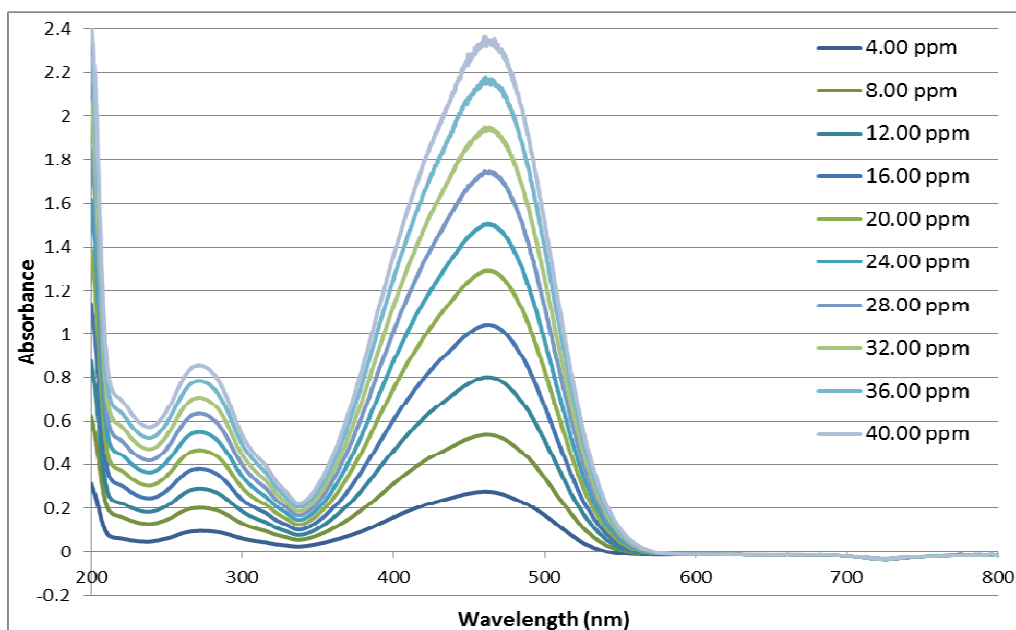


Figure 4.23: UV-vis absorption spectra for different concentration of MO without photocatalyst.

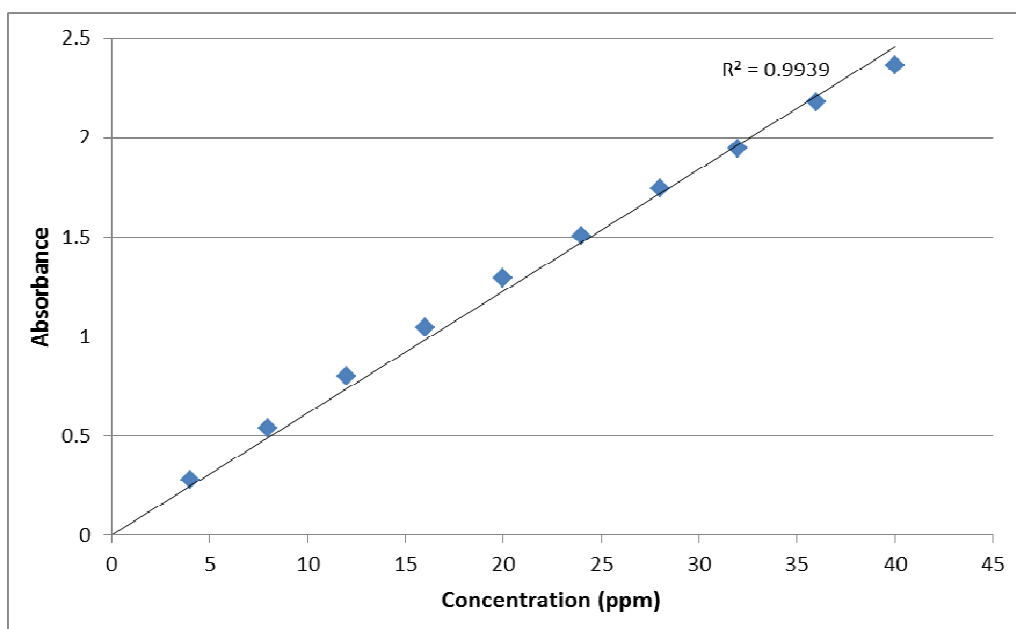


Figure 4.24: Absorbance versus concentration for MO dye.

First, the study of photodegradation on the MB dye will be discussed. The concentration of the MB was ranging from 2.00 to 12.0 ppm. The catalyst loading used for the following experiments is adopted from the optimum catalyst loading obtained from section 4.2.6.2. The photocatalyst loading for ZnO, TiO<sub>2</sub> and Fe<sub>3</sub>O<sub>4</sub> were 2.5, 3.0 and 3.0 wt% respectively.

From Figure 4.25, it can be seen that the MB dye decomposition is accelerated by the presence of ZnO and TiO<sub>2</sub> photocatalyst, except the Fe<sub>3</sub>O<sub>4</sub> nanoparticles. For only 10 minutes, ZnO has been able to decomposed 85.7 to 100% of MB for 12.0 ppm to 2.00 ppm concentration, respectively. All solutions were totally degraded in just 20 minutes of irradiation duration. This shows that the ZnO photocatalyst is an active photocatalytic nanoparticles. On the other hand, it also indicates that for all the concentrations used for MB dye, there were still sufficient sites for the dye molecules to be adsorbed on the ZnO nanoparticles for the photocatalytic process to take place. In another word, there is a limitation for the amount of dye being adsorbed due to the effect of molecular diffusivity. The dye molecules can diffuse faster if diffusivity is higher, which relates to the available sites on the photocatalyst surface; subsequently the fraction adsorbed with diffusivity will reach a plateau. The plateau indicates that the organic molecules have fully penetrated on the photocatalyst surface, thus no more adsorption is possible (Gupta, Saurava et al. 2015). This condition can be view more clearly for the decomposition of MB by the TiO<sub>2</sub> nanoparticles. As can be seen from Figure 4.25, 54.9 to 92.1% of MB was

degraded for 12.0 to 2.00 ppm concentration, respectively, in the 10 minutes irradiation duration. This means that MB with 2.00 ppm concentration was just optimum for all of its molecules to be adsorbed on the photocatalyst surface, with the amount of the photocatalyst used. This is in agreement with the report by Gupta et al. (2015) that there is also a limitation for the photocatalyst loading (Gupta, Saurava et al. 2015). Therefore, as the concentration further increases, it may compete for adsorption with the intermediates formed during the photocatalytic degradation and subsequently slow down the overall photocatalytic degradation process. In addition, increases in concentration causes reduction in light penetration thus resulted in a reduction of OH• radicals formation (Kanakaraju, Kockler et al. 2015).

As for the Fe<sub>3</sub>O<sub>4</sub> photocatalyst, there was very little degradation took place, especially for the higher concentration of the dyes, Figure 4.25. The percentage degradation for 8.00 to 2.00 ppm concentration was 29.9 to 72.8%, respectively, as compared to the solution without photocatalyst with 24.9% degradation, for the 60 minutes irradiation duration. This was expected since the Fe<sub>3</sub>O<sub>4</sub> nanoparticles is not a promising photocatalytic materials (Singh, Barick et al. 2013). The absorbance versus irradiation time graph shows the gradual decreased of the MB dye with the presence of Fe<sub>3</sub>O<sub>4</sub> nanoparticles.

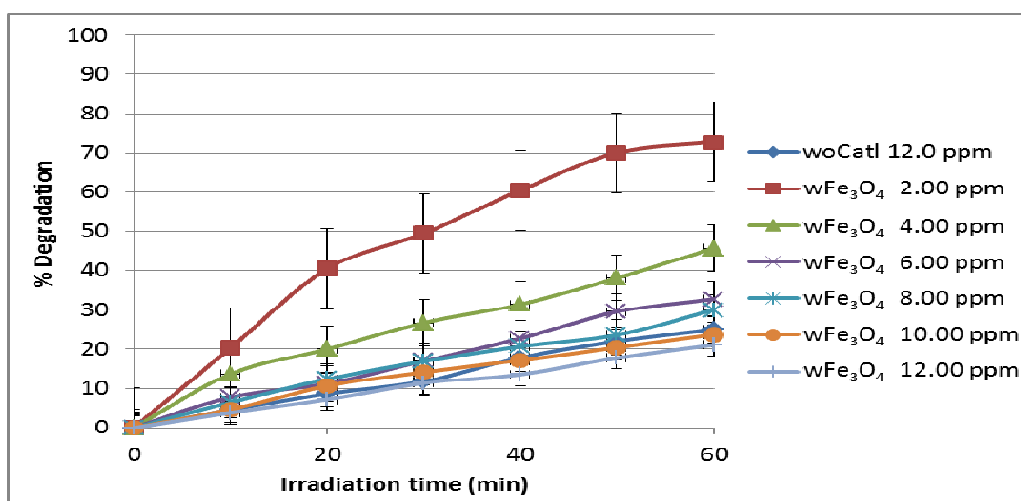
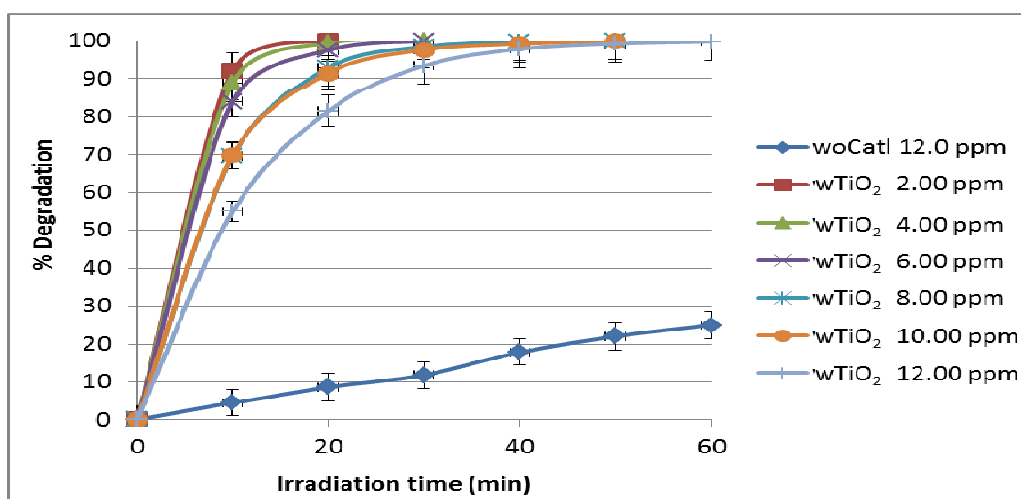
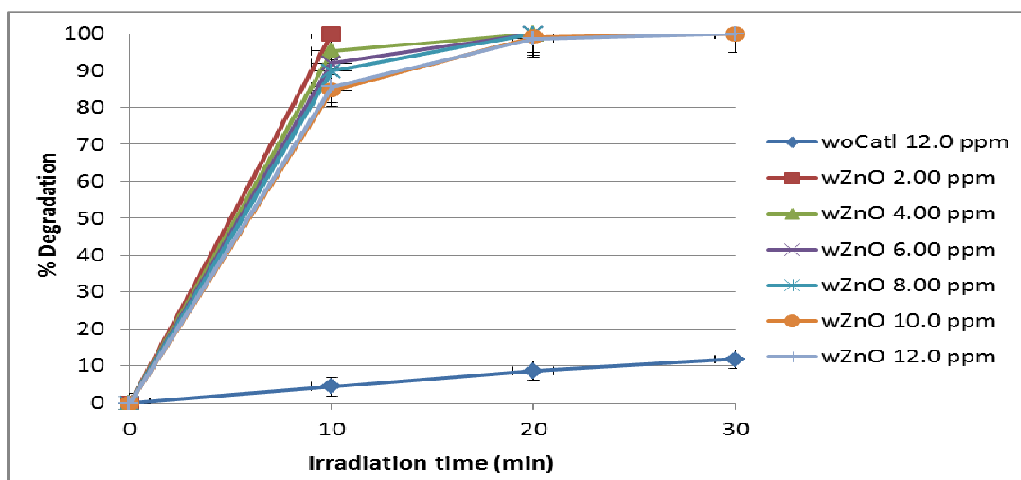


Figure 4.25: Percentage degradation with different concentration of MB for ZnO, TiO<sub>2</sub> and Fe<sub>3</sub>O<sub>4</sub> photocatalyst.

Figure 4.26 shows the rate of degradation, kinetic constant  $k$ , for all the three photocatalysts materials. It clearly observed that the ZnO photocatalyst shows the steepest slopes for all solutions as compared to other photocatalysts, which are  $\text{TiO}_2$  and  $\text{Fe}_3\text{O}_4$ . This indicates that ZnO is an outstanding photocatalyst as compared to its counter parts,  $\text{TiO}_2$  and  $\text{Fe}_3\text{O}_4$  nanoparticles. Although the amount of loading for ZnO is slightly less than  $\text{TiO}_2$  and  $\text{Fe}_3\text{O}_4$  nanoparticles, it might be due to the ability of the ZnO nanoparticles to absorb more light quanta than  $\text{TiO}_2$  (Gupta, Saurava et al. 2015).

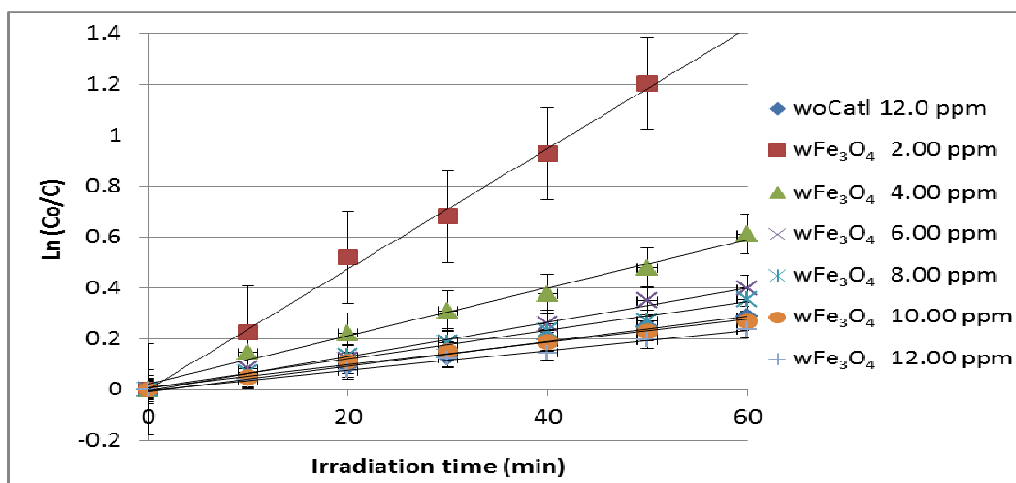
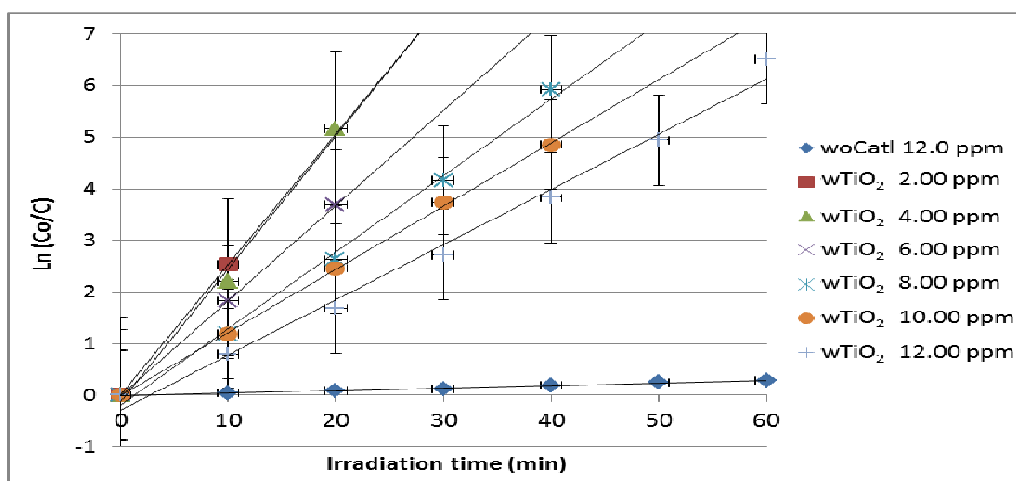
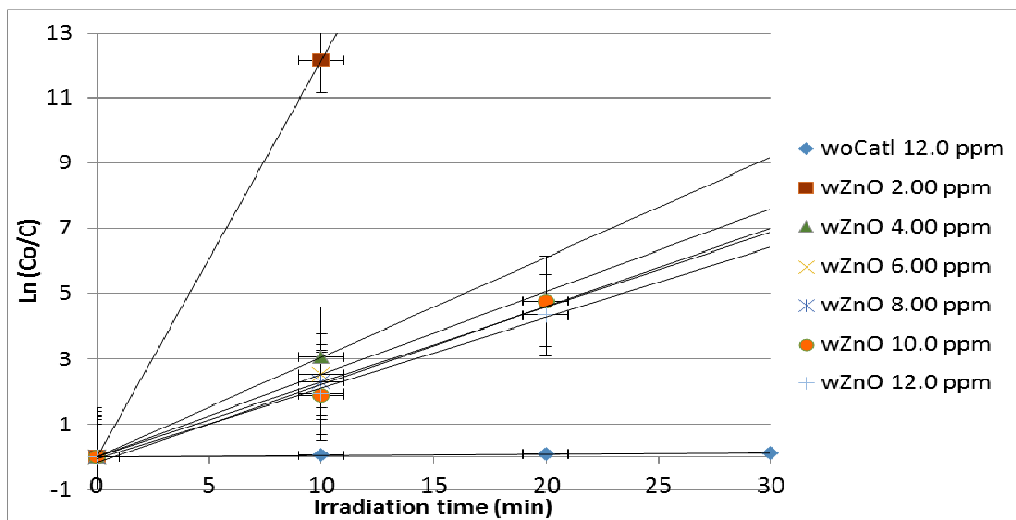


Figure 4.26: First-order kinetics on the effect of initial concentration of MB for ZnO, TiO<sub>2</sub> and Fe<sub>3</sub>O<sub>4</sub> photocatalyst.

The kinetic constants values on MB dye for ZnO, TiO<sub>2</sub> and Fe<sub>3</sub>O<sub>4</sub> photocatalysts was given in Figure 4.27. The values clearly show that the kinetic constant are highest for the lowest dye concentration, and for the photocatalyst is the ZnO nanoparticles. This is due to the availability of the organic dye to be adsorbed onto the photocatalyst surface as well as the opacity of the solutions that caused by the increase of the organic dye concentration which inhibit similar amount of light photon to reach the photocatalyst surface (Faisal, Ibrahim et al. 2015). The kinetic constant values of ZnO, TiO<sub>2</sub> and Fe<sub>3</sub>O<sub>4</sub> photocatalysts are recorded as 1.2160 ( $R^2 = 1.0000$ ), 0.2582 ( $R^2 = 0.9929$ ) and 0.0237 min<sup>-1</sup> ( $R^2 = 0.9963$ ), respectively. These results indicate that all photocatalysts used were able to photodegrade the MB dye but with different potential and capability.

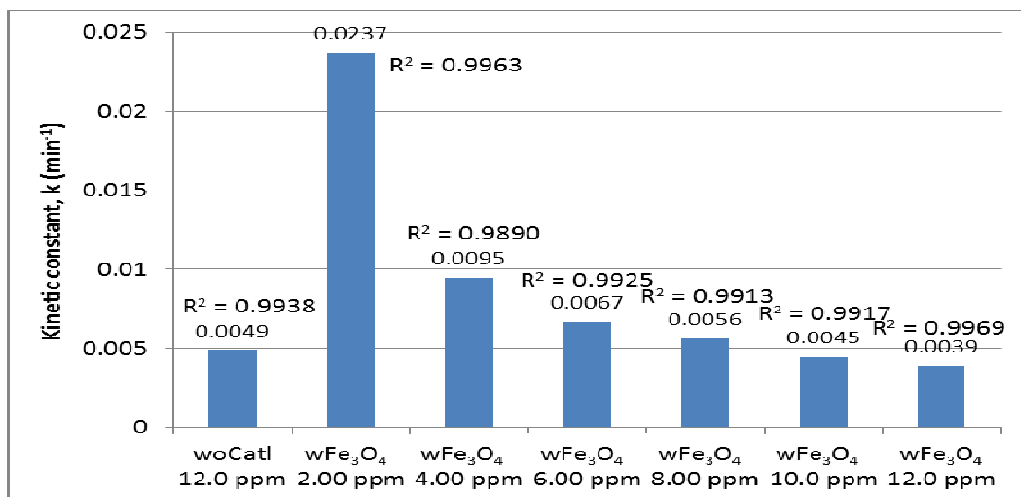
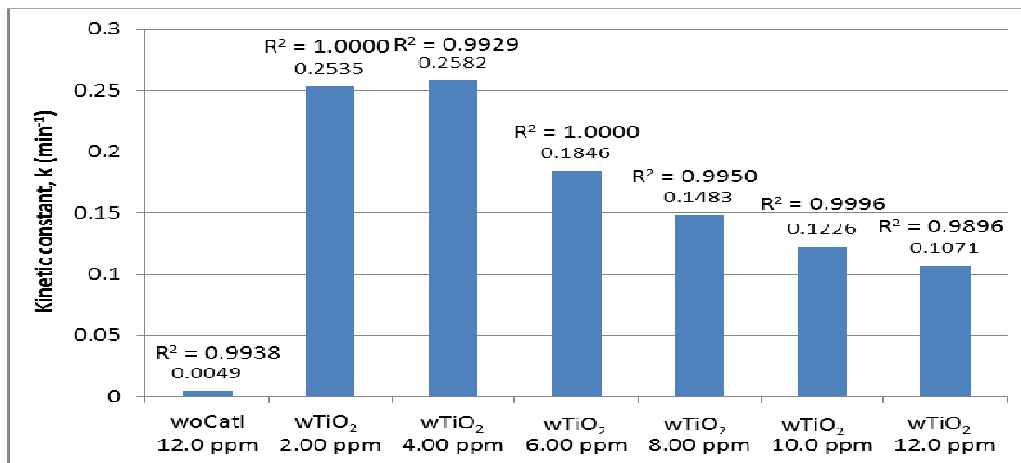
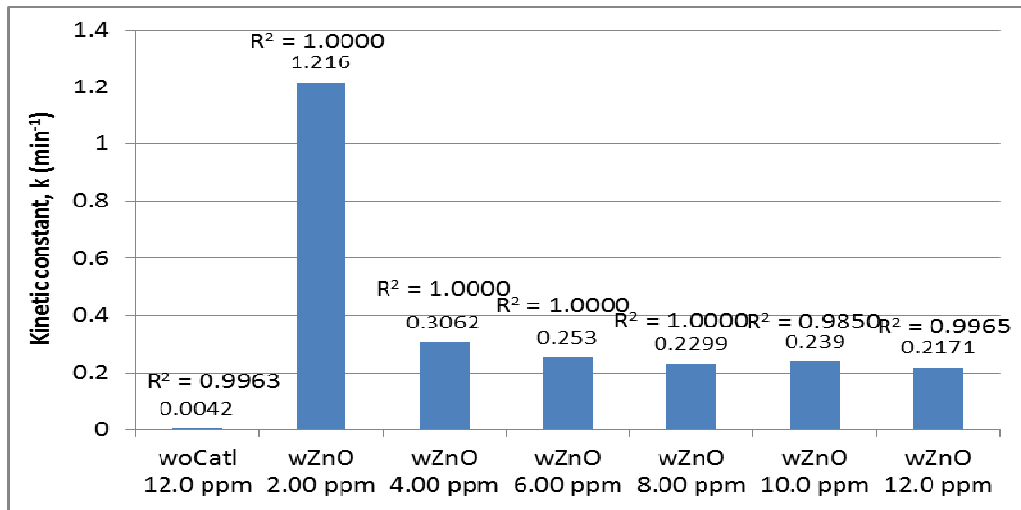


Figure 4.27: Kinetic constant,  $k$ , on the effect of initial concentration of MB for ZnO, TiO<sub>2</sub> and Fe<sub>3</sub>O<sub>4</sub> photocatalyst.

From Figure 4.28, it can be seen that the PR solution without the photocatalyst has very little degradation for the entire duration of 60 minutes irradiation, with only 2.0% decomposed after 60 minutes of UV irradiation. However, for solutions with the presence of ZnO photocatalyst, more than 30% of organic contaminants have been degraded in just 10 minutes of irradiation. The degradation process for all solutions took place gradually and the PR solution with 8.00 ppm concentration was almost completely (99.6%) degraded after the irradiation period of 30 minutes. The degradation efficiency of the ZnO photocatalyst on PR was slowly decreased as the concentration of the PR solutions increases, as a result of increased photon adsorption competition as well as decrease of available reactive sites for the photodecomposition process to occur. The large number of dye molecules on the catalyst surface hinders the adsorption of  $\text{OH}^-$  ions for the production of  $\text{OH}\bullet$  radicals which is the main active reagent in the photocatalytic mechanism (Yassitepe, Yatmaz et al. 2008).

Besides, according to the Beer-Lambert law, the path length of photons entering the solution decreases as its concentration increased. In other words, the path length that photons radiate through is inversely proportional to the concentration of the solution (Beer's Law equation). As a consequence, the density of photons being absorbed on the photocatalyst surface dropped significantly, therefore lowering the photocatalytic rates (Faisal, Khan et al. 2012).

There is also an instantaneous decomposition for the PR solutions with  $\text{TiO}_2$  photocatalyst, as shown in Figure 4.28. For the first 10 minutes, solutions with 8.00 and 16.0 ppm concentration showed higher percentage of degradation if compared to the other dye solutions with higher concentrations. Low concentration of organic dye solution shall permit more light photons to be absorbed by the photocatalyst, and hence higher degradation rate is recorded. Additionally, low concentration of dye solution shall have less competition for organic molecule-photon interaction, under the same amount of photon influx. At the end of 60 minutes irradiation, percentage degradation for the 8.00 and 48.0 ppm solutions were recorded at 97.8 and 76.3%, respectively.

As for the  $\text{Fe}_3\text{O}_4$  photocatalyst reactions on the PR solutions, no significant changes could be observed from Figure 4.28. The percentage degradation was very little and significant, with the highest degradation of about 1.0%, as can be seen from the absorbance versus irradiation time graph, the dropped of the absorbance values were very minute. This figure shows insignificant changed in the absorbance for all solutions even after 60 minutes of irradiation duration. It shows that  $\text{Fe}_3\text{O}_4$  photocatalyst has almost negligible effect to catalyze the decomposition of the PR organic contaminant, similar to many reported results previously (Singh, Barick et al. 2013).

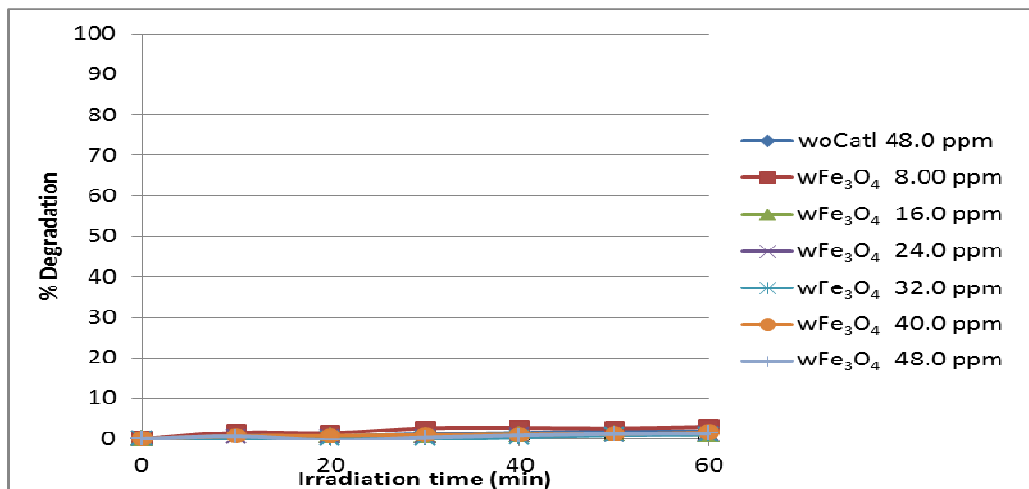
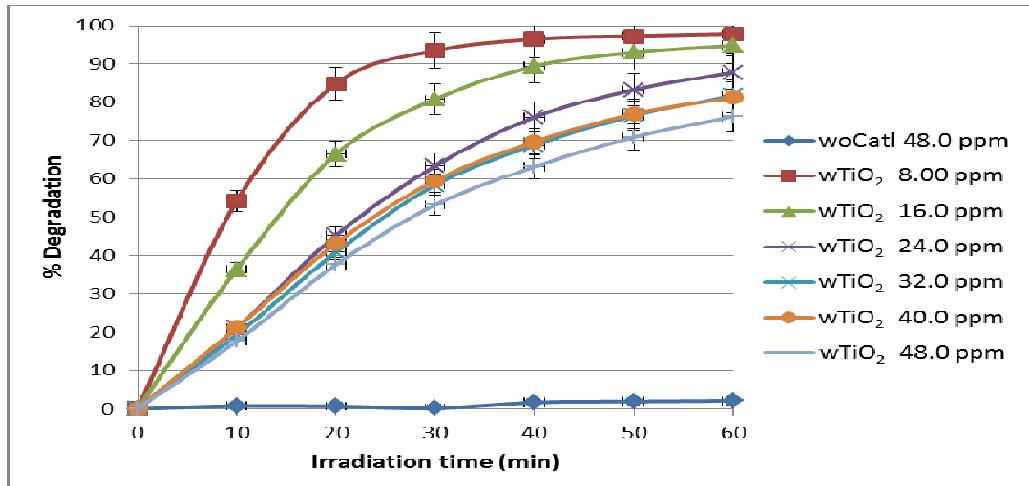
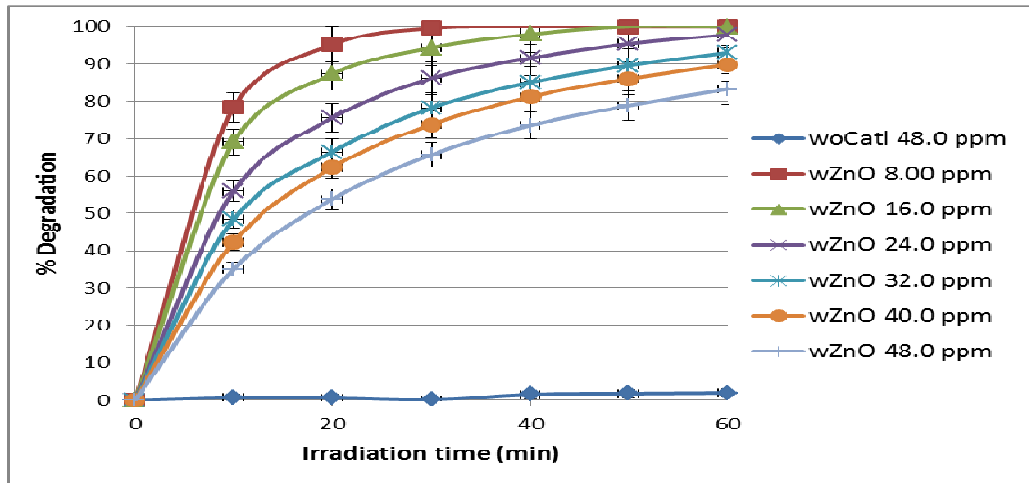


Figure 4.28: Percentage degradation with different concentration of PR for ZnO, TiO<sub>2</sub> and Fe<sub>3</sub>O<sub>4</sub> photocatalyst.

Figure 4.29 shows the first-order kinetic study of PR for ZnO, TiO<sub>2</sub> and Fe<sub>3</sub>O<sub>4</sub> photocatalysts. The results clearly showed that higher degradation rate was achieved for low concentration solutions, mainly 8.00 and 16.0 ppm concentrations, which are 0.1782 min<sup>-1</sup> ( $R^2 = 0.9854$ ) and 0.0948 min<sup>-1</sup> ( $R^2 = 0.9959$ ) for ZnO and 0.0658 min<sup>-1</sup> ( $R^2 = 0.9412$ ) and 0.0517 min<sup>-1</sup> ( $R^2 = 0.9911$ ) for TiO<sub>2</sub> photocatalysts, respectively. Other concentrations are shown in Figure 4.30. This clearly explained that with the small amount of the organic contaminant, the added photocatalyst is very effective in promoting photocatalytic decomposition in the system. In other words, the organic contaminant still have ample space to be absorbed and interact on the active site of the photocatalyst surface, therefore the degradation rate was higher. However, when the concentration was higher, the degradation rate gradually decreases due to the competition between the contaminant with the hydroxyl ions to be absorbed on the active site of the photocatalyst surface. In addition, when the amount of contaminant was higher, it will have inhibitory effect on the photodegradation process due to the photons interception before reaching the catalyst surface, decreasing the absorption of photons by the catalyst (Gao, Jia et al. 2011).

On the other hand, in the dilute PR solutions, the increase of incidental photonic flux irradiating the catalyst consequently increase the OH• radical production rate thus allow higher rate of degradation (Han, Liao et al. 2012). First-order kinetic graph for the Fe<sub>3</sub>O<sub>4</sub> photocatalyst shows that the lowest

concentration has higher degradation rate as discussed above. From the figure, there was inconclusive degradation rate results could be obtained for the 16.0 to 48.0 ppm concentrations of the PR dye, due to the minimal/negligible photocatalytic effect of  $\text{Fe}_3\text{O}_4$ .

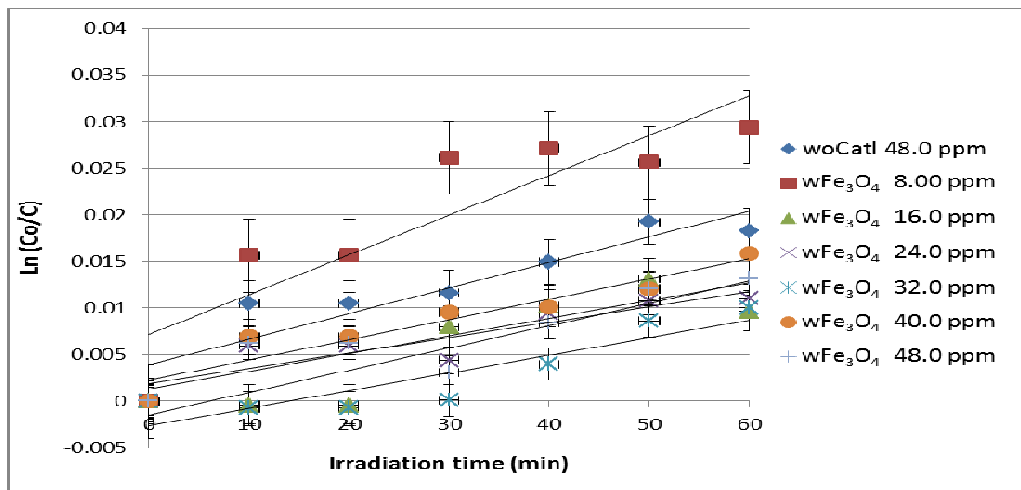
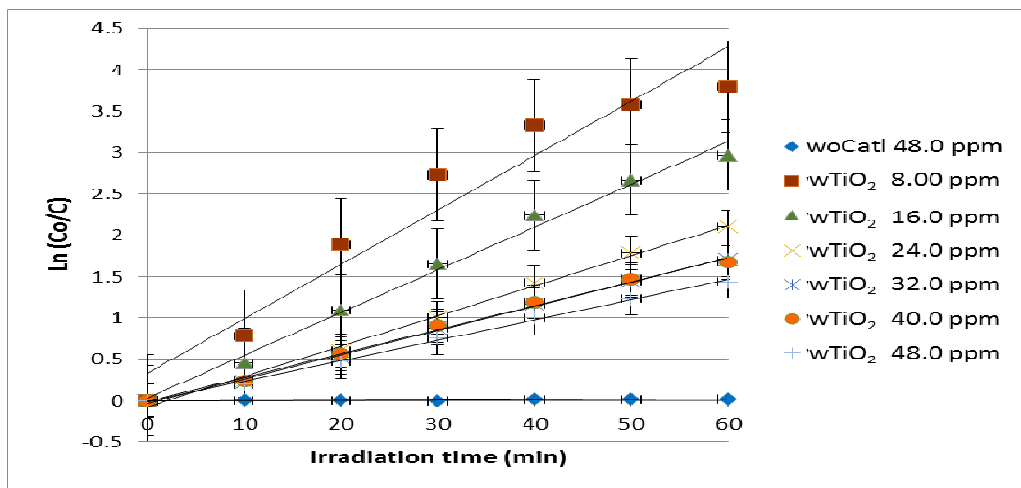
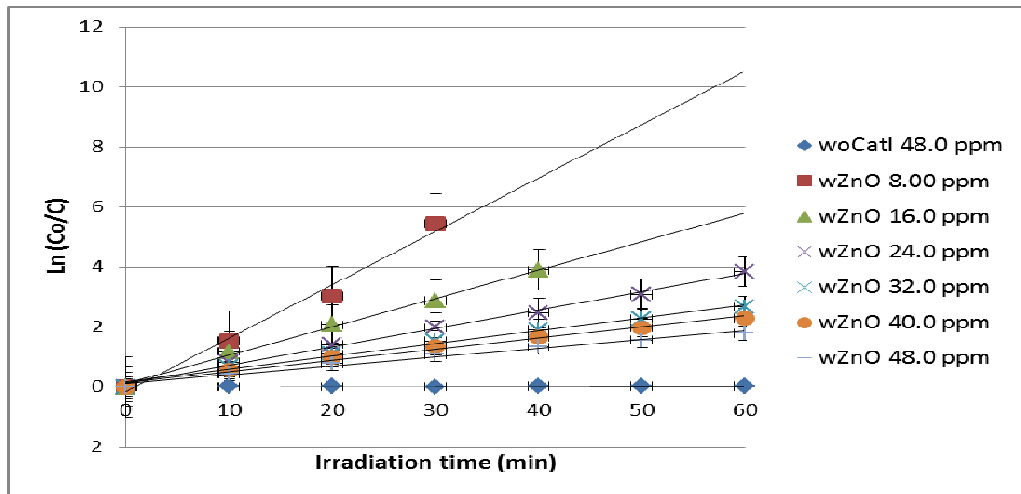


Figure 4.29: First-order kinetics on the effect of initial concentration of PR for ZnO, TiO<sub>2</sub> and Fe<sub>3</sub>O<sub>4</sub> photocatalyst.

The absolute values for the kinetic constants for all the photocatalysts, ZnO, TiO<sub>2</sub> and Fe<sub>3</sub>O<sub>4</sub>, on the PR dye were given in Figure 4.30. From the figure, it is very obvious that at the lowest organic dye concentration (8.00 ppm) highest degradation rate was achieved. From the result, it shows that the degradation rates were decreased with the increase of the photocatalyst concentration, for the ZnO and TiO<sub>2</sub> photocatalysts. It also showed that the degradation rate for the Fe<sub>3</sub>O<sub>4</sub> photocatalyst was stagnant for all the concentrations. This is well understood since Fe<sub>3</sub>O<sub>4</sub> is not an effective photocatalyst, as reported elsewhere (Singh, Barick et al. 2013). Generally, the bar graphs show that the photodecomposition rate decreases with the increased of the organic dye concentration, except for the Fe<sub>3</sub>O<sub>4</sub> photocatalyst that is inconclusive.

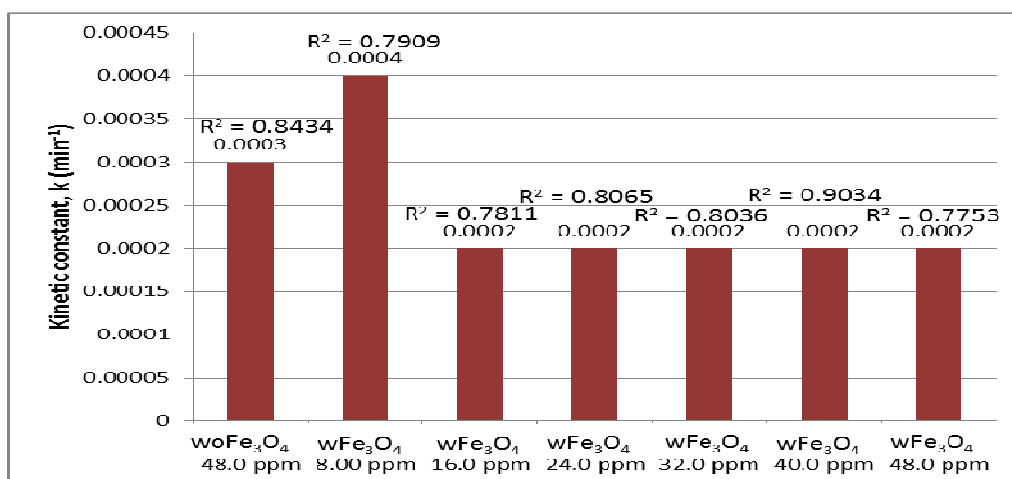
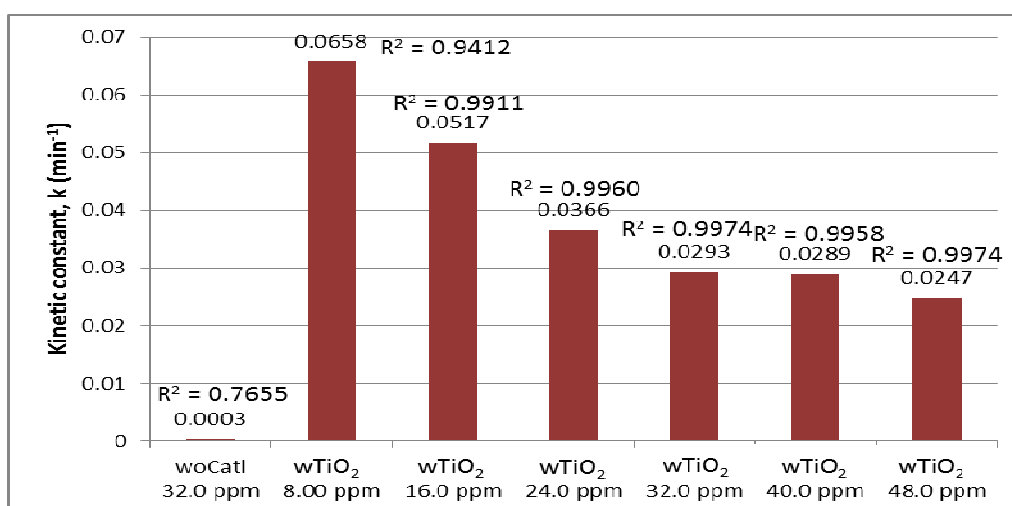
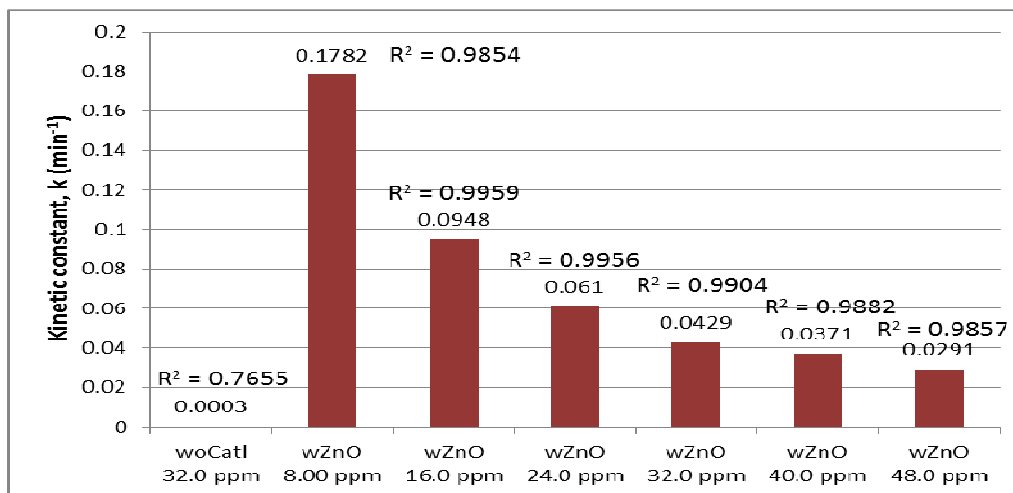


Figure 4.30: Kinetic constant,  $k$ , on the effect of initial concentration of PR by ZnO, TiO<sub>2</sub> and Fe<sub>3</sub>O<sub>4</sub> photocatalyst.

In addition to MB, MO also was used as organic contaminant for the photocatalytic measurement. Figure 4.31 shows the percentage degradation of MO in the presence of ZnO photocatalyst. The results show a smooth and consistent degradation for all different concentrations. Solution without photocatalyst showed no effect of degradation for the whole irradiation duration. Sample solution with 12.0 ppm concentration achieved almost complete degradation in 50 minutes. Whereas for all the other solutions, 97.7 to 79.6% degradations were achieved for the 16.0 to 32.0 ppm concentrations in the 60 minutes irradiation. This result clearly showed that the percentage degradation was inversely proportional to dye concentration. This was understandable that when the amount of catalyst was fixed, the number of the organic compound that managed to interact and being absorbed onto the photocatalyst surface was limited. This can be explained due to the photocatalytic degradation process takes place generally on the surface of the catalyst (Han, Liao et al. 2012).

On the other hand, the percentage degradation for the TiO<sub>2</sub> photocatalyst on the MO solutions showed a linear increment and in a very slow pace. Even with the lowest concentration of MO (12.0 ppm) only 45.9% of degradation was achieved, as compared to the highest concentration, 32.0 ppm, at only 28.6% degradation, in 60 minutes of irradiation. This results reflected that MO is a dominant organic contaminant as compared to the PR dye since only very little of organic contaminant was degraded by TiO<sub>2</sub> photocatalyst. Besides the results also reflect the photocatalytic capability of

the TiO<sub>2</sub> semiconductor nanoparticles is slightly inferior if compare to the ZnO nanoparticles. It indicates that ZnO is more photoreactive than TiO<sub>2</sub>. This is due to the ZnO having slightly lower band gap and higher binding energy of 3.2 eV and 60 meV, respectively.

Figure 4.31 shows the percentage degradation of MO solutions by the Fe<sub>3</sub>O<sub>4</sub> photocatalyst. The percentage degradation is almost zero and insignificant, with the highest change of 1.0% for the solution without photocatalyst. Since there are no significant changes in the percentage degradation, the absorbance versus time graph is also provided to show that no degradation has taken place across all different concentration.

The graph for Fe<sub>3</sub>O<sub>4</sub> photocatalyst for all the concentrations were all in the horizontal lines; indicating no degradation took place, as MO is an azo and very stable dye (Hakamada, Hirashima et al. 2012).

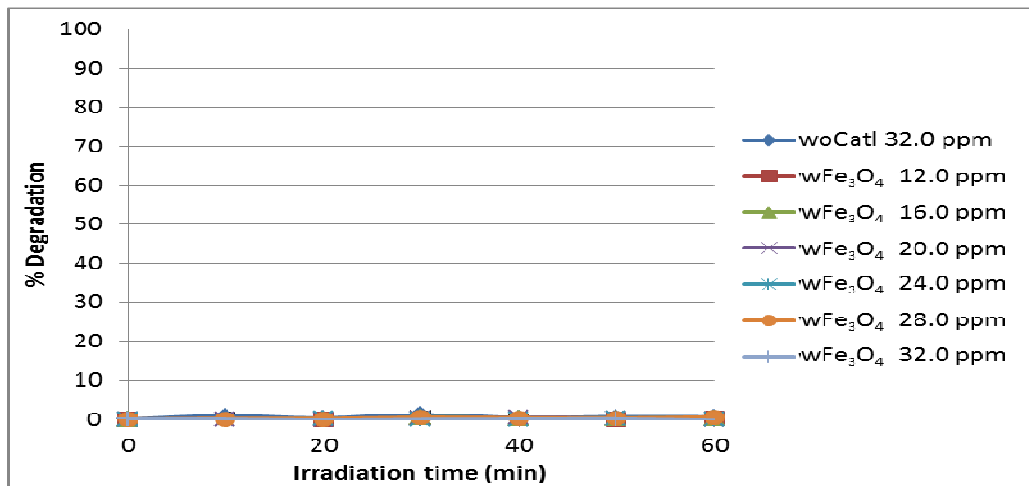
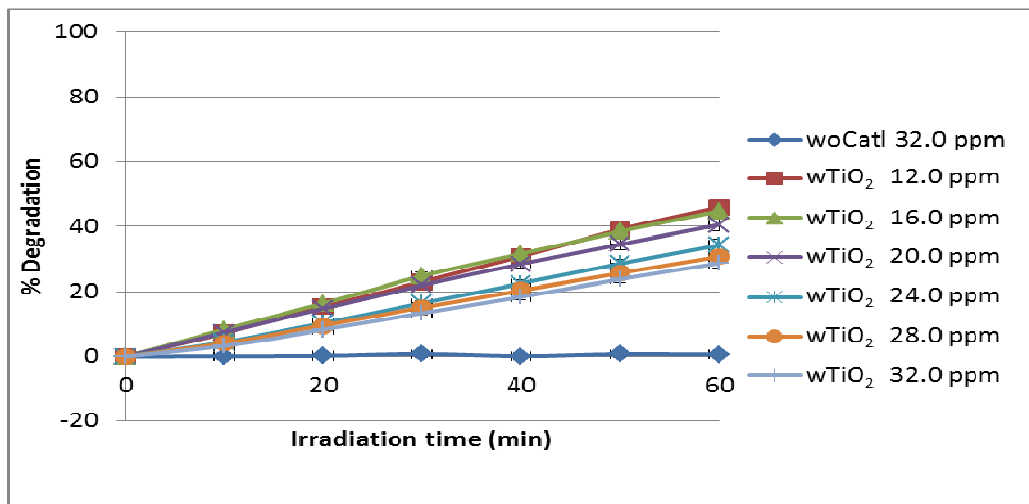
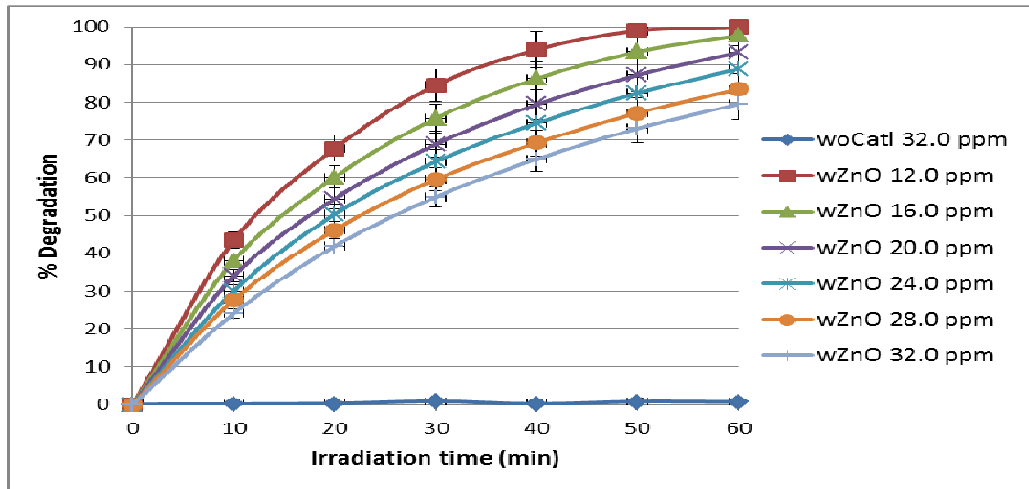


Figure 4.31: Percentage degradation with different concentration of MO for ZnO, TiO<sub>2</sub> and Fe<sub>3</sub>O<sub>4</sub> photocatalyst.

The following results are the first-order kinetic for the MO solutions with the presence of ZnO, TiO<sub>2</sub> and Fe<sub>3</sub>O<sub>4</sub> photocatalysts. Figure 4.32 shows the degradation rate for the ZnO photocatalyst with the lowest concentration, 12.0 ppm (0.0868 min<sup>-1</sup>,  $R^2 = 0.9427$ ), was the best performer amongst all the solutions followed by higher concentration. This is very well understood since the degradation is more achievable before the optimum concentration of the solution is achieved, there were lots of available reactive sites on the photocatalyst for the organic contaminants to be absorbed and undergoes the photocatalytic process. On the other hand, since the amount of the organic contaminant was still very mild, the incidental photonic flux into the dilute MO solution and arrived at the photocatalyst surface were abundance. Therefore, the production rate of OH• radical from hydroxyl ions increases, while achieving the optimum concentration, which allowed the higher degradation rate to be achieved (Gopal, Lo et al. 2012). Subsequently, with the increased of the MO concentration, it will create an opacity effect in the solution and cause photons interception before they can reach the catalyst surface and hence decreases the absorption of photons by the catalyst, leading to the distortion of degradation efficiency (Hilal, Al-Nour et al. 2010).

For the TiO<sub>2</sub> photocatalyst, the first-order kinetics result for MO for two of its lowest concentrations were quite close to each other with the values of 0.0103 ( $R^2 = 0.9925$ ) and 0.0099 min<sup>-1</sup> ( $R^2 = 0.9989$ ) for 12.0 and 16.0 ppm, respectively.

The first-order kinetics for the  $\text{Fe}_3\text{O}_4$  photocatalyst shows an inconsistent degradation rate with even a negative value for one of the concentration, as shown in Figure 4.32. As mentioned earlier, this was due to the very small changes on the measurements across the irradiation duration.

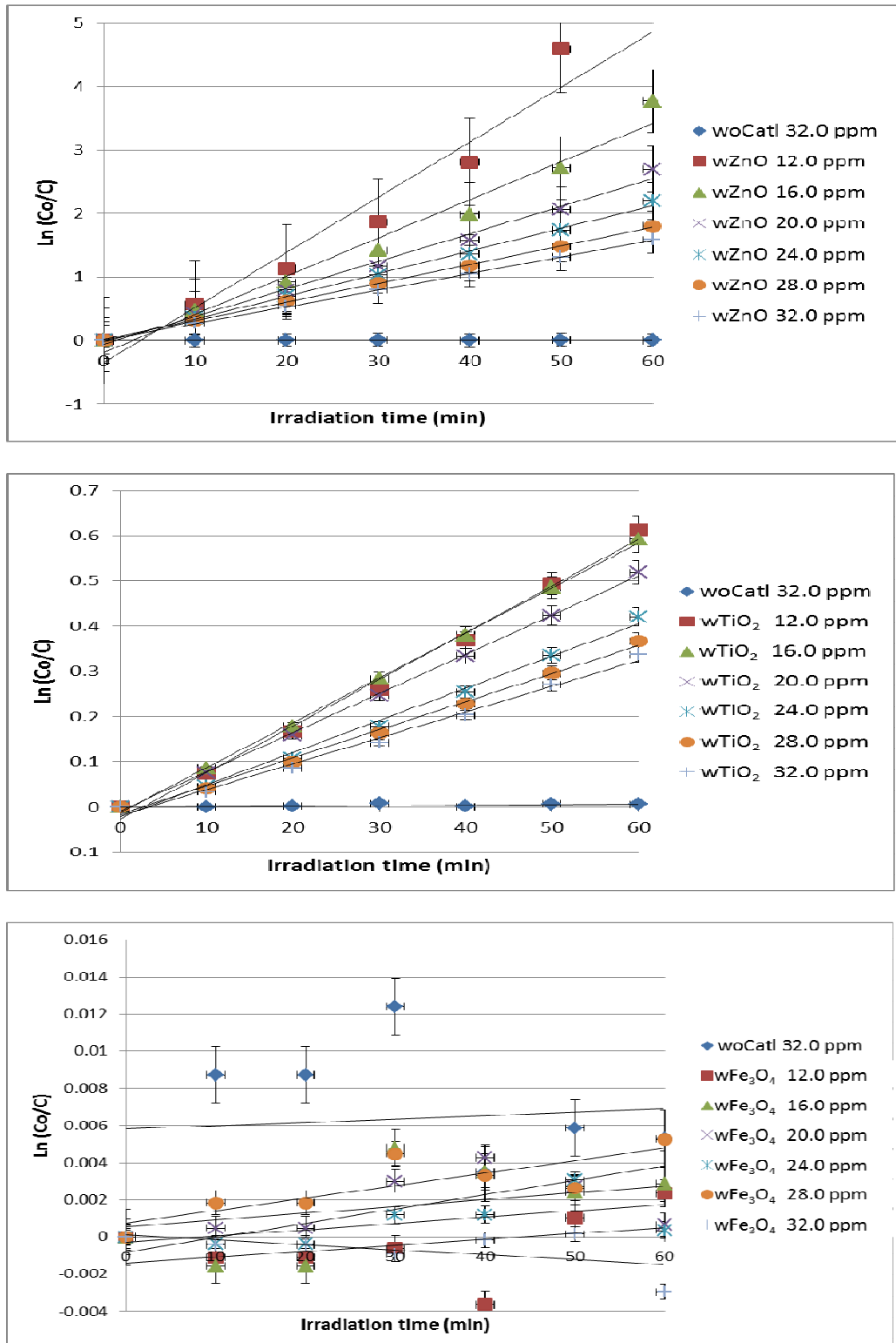


Figure 4.32: First-order kinetics on the effect of initial concentration of MO for ZnO, TiO<sub>2</sub> and Fe<sub>3</sub>O<sub>4</sub> photocatalyst.

Figure 4.33 shows the bar graphs of the kinetic constant for MO dye degraded by ZnO, TiO<sub>2</sub> and Fe<sub>3</sub>O<sub>4</sub> photocatalysts. Both ZnO and TiO<sub>2</sub> photocatalysts show very obvious changes of the degradation rates, started with highest degradation rate for the lowest concentration, 12.0 ppm (0.0868 min<sup>-1</sup>,  $R^2 = 0.9427$  for ZnO and 0.0103 min<sup>-1</sup>,  $R^2 = 0.9925$  for TiO<sub>2</sub>), and gradually decreased as the concentration increases to the highest concentration, 32.0 ppm (0.0262 min<sup>-1</sup>,  $R^2 = 0.9998$  for ZnO and 0.0057 min<sup>-1</sup>,  $R^2 = 0.9912$  for TiO<sub>2</sub>). As the organic dye concentration increases, the degradation rate was decreased (Khayyat, Akhtar et al. 2012). This has been well explained earlier that increasing dye concentration inhibited the competitive absorption with hydroxyl ions, OH<sup>-</sup>, thus decreased the formation of the •OH radicals. Besides, the increased of dye concentration inhibited the UV light transmission deeper into the solution, thus reduced the number of light photons absorbed by the photocatalyst surfaces, hence, significantly lowering the photocatalytic reaction rate (Kaneva, Dimitrov et al. 2011).

The results of the kinetic constant for the Fe<sub>3</sub>O<sub>4</sub> photocatalyst on the degradation of MO obviously shows insignificant pattern therefore no conclusion could be deduced for the Fe<sub>3</sub>O<sub>4</sub> photocatalyst to indicate its ability to degrade MO dye. This result was in agreeable with many researchers on the ability of the Fe<sub>3</sub>O<sub>4</sub> photocatalyst (Singh, Barick et al. 2013).

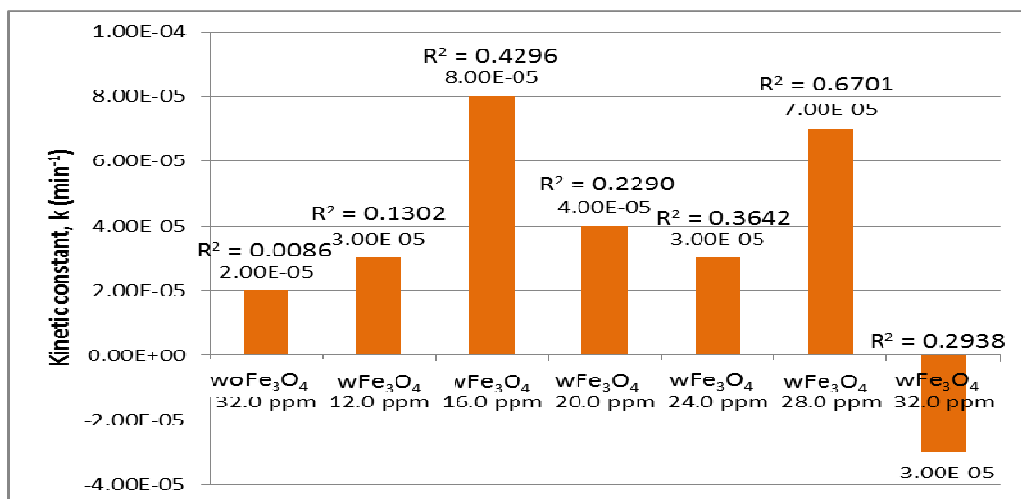
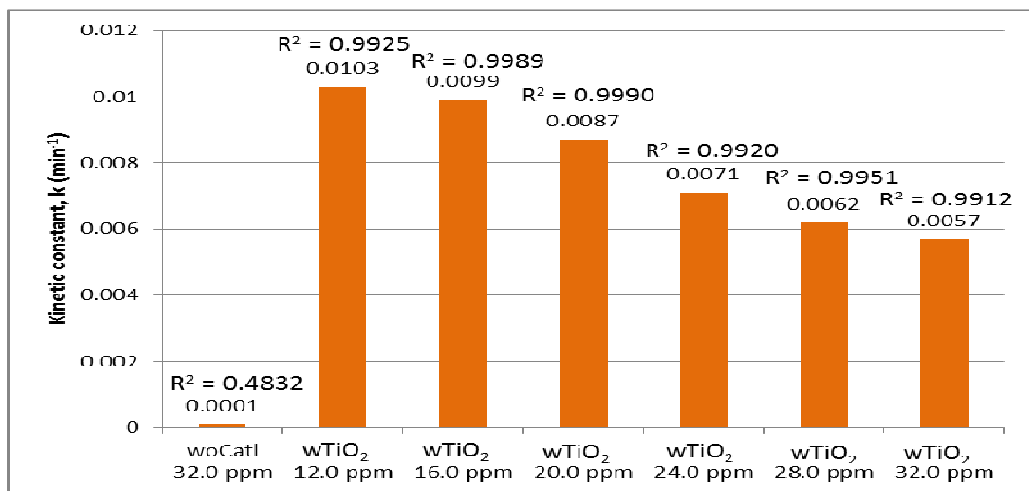
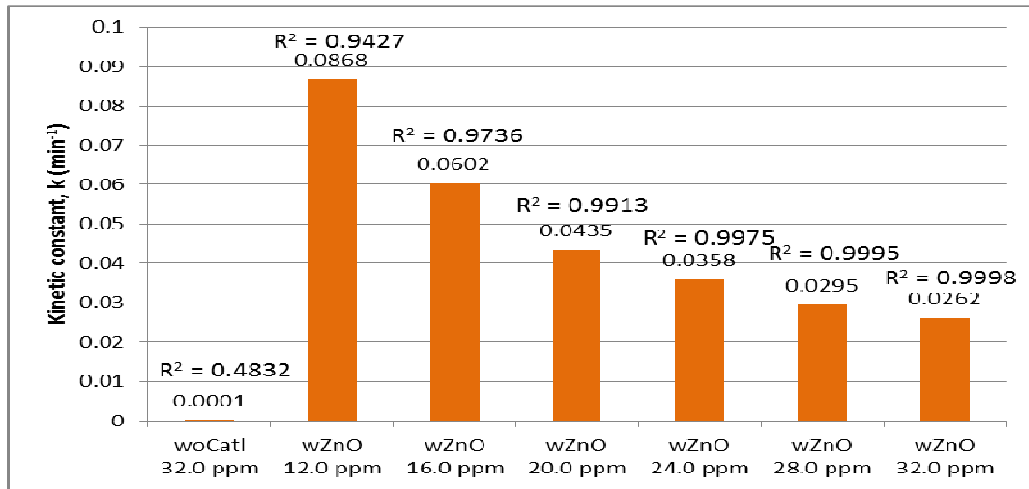


Figure 4.33: Kinetic constant, K, on the effect of initial concentration of MO for ZnO, TiO<sub>2</sub> and Fe<sub>3</sub>O<sub>4</sub> photocatalyst.

#### 4.2.6.4 *Effect of Irradiation Duration on the Three Dyes by ZnO, TiO<sub>2</sub> and Fe<sub>3</sub>O<sub>4</sub> Photocatalysts*

It is commonly understood that the amount of degradation will increase with irradiation duration. This is because more photons reached the photocatalyst surface and subsequently produced more •OH radicals. As a consequence, more organic dye are able to be decomposed. The detail degradation for the MB dye is shown in Figure 4.34. It can be seen that with the addition of the ZnO photocatalyst into the solution, the maximum absorption peak at 665 nm dropped slightly. This is due to the red shift of the spectral band of the n-p\* transition occurs within the organic dye molecules (Heger, Jirkovsk et al. 2005). This indicates that very minimal absorption process has taken place while the solution was allowed to be in the dark (~14.3%). Since the photocatalytic interaction takes place on the material surface, therefore, during the insertion of the catalyst into the MB solution, certain amount of organic contaminant has been absorbed onto the surface and the photocatalytic processes shall be initiated (Han, Liao et al. 2012).

Subsequently, after the solution is being irradiated by the UV light, the 12.0 ppm MB solution was fully degraded in just 30 minutes of irradiation. This shows that the organic contaminant contains in the solution was still manageable in the ZnO photocatalyst; which means that there was still

sufficient active surface area as well as light photons arrived at the surface of the photocatalyst for the degradation of the organic contaminants (Cheng, Yu et al. 2016).

The degradation process was similar for the  $\text{TiO}_2$  photocatalyst, except it took longer irradiation duration to fully degrade the MB dye, as shown in Figure 4.34. A significant dropped was also observed when the  $\text{TiO}_2$  photocatalyst was added into the solution in dark condition for about 30 minutes ( $\sim 13.4\%$ ). Subsequently, when the solution was irradiated with the UV light, the peak gradually dropped to zero. This shows that the MB dye was completely degraded by the  $\text{TiO}_2$  photocatalyst after 60 minutes of irradiation duration.

In another photocatalytic process, MB dye was added with the  $\text{Fe}_3\text{O}_4$  photocatalyst, as shown in Figure 4.34. When the mixed solution was allowed to be in the dark for about 30 minutes, a significant dropped was measured ( $\sim 18.9\%$ ). However, when the solution was irradiated with the UV light for a 10 minutes interval, only very tiny drop was recorded. The solution was irradiated for 60 minutes and a measurement was taken for every 10 minutes interval. For every 10 minutes interval, the recorded results showed a constant drop but in a very small magnitude of absorbance. This shows a weak performance of the  $\text{Fe}_3\text{O}_4$  photocatalyst in degrading the MB dye.

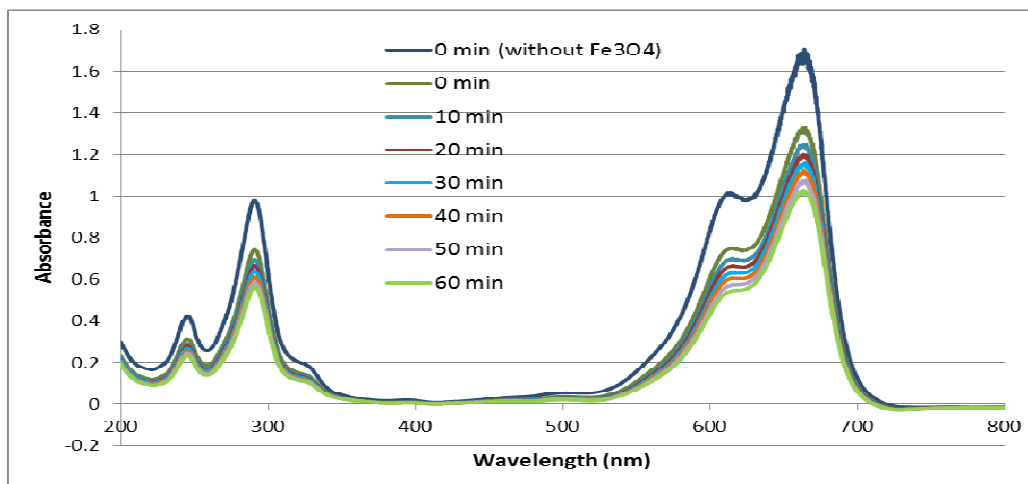
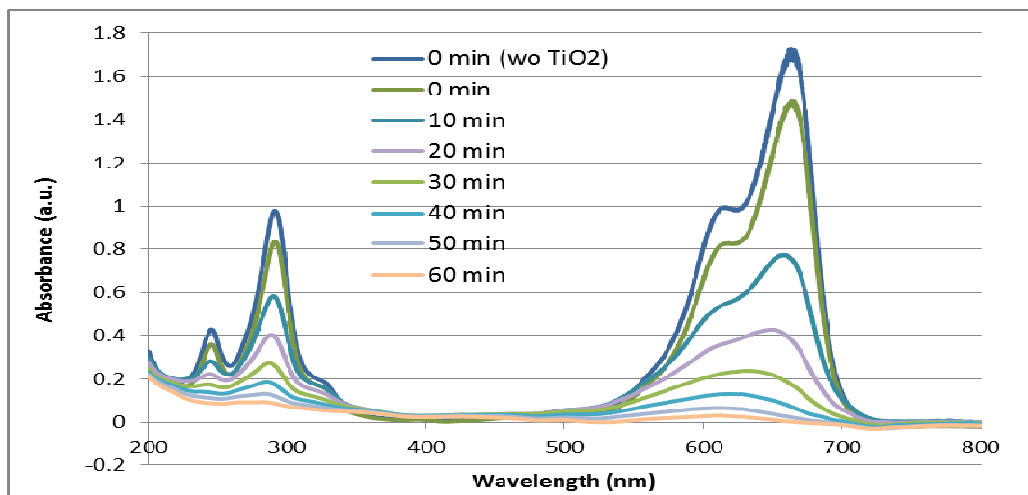
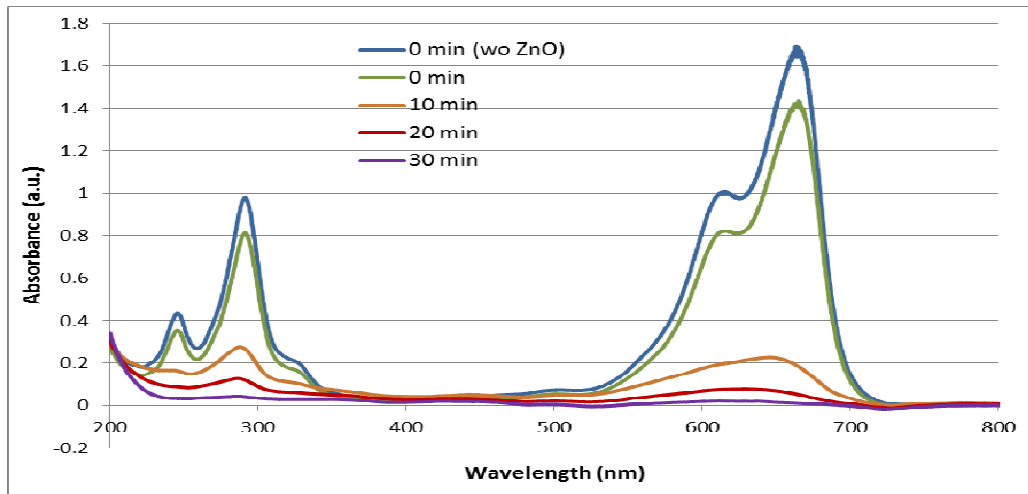
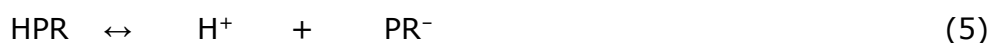


Figure 4.34: Degradation of 12.0 ppm MB for ZnO (2.5 wt%), TiO<sub>2</sub> (3.0 wt%) and Fe<sub>3</sub>O<sub>4</sub> (3.0 wt%) with the respective irradiation duration.

Figure 4.35 shows the photocatalytic degradation of PR dye by the ZnO photocatalyst. When ZnO photocatalyst was added into the PR solution and allowed to be in the dark (~21.2% dropped at the main peak), colour changes was observed for the solution. And when the UV-Vis measurement was made, a usual drop of the main peak (435 nm) was observed. However, very interesting changes happened to the spectrum at another absorption peak (560 nm), which the absorption rate increases significantly.

These two absorption peaks represent the absorption spectra for proton donor (HPR) and proton acceptor (PR<sup>-</sup>) forms of PR with the inclusion of ZnO photocatalyst (Rendina 1971). Since PR is a weak acid, the proton donor form dissociates reversibly into a proton donor and proton acceptor form.



Therefore, this phenomenon which was initiated by the dissociation of the PR solution has given rise of those two observed maximum (Rendina 1971). This condition was also governed by the ZnO surface chemistry with the establishment of acid and base equilibriums when the catalyst in water solution (Comparelli, Fanizza et al. 2005):





As can be seen from Figure 4.35, a significant dropped, for both peaks, was observed when the solution was irradiated with the UV light in just 10 minutes. This indicates that the decomposition of the organic compounds has taken place. By continuously exposed the solution under the UV light, a significant decomposition of the organic dye has taken place and a complete degradation was observed after 50 minutes irradiation.

Similar photodegradation mechanisms of PR are observed for  $\text{TiO}_2$  nanomaterials. A significant dropped was observed when the solution was left in the dark (~6.8%). As expected,  $\text{Fe}_3\text{O}_4$  nanoparticles has almost negligible photocatalytic capability. As expected, a slight dropped was observed when the solution was left in the dark (~8.3%). The absorption rate of the organic dye solution does not encounter any changes even after 60 minutes of continuous UV irradiation.

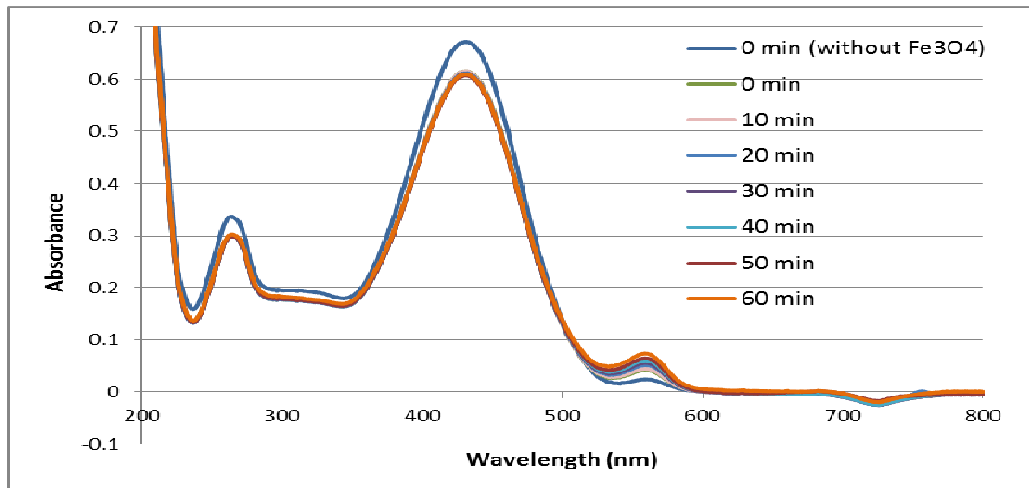
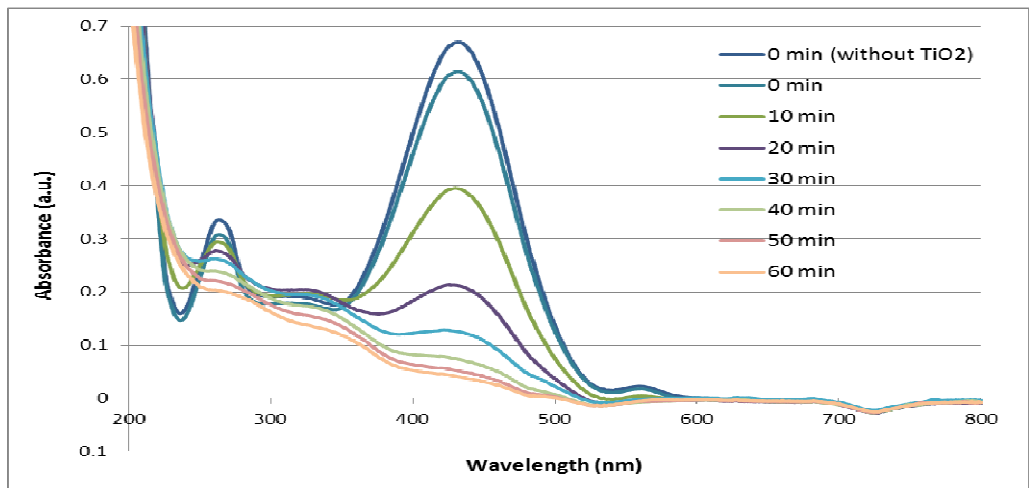
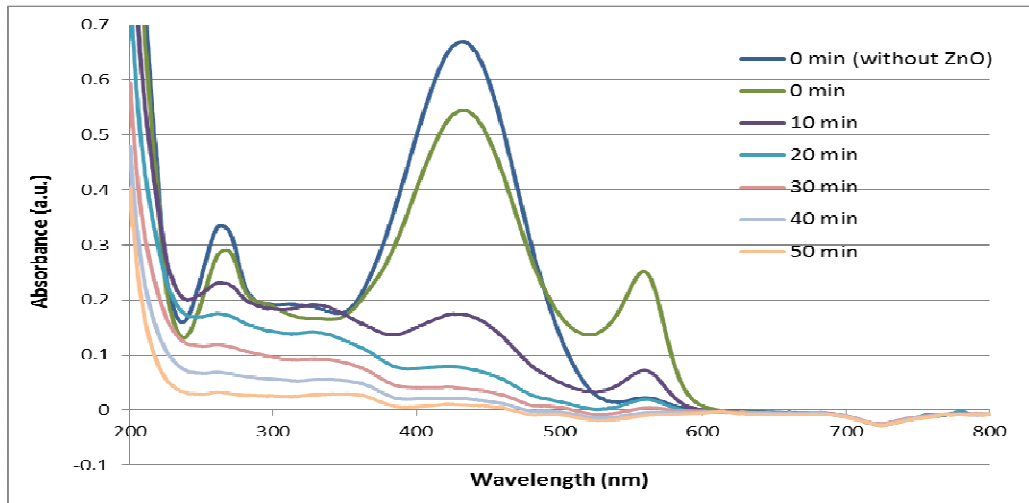


Figure 4.35: Degradation of 16.0 ppm PR for ZnO (2.5 wt%), TiO<sub>2</sub> (3.0 wt%) and Fe<sub>3</sub>O<sub>4</sub> (3.0 wt%) with the respective irradiation duration.

Next, the photocatalytic measurement was conducted on the MO dye with the presence of ZnO, TiO<sub>2</sub> and Fe<sub>3</sub>O<sub>4</sub> photocatalysts, as indicated in Figure 4.36. As can be seen in all the figures, organic contaminant was immediately decomposed after the photocatalyst was added, even before irradiated with UV light (~6.9%). This has immensely showed the significance of the presence of the photocatalyst as a photodegradation agent. On the other hand, coupled with UV light irradiation, the photodegradation process has significantly taken place, as can be observed in Figure 4.36 for the MO solution with the addition of the ZnO photocatalyst, after being irradiated for 10 minutes. The absorption peak at 465 nm dropped significantly. The decomposition processes were gradually increased with the increase of the irradiation time. At the end of the 60 minutes irradiation, 97.7% of decomposition was achieved.

For TiO<sub>2</sub> photodecomposition process on the MO dye, pre-irradiation period showed a significant dropped when the solution was left in the dark (~6.9%). In addition, when the solution was irradiated with the UV light, the degradation rate was equal for every interval of irradiation. The highest degradation of 44.6% was achieved after the solution was irradiated for 60 minutes.

Lastly, Figure 4.36 shows the degradation of the MO dye by Fe<sub>3</sub>O<sub>4</sub> photocatalyst. As the Fe<sub>3</sub>O<sub>4</sub> catalyst was added into the MO solution, a small

decomposition took place ( $\sim 6.8\%$ ). However, when the solution was placed under the UV light irradiation, no effect of degradation was detected. This shows that the  $\text{Fe}_3\text{O}_4$  photocatalyst has no photocatalytic effect on the MO dye.

The experiment on MO dye shows that the dye is a very recalcitrant dye, as compared to MB and PR dyes. As mentioned earlier, MO is an azo dye and is very stable. MO is a polar molecule, which could be adsorbed on the photocatalyst surface via van der Waals attraction force. High concentrations of hydroxyl groups (OH) are present on the  $\text{Fe}_3\text{O}_4$  surface. Therefore, surface OH groups could form Hydrogen bonds with O, N and S atoms in MO, which can enhance the adsorption of MO (Wang, Ming et al. 2012). Besides, MO molecule is negatively charged across all the pH values, which is reported between pH 3 to 11. At lower pH, MO molecule will be changed into its anionic form of  $\text{C}_{14}\text{H}_{15}\text{N}_3\text{SO}_3^-$ , where at as high pH, MO molecule will be changed into its anionic form of  $\text{C}_{14}\text{H}_{15}\text{N}_3\text{SO}_3^-$  (Wang, Ming et al. 2012).

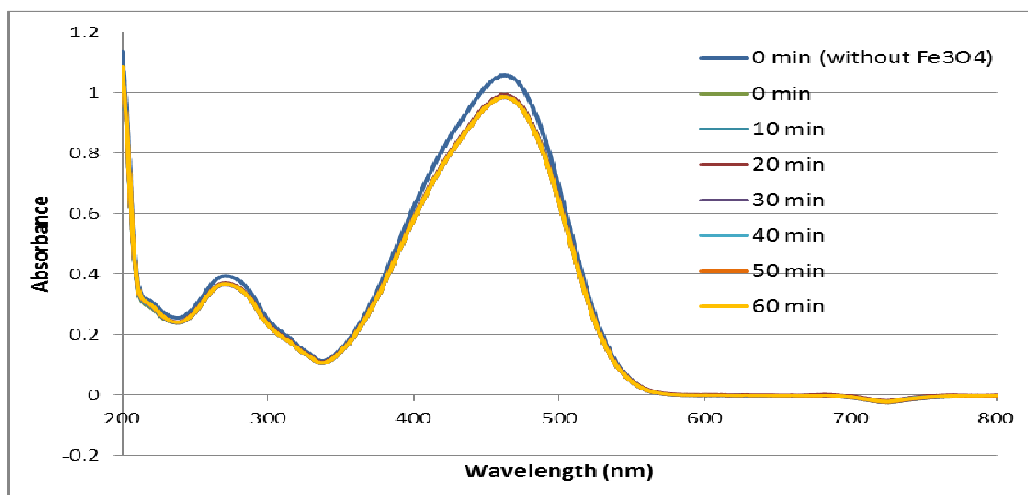
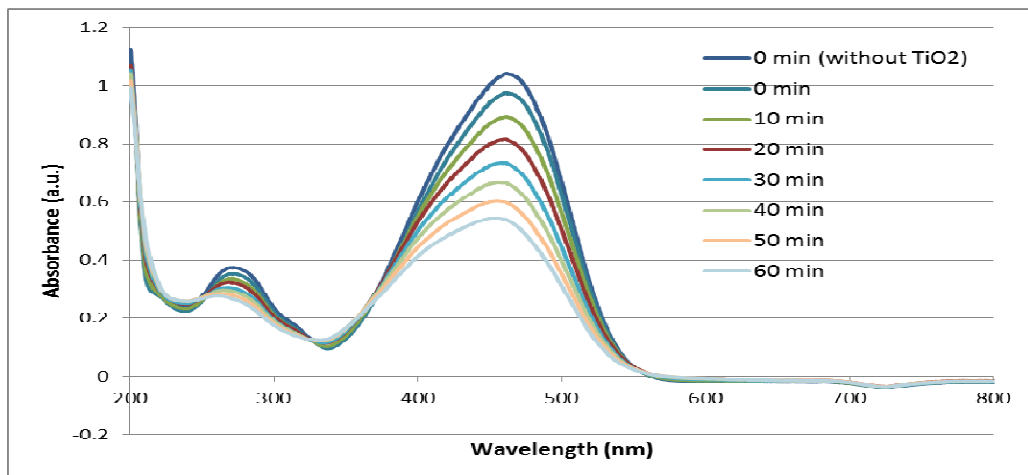
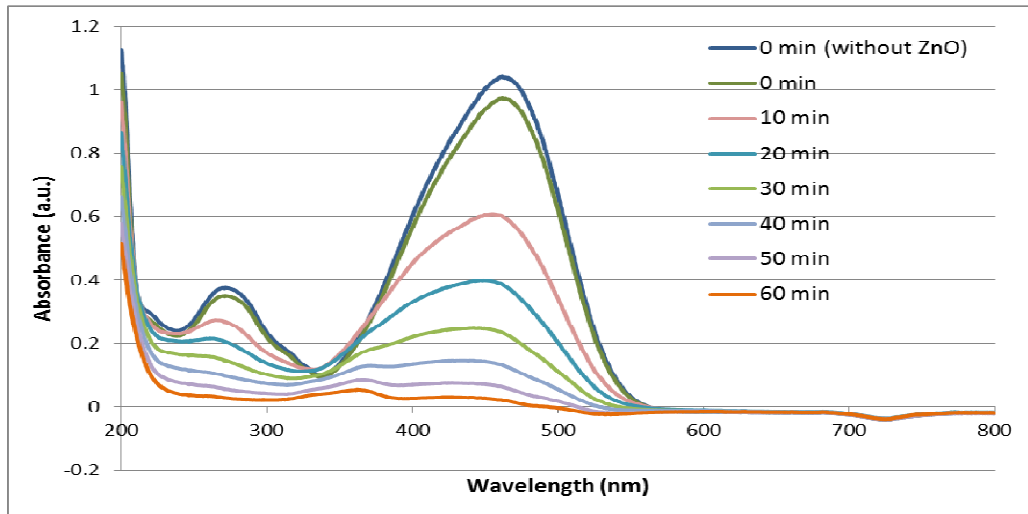


Figure 4.36: Degradation of 16.0 ppm MO for ZnO (2.5 wt%), TiO<sub>2</sub> (3.0 wt%) and Fe<sub>3</sub>O<sub>4</sub> (3.0 wt%) with the respective irradiation duration.

Finally, the summary of the kinetic constants for MB, PR and MO dyes with ZnO, TiO<sub>2</sub> and Fe<sub>3</sub>O<sub>4</sub> photocatalysts were listed in Table 4.7. It can be seen that the highest degradation rate was achieved by the ZnO nanoparticle for all the 3 dyes, followed by TiO<sub>2</sub> and Fe<sub>3</sub>O<sub>4</sub>, as provided in Table 4.7 below. In addition, MB is more prominent for photodegradation while MO is more stable against photodegradation. This is because MB is a potent cationic and thiazine dye (Jo and Tayade 2014). In addition, MB is a very effective photosensitizer due to its triplet states of appropriate energies possession and a significant quantum yield ( $\phi_{\Delta} = 0.52$ ) in aqueous (DeRosa and Crutchley 2002). On the other hand, MO is an azo and a very stable dye (Hakamada, Hirashima et al. 2012).

Table 4.7: Kinetic constants for MB, PR and MO dye with ZnO, TiO<sub>2</sub> and Fe<sub>3</sub>O<sub>4</sub> photocatalysts.

Dyes & Conc. (ppm)	ZnO		TiO <sub>2</sub>		Fe <sub>3</sub> O <sub>4</sub>	
	<i>k</i> (min <sup>-1</sup> )	<i>R</i> <sup>2</sup>	<i>k</i> (min <sup>-1</sup> )	<i>R</i> <sup>2</sup>	<i>k</i> (min <sup>-1</sup> )	<i>R</i> <sup>2</sup>
MB 8 ppm	0.2299	1.0000	0.1483	0.9950	0.0056	0.9913
MB 12 ppm	0.2171	0.9965	0.1071	0.9896	0.0039	0.9969
PR 8 ppm	0.1782	0.9854	0.0658	0.9412	0.0004	0.7909
PR 16 ppm	0.0948	0.9959	0.0517	0.9911	0.0002	0.7811
MO 12 ppm	0.0868	0.9427	0.0103	0.9925	3.00 E-05	0.1302
MO 16 ppm	0.0602	0.9736	0.0099	0.9989	8.00 E-05	0.4296

### **4.3 Summary**

From this study, all the oxide nanoparticles used were of standard crystal structures and well dispersed. There were no impurities observed during the characterization of the nanoparticles. For the solutions without the photocatalytic materials, MB dye showed significant decomposition under UV light irradiation for 60 minutes duration, whereas PR was only slightly decomposed. On the other hand, MO is the most photostable dye because it did not show any traceable degradation at all. This shows that not all dyes can be decomposed by UV light irradiation. Certainly, tough and recalcitrant dyes may not have any decomposition even being irradiated under UV light for a long duration.

By using MB as a model dye, optimum photocatalyst loadings for the three photocatalysts were obtained. It was found that the optimum loading for ZnO was 2.5wt%, whereas for TiO<sub>2</sub> and Fe<sub>3</sub>O<sub>4</sub> was 3.0wt%. In the photodecomposition of MB, it was completely decomposed between 10 to 20 minutes of irradiation duration by the presence of ZnO photocatalyst. For the TiO<sub>2</sub> photocatalyst, MB was decomposed in between 20 to 30 minutes irradiation. Nonetheless, Fe<sub>3</sub>O<sub>4</sub> photocatalyst was just able to decomposed 72.8% of the MB in 60 minutes of irradiation.

For the decomposition of PR, ZnO and TiO<sub>2</sub> photocatalysts were able to degrade PR solutions within 30 and 50 minutes of irradiation, respectively.

However,  $\text{Fe}_3\text{O}_4$  showed only very mild decomposition even after 60 minutes of irradiation. In the photodecomposition of MO, it was completely decomposed by ZnO in 50 minutes of irradiation, whereas  $\text{TiO}_2$  decomposed 45.9% of MO in 60 minutes of irradiation. On the other hand, no trace of decomposition could be detected for the 60 minutes irradiation with the presence of  $\text{Fe}_3\text{O}_4$  nanoparticles.

It can be concluded that ZnO is the superior photocatalyst followed by  $\text{TiO}_2$ , whereas  $\text{Fe}_3\text{O}_4$  showed very mild photocatalytic capability. In term of photostability of the dyes, it showed that MO is the most stable dye followed by PR and MB. This result was consistent for all the dyes whether they are irradiated under UV light irradiation with or without the presence of photocatalysts.

## **CHAPTER 5**

### **Zinc Oxide/Iron Oxide (magnetite) Nanocomposite**

#### **5.1 Introduction**

In current advanced technology era, huge number of industries has utilised various kinds of synthetic organic dyes into their products. These modern synthetic dyes are generally resistive to natural/biological degradation. Therefore, it will cause serious threat to the environment. Huge amount of wastewater released from the industries each day which accumulatively leading to significant damage to the environment if proper safety measures are not taken seriously. Precaution and safety measure needed in ensuring the effluent released into the environment is safe or at least in an acceptable level of contamination.

There were different kinds of organic compounds recognised as the contamination sources to the environment. The major organic compounds that mostly came from the industrial effluent include dyes, phenols, chlorophenols, aliphatic alcohols, aromatics, polymers and carboxylic acids. The industries that mainly produced those numerous pollutions includes paper mill, textile, cosmetic industries and land fill leachate (Schwarzenbach, Egli et al. 2010).

One of the fastest emerging technologies that available in the removal of the textile dyes from the effluent is *via* photodegradation induced by semiconductor materials. Recently, there has been a growing interest throughout the globe in using semiconductor materials as photocatalysts (Hoffmann, Martin et al. 1995).

## **5.2 Background Study**

The use of semiconductor with light illumination has been successfully utilised to degrade variety of organic contaminants in water (Behnajady, Modirshahla et al. 2006). The most extensively used semiconductors to study their photocatalytic properties are  $\text{TiO}_2$ , ZnO and CdS (Kansal, Singh et al. 2007). The efficiency of a semiconductor oxide as a photocatalyst depends on the electron-hole separation efficiency and the adsorption capability. Thus, a major obstacle in achieving high photocatalytic efficiency in semiconductors is to reduce the recombination rate of the charge carriers (Chen and Mao 2007). Therefore, modifications required necessary to prevent the recombination of the photogenerated charge carriers. This could be done by doping of metals, such as  $\text{Sn}^{4+}$ ,  $\text{Na}^+$ ,  $\text{Ag}^+$ ,  $\text{Mg}^{2+}$  and  $\text{Cr}^{3+}$  into the semiconductor surface which will modify its bandgap (Wu and Huang 2010, Jia, Fan et al. 2011, Lu, Liu et al. 2011, Wu, Shen et al. 2011, Chamjangali, Bagherian et al. 2015). On the other hand, by taking proper steps during the

preparation, crystalline morphology and surface microstructure of the prepared semiconductors can be well controlled (Yu, Li et al. 2005).

However, another problem arises as after the photocatalytic processes, there is a need to separate the photocatalyst material from the treated water. Therefore, by introducing magnetic materials into the photocatalyst, it will be an efficient and convenient method for separating and recycling the photocatalyst by applying an external magnetic field (Hou, Tian et al. 2015, Kim, Woo et al. 2016).

This magnetically separable photocatalysts have different level of ability in its optical, magnetic and catalytic properties if compared to their single compound materials (Alamo-Nole, Bailon-Ruiz et al. 2013). Therefore, a good magnetic material has to be chosen to fully utilise the magnetic properties for effective separation. Due to low cost, good magnetic properties and environmentally friendly,  $\text{Fe}_3\text{O}_4$  nanopowder has been chosen as the magnetic source as compared to other magnetic materials ( $\gamma\text{-Fe}_2\text{O}_3$  and  $\text{MFe}_2\text{O}_4$ , where M is a divalent metal, e.g.  $\text{Ba}^{2+}$ ,  $\text{Ni}^{2+}$ ,  $\text{Co}^{2+}$ , or  $\text{Zn}^{2+}$ ) (Lopez, Gonzalez et al. 2010, El Ghandoor, Zidan et al. 2012, Zhu, Hojamberdiev et al. 2013).

There have been few methods in preparation and application of  $\text{ZnO}/\text{Fe}_3\text{O}_4$  nanopowder in the photodegradation of organic pollutants under ultraviolet irradiation. First reported by Hong et al. (2008) that the

ZnO/Fe<sub>3</sub>O<sub>4</sub> nanopowder was prepared by co-precipitation method and their photocatalytic activities were investigated (Hong, Zhang et al. 2008, El Ghandoor, Zidan et al. 2012). Another researcher prepared with different molar ratios by two-step method and photodegradation on methyl orange as investigated (Xia, Wang et al. 2011). Singh et al. (2013) prepared Fe<sub>3</sub>O<sub>4</sub> embedded ZnO nanopowder by a facile soft-chemical approach and applied them for photodegradation on three types of pollutants (Singh, Barick et al. 2013). Last, but not the least recently, a group of researcher have prepared recoverable ZnO/Fe<sub>3</sub>O<sub>4</sub> nanopowder in diethylene glycol at 160 °C and applied them for photodegradation of phenol (Feng and Lou 2015).

Therefore, this study is aimed to bring forward a simple and easy processing method in preparing the photocatalyst, besides it can also be easily retrieved without any sludge being left behind or involved any additional cost for subsequent treatment.

### **5.3 Results and Discussion**

#### *5.3.1 Different sintering temperature*

The prepared samples were sintered at different sintering temperature, which were 200, 250, 300, 350, 400 and 450 °C, respectively. All samples were sintered for the duration of 5 hours. The FESEM micrographs for the 20 wt% doped Fe<sub>3</sub>O<sub>4</sub> of ZnO/Fe<sub>3</sub>O<sub>4</sub> nanocomposites which were prepared at different sintering temperature were shown in Figure 5.1. The micrographs showed well mixed nanoparticles between small and large particle size and quite evenly distributed across the samples. In addition, all samples also exhibit moderate porosity which will greatly contribute significant surface area for the degradation process to take place.

Generally, the small size particles are spherical shape whereas the medium and larger size particles are mixture of rod-like and cubic shape. Those rod-like and cubic shapes are ZnO particles whereas spherical shapes are generally Fe<sub>3</sub>O<sub>4</sub> particles. The surfaces of the particles are quite smooth, which shows no sign of over stressed being applied onto the powder during mixing. The sintering temperatures have negligible effect on the shape and size distribution of the prepared nanoparticles. The average particle size as measured from the micrographs are (172.3 ± 9.6) nm, (157 ± 11) nm, (164 ± 12) nm, (152.8 ± 7.2) nm, (153.1 ± 6.2) nm and (168.5 ± 8.2) nm, for 200, 250, 300, 350, 400 and 450 °C sintering temperature, respectively.

From these results, it shows that the sintering temperature between 200 to 450 °C has no significant impact on the particle size of the nanocomposites. This can relate to an experiment by Yassitepe (2008) in sintering the ZnO nanoparticles at 700 °C, which not changing much of its microstructure and surface area (Yassitepe, Yatmaz et al. 2008). Therefore, there is no significant changes could be observed for all the prepared nanocomposites with the sintering temperature used in this study.

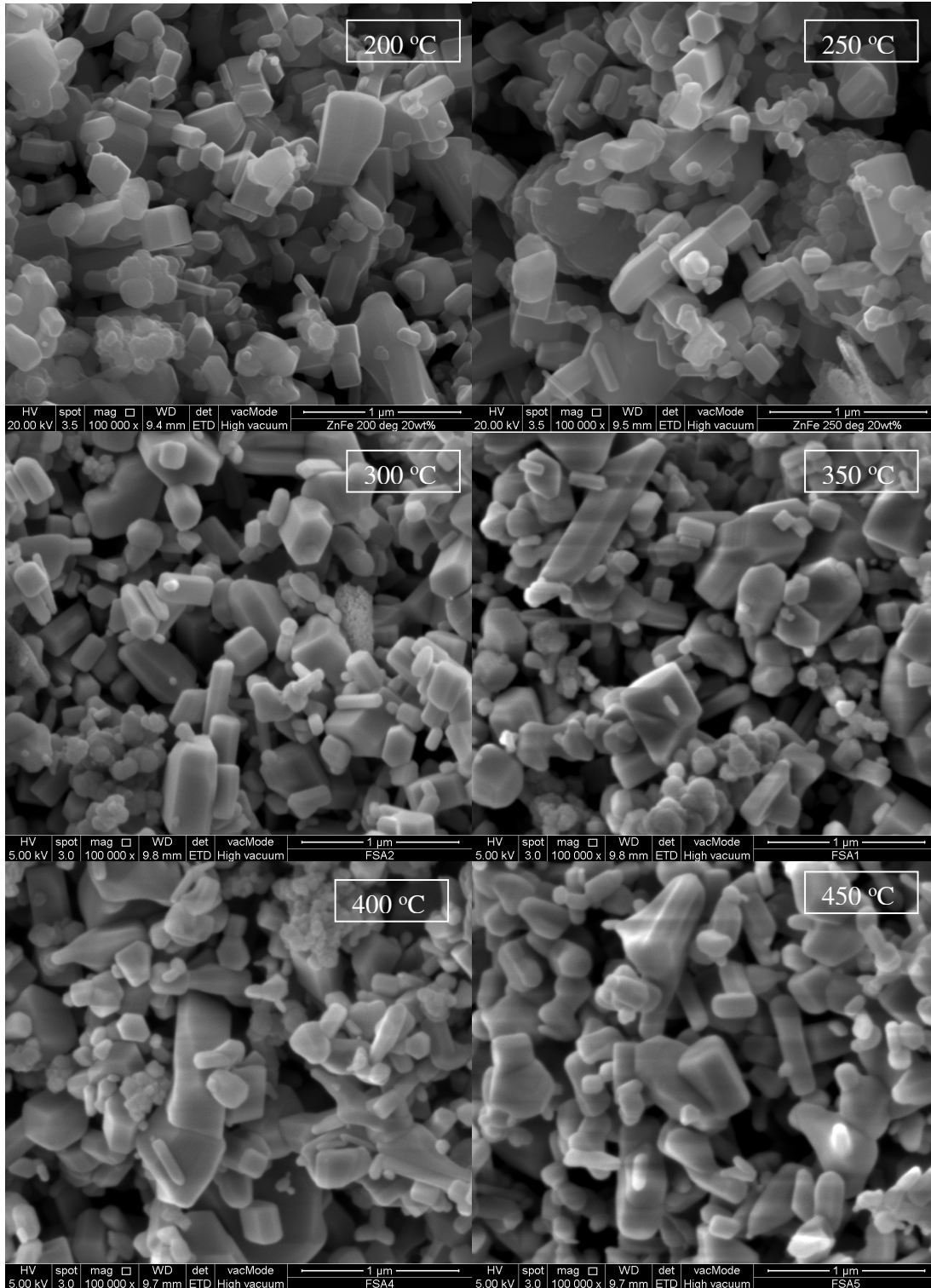


Figure 5.1: FESEM microstructures for 20 wt% doped Fe<sub>3</sub>O<sub>4</sub> of ZnO/Fe<sub>3</sub>O<sub>4</sub> nanocomposites with different sintering temperature (200, 250, 300, 350, 400 and 450 °C).

The X-ray powder diffraction patterns (XRD) of the prepared nanocomposites, sintered at different sintering temperatures, were depicted in Figure 5.2. All samples show peaks for (100), (002), (101), (102), (110), (103), (200), (112), (201), (004) and (202) planes of ZnO, and (220), (311), (400), (422), (511) and (440) planes of Fe<sub>3</sub>O<sub>4</sub> crystals, that agreed well with the hexagonal wurtzite phase for the ZnO (JCPDF Card No: 5-0664), and the cubic single phase structure for the Fe<sub>3</sub>O<sub>4</sub> (JCPDS Card No: 79-0417, Magnetite – synthetic). The intensities of all samples peaks were quite similar. Therefore, we can conclude that the crystal structures of the prepared nanocomposites were not affected by the sintering temperature, as no obvious changes on the crystallinity of the nanocomposites was observed.

The average crystallite size as calculated by using the Scherer equation are (83.5 ± 6.2) nm, (78.4 ± 4.8) nm, (121 ± 13) nm, (96.4 ± 5.8) nm, (83.6 ± 6.2) nm and (122 ± 21) nm, for the 200, 250, 300, 350, 400 and 450 °C sintering temperature, respectively. These results show that the sintering temperature has no significant effect on the average crystallite size of the nanocomposites. Current applied sintering temperature can be compared with a study when ZnO nanoparticles that was sintered at 700 °C shows very high porosity and variation of microstructure which is useful for photocatalytic reaction (Yassitepe, Yatmaz et al. 2008).

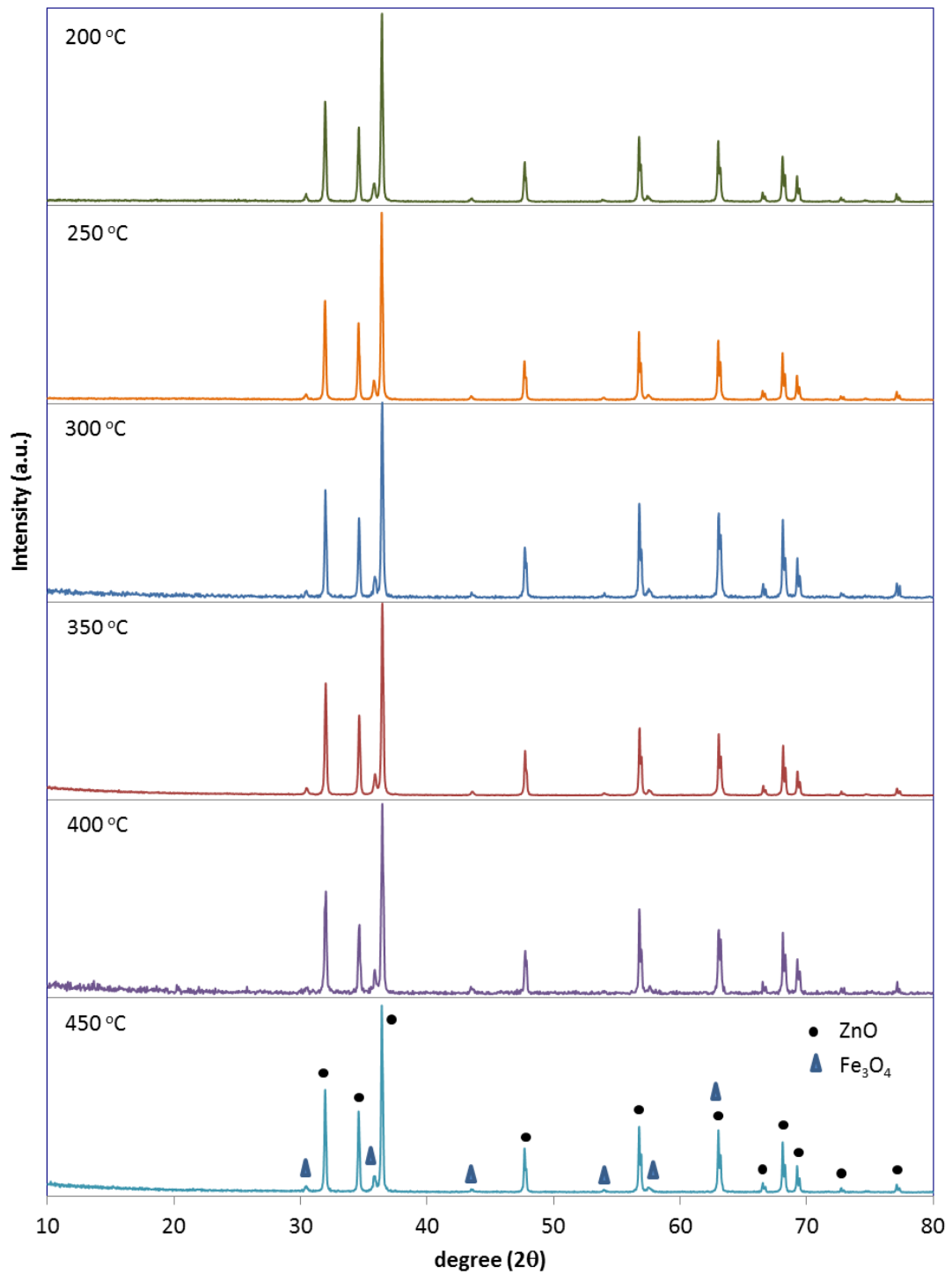


Figure 5.2: XRD for ZnO/Fe<sub>3</sub>O<sub>4</sub> nanocomposites with different sintering temperature (200, 250, 300, 350, 400 and 450 °C).

Table 5.1 shows the BET surface area and pore size for ZnO/Fe<sub>3</sub>O<sub>4</sub> nanocomposites with different sintering temperature. The results do not significantly reflect the effect of the sintering temperature since the values did not change much. This shows that the applied sintering temperature between 200 to 450 °C did not cause any changes in the microstructure of the nanocomposites. Therefore the BET was not affected by the applied sintering temperature where the values averages are between 1.9 to 2.6 m<sup>2</sup>/g.

Table 5.1: BET data for different sintering temperature for ZnO/Fe<sub>3</sub>O<sub>4</sub> nanocomposites

Sintering temperature (°C)	BET Surface Area (m <sup>2</sup> /g)	Pore Volume (cm <sup>3</sup> /g)	Average Pore Size (nm)
200	2.516	0.03164	40.68
250	2.613	0.02645	31.54
300	2.312	0.04053	50.99
350	2.787	0.02185	31.36
400	1.923	0.03524	73.30
450	2.417	0.01728	28.59

Figure 5.3 shows the Energy dispersive X-ray spectroscopy (EDX) spectrums for the ZnO/Fe<sub>3</sub>O<sub>4</sub> nanocomposites for different sintering temperature. All the spectrums show the nanocomposites possessed the precursor element used to prepare the ZnO/Fe<sub>3</sub>O<sub>4</sub> nanocomposites. On the

other hand, the suspected element C was coming from the carbon tape that was holding each of the nanocomposites (Su, Chiou et al. 2012). The weight percent (wt%) and the atomic percent (At%) for the elements is given in Table 5.2. As a summary, EDX measurement and the XRD analysis have successfully verified the purity of the prepared nanocomposites which exhibit single phase structure with high crystallinity form.

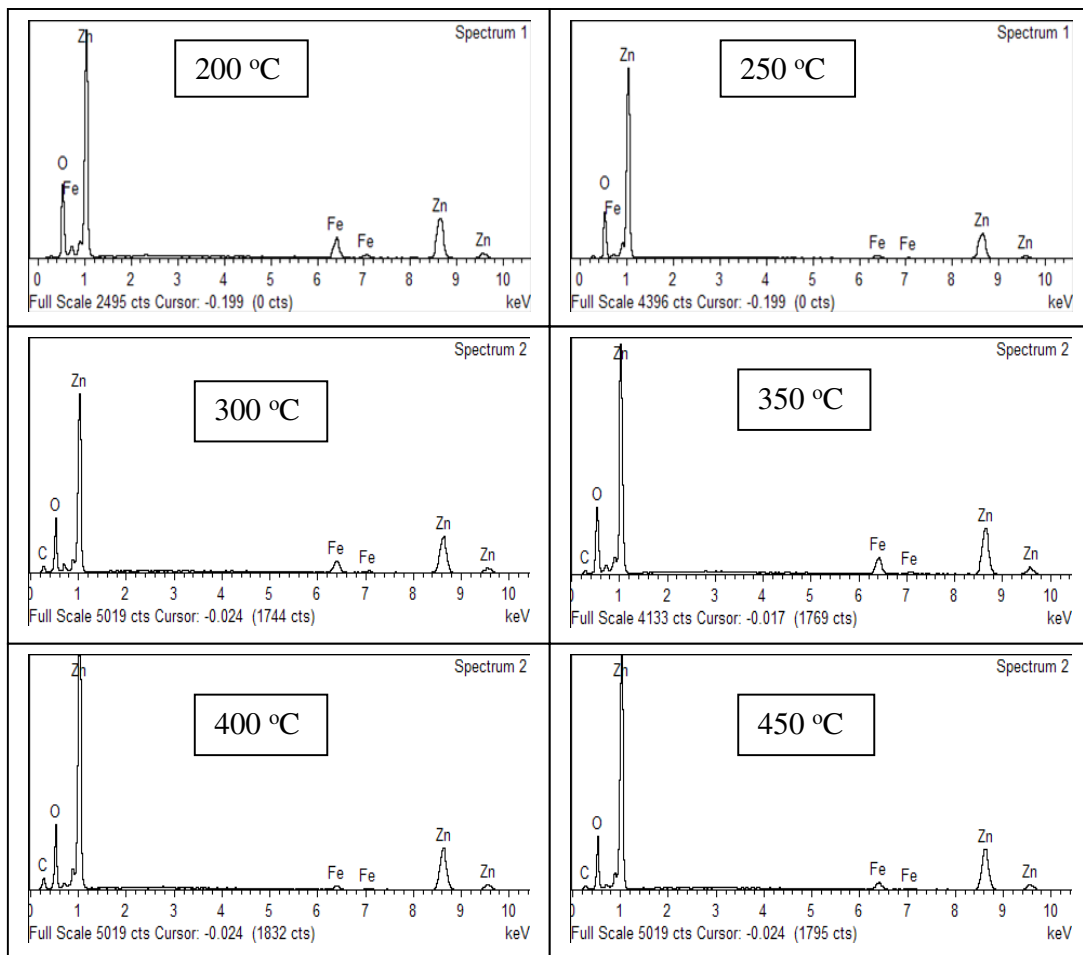


Figure 5.3: Energy dispersive X-ray spectroscopy (EDX) for different sintering temperature for ZnO/Fe<sub>3</sub>O<sub>4</sub> nanocomposites.

Table 5.2: EDX data for different sintering temperature for ZnO/Fe<sub>3</sub>O<sub>4</sub> nanocomposites

Sintering temperature (°C)	Element	Weight percentage (Wt%)	Atomic percentage (At%)
200	O	27.90	60.65
	Fe	10.90	6.79
	Zn	61.20	32.56
	Total	100.00	100.00
250	O	30.04	63.52
	Fe	3.10	1.88
	Zn	66.86	34.60
	Total	100.00	100.00
300	C	11.12	26.53
	O	25.14	45.03
	Fe	6.68	3.43
	Zn	57.06	25.01
	Total	100.00	100.00
350	C	5.31	14.45
	O	24.32	49.67
	Fe	8.31	4.87
	Zn	62.06	31.02
	Total	100.00	100.00

400	C	15.64	33.61
	O	27.06	43.65
	Fe	1.87	0.86
	Zn	55.43	21.88
	Total	100.00	100.00
450	C	7.76	20.14
	O	24.15	47.06
	Fe	3.88	2.17
	Zn	64.21	30.63
	Total	100.00	100.00

### 5.3.2 Different weight percent of Fe<sub>3</sub>O<sub>4</sub>

The doping of Fe<sub>3</sub>O<sub>4</sub> is to obtain magnetic properties possessed by the Fe<sub>3</sub>O<sub>4</sub> nanoparticles. However, the optimum amount of Fe<sub>3</sub>O<sub>4</sub> doped need to be measure to maintain the photocatalytic capability of the nanocomposite. The microstructures for the ZnO/Fe<sub>3</sub>O<sub>4</sub> nanocomposite samples with different weight percent (wt%) of Fe<sub>3</sub>O<sub>4</sub> are shown in Figure 5.4. As can be observed in the micrographs, it is clearly seen that there are mixture of two distinctively small and large particles with various size but fairly distributed throughout the samples. The shape of the small size particles are generally in spherical and slightly mixed with elongated structures, while the larger size particles are of cubic and rod shapes. Highly porous structures are also observed throughout all the samples.

The average particle size of the nanocomposites for 20, 15, 12, 10, 5 and 1 wt% of Fe<sub>3</sub>O<sub>4</sub>, as directly measured from the micrographs, are (140.2 ± 9.0) nm, (163 ± 10) nm, (156.3 ± 8.3) nm, (159 ± 12) nm, (171 ± 12) nm and (149.6 ± 8.5) nm, respectively. The number of smaller size particles were fairly distributed across all samples. In addition, it is good to mention that no agglomeration was spotted due to the addition of Fe<sub>3</sub>O<sub>4</sub> nanoparticles although smaller size particle tends to agglomerate. Therefore, the micrographs showed that when Fe<sub>3</sub>O<sub>4</sub> nanoparticles were introduced into the ZnO nanopowder, they were well mixed and evenly distributed throughout the whole sample.

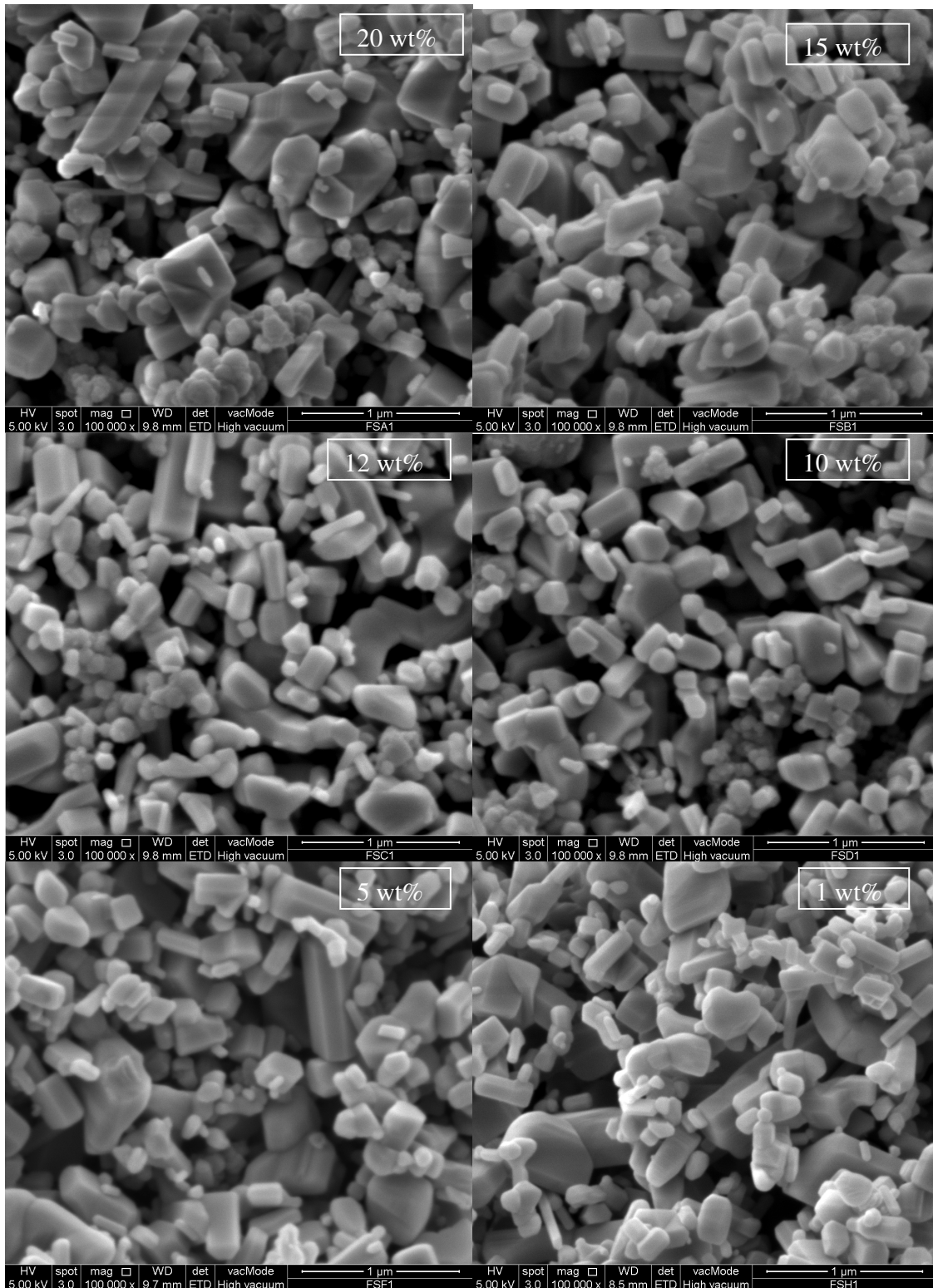


Figure 5.4: FESEM microstructures for ZnO/Fe<sub>3</sub>O<sub>4</sub> nanocomposites with different wt% of Fe<sub>3</sub>O<sub>4</sub> (20, 15, 12, 10, 5 and 1wt%).

Figure 5.5 is the X-ray diffraction (XRD) patterns for the prepared ZnO/Fe<sub>3</sub>O<sub>4</sub> nanocomposites with different weight percent (wt%) of Fe<sub>3</sub>O<sub>4</sub> nanoparticles. It clearly indicates the existence of the ZnO and Fe<sub>3</sub>O<sub>4</sub> nanoparticles. The pattern revealed the characteristic peaks for (100), (002), (101), (102), (110), (103), (200), (112), (201), (004) and (202) planes of ZnO, and (220), (311), (400), (422), (511) and (440) planes of Fe<sub>3</sub>O<sub>4</sub> crystals. All peaks can be indexed to the wurtzite crystal structure according to the standard JCPDF Card No. (5-0664), which represents ZnO nanoparticles, and cubic single phase structure according to the standard pattern for JCPDS Card No. (79-0417) of Magnetite – synthetic, which represents nano size Fe<sub>3</sub>O<sub>4</sub> nanoparticles (Saikia, Bhuyan et al. 2015).

From the diagrams, it can be seen that all samples have almost similar prominent peaks, which indicates that the prepared samples were well mixed and retained their crystal structure. However, the peaks of cubic single phase for Fe<sub>3</sub>O<sub>4</sub> were not significant and cannot be observed for certain samples with low doping of Fe<sub>3</sub>O<sub>4</sub> nanoparticle, especially for the 5wt% and 1wt% samples. This might be due to a very minute amount of doped Fe<sub>3</sub>O<sub>4</sub> nanoparticle; therefore the appearance of the Fe<sub>3</sub>O<sub>4</sub> crystalline phase structure was not significant or obvious to be detectable by the instrument as a result of hindrances by the ZnO nanoparticles. These basically explained that we were able to mix the ZnO and Fe<sub>3</sub>O<sub>4</sub> nanoparticles by simple mechanical mixing and sintering at low temperature.

The average crystallite size as calculated by using the Scherer equation are  $(121 \pm 13)$  nm,  $(116 \pm 15)$  nm,  $(116 \pm 15)$  nm,  $(137 \pm 15)$  nm,  $(110 \pm 14)$  nm and  $(150 \pm 13)$  nm, for the 20, 15, 12, 10, 5 and 1 wt% of doped Fe<sub>3</sub>O<sub>4</sub> nanocomposite sample, respectively.

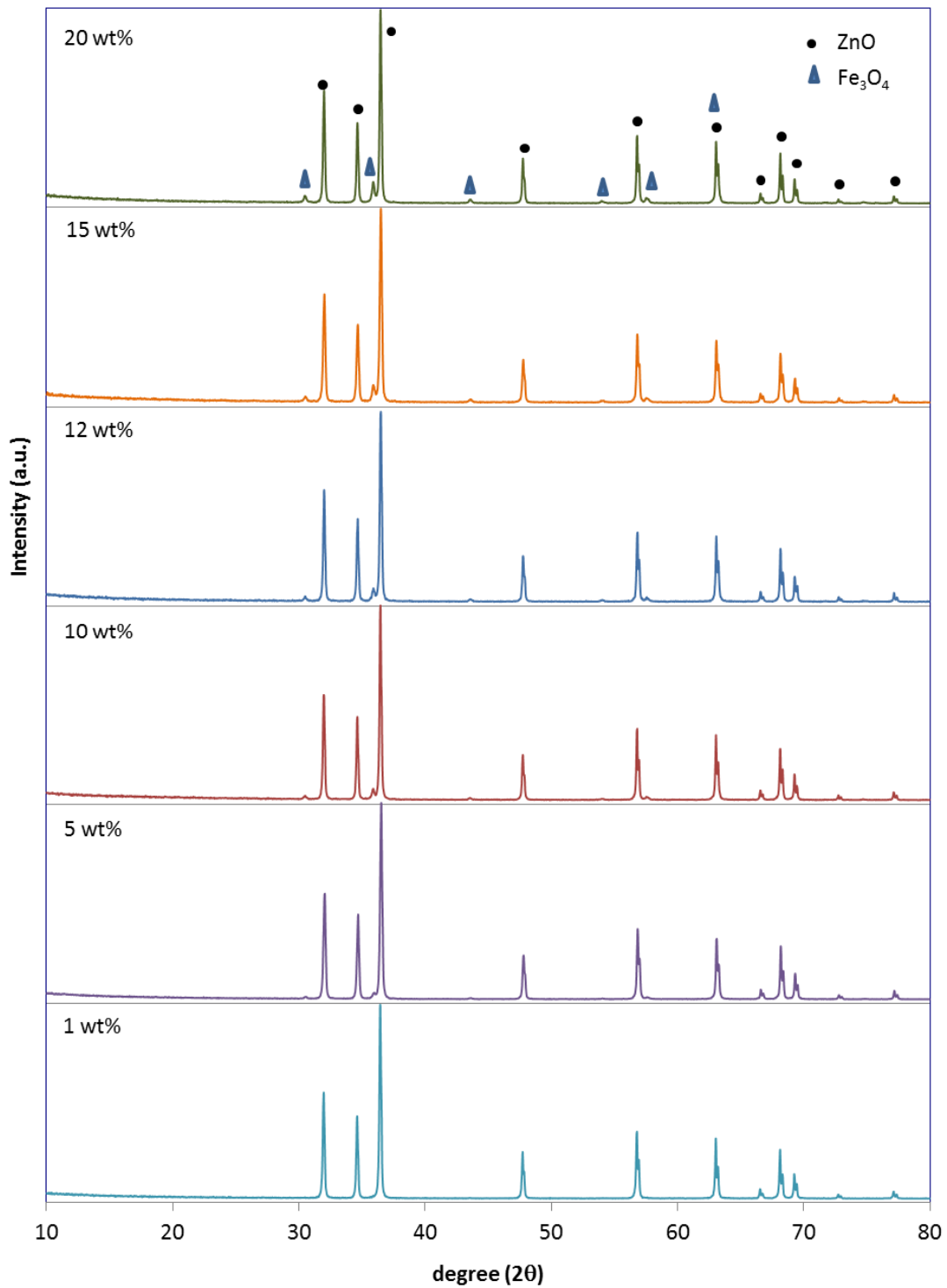


Figure 5.5: XRD for ZnO/Fe<sub>3</sub>O<sub>4</sub> nanocomposites with different wt% of Fe<sub>3</sub>O<sub>4</sub> (20, 15, 12, 10, 5 and 1wt%) sintered at 300 °C.

Table 5.2 shows the BET surface area and pore size of all the nanocomposites samples with different wt% of Fe<sub>3</sub>O<sub>4</sub>. There are no significant changes in the BET surface area as compared to undoped ZnO nanoparticles even when the amount of Fe<sub>3</sub>O<sub>4</sub> doped was 20 wt%, except for the 10 and 1 wt% samples. Nonetheless, the pore volume and average pore size for the nanocomposites samples have increased as compared to the undoped ZnO nanoparticles. Therefore, with the increase of these pores would certainly assist in the photocatalytic process, although there is not much changes in their BET surface area.

Table 5.2: BET data for different wt% of Fe<sub>3</sub>O<sub>4</sub> for ZnO/Fe<sub>3</sub>O<sub>4</sub> nanocomposites

Weight percent of Fe <sub>3</sub> O <sub>4</sub> (wt%)	BET Surface Area (m <sup>2</sup> /g)	Pore Volume (cm <sup>3</sup> /g)	Average Pore Size (nm)
20	2.787	0.02185	31.36
15	2.573	0.01736	26.99
12	2.849	0.02052	28.82
10	1.676	0.00948	22.62
5	2.700	0.01545	22.89
1	0.8844	0.01333	60.28

Energy dispersive X-ray spectroscopy (EDX) spectrums for all different wt% of  $\text{Fe}_3\text{O}_4$  samples are shown in Figure 5.6. All spectrums show the elemental mapping of the prepared nanocomposites, which includes the presence of O, Zn and Fe. The weight percent (wt%) and the atomic percent (At%) for the elements is given in Table 5.4. The EDX measurement and the XRD analysis have verified the purity of the prepared nanocomposites.

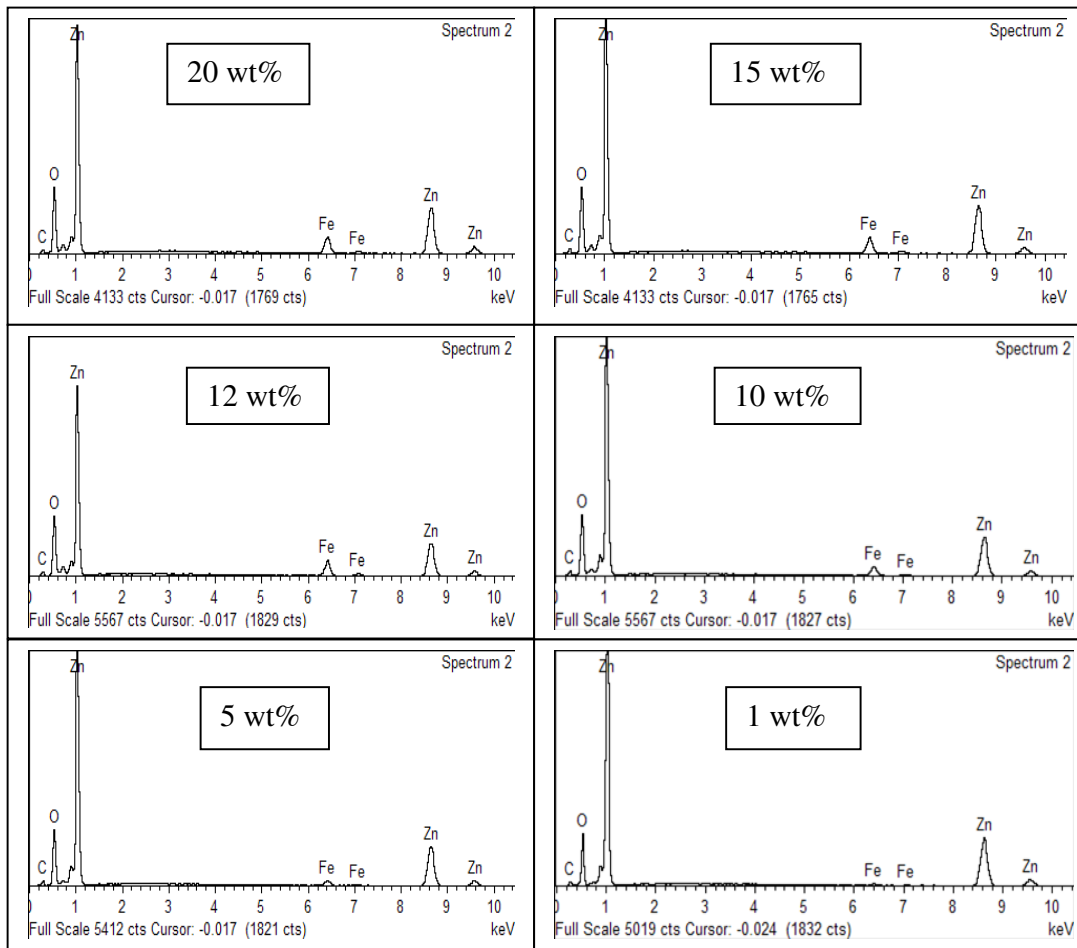


Figure 5.6: Energy dispersive X-ray spectroscopy (EDX) for different wt% of  $\text{Fe}_3\text{O}_4$  for ZnO/ $\text{Fe}_3\text{O}_4$  nanocomposites.

Table 5.4: EDX data for different wt% of Fe<sub>3</sub>O<sub>4</sub> for ZnO/Fe<sub>3</sub>O<sub>4</sub> nanocomposites

Weight percentage (wt%) of doped Fe <sub>3</sub> O <sub>4</sub>	Element	Weight percentage (wt%)	Atomic percentage (At%)
20	C	5.31	14.44
	O	24.32	49.67
	Fe	8.31	4.87
	Zn	62.06	31.02
	Total	100.00	100.00
15	C	6.93	18.22
	O	24.27	47.92
	Fe	7.46	4.22
	Zn	61.34	29.64
	Total	100.00	100.00
12	C	7.64	18.91
	O	27.36	50.82
	Fe	9.30	4.95
	Zn	55.70	25.32
	Total	100.00	100.00

10	C	7.62	18.94
	O	27.25	50.89
	Fe	5.24	2.81
	Zn	59.89	27.36
	Total	100.00	100.00
5	C	8.04	20.24
	O	25.93	49.01
	Fe	2.64	1.43
	Zn	63.39	29.32
	Total	100.00	100.00
1	C	7.01	18.78
	O	23.33	46.88
	Fe	0.87	0.50
	Zn	68.79	33.84
	Total	100.00	100.00

### 5.3.3 Transmission Electron Microscopy (TEM)

Figure 5.7 shows the transmission electron microscopy (TEM) image and histogram for the 10 wt% doped Fe<sub>3</sub>O<sub>4</sub> sintered at 300 °C for the ZnO/Fe<sub>3</sub>O<sub>4</sub> nanocomposites. The micrograph indicates the nanocomposite was well dispersed without any agglomeration. The nanocomposites were irregular in shape with cubic and some elongated microstructure. It presents a wide range of particle size distribution with an average particle size of (162 ± 12) nm. The size distribution histogram shows the details of the size distribution which was obtained from the direct measurement from the TEM micrograph. The average particle size was slightly different from the crystallite size obtained from the XRD. Nevertheless the size is quite similar to the size measured from the FESEM micrographs.

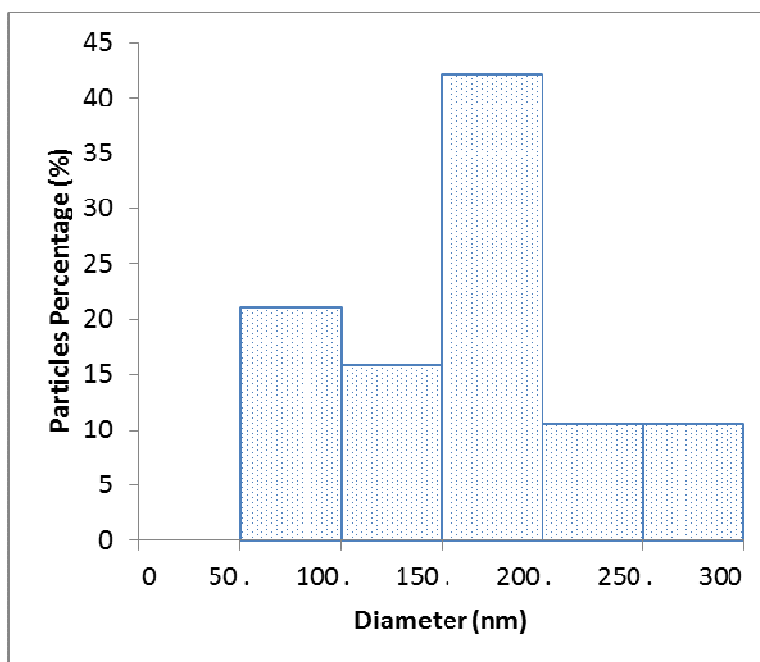
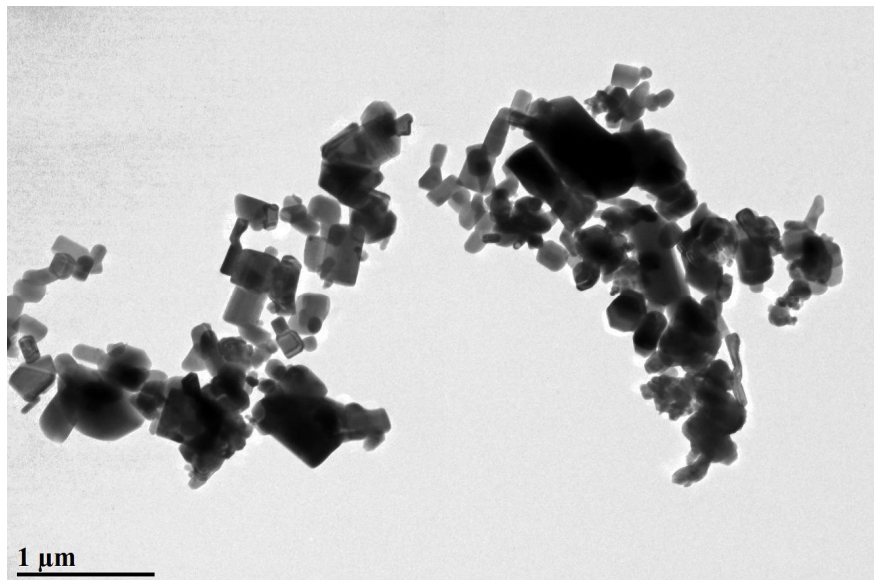


Figure 5.7: TEM micrograph and Particle size distribution histogram for 10 wt% doped Fe<sub>3</sub>O<sub>4</sub> of ZnO/Fe<sub>3</sub>O<sub>4</sub> nanocomposites.

#### *5.3.4 Photocatalytic analysis for Different Loading of ZnO/Fe<sub>3</sub>O<sub>4</sub>*

The photocatalytic performance of the 20 wt% doped Fe<sub>3</sub>O<sub>4</sub> sintered at 300 °C of ZnO/Fe<sub>3</sub>O<sub>4</sub> nanocomposite was evaluated by the degradation of MB under the UV light illumination. The photocatalytic study was first performed to determine the most optimum amount of the photocatalyst loading, by fixing other variables to constant. The sample solutions were prepared with the loading from 1.0 to 10.0 wt% of ZnO/Fe<sub>3</sub>O<sub>4</sub> nanocomposites. All mixed samples were then stored in dark for about 30 minutes before transferred into the ultraviolet chamber. An aliquot were collected from each samples at an interval of 10 minutes to observe the degradation effects.

The decomposition results for various photocatalyst loading with ZnO/Fe<sub>3</sub>O<sub>4</sub> nanocomposites sintered at 300 °C is presented in Figure 5.8. MB without the presence of photocatalyst was degraded at a very slow rate, achieving merely 17% of degradation after 30 minutes of illumination. On the other hand, samples with photocatalyst show significant degradation for similar irradiation duration. For photocatalytic process to take place, there have to be sufficient photon energy arriving on the photocatalytic surface. This leads to the formation of a positive hole (h<sup>+</sup>) in the valence band and an electron (e<sup>-</sup>) in the conduction band. The positive hole could either oxidise the organic substances or produce very reactive OH• radicals. The OH• radicals act as the primary oxidants in the photocatalytic system [Ahmed, S. et al., 2010]. Therefore, higher photocatalyst loading provides higher

degradation rate. As for 1.0 and 2.0 wt% of the catalysts, the percentage degradation were lower than other samples. For samples with 6.0 to 10.0 wt% catalyst, the percentage degradations were close to each other and able to degrade more than 60% of MB in 10 minutes. Comparatively, samples with 1.0 and 2.0 wt% catalyst only able to achieve degradation less than 50% after 10 minutes of irradiation. It is well-understood since lower content of photocatalyst material shall have less reactive sites for photodecomposition process, subsequently leads to lower degradation rate.

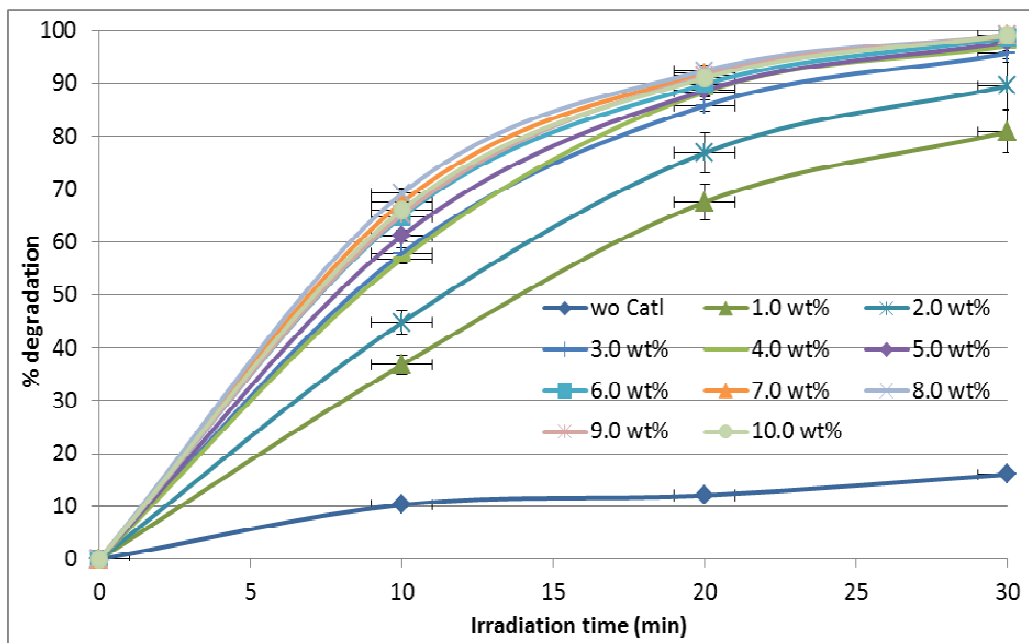


Figure 5.8: Percentage degradation of MB by different loading of ZnO/Fe<sub>3</sub>O<sub>4</sub> nanocomposites.

The rate of the degradation could be explained more clearly as in Figure 5.9. It shows that the photocatalytic degradation of MB follows pseudo-first-order kinetics according to Langmuir-Hinshelwood (LH) model,

where the photocatalytic reaction can be described by  $\ln(C_0/C) = kt$ , where  $C_0$  and  $C$  are the initial and actual concentration of MB and  $k$  is the degradation rate parameter.

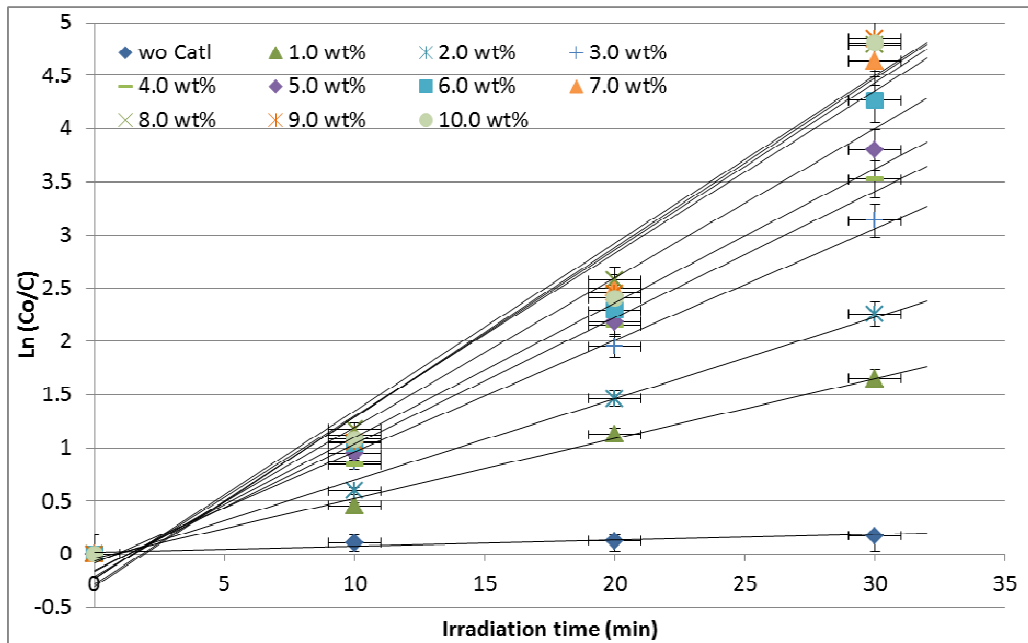


Figure 5.9: Degradation rate for MB by different loading of ZnO/Fe<sub>3</sub>O<sub>4</sub> nanocomposites.

As can be seen in Figure 5.10, the degradation rate is found to increase with the catalyst loading. It is definite that the degradation without catalyst was the lowest, with the rate of  $0.0054 \text{ min}^{-1}$ . The value is then increased from  $0.0563 \text{ min}^{-1}$  for 1.0 wt% to  $0.1593 \text{ min}^{-1}$  for 9.0 wt%. The degradation rate dropped slightly for the sample with 10.0 wt% catalyst to  $0.1574 \text{ min}^{-1}$ . The dropped in photodegradation rate could be due to the opacity of the solution with high concentration of photocatalyst material, which decrease the light absorption and subsequently affect the

photocatalytic process (Han, Wang et al. 2012). Figure 5.10 clearly shows an inclination in the degradation rate as the amount of the photocatalyst loading increased. The increased in the photocatalytic process was due to the increase of the surface area, therefore increases the active sites availability (Han, Liao et al. 2012). These results conclude that sample with 9.0 wt% photocatalyst loading is the optimum loading for the photodegradation process.

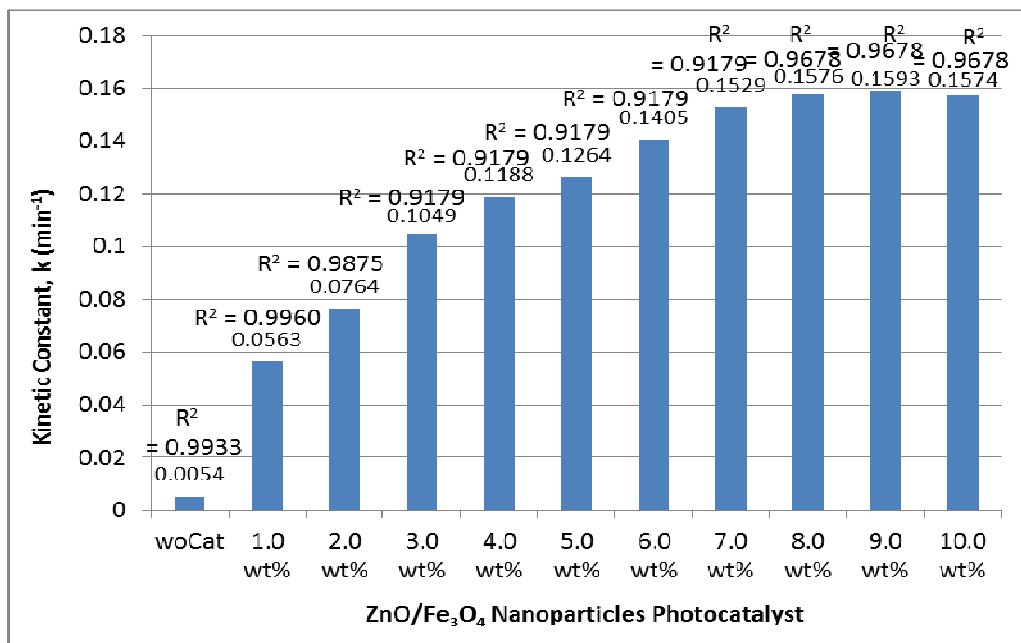


Figure 5.10: Degradation rate of MB by different loading of ZnO/Fe<sub>3</sub>O<sub>4</sub> nanocomposites.

### 5.3.5 Photocatalytic Study on the Effect of Sintering Temperature with ZnO/Fe<sub>3</sub>O<sub>4</sub> Nanocomposite Material

Figure 5.11 shows the effect of sintering temperature on the 20 wt% doped Fe<sub>3</sub>O<sub>4</sub> of ZnO/Fe<sub>3</sub>O<sub>4</sub> nanocomposite material. The dark adsorption is insignificant (less than 5%). The degradation started to take place for all samples within the first 10 minutes of irradiation, as shown in Figure 5.11. As the irradiation time was increased to 20 minutes, the degradation has achieved more than 85% for all samples. From the result, almost 100% degradation was achieved for all samples at the end of 30 minutes. These results indicate that the sintering treatment did not perturb the stability and significantly change the photodegradation capability of the nanocomposites.

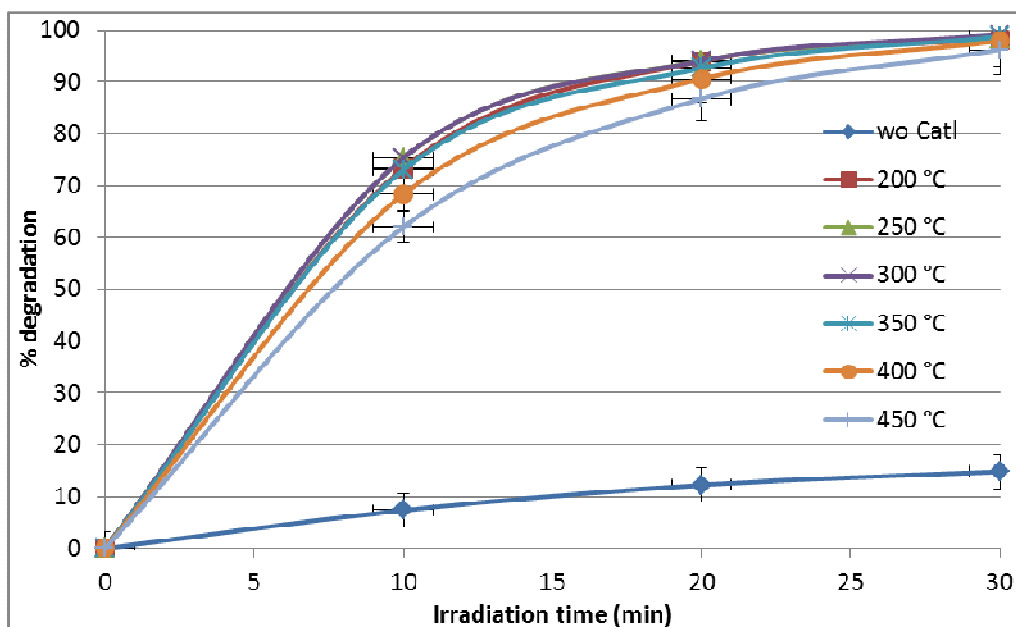


Figure 5.11: Percentage degradation of MB for 20 wt% doped Fe<sub>3</sub>O<sub>4</sub> of ZnO/Fe<sub>3</sub>O<sub>4</sub> nanocomposites with different sintering temperatures.

Based on the kinetic analysis as shown in Figure 5.12, all samples fit nicely to the pseudo-first-order kinetics of the LH model. It is clear that the highest degradation rate is recorded for the nanocomposite samples sintered at 300 °C. This result could be due to its highest pore volume and one of the highest pore size amongst all samples sintered at different temperature, as recorded in Table 5.1, albeit the BET surface area is slightly lower than most of the samples.

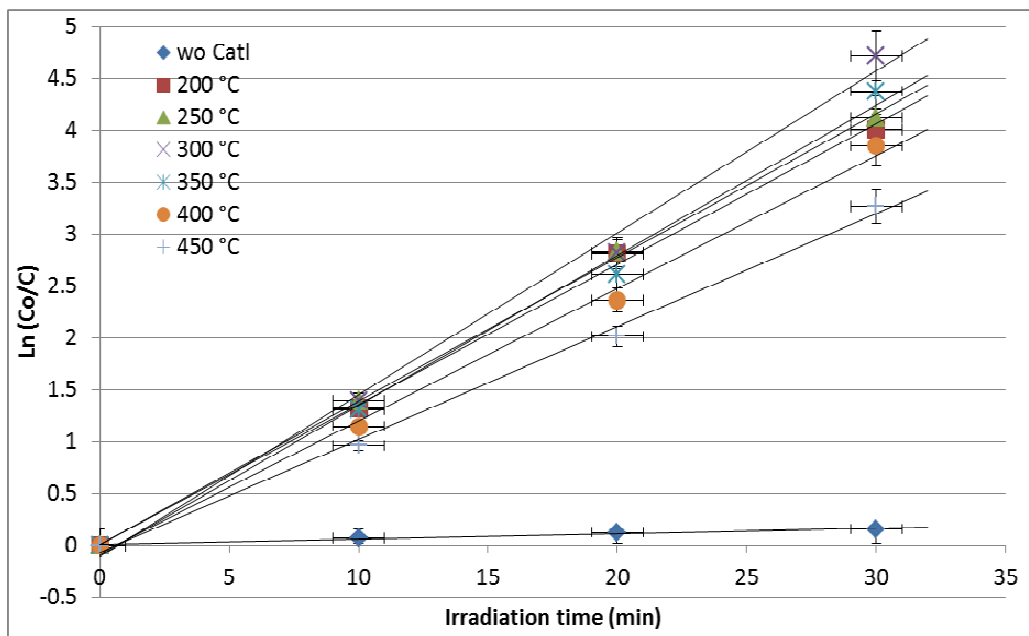


Figure 5.12: First-order kinetics for the degradation of MB with different sintering temperature for ZnO/Fe<sub>3</sub>O<sub>4</sub> nanocomposites.

From Figure 5.13, samples with 400 and 450 °C sintering temperatures were among the lowest degradation rates, with 0.1277 and 0.1087 min<sup>-1</sup>, respectively. For the sample sintered at 400 °C, its pore size and pore

volumes were amongst the highest with 73.30 nm and 0.03524 cm<sup>3</sup>/g, respectively, as compared to the other samples. However, its BET surface area was the lowest, only 1.923 m<sup>2</sup>/g. This could be the possible contribution to the lower degradation rate. On the other hand, for sample sintered at 450 °C, albeit its BET surface area was quite similar to other high degradation samples, however its pore volume and pore size were amongst the lowest with 0.01728 cm<sup>3</sup>/g and 28.59 nm, respectively.

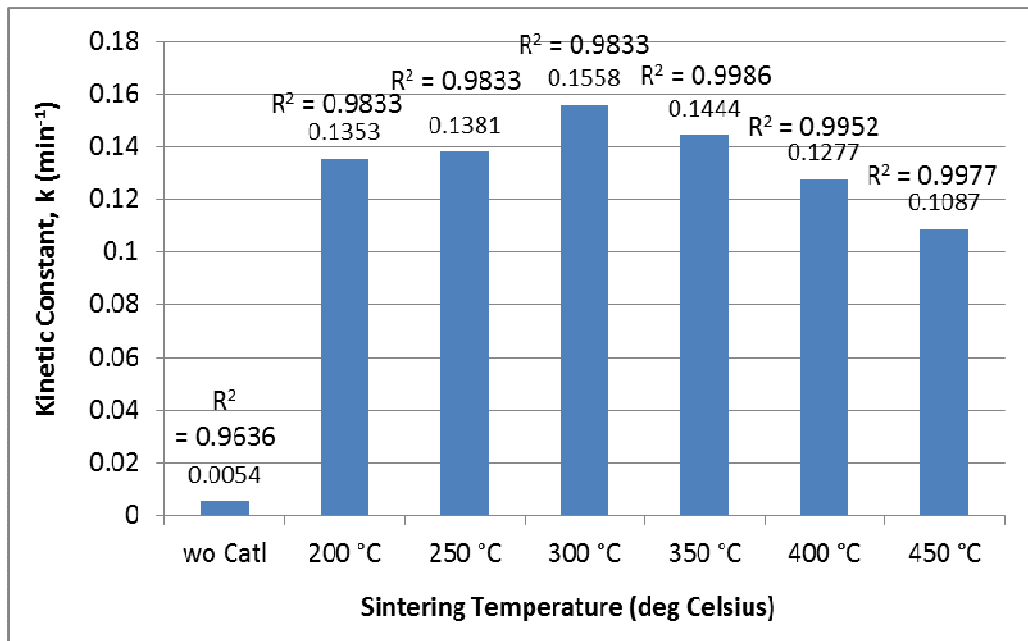


Figure 5.13: Kinetic constant for ZnO/Fe<sub>3</sub>O<sub>4</sub> samples with different sintering temperature.

### *5.3.6 Photocatalytic Study on the Effect of Different wt% Fe<sub>3</sub>O<sub>4</sub> Doped into the Nanocomposite Material*

Figure 5.14 shows the photocatalytic study of the nanocomposite materials with different Fe<sub>3</sub>O<sub>4</sub> doping. The result shows that all samples with photocatalysts were active and able to degrade MB in just 30 minutes of irradiation. The graphs show all samples able to degrade more than 90% of organic dye in just 20 minutes. The results clearly show that irrespective of the amount of the Fe<sub>3</sub>O<sub>4</sub> that was doped into the ZnO nanoparticles, the degradation process took place significantly and able to degrade the dye solution effectively. Nevertheless, this clearly explained that ZnO/Fe<sub>3</sub>O<sub>4</sub> nanocomposites photocatalyst is still showing promising photocatalytic capability while possessing additional feature – the magnetic characteristic. There is another study on iron doped photocatalyst, which was also reported to possess significant degradation capability while carrying the magnetic feature.

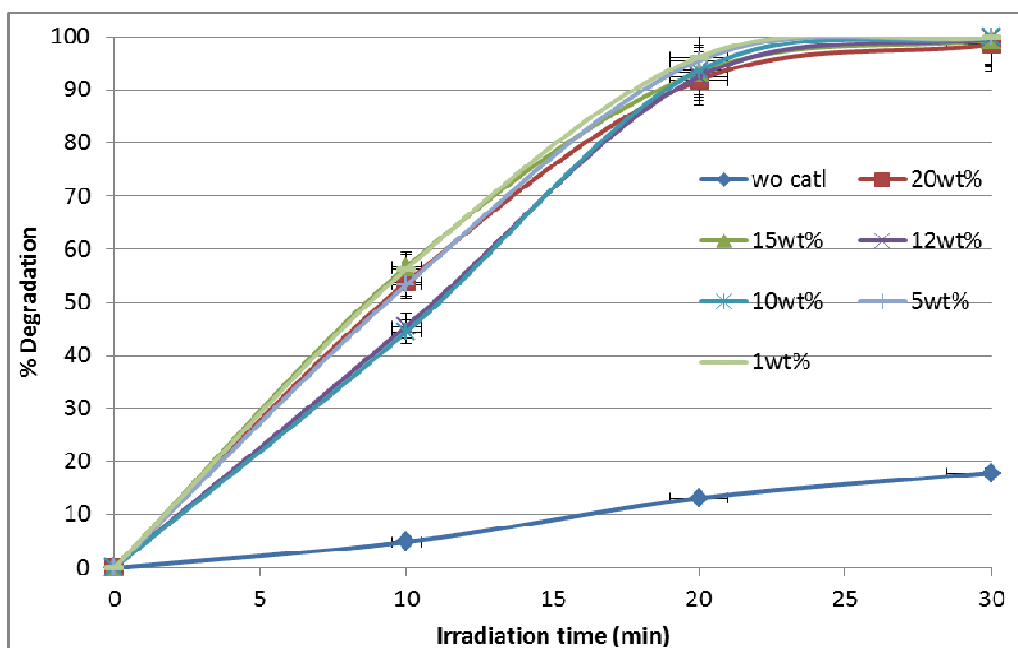


Figure 5.14: Percentage degradation of MB for samples with different wt% of  $\text{Fe}_3\text{O}_4$  doped into  $\text{ZnO}/\text{Fe}_3\text{O}_4$  nanocomposite

As can be seen from Figure 5.15, the lowest degradation rates amongst all  $\text{Fe}_3\text{O}_4$  doped samples were the highest  $\text{Fe}_3\text{O}_4$  doped nanocomposite material (12 wt% to 20 wt%). On the other hand, the samples with  $\text{Fe}_3\text{O}_4$  doped of 1 wt% to 10 wt% are found to have quite similar degradation rates and are the highest among all the nanocomposites samples. This showed that the photocatalytic capability of the  $\text{ZnO}$  nanoparticle was not affected when small amount of  $\text{Fe}_3\text{O}_4$  nanoparticles are doped into the samples (Bhukal, Shivali et al. 2014). This could be explained that the incorporation  $\text{Fe}_3\text{O}_4$  nanoparticle is in the optimum level and has not overloaded that can hinder the reactive surface of the  $\text{ZnO}$  nanoparticle, which is essential for the photocatalytic process to take place. A similar

study was also reported where the degradation rate decreases with the increased of the  $\text{Fe}_3\text{O}_4$  added (Bhukal, Shivali et al. 2014).

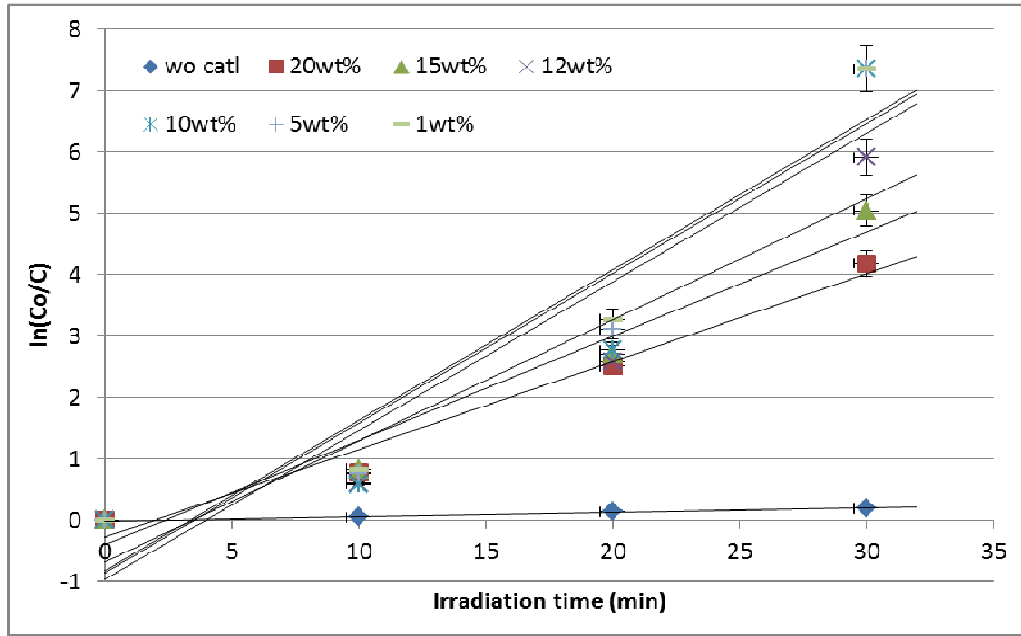


Figure 5.15: Degradation rate of MB for samples with different wt% of  $\text{Fe}_3\text{O}_4$  doped into  $\text{ZnO}/\text{Fe}_3\text{O}_4$  nanocomposites.

The values for kinetic constants  $k$ , are depicted in Figure 5.16. Results show that similar kinetic constant value was achieved for 1 wt%, 5 wt% and 10 wt%  $\text{Fe}_3\text{O}_4$  doped nanocomposite samples. From the results, we can also conclude that the photocatalytic efficiency is still maintained at the optimum level until 10 wt% doped of  $\text{Fe}_3\text{O}_4$  nanoparticle, in which beyond the optimum doping, the  $k$  value is significantly dropped from 0.1973 to 0.1430  $\text{min}^{-1}$  for the 12 to 20 wt% of  $\text{Fe}_3\text{O}_4$  doped nanocomposite material, respectively.

Therefore, we can conclude that by doping iron oxide ( $\text{Fe}_3\text{O}_4$ ) to ZnO nanoparticle, the photocatalytic efficiency is maintained while the new magnetic characteristic can be incorporated to the catalyst effectively. However, the photocatalytic efficiency dropped significantly when more than 10 wt%  $\text{Fe}_3\text{O}_4$  nanoparticle was doped into the nanocomposite material. This could be due to the significant hindrances of the active surface area on the ZnO nanoparticle by the high content of  $\text{Fe}_3\text{O}_4$  nanoparticle at high level of doping, consequently decreasing the reactive sites for the photocatalytic process to take place (Han, Liao et al. 2012).

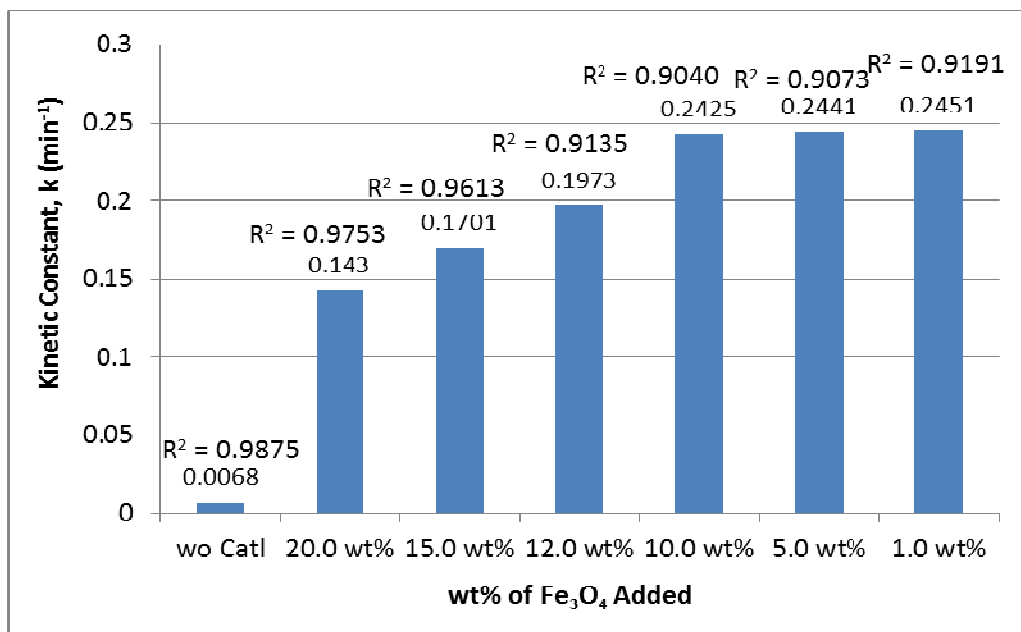


Figure 5.16: Kinetic constant for ZnO/ $\text{Fe}_3\text{O}_4$  samples with different wt% of doped  $\text{Fe}_3\text{O}_4$  nanoparticles

### 5.3.7 Vibrating Sample Magnetometry Analysis (VSM)

Figure 5.17 shows room temperature magnetization curves as a function of magnetic field for ZnO and ZnO/Fe<sub>3</sub>O<sub>4</sub> nanocomposite. It is very obvious that ZnO nanoparticle do not exhibit any obvious magnetic properties, which is diamagnetic in characteristic, whereas for 10 wt% doped Fe<sub>3</sub>O<sub>4</sub> sintered at 300 °C of ZnO/Fe<sub>3</sub>O<sub>4</sub> nanocomposite it shows an obvious magnetic hysteresis loops with ferromagnetic feature, soft ferromagnetic characteristic. These features were agreeable with Dutta and his co-researchers (2009) finding on different ZnO materials; chemically prepared ZnO, with and without calcine at 550 °C, ball milled ZnO and as received ZnO. They obtained significant finding where the ZnO sample calcined at 550 °C shows room temperature ferromagnetism, whereas none calcined shows paramagnetic behaviour, and on the other hand, the ball milled ZnO shows an even more pronounced diamagnetism [Dutta et al., 2009]. There were minimal coercivity exhibited by the samples and magnetic moments are induced in the presence of magnetic field. The ZnO/Fe<sub>3</sub>O<sub>4</sub> nanocomposite shows high susceptibility therefore easily magnetised, where magnetic field of 1088 Oe is sufficient to induce 84% of the total magnetization. The saturation magnetization for the ZnO/Fe<sub>3</sub>O<sub>4</sub> nanocomposite was 6.124 emu/g.

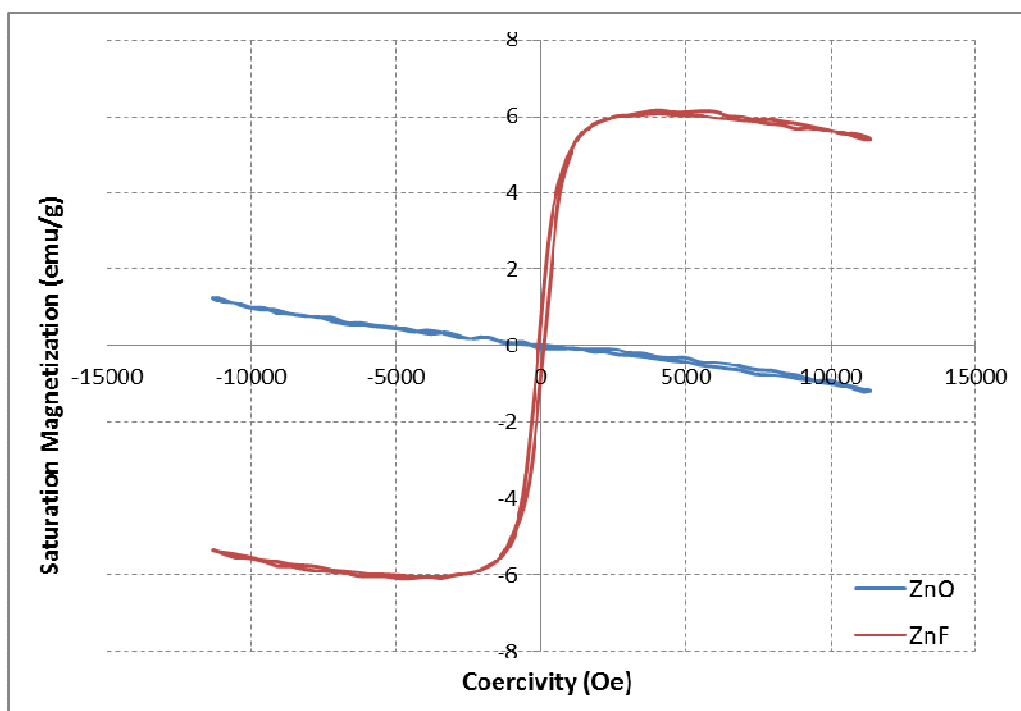


Figure 5.17: Hysteresis loop for ZnO and 10 wt% doped  $\text{Fe}_3\text{O}_4$  sintered at 300 °C of ZnO/ $\text{Fe}_3\text{O}_4$  (ZnF) nanoparticles.

### 5.3.8 Magnetic Separation

As indicated at the beginning of this study, one of the objectives is to produce a comparatively good photocatalyst that able to degrade organic dyes, as well as possessing magnetic feature which then can separate the photocatalyst from the solution in a much simpler manner. Besides environmentally friendly, it is also cost efficient. Such photocatalyst shall hold great potential to be utilised for large scale water treatment system.

From Figure 5.18, it shows the effect of the magnetically induced separation of ZnO/Fe<sub>3</sub>O<sub>4</sub> nanocomposites by exploiting their magnetic property. A total of 9.0 wt% loading of ZnO/Fe<sub>3</sub>O<sub>4</sub> nanocomposites was dispersed in treated solution and the dispersion appears to be brownish in color due to the formation of a suspension (before separation). Upon placing the vial near to a magnet with a magnetic field strength of 0.6 T, the progressive separation of a colloidal suspension is observed. The effect of the magnetically induced separation is clearly visible, where a brownish mass within the proximity of the vial wall, is attracted toward the magnet. Subsequently, the turbidity of the solution due to the colloidal suspension becomes increasingly discoloured and finally becomes clear. The suspension is attracted toward the wall of the vial that is closer to the magnet, which implies the complete physical separation. The ease in separation of ZnO/Fe<sub>3</sub>O<sub>4</sub> nanocomposites is attributed to the high magnetic susceptibilities of the Fe<sub>3</sub>O<sub>4</sub> doped in the ZnO/Fe<sub>3</sub>O<sub>4</sub> nanocomposites. Upon removal of the magnetic field, the colloidal ZnO/Fe<sub>3</sub>O<sub>4</sub> nanocomposites remain dispersible and no irreversible agglomeration occurred. This indicates that this ZnO/Fe<sub>3</sub>O<sub>4</sub> nanocomposites is suitable for the magnetically-separable photocatalytic application.

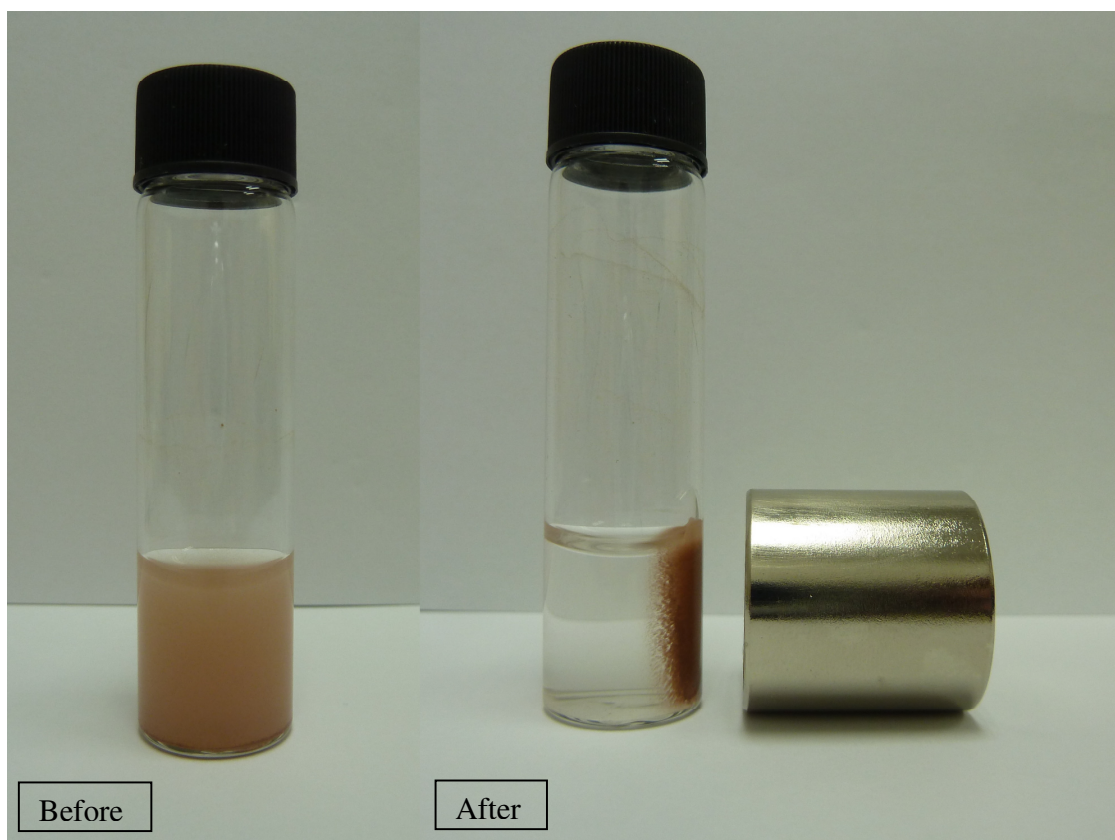


Figure 5.18: Separation of ZnO/Fe<sub>3</sub>O<sub>4</sub> nanocomposites in degraded MB dye solution by applying a magnetic field with a 0.6 T magnet.

### 5.3.9 Repeatability Analysis

In elucidating the stability of the ZnO/Fe<sub>3</sub>O<sub>4</sub> nanocomposites photocatalytic activity, the repeatability analysis was performed under the similar experimental conditions. The recyclability experiment for the nanocomposites photocatalyst is very important to determine the stability of the photocatalyst and the long term use in practical application. After completing the photodecomposition for the first run, the same

nanocomposite was retrieved using external magnetic field and reused for the following analysis, up to three runs. Based on the results, as seen in Figure 5.19, no significant changes appear in degradation efficiency, as only slight deterioration was recorded throughout the analysis. As for the first run, the percentage degradation of the MB dye achieved was 97.18%. On the second run, the percentage degradation dropped by 1.08% as compared to the first run. Nonetheless, in the third run, the photodecomposition of the organic dye by the nanocomposites is 97.33%, which is slightly more by 0.17% than that of the first run.

The dropped in efficiency might be due to the deactivation of the ZnO/Fe<sub>3</sub>O<sub>4</sub> nanocomposites caused by the absorption of the organic dye molecules on the surface of the ZnO/Fe<sub>3</sub>O<sub>4</sub> nanocomposites. Thus, the electron transfer processes is perturbed during the photocatalytic process between nanocomposite surface and water molecules and suppress the hydroxyl radicals formation. This deactivation is due to the memory effect on the ZnO/Fe<sub>3</sub>O<sub>4</sub> nanocomposites surface which has been occupied by the earlier remnant of the organic dye (Yassitepe, Yatmaz et al. 2008).

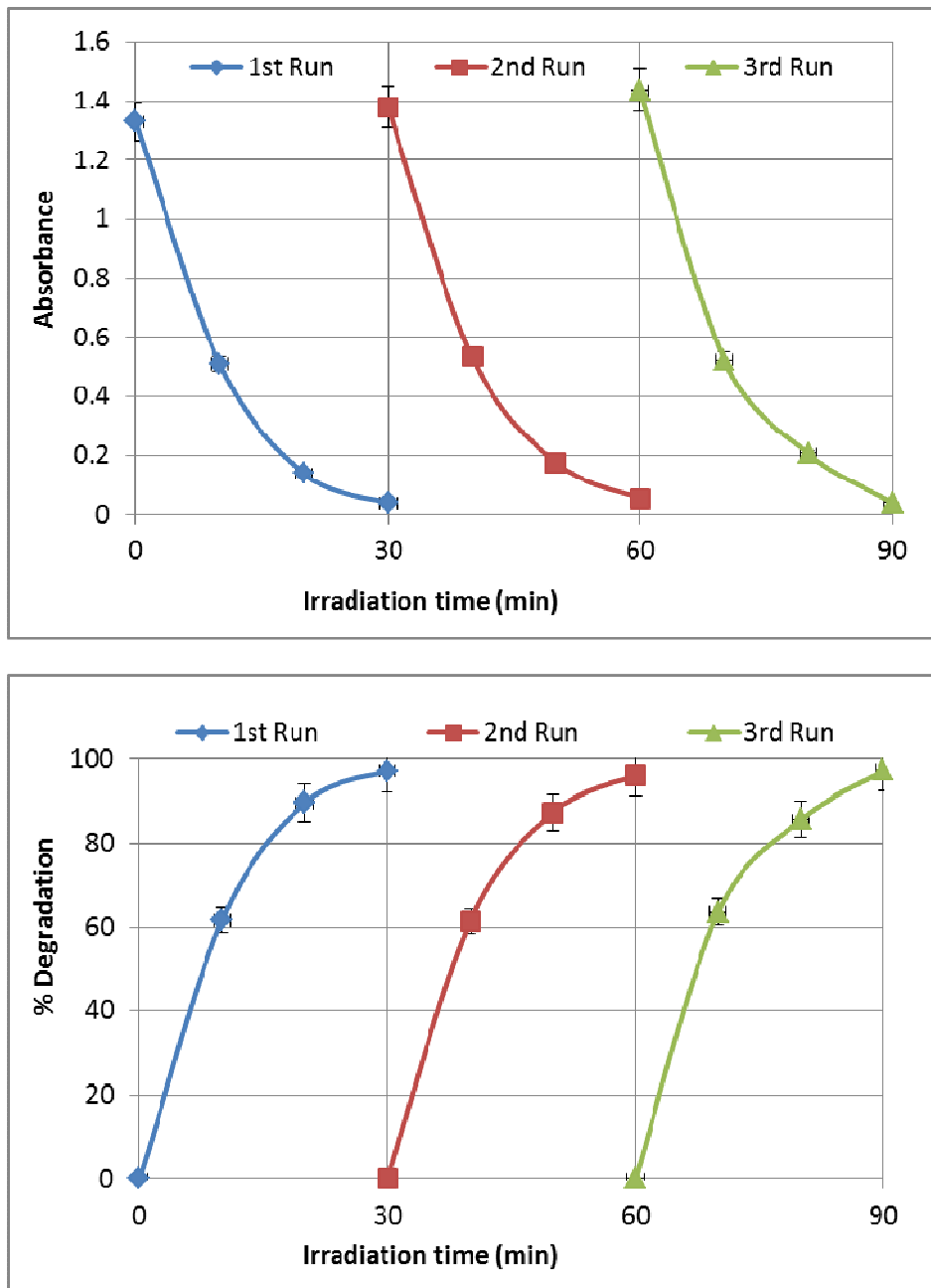


Figure 5.19: Repeatability experiment for ZnO/Fe<sub>3</sub>O<sub>4</sub> nanocomposites.

#### **5.4 Summary**

From the detail discussions and the obtained results, it shows that magnetic ZnO/Fe<sub>3</sub>O<sub>4</sub> nanocomposite has been successfully prepared. We managed to scrutinise the necessary details of the magnetic nanocomposites, such as concentration of photocatalyst used, appropriate doping amount of Fe<sub>3</sub>O<sub>4</sub> nanoparticle in the nanocomposite and optimised sintering temperature. The optimum loading amount of the ZnO/Fe<sub>3</sub>O<sub>4</sub> nanocomposite was 9.0 wt%. The optimum amount for Fe<sub>3</sub>O<sub>4</sub> doped into the nanocomposite was 10 wt% and the sintering temperature was at 300 °C. The ZnO/Fe<sub>3</sub>O<sub>4</sub> nanocomposite was also successfully reused with no significant changes arise in the degradation efficiency.

## **CHAPTER 6**

### **Fabrication of Titanium Dioxide/Iron Oxide (magnetite)**

#### **6.1 Introduction**

Since the discovery of the photocatalytic splitting of water by using titanium oxide (TiO<sub>2</sub>) electrodes by Fujishima, many research have been devoted to TiO<sub>2</sub> due to its various photocatalytic advantages, such as low toxicity, structural stability, highly abundance and low cost (Ren, Wen et al. 2015). With its wide band gap and capability of producing reactive oxygen species (ROS) in water under UV irradiation, TiO<sub>2</sub> nanoparticle has been proven as an effective photocatalyst in degrading organic contaminants by producing harmless end products, generally CO<sub>2</sub> and water (Dindar and Içli 2001, Linley, Liu et al. 2014).

#### **6.2 Background Study**

The application of TiO<sub>2</sub> as a photocatalyst has long been focused and scrutinised by many researchers in making the oxide one of the prominent material for effective removal of organic contaminants from the wastewater (Ren, Wen et al. 2015). This is due to its possession on several advantages and continuous breakthroughs, thus brought it to various application, such as purification and treatment of hazardous materials in water and air,

disinfection, and even for medical therapy (Chong, Jin et al. 2010). However, the application of TiO<sub>2</sub> in water purification has faced many challenges, especially the difficulty associated with recovering of the dispersed nanoparticle and the reusability of the oxide after water treatment remains as the major obstacle towards the practicality application for industrial process. These have brought the negative impact to its high photocatalytic efficiency and potential in many applications besides posing an environmental treat when it is released into the natural bodies of water (Linley, Liu et al. 2014).

Many methods have been studied in overcoming those obstacles by producing the nanoparticle as thick films deposited onto suitable substrates as supporting materials such as glass, sand, membranes, or magnetic nanoparticles to improve the separation efficiency (Linley, Liu et al. 2014). Although by applying this immobilization technique could solve the problem related to the photocatalytic separation after treatment, another drawback arises. The immobilization mode inhibits the dispersion capability as well as reducing the active surface area of the photocatalyst therefore greatly lowered the interaction with the contaminants, in turn leading to the relevant decrease in the photocatalytic efficiencies (Comparelli, Fanizza et al. 2005, Linley, Liu et al. 2014).

This can be solved by investigating nanostructured support materials, such as magnetic nanoparticles, besides retaining the ability to effectively

disperse in solution, it also provides a convenient approach for removing and recycling magnetic particles by applying external magnetic fields (Linley, Liu et al. 2014). Therefore, in this section, TiO<sub>2</sub> nanoparticle was incorporated with iron oxide (Fe<sub>3</sub>O<sub>4</sub>), utilizing its unique magnetic properties for the convenient separation purposes at the end of each treatment. The Fe<sub>3</sub>O<sub>4</sub> nanoparticle with different weight fractions were added to the TiO<sub>2</sub> nanoparticle and were sintered between 200 to 450 °C. The optimum addition of Fe<sub>3</sub>O<sub>4</sub> nanoparticle and sintering temperature were determined through a series of photocatalytic performances measurements on the degradation of organic dyes (i.e. methylene blue (MB)).

### **6.3 Results and Discussion**

#### *6.3.1 Morphology and Crystalline Structure of the Nanocomposite with Different Sintering Temperature*

Figure 6.1 shows the morphology obtained from FESEM for the 20 wt% doped Fe<sub>3</sub>O<sub>4</sub> of TiO<sub>2</sub>/Fe<sub>3</sub>O<sub>4</sub> nanocomposites prepared at different sintering temperatures. All samples showed homogeneous particle size with spherical in shape. No agglomeration was observable across all micrographs with highly porous structure. The average particle size as measured from the micrographs are (82.3 ± 4.6) nm, (79.1 ± 6.2) nm, (97.5 ± 7.2) nm, (112 ±

12) nm,  $(103 \pm 22)$  nm and  $(118 \pm 15)$  nm, for 200, 250, 300, 350, 400 and 450 °C sintering temperature, respectively.

This conveyed that sintering temperatures between 200 to 450 °C have no significant effect on the size and shape of the final nanocomposites. Similar morphology has been shown by Yassitepe et al. (2008) when they sintered their nanoparticle to 700 °C. Nonetheless, when the samples were sintered at 1050 °C, a significant changed in morphology was observed, such as less porosity and bridges started to appear between the nanoparticles (Yassitepe, Yatmaz et al. 2008). The FESEM results clearly show that the sintering process in current study do not cause any significant changes on the morphological properties of the nanocomposite materials. Sintering process instead can improve the homogenization/densification to powder mixtures and have been used widely in metallurgy and ceramic processing (Bakhsh, Khalid et al. 2014).

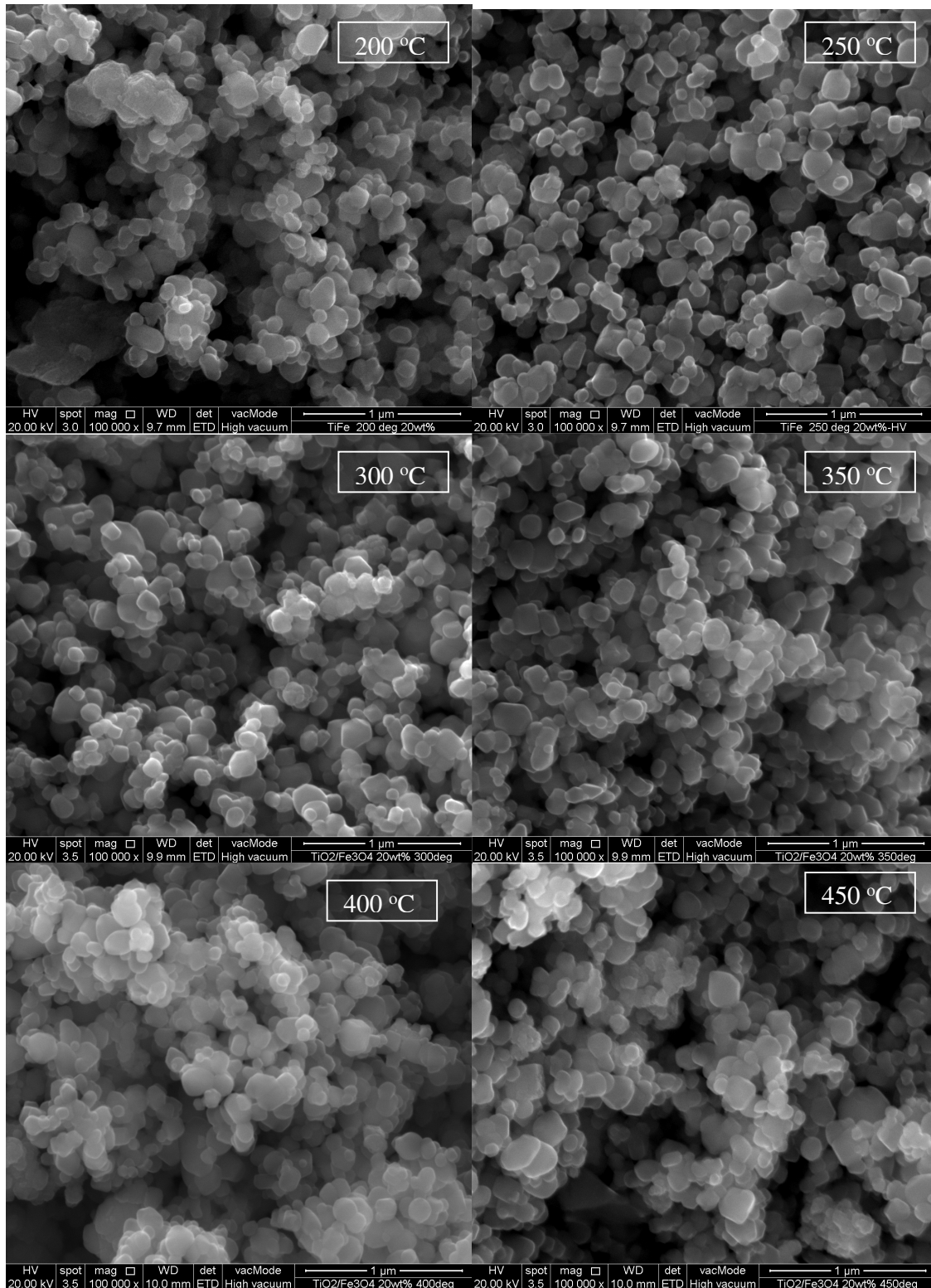


Figure 6.1: FESEM microstructures for TiO<sub>2</sub>/Fe<sub>3</sub>O<sub>4</sub> nanocomposites for different sintering temperature (200, 250, 300, 350, 400 and 450 °C).

Figure 6.2 shows the XRD results for the prepared 20 wt% doped  $\text{Fe}_3\text{O}_4$  of  $\text{TiO}_2/\text{Fe}_3\text{O}_4$  nanocomposites sintered at different sintering temperatures. Similar peaks appeared in all samples which represented by the  $\text{TiO}_2$  and  $\text{Fe}_3\text{O}_4$  phases. The  $\text{TiO}_2$  peaks for (101), (103), (004), (112), (200), (105), (211), (118), (116), (220) and (215) diffraction planes represent the characteristic pattern of pure anatase phase of tetragonal structure, in agreement with the literature (JCPDS file #21-1272) [AdachiJiu2008], whereas the  $\text{Fe}_3\text{O}_4$  peaks for (220), (311), (400), (422), (511) and (440) diffraction planes represent the crystal of cubic spinel structure, in accordance with the literature as well (JCPDS file #19-0629) [WuXiao2011]. From these results, it confirmed that all of the  $\text{TiO}_2/\text{Fe}_3\text{O}_4$  nanocomposites have been prepared without any impurities as there was no additional peak appeared in any of the XRD results.

The average crystallite size as calculated by using the Scherer equation are  $(75.4 \pm 3.9)$  nm,  $(78.5 \pm 8.9)$  nm,  $(93.7 \pm 8.3)$  nm,  $(105 \pm 13)$  nm,  $(107.1 \pm 9.3)$  nm and  $(119 \pm 18)$  nm, for the 200, 250, 300, 350, 400 and 450 sintering temperature, respectively. These results show that generally the average crystallite size of the nanocomposites is increased at the elevated sintering temperature.

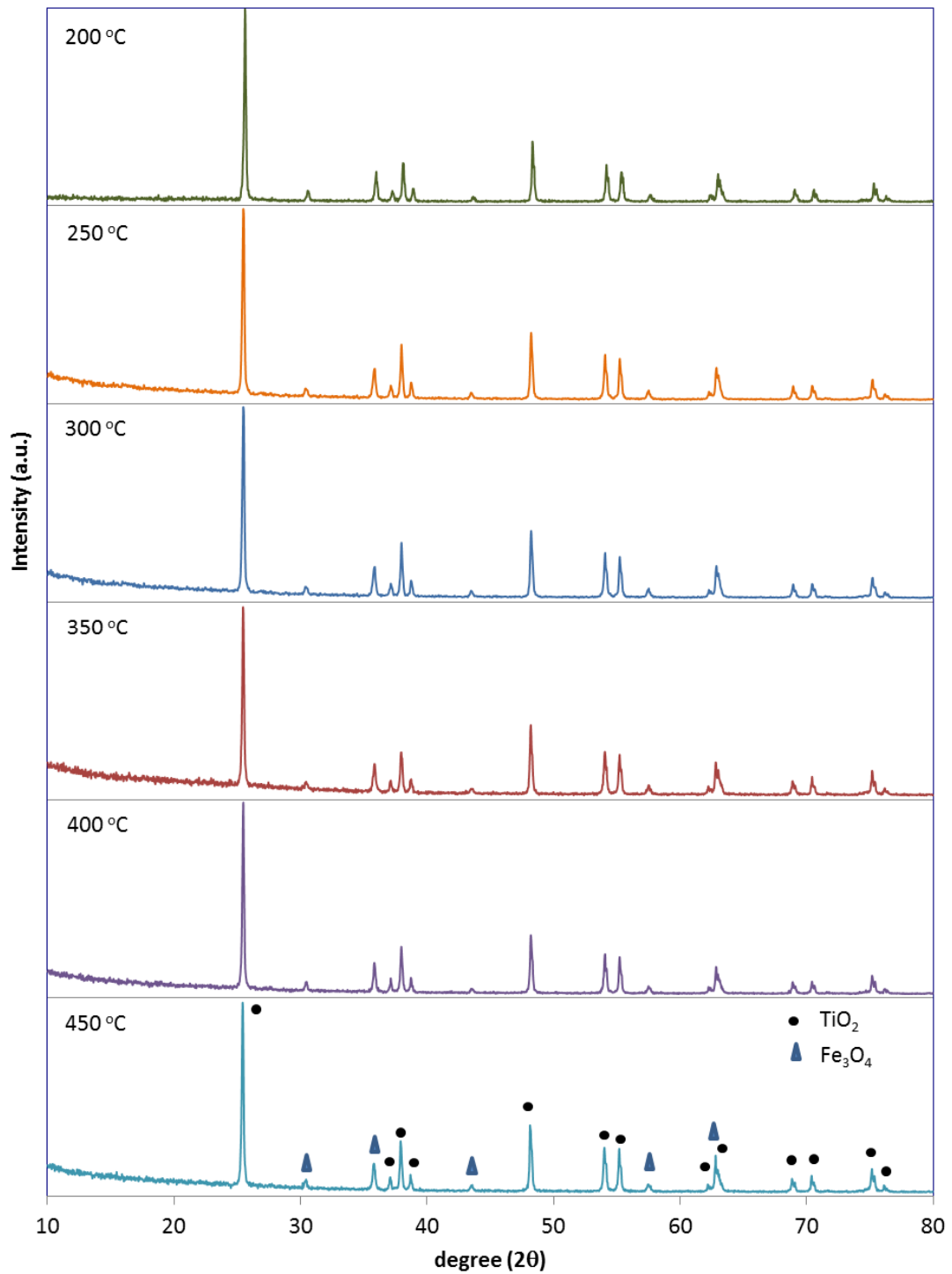


Figure 6.2: XRD for TiO<sub>2</sub>/Fe<sub>3</sub>O<sub>4</sub> nanocomposites for different sintering temperature (200, 250, 300, 350, 400 and 450 °C).

The BET surface area and pore size for TiO<sub>2</sub>/Fe<sub>3</sub>O<sub>4</sub> nanocomposites sintered at different temperature are given in Table 6.1. From the table, there is no significant difference on the surface area except for the sample sintered at 400 °C, which has the value of 9.054 m<sup>2</sup>/g. Although the value is different, the differences are insignificant. Similarly, the pore size and pore volume are also very close amongst all samples, except for the sample sintered at 350 °C, with the values of 47.59 nm and 0.09344 cm<sup>3</sup>/g, respectively. These differences would certainly contribute some impact to the photocatalytic performance of these TiO<sub>2</sub>/Fe<sub>3</sub>O<sub>4</sub> nanocomposites.

Table 6.1: BET data for different sintering temperature for TiO<sub>2</sub>/Fe<sub>3</sub>O<sub>4</sub> nanocomposites

Sintering temperature (°C)	BET Surface Area (m <sup>2</sup> /g)	Pore Volume (cm <sup>3</sup> /g)	Average Pore Size (nm)
200	7.926	0.05036	25.31
250	7.812	0.04978	26.09
300	7.835	0.05421	27.67
350	7.854	0.09344	47.59
400	9.054	0.04758	21.02
450	7.507	0.05088	27.11

From Figure 6.3, the EDX spectrum results for TiO<sub>2</sub>/Fe<sub>3</sub>O<sub>4</sub> nanocomposites were reported. All the spectrums show the elements O, Ti

and Fe, which are the core elements of the  $\text{TiO}_2/\text{Fe}_3\text{O}_4$  nanocomposites. The element C depicted in all of the spectrums is due to the carbon tape that was holding the nanocomposites. The weight percent (wt%) and the atomic percent (At%) for the elements is given in Table 6.2. This result, together with the XRD analysis indicates the prepared  $\text{TiO}_2/\text{Fe}_3\text{O}_4$  nanocomposites are of high purity.

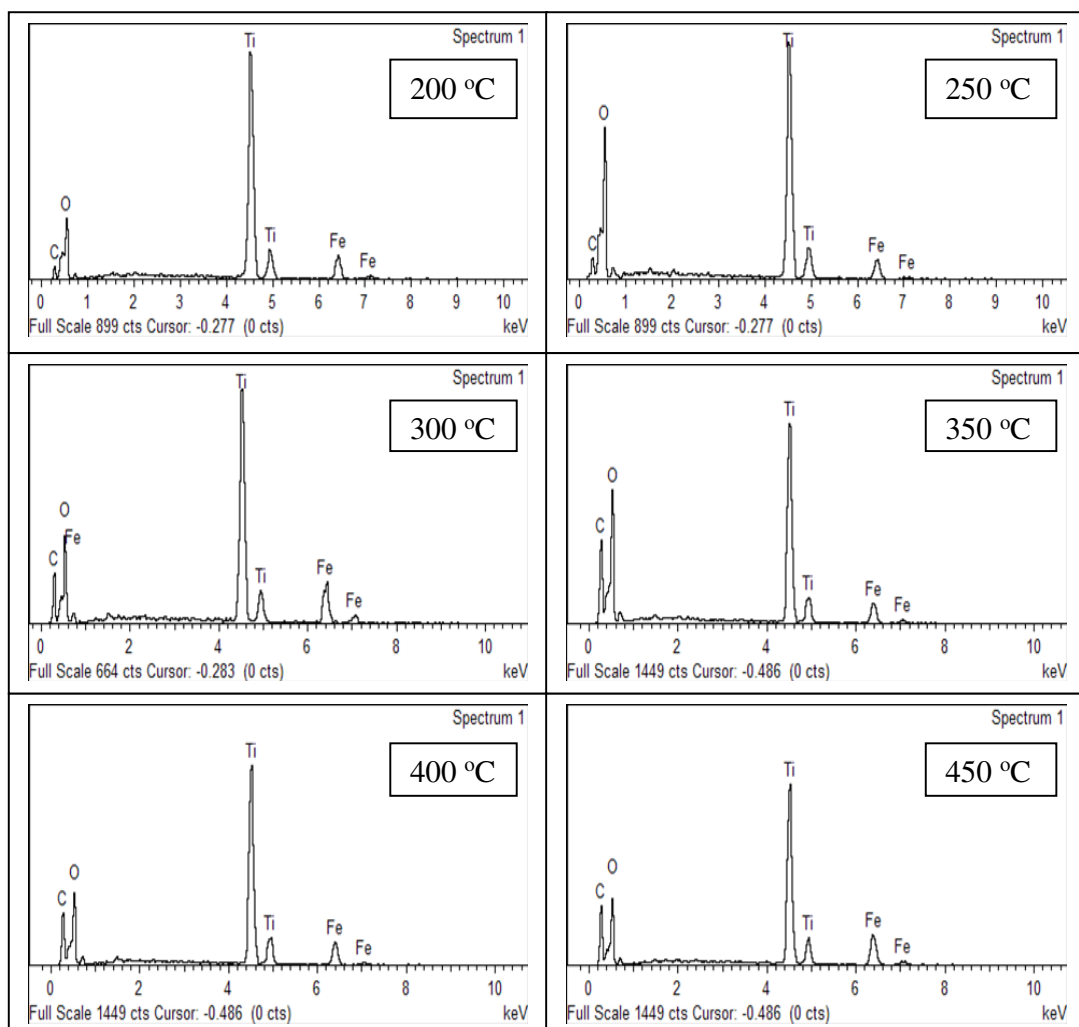


Figure 6.3: Energy dispersive X-ray spectroscopy (EDX) for different sintering temperature for  $\text{TiO}_2/\text{Fe}_3\text{O}_4$  nanocomposites.

Table 6.2: EDX data for different sintering temperature for TiO<sub>2</sub>/Fe<sub>3</sub>O<sub>4</sub> nanocomposites

Sintering temperature (°C)	Element	Wt%	At%
200	C	5.31	10.90
	O	40.07	61.67
	Ti	45.77	23.53
	Fe	8.85	3.90
	Total	100.00	100.00
250	C	4.89	8.63
	O	55.97	74.32
	Ti	34.08	15.12
	Fe	5.06	1.93
	Total	100.00	100.00
300	C	15.70	28.11
	O	38.94	52.29
	Ti	33.71	15.12
	Fe	11.65	4.48
	Total	100.00	100.00

350	C	19.37	30.43
	O	48.55	57.24
	Ti	26.74	10.53
	Fe	5.34	1.80
	Total	100.00	100.00
400	C	17.42	29.95
	O	40.63	52.42
	Ti	34.47	14.86
	Fe	7.48	2.77
	Total	100.00	100.00
450	C	20.27	34.68
	O	37.10	47.67
	Ti	32.14	13.79
	Fe	10.49	3.86
	Total	100.00	100.00

### *6.3.2 Morphology and Crystalline Structure of Nanocomposite Doped with Different wt% of Fe<sub>3</sub>O<sub>4</sub>*

The microstructures for TiO<sub>2</sub>/Fe<sub>3</sub>O<sub>4</sub> nanocomposites with different weight percentage of Fe<sub>3</sub>O<sub>4</sub> sintered at 300 °C, are shown in Figure 6.4. The variation of doping of Fe<sub>3</sub>O<sub>4</sub> is to obtain magnetic properties possessed by the Fe<sub>3</sub>O<sub>4</sub> nanoparticles. However, the appropriate amount of Fe<sub>3</sub>O<sub>4</sub> doped need to be measured to obtain the optimum photocatalytic capability of the nanocomposite. From the micrographs, there were no significant different in the microstructure for all the samples. All samples show the TiO<sub>2</sub>/Fe<sub>3</sub>O<sub>4</sub> nanocomposites were homogeneously distributed and spherically in shape. There were no serious agglomerations as can be observed from the micrographs.

The FESEM images show high porosity across all samples. These features would contribute to a more pronounced photocatalytic performance. The average particle size as directly measured from the micrographs are (97.2 ± 9.0) nm, (82.4 ± 3.5) nm, (100.9 ± 5.3) nm, (88.3 ± 3.7) nm, (101.0 ± 3.6) nm and (92.6 ± 7.2) nm for 20, 15, 12, 10, 5 and 1 wt% of Fe<sub>3</sub>O<sub>4</sub> doped, respectively, for the TiO<sub>2</sub>/Fe<sub>3</sub>O<sub>4</sub> nanocomposites.

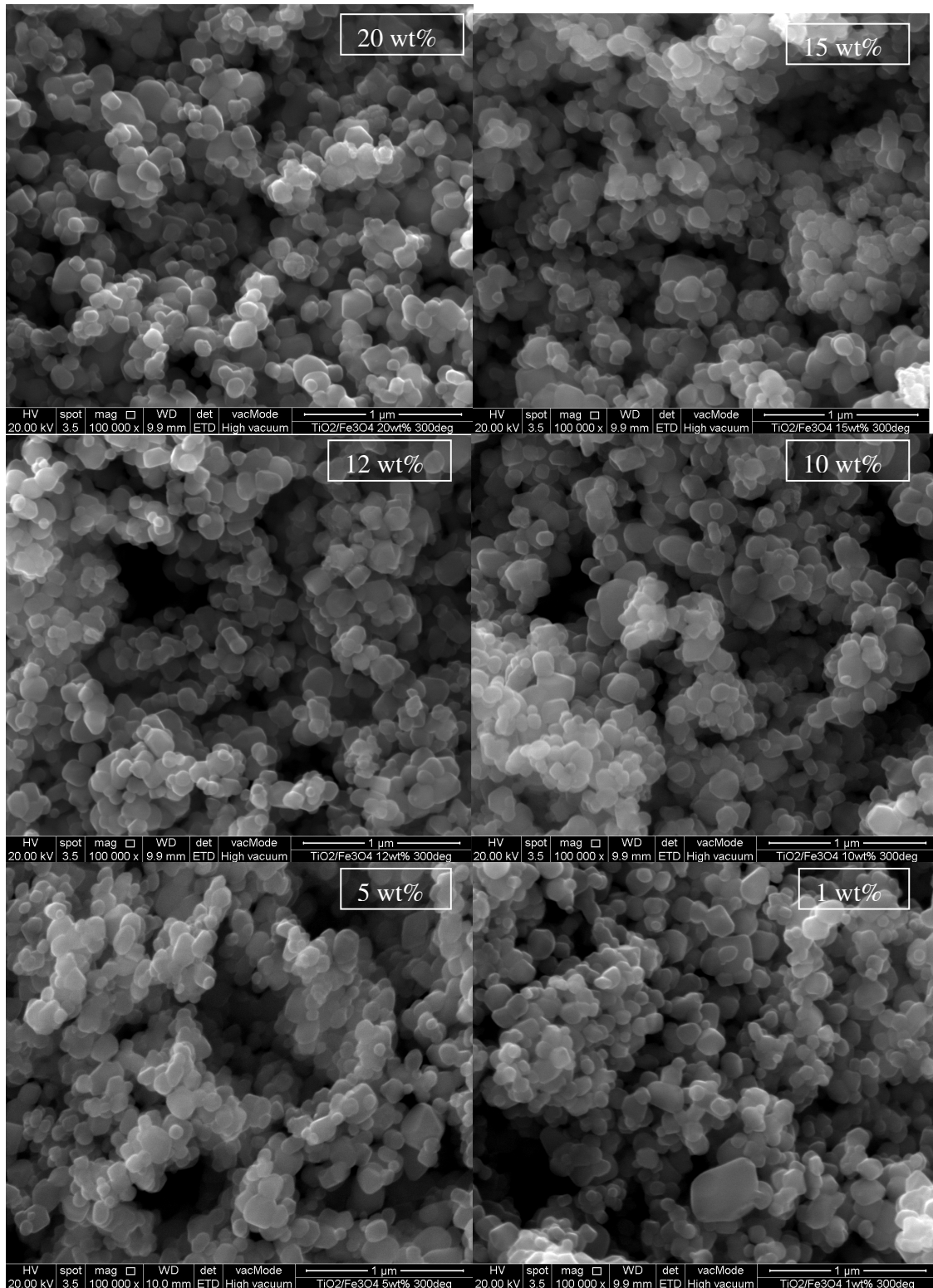


Figure 6.4: FESEM microstructures for  $\text{TiO}_2/\text{Fe}_3\text{O}_4$  nanocomposites for different wt% of  $\text{Fe}_3\text{O}_4$  (20, 15, 12, 10, 5 and 1 wt%).

The XRD results for the different wt% of Fe<sub>3</sub>O<sub>4</sub> doped TiO<sub>2</sub>/Fe<sub>3</sub>O<sub>4</sub> nanocomposites, as shown in Figure 6.5, show well mixed nanocomposites with no impurities was detected. All the peaks for (101), (103), (004), (112), (200), (105), (211), (118), (116), (220) and (215) diffraction planes, can be represented by the characteristic pattern of pure anatase phase of TiO<sub>2</sub> tetragonal structure, in agreement with the literature (JCPDS file #21-1272), as well as the peaks for (220), (311), (400), (422), (511) and (440) diffraction planes, represent the Fe<sub>3</sub>O<sub>4</sub> crystal of cubic spinel structure (JCPDS file #19-0629).

This XRD results confirmed that the prepared nanocomposites retained the crystalline structure and purity of the nanoparticles that were used in the preparation of the TiO<sub>2</sub>/Fe<sub>3</sub>O<sub>4</sub> nanocomposites. The average crystallite size is obtained by using the Scherer equation, yield the values of (105 ± 13) nm, (117 ± 16) nm, (103 ± 16) nm, (124 ± 18) nm, (134 ± 20) nm and (120 ± 17) nm, for the 20, 15, 12, 10, 5 and 1 wt% of doped Fe<sub>3</sub>O<sub>4</sub>, respectively. The average crystallite size for Fe<sub>3</sub>O<sub>4</sub> is slightly smaller than the TiO<sub>2</sub>. Therefore, with lesser amount of Fe<sub>3</sub>O<sub>4</sub> added to the nanocomposite, the formation of the average crystallite size would change and was slightly larger. These results show that the doping of Fe<sub>3</sub>O<sub>4</sub> nanoparticles has no significant impact on the average crystallite size of the nanocomposites.

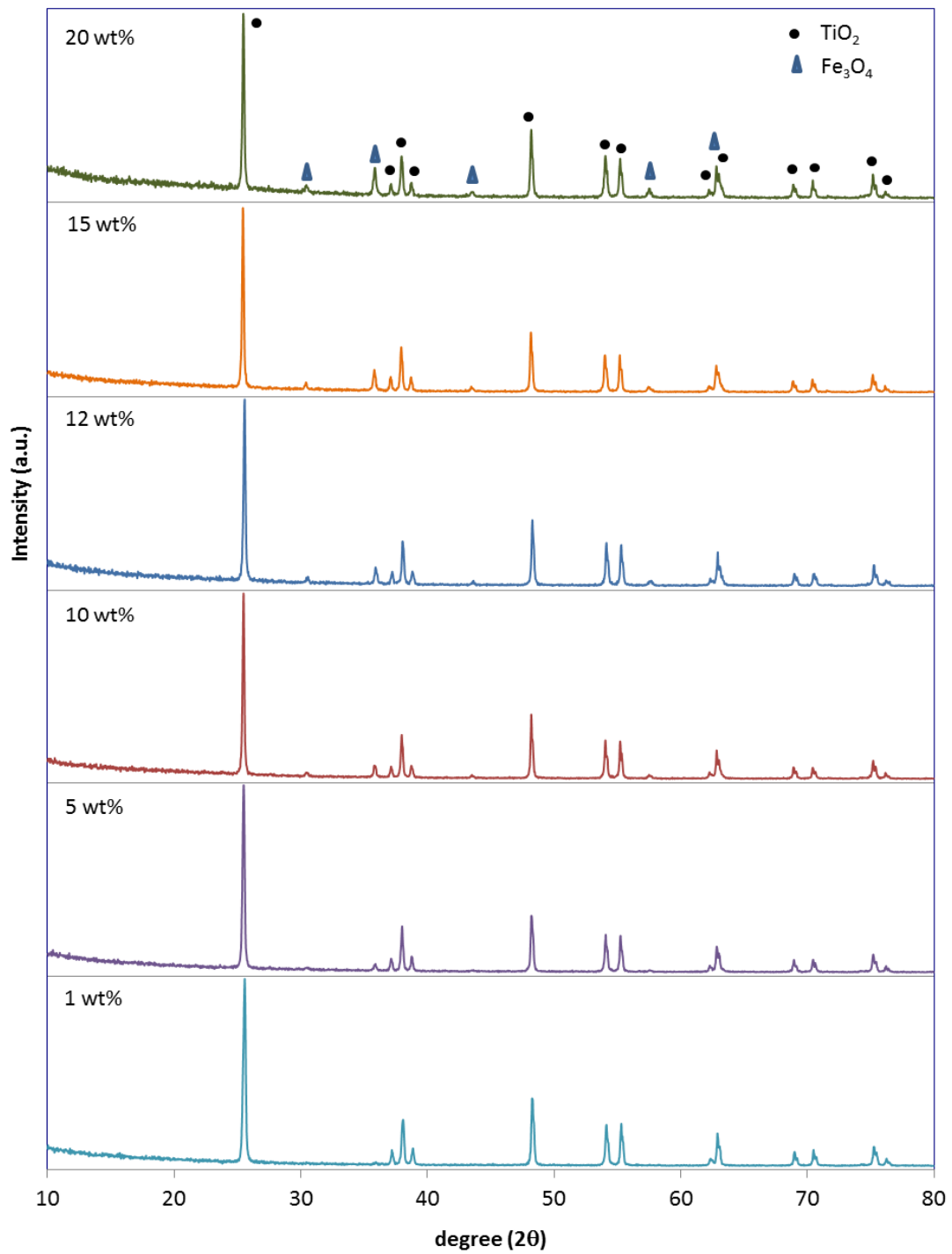


Figure 6.5: XRD for TiO<sub>2</sub>/Fe<sub>3</sub>O<sub>4</sub> nanocomposites for different wt% of Fe<sub>3</sub>O<sub>4</sub> (20, 15, 12, 10, 5 and 1 wt%).

Table 6.2 shows the BET surface area and pore size for the TiO<sub>2</sub>/Fe<sub>3</sub>O<sub>4</sub> nanocomposites with different wt% of Fe<sub>3</sub>O<sub>4</sub>. The table shows insignificant differences for the surface area and pore size throughout all the samples.

Table 6.2: BET data for different wt% of Fe<sub>3</sub>O<sub>4</sub> for TiO<sub>2</sub>/Fe<sub>3</sub>O<sub>4</sub> nanocomposites

Weight percent of Fe <sub>3</sub> O <sub>4</sub> (wt%)	BET Surface Area (m <sup>2</sup> /g)	Pore Volume (cm <sup>3</sup> /g)	Average Pore Size (nm)
20	7.854	0.09344	47.59
15	7.513	0.06132	40.57
12	7.672	0.07315	36.38
10	6.836	0.05841	42.11
5	6.578	0.06561	39.89
1	6.977	0.05935	34.03

The EDX for different wt% of Fe<sub>3</sub>O<sub>4</sub> doped into the TiO<sub>2</sub>/Fe<sub>3</sub>O<sub>4</sub> nanocomposites were depicted in Figure 6.6. Similarly, as could be observed from the spectrum, the main elements, such as O, Ti and Fe, were the elements detected, which are the main elements of the TiO<sub>2</sub>/Fe<sub>3</sub>O<sub>4</sub> nanocomposites. The EDX data, wt% and At%, for different wt% doped Fe<sub>3</sub>O<sub>4</sub> of TiO<sub>2</sub>/Fe<sub>3</sub>O<sub>4</sub> nanocomposites was listed in Table 6.4. These results coupled with the XRD analysis confirmed the purity of the prepared

TiO<sub>2</sub>/Fe<sub>3</sub>O<sub>4</sub> nanocomposites which scrutinised their crystalline and single phase structure.

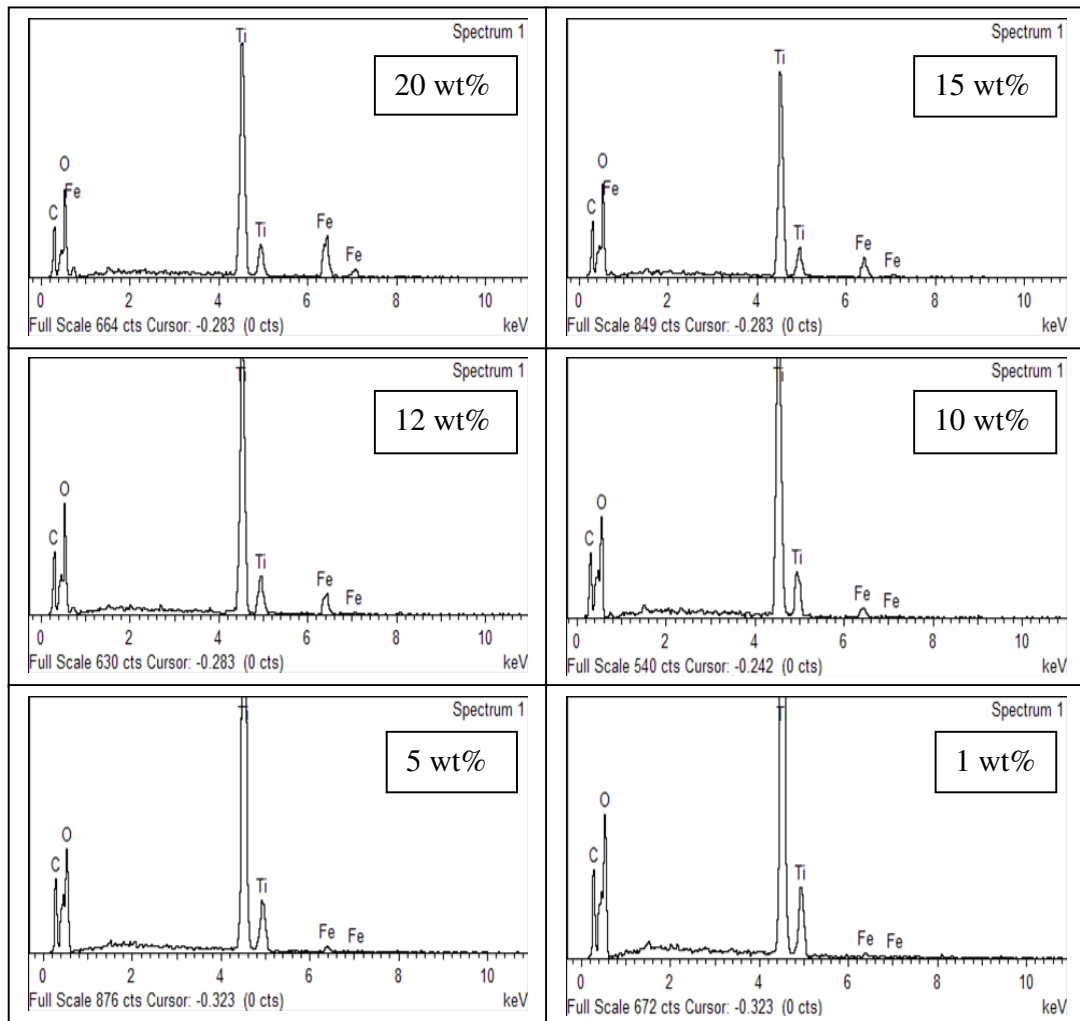


Figure 6.6: Energy dispersive X-ray spectroscopy (EDX) for different wt% of Fe<sub>3</sub>O<sub>4</sub> for TiO<sub>2</sub>/Fe<sub>3</sub>O<sub>4</sub> nanocomposites.

Table 6.4: EDX data for different wt% of Fe<sub>3</sub>O<sub>4</sub> for TiO<sub>2</sub>/Fe<sub>3</sub>O<sub>4</sub> nanocomposites

wt% Fe <sub>3</sub> O <sub>4</sub>	Element	wt%	At%
20	C	19.37	30.43
	O	48.55	57.24
	Ti	26.74	10.53
	Fe	5.34	1.80
	Total	100.00	100.00
15	C	16.41	27.52
	O	44.91	56.54
	Ti	33.27	13.99
	Fe	5.41	1.95
	Total	100.00	100.00
12	C	15.13	26.15
	O	43.28	56.15
	Ti	36.40	15.78
	Fe	5.19	1.92
	Total	100.00	100.00
10	C	14.12	25.13
	O	41.20	55.06
	Ti	42.50	18.98
	Fe	2.18	0.83
	Total	100.00	100.00

5	C	14.08	25.02
	O	41.39	55.21
	Ti	43.48	19.37
	Fe	1.05	0.40
	Total	100.00	100.00
1	C	12.97	23.03
	O	43.13	57.47
	Ti	43.22	19.24
	Fe	0.68	0.26
	Total	100.00	100.00

### 6.3.3 Transmission Electron Microscopy (TEM)

The transmission electron microscopy (TEM) micrograph and histogram for the 1 wt% doped Fe<sub>3</sub>O<sub>4</sub> sintered at 350 °C for TiO<sub>2</sub>/Fe<sub>3</sub>O<sub>4</sub> nanocomposites are shown in Figure 6.7. The micrograph shows the nanocomposites were globular and granular in shape with various size of microstructures.

It depicts a wide range of particle size distribution and the average particle size as directly measured from the micrograph is (86.2 ± 9.0) nm. The details of the size distribution could be obtained from the particle size distribution histogram in Figure 6.7. The average particle size was quite different if compared to the crystallite size obtained from the XRD analysis. On the other hand, the average particle size is quite close to the size measured from the FESEM micrograph.

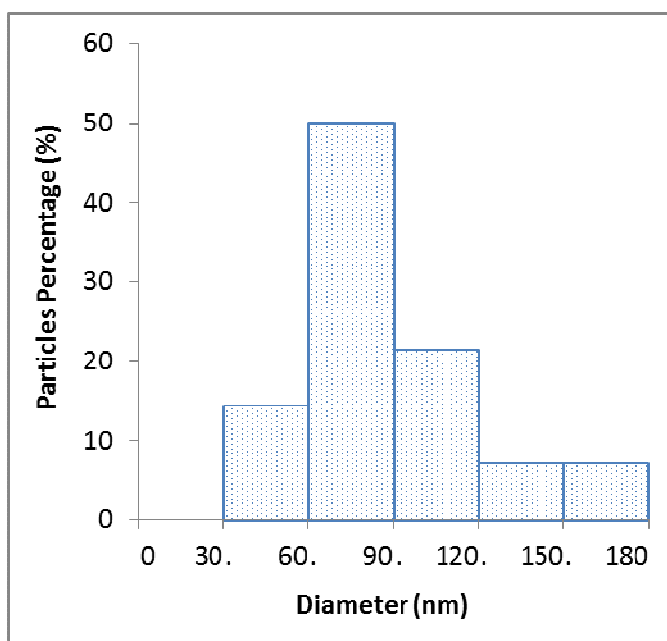
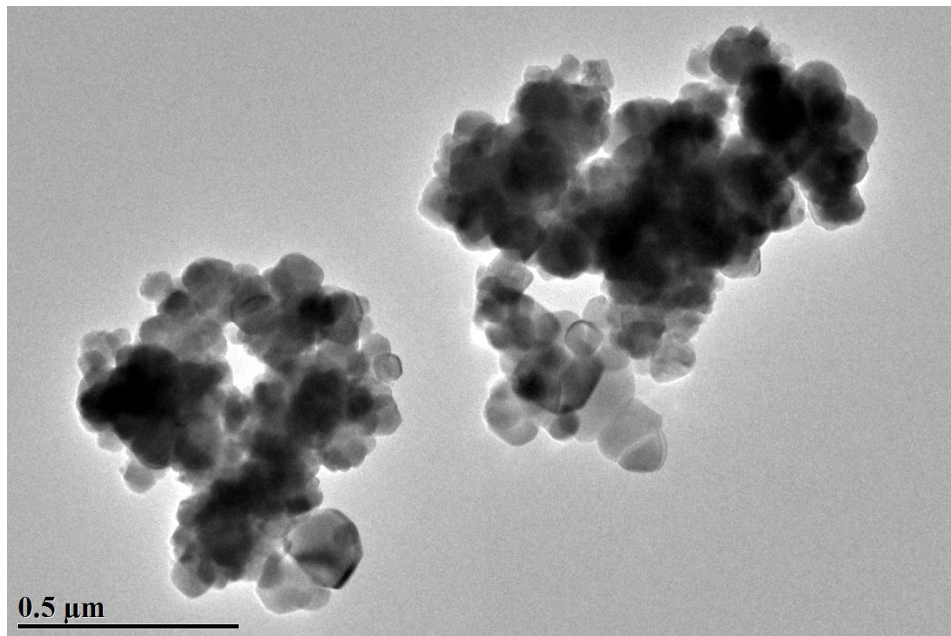


Figure 6.7: TEM micrograph and Particle size distribution histogram for  $\text{TiO}_2/\text{Fe}_3\text{O}_4$  nanocomposites.

#### 6.3.4 Photocatalytic Study for Different Loading of $\text{TiO}_2/\text{Fe}_3\text{O}_4$

The photocatalytic study on the 20 wt% doped  $\text{Fe}_3\text{O}_4$  sintered at 300 °C of  $\text{TiO}_2/\text{Fe}_3\text{O}_4$  nanocomposites with different percentage of loading was given in Figure 6.8. Sample without photocatalyst showed it was self-degradable although in a very low degradation rate. For samples with  $\text{TiO}_2/\text{Fe}_3\text{O}_4$  nanocomposites, significant degradation was achieved as more than 90% photodecomposition of the dye was recorded at the end of 90 minutes of irradiation. The photocatalytic degradation rate of MB by using the  $\text{TiO}_2/\text{Fe}_3\text{O}_4$  nanocomposites follows the pseudo-first-order kinetics of the LH model. Sample with 1 wt% loading of  $\text{TiO}_2/\text{Fe}_3\text{O}_4$  nanocomposites appeared to be the slowest performer whereas sample with 3 wt% loading of  $\text{TiO}_2/\text{Fe}_3\text{O}_4$  nanocomposites was the fastest. This could be explained due to smaller surface area possessed by the 1 wt% sample as compared to the 3 wt% sample. As the amount of loading was less, the availability of the active surface area was insufficient for optimum amount of organic contaminants to be absorbed on the photocatalyst surface, therefore lower the photocatalytic rate as compared to the other samples with higher loadings (Emeline, Zhang et al. 2012). Although with increasing of the photocatalyst loading increased the adsorptive effect, however extreme addition of the photocatalyst loading creates the opacity effect to the solution which caused shallow penetration of light into the solution. Subsequently, it will lower the amount of photons light reaching the surface of the photocatalyst and hence distort the photodegradation rate (Devi and Kavitha 2013).

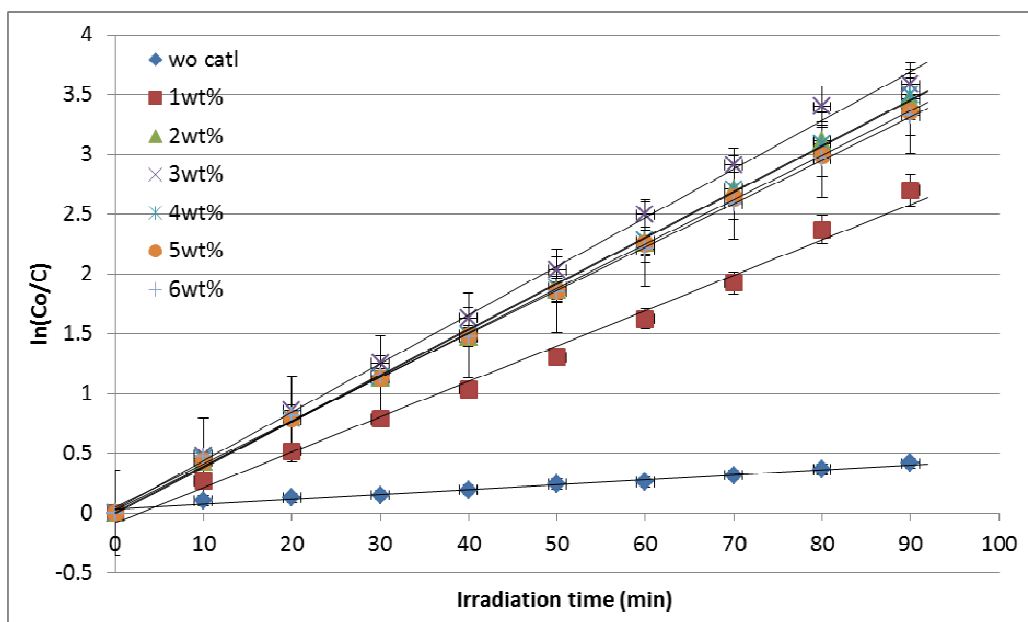
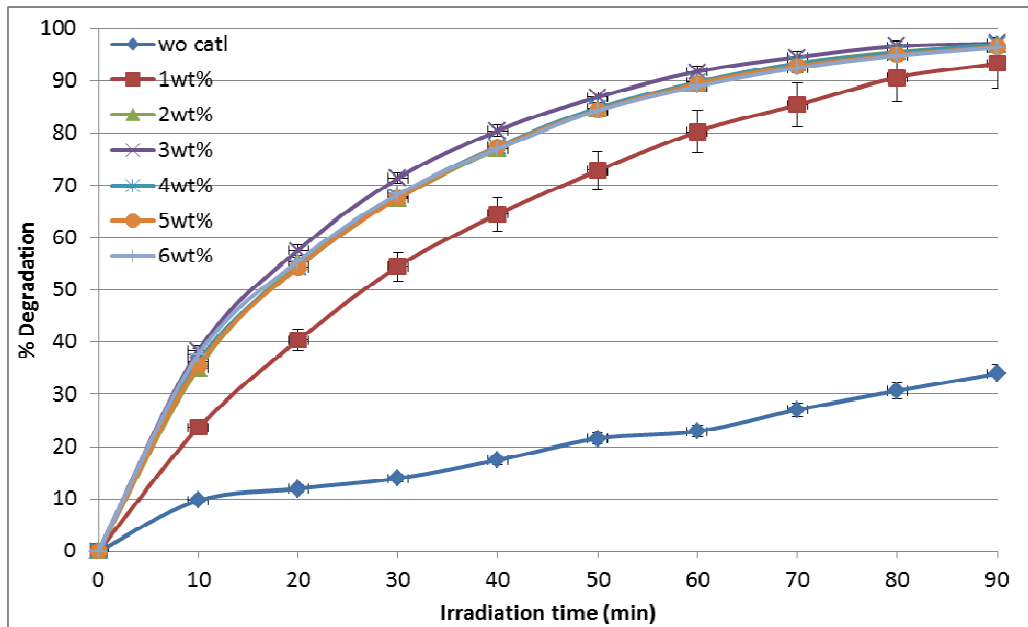


Figure 6.8: Percentage degradation and degradation rate of MB by different loading of  $\text{TiO}_2/\text{Fe}_3\text{O}_4$  nanocomposite

Figure 6.9 shows the numerical values and bar graphs for the degradation rates with the increase of the TiO<sub>2</sub>/Fe<sub>3</sub>O<sub>4</sub> nanocomposites loading. As the amount of loading increases, it is clearly seen that the degradation rate was gradually increased, i.e. from 0.0296 to 0.0406 min<sup>-1</sup>, for the 1 wt% to 3 wt%, respectively. The significant increase in the degradation rate is due to the increase in the surface area, thus the availability of the active sites (Chong, Jin et al. 2010). However, as the amount of loading increases further, the degradation rate shows a declination to 0.0362 min<sup>-1</sup> for the 6 wt% loading. This is due to the opacity of the colloidal suspension in the solution which decreases the amount of light photon to reach greater number of the nanocomposites (Dozzi and Selli 2013). Therefore, as the loading increases, shorter path could be reached by the light, and as a consequent decreased the degradation rate. From the figure, it is confirmed that the degradation rate with 3 wt% of TiO<sub>2</sub>/Fe<sub>3</sub>O<sub>4</sub> nanocomposites loading was the highest rate with the value of the kinetic constant of 0.0406 min<sup>-1</sup> and R<sup>2</sup> of 0.9977.

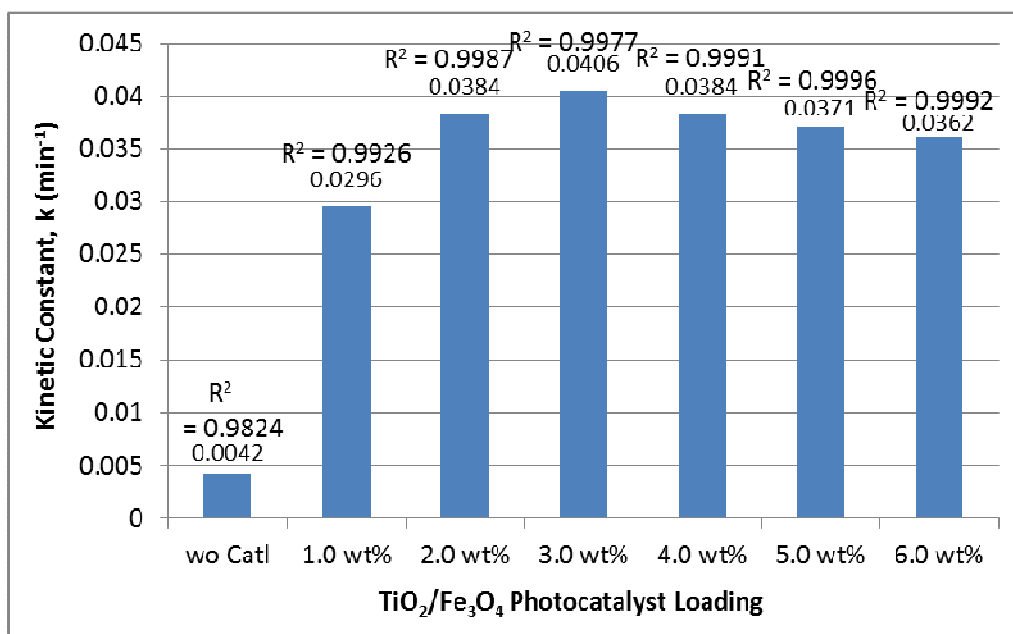


Figure 6.9: Kinetic constant of MB by different loading of TiO<sub>2</sub>/Fe<sub>3</sub>O<sub>4</sub> nanocomposite

### 6.3.5 Photocatalytic Study for Different sintering temperature

Figure 6.10 shows percent degradation of the 20 wt% doped Fe<sub>3</sub>O<sub>4</sub> of TiO<sub>2</sub>/Fe<sub>3</sub>O<sub>4</sub> nanocomposites samples that sintered at different temperature. The results showed that all samples able to degrade the organic dye significantly, with just small deviation observed. All samples managed to achieve more than 95.0% organic contaminant photodegradation after 90 minutes irradiation duration, except for the sample sintered at 450 °C with only 90.1%. This slight difference in the percentage degradation could be due to its highest crystallite size, which is (119 ± 18) nm, as compared to its counterpart. As a consequent, it possessed slightly lower surface area, as

recorded in Table 6.1. Since surface areas determine the amount of the active sites, therefore, its percentage degradation was slightly lower.

It is in agreeable with the preparation of titanium–tungsten ( $\text{TiO}_2/\text{WO}_3$ ) mixed oxides by Dozzi et al. (2016) who reported smaller size of anatase nanoparticles were formed when small amounts of tungsten was added to titania. As a consequence, the composites formed have slightly larger specific surface area as compared to pure  $\text{TiO}_2$ . This is due to the ability of tungsten inhibiting the crystal growth of anatase. Therefore, the slight increase in surface area has contributed to the higher photocatalytic degradation of the  $\text{TiO}_2/\text{WO}_3$  materials (Dozzi, Marzorati et al. 2016).

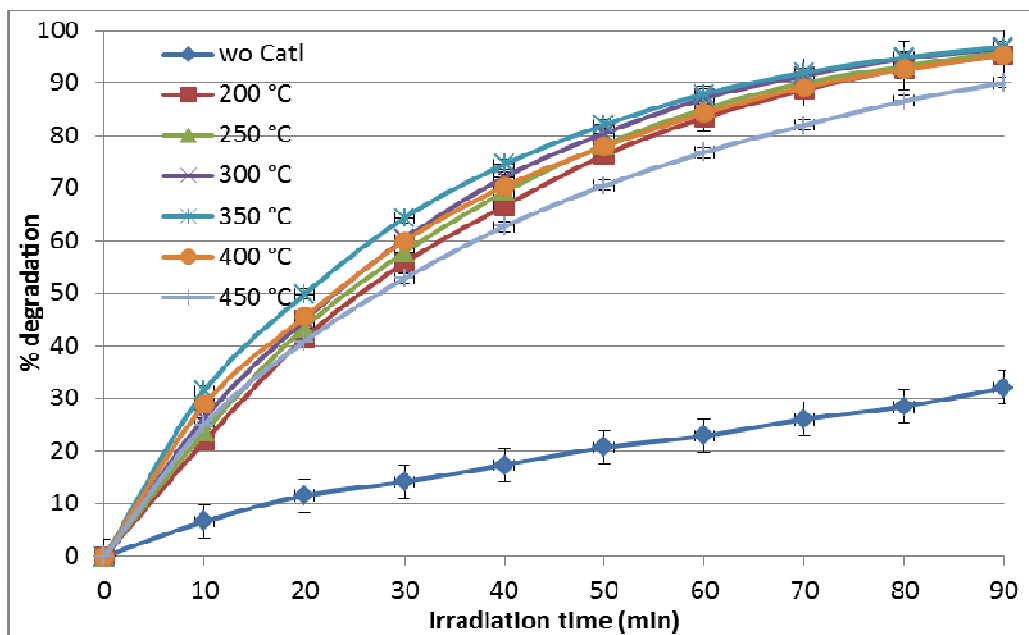


Figure 6.10: Percentage degradation of MB by  $\text{TiO}_2/\text{Fe}_3\text{O}_4$  nanocomposite at different sintering temperature.

From the degradation rate results in Figure 6.11, it shows that all samples having quite similar degradation rate except the sample with 450 °C sintering temperature. The degradation rate of MB for the nanocomposites sintered at different sintering temperature follows the pseudo-first-order kinetic of the LH model. It shows that samples with 300 and 350 °C sintering temperatures were having the highest degradation rate. From Figure 6.12, it can be seen that the kinetic constant for 300 and 350 °C sintering temperature were 0.0375 and 0.0377 min<sup>-1</sup>, respectively. It is obvious that the nanocomposite sintered at 350 °C was having the highest kinetic constant, and hence fastest rate to degrade the organic contaminant.

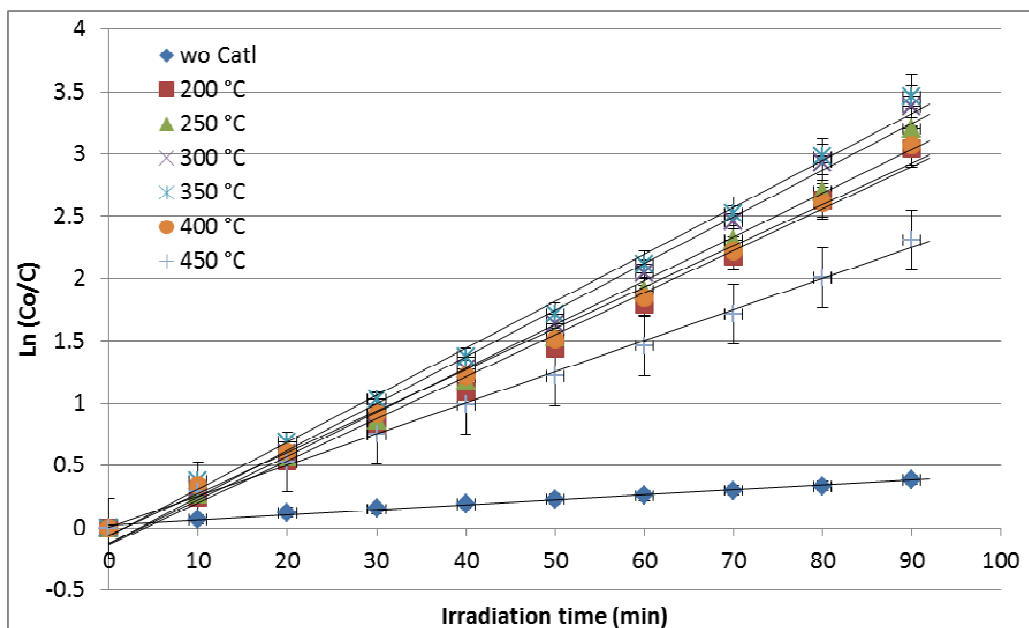


Figure 6.11: First order kinetic of MB by different sintering temperature of TiO<sub>2</sub>/Fe<sub>3</sub>O<sub>4</sub> nanocomposite.

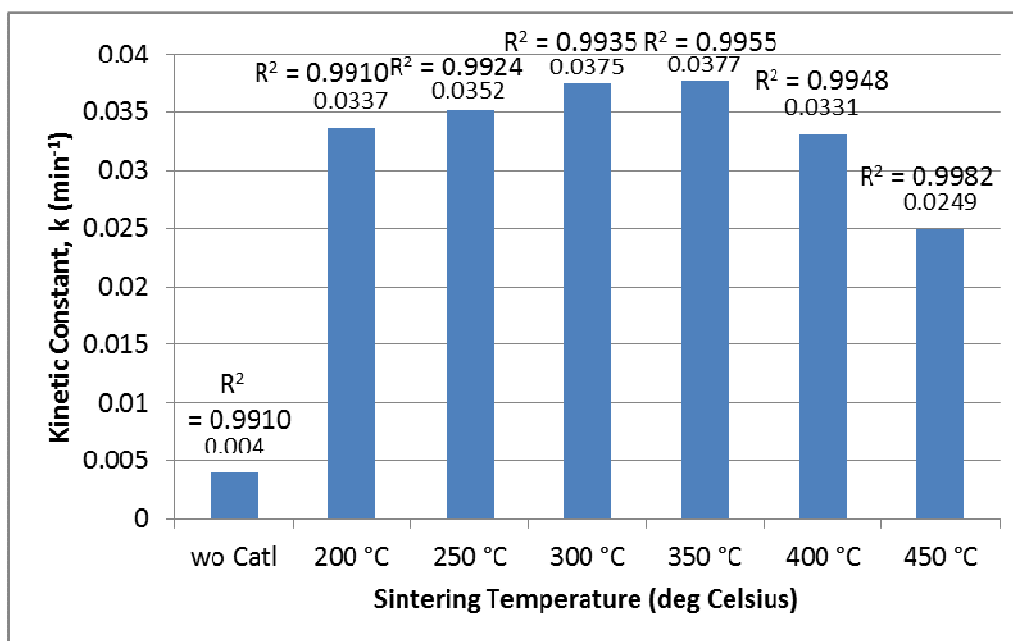


Figure 6.12: Kinetic constant of MB by different sintering temperature of TiO<sub>2</sub>/Fe<sub>3</sub>O<sub>4</sub> nanocomposite.

### 6.3.6 Photocatalytic Study for different wt% of Fe<sub>3</sub>O<sub>4</sub>

All samples were added with 3 wt% of TiO<sub>2</sub>/Fe<sub>3</sub>O<sub>4</sub> nanocomposites, an optimum loading as obtained from the previous study. From Figure 6.13, it can be seen that all samples with TiO<sub>2</sub>/Fe<sub>3</sub>O<sub>4</sub> nanocomposites were able to significantly degrade the MB dye. It shows that sample with 1 wt% doped of Fe<sub>3</sub>O<sub>4</sub> gained the highest percentage of degradation, achieving 98.7% in 60 minutes of irradiation. As more Fe<sub>3</sub>O<sub>4</sub> was doped into the TiO<sub>2</sub>/Fe<sub>3</sub>O<sub>4</sub> nanocomposites, the photocatalytic performance gradually dropped, as well as the final percentage degradation at the end of the 60 minutes irradiation. This could be due to the decreased of the effective surface area for TiO<sub>2</sub>

nanoparticle as higher amount of the  $\text{Fe}_3\text{O}_4$  nanoparticle was mixed with  $\text{TiO}_2$  nanoparticle. Therefore, when more  $\text{Fe}_3\text{O}_4$  nanoparticle was attached to  $\text{TiO}_2$  nanoparticle, the photocatalytic active surface area of the  $\text{TiO}_2/\text{Fe}_3\text{O}_4$  nanocomposites would decrease as well. This is because  $\text{Fe}_3\text{O}_4$  do not possess any promising photocatalytic activity (Singh, Barick et al. 2013). Therefore, as more  $\text{Fe}_3\text{O}_4$  nanoparticle was added, less effective surface area, contributed by the  $\text{TiO}_2$  nanoparticle, remains; thus decreasing the degradation efficiency of the nanocomposite material on the organic contaminant.

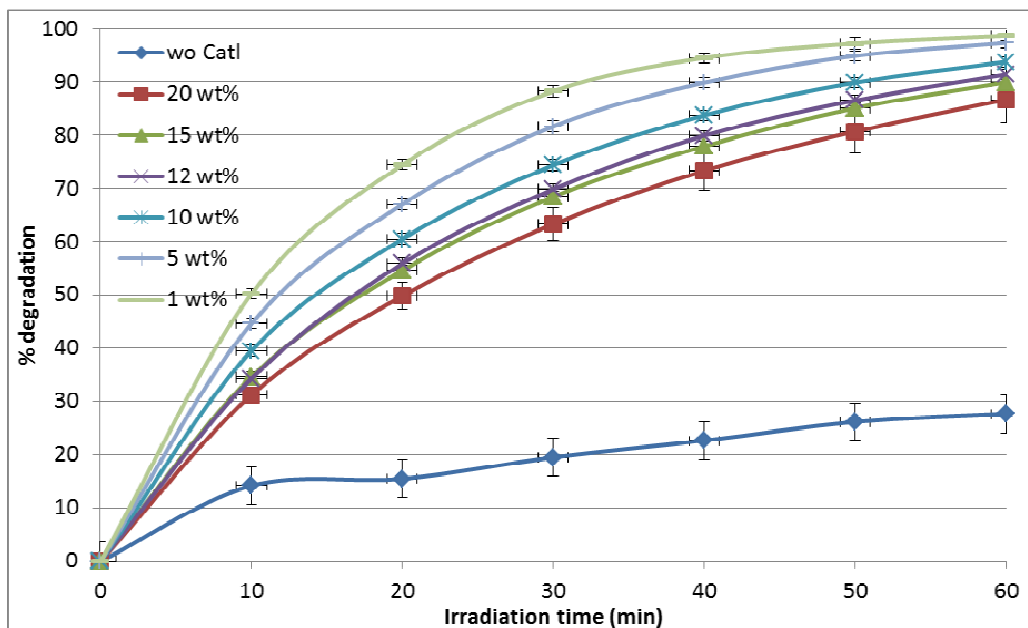


Figure 6.13: Percentage degradation of MB by different substitution of  $\text{Fe}_3\text{O}_4$  into  $\text{TiO}_2/\text{Fe}_3\text{O}_4$  nanocomposite

The doping of the  $\text{Fe}_3\text{O}_4$  into the  $\text{TiO}_2/\text{Fe}_3\text{O}_4$  nanocomposites has perturbed the performance of the nanocomposites. Figure 6.14 shows a gradual decrease of the degradation rate with the addition of the  $\text{Fe}_3\text{O}_4$  nanoparticle into the  $\text{TiO}_2/\text{Fe}_3\text{O}_4$  nanocomposites. The figure also shows that the gradients for all the samples doped with different wt% of  $\text{Fe}_3\text{O}_4$  agreed well to the pseudo-first-order kinetic of the LH model.

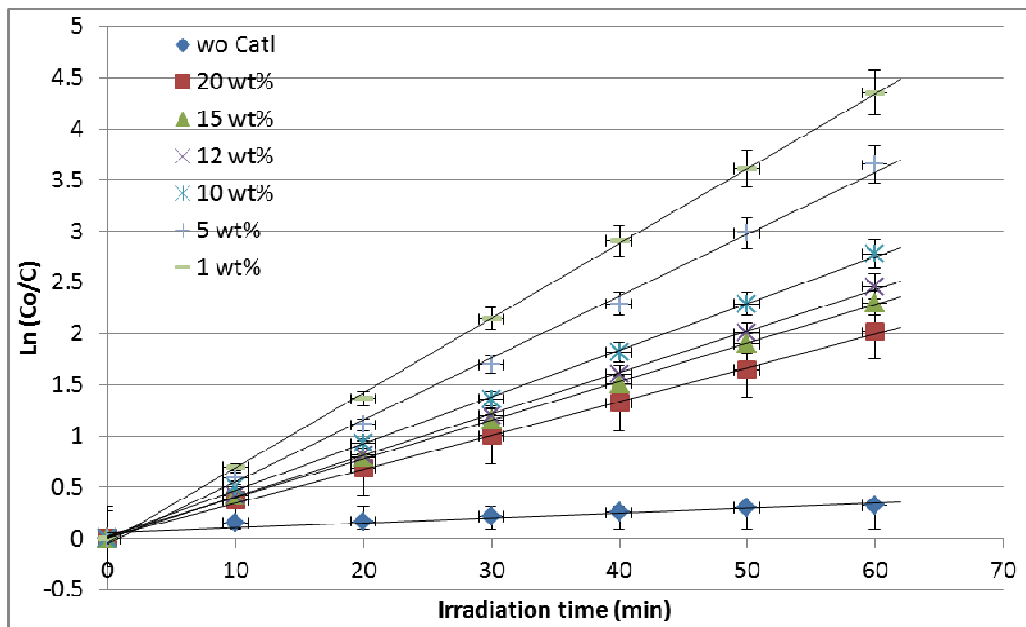


Figure 6.14: Degradation rate of MB by different addition of  $\text{Fe}_3\text{O}_4$  into  $\text{TiO}_2/\text{Fe}_3\text{O}_4$  nanocomposite

The overall values for the kinetic constants for different wt% of  $\text{Fe}_3\text{O}_4$  doped into the  $\text{TiO}_2/\text{Fe}_3\text{O}_4$  nanocomposites were given in Figure 6.15. The value of the kinetic constant is  $0.0729 \text{ min}^{-1}$  when only 1wt% of  $\text{Fe}_3\text{O}_4$  was doped into the  $\text{TiO}_2/\text{Fe}_3\text{O}_4$  nanocomposites. However, the value dropped

more than half to  $0.0330 \text{ min}^{-1}$  when the amount of  $\text{Fe}_3\text{O}_4$  doped increased to 20wt%. A steep decline is observed for the kinetic constant when  $\text{Fe}_3\text{O}_4$  doped into the  $\text{TiO}_2/\text{Fe}_3\text{O}_4$  nanocomposites increases from 1 to 20wt%. This results show that doping of  $\text{Fe}_3\text{O}_4$  into the nanocomposite significantly hinder the active sites of the  $\text{TiO}_2/\text{Fe}_3\text{O}_4$  nanocomposites. Since the introduction of the  $\text{Fe}_3\text{O}_4$  into the nanocomposite did not contribute to its photocatalytic performance but instead worsen it, therefore it is good to have optimum amount of  $\text{Fe}_3\text{O}_4$  in the nanocomposite so that the magnetic properties can be incorporated while maintaining its photodegradation efficiency. The optimum amount of  $\text{Fe}_3\text{O}_4$  doped is 1.0 wt%.

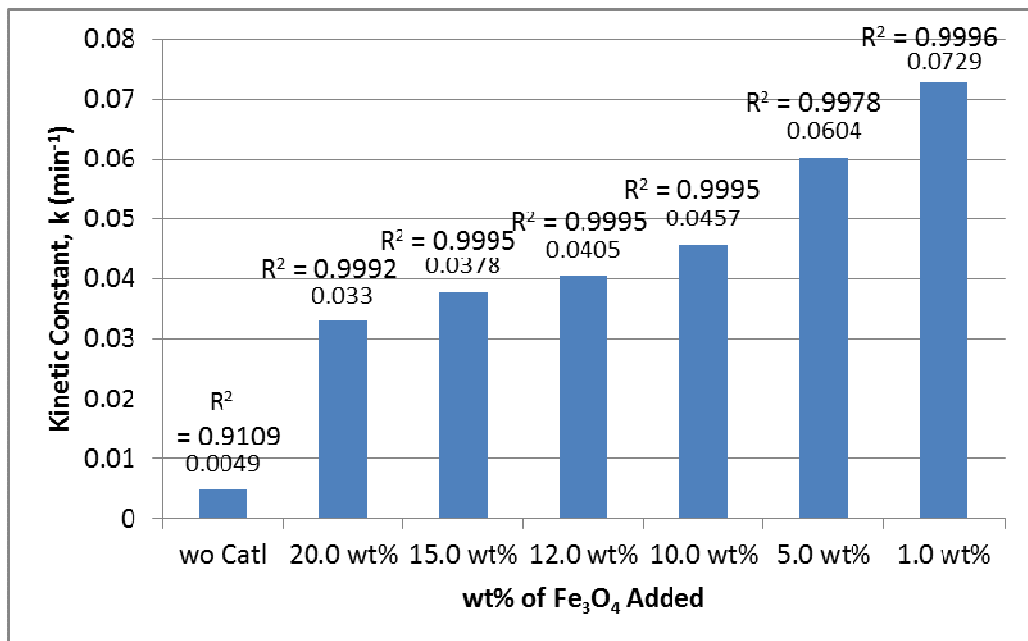


Figure 6.15: Kinetic constant of MB by different substitution of  $\text{Fe}_3\text{O}_4$  into  $\text{TiO}_2/\text{Fe}_3\text{O}_4$  nanocomposite

### 6.3.7 Vibrating Sample Magnetometry Analysis (VSM)

The prepared  $\text{TiO}_2/\text{Fe}_3\text{O}_4$  nanocomposites magnetic characteristic was measured by using the VSM and the result is shown in Figure 6.16. From the figure, it was clearly shown that  $\text{TiO}_2/\text{Fe}_3\text{O}_4$  nanocomposites has gained significant magnetic characteristic after it was added with  $\text{Fe}_3\text{O}_4$  nanoparticle.  $\text{TiO}_2$  nanoparticles on the other hand, do not possess any noticeable magnetic properties. The  $\text{TiO}_2$  nanoparticle shows none existence of magnetic properties, which is obviously a diamagnetic characteristic. On the other hand,  $\text{TiO}_2/\text{Fe}_3\text{O}_4$  nanocomposites clearly exhibits ferromagnetic hysteresis loops, which is the soft ferromagnetic characteristic. Saturation magnetisation are induced in the presence of magnetic field and very minor coercivity were shown by the  $\text{TiO}_2/\text{Fe}_3\text{O}_4$  nanocomposites.  $\text{TiO}_2/\text{Fe}_3\text{O}_4$  nanocomposites exhibits high susceptibility from the induction magnetisation results where magnetic field of 1584 Oe is required to induce 92.7% of the total magnetization. It has a magnetisation value of 5.543 emu/g when the applied magnetic field was 4033 Oe.

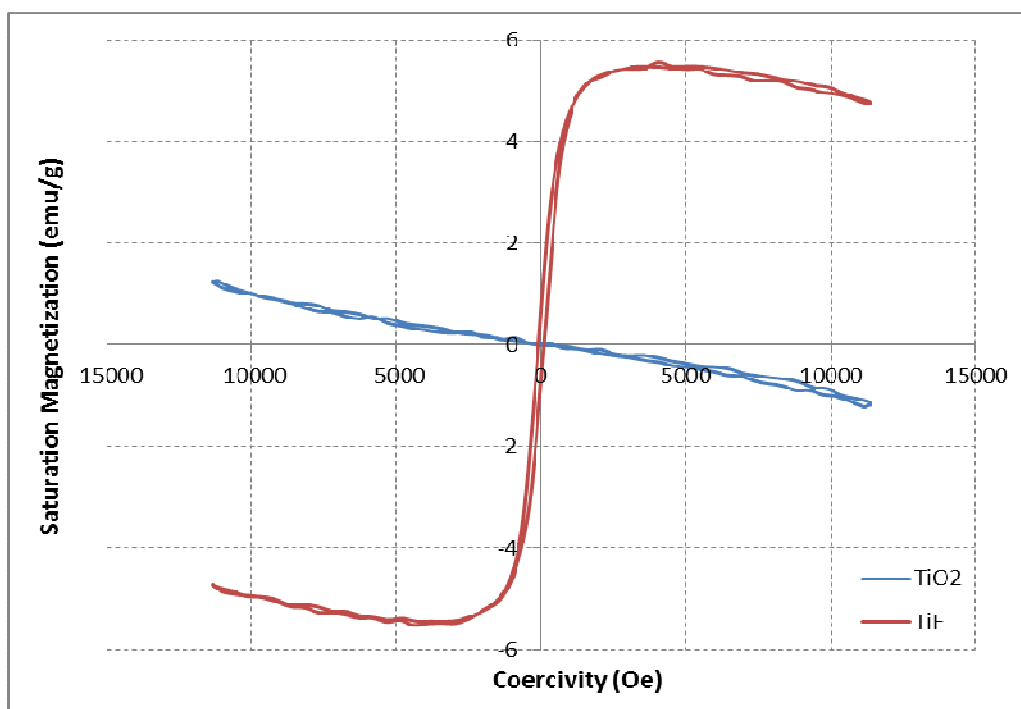


Figure 6.16: Hysteresis loop for  $\text{TiO}_2$  ( $\text{TiO}_2$ ) and  $\text{TiO}_2/\text{Fe}_3\text{O}_4$  (TiF) nanocomposite powders.

### 6.3.8 Magnetic separation analysis

Figure 6.17 shows the exploitation of the magnetic properties to separate the  $\text{TiO}_2/\text{Fe}_3\text{O}_4$  nanocomposites through magnetic induction. The amount used to disperse the  $\text{TiO}_2/\text{Fe}_3\text{O}_4$  nanocomposites is 3.0 mg, which is the optimum amount obtained from the study. When the  $\text{TiO}_2/\text{Fe}_3\text{O}_4$  nanocomposite has completely degraded the MB dye, the suspension appears to be light-orange in colour. In an instant after the vial with the treated solution was placed near a permanent magnet with magnetic field strength of

0.6 T, the separation of the colloidal suspension is detected. The motion of the colloidal suspension was clearly seen moving towards the magnet and a light-orange mass gathered proximity of the vial wall. The colloidal suspension gradually becomes discoloured and finally becomes clear. The suspension of the  $\text{TiO}_2/\text{Fe}_3\text{O}_4$  nanocomposites was attracted toward the wall of the vial closer to the magnet. This implies the complete physical separation of the suspension is achieved. The  $\text{TiO}_2/\text{Fe}_3\text{O}_4$  nanocomposites remains dispersible and no irreversible agglomeration occurred after the removal of the magnetic field. This shows that  $\text{TiO}_2/\text{Fe}_3\text{O}_4$  nanocomposites has been successfully prepared with its ability to be separated by applying the magnetic field.

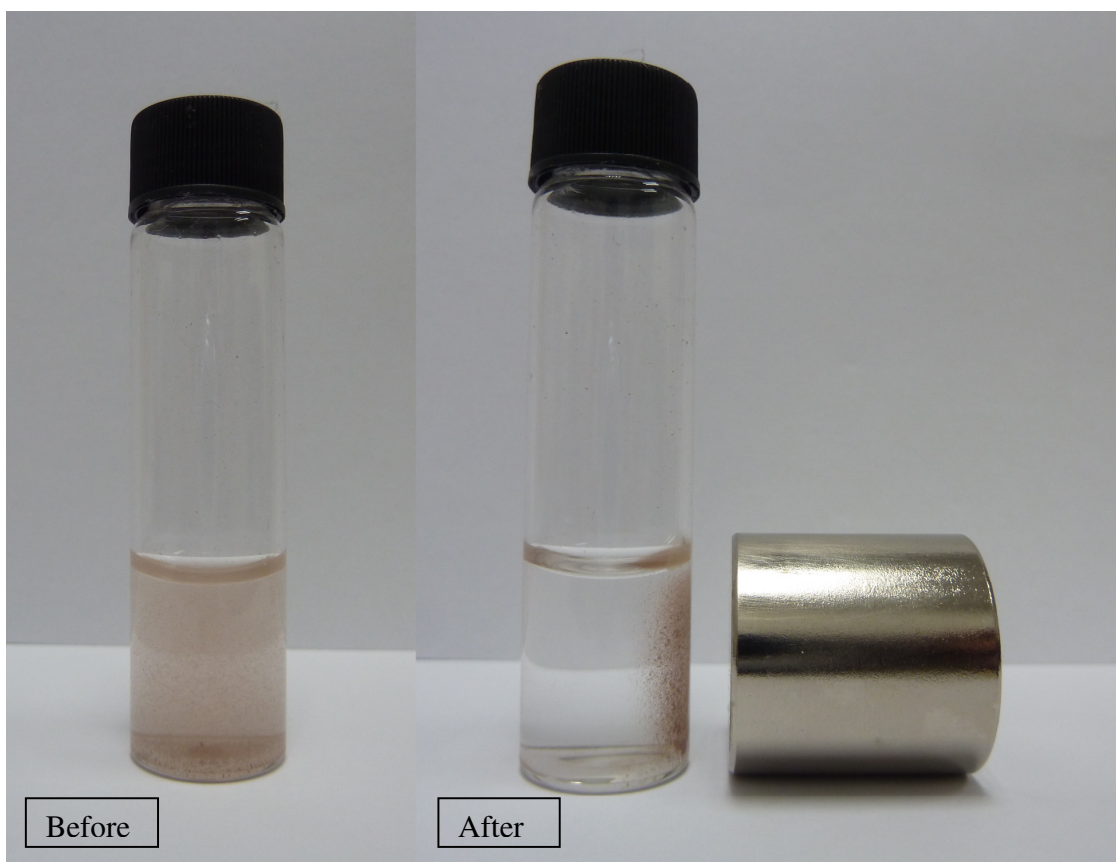


Figure 6.17: Separation of  $\text{TiO}_2/\text{Fe}_3\text{O}_4$  powder in degraded MB dye solution by applying a magnetic field.

### 6.3.8 Repeatability analysis

In order to gain an insight on photocatalytic stability of the 1 wt% doped  $\text{Fe}_3\text{O}_4$  sintered at 350 °C of  $\text{TiO}_2/\text{Fe}_3\text{O}_4$  nanocomposites, the recycling experiment was conducted through similar experimental conditions. It is very important for the  $\text{TiO}_2/\text{Fe}_3\text{O}_4$  nanocomposites photocatalyst to go

through the recycling experiment in making sure the photocatalyst is durable, stable and last long for practical application purposes. After the photodecomposition for the first run, the nanocomposite was retrieved through magnetic separation so that it can be used for the subsequent analysis. Figure 6.18 shows that no significant changes were seen in terms of degradation efficiency throughout the three runs, with the percentage of degradation of 84.19, 87.32 and 87.92% for the first, second and third run, respectively. It shows that this  $\text{TiO}_2/\text{Fe}_3\text{O}_4$  nanocomposites has no memory effect since the percentage of decomposition do not decrease after retrieved and reused for 3 times. In addition, this also shows that the prepared  $\text{TiO}_2/\text{Fe}_3\text{O}_4$  nanocomposites have high photocatalytic stability which can be retrieved easily by using external magnetic field and to be reused in the subsequent treatment process.

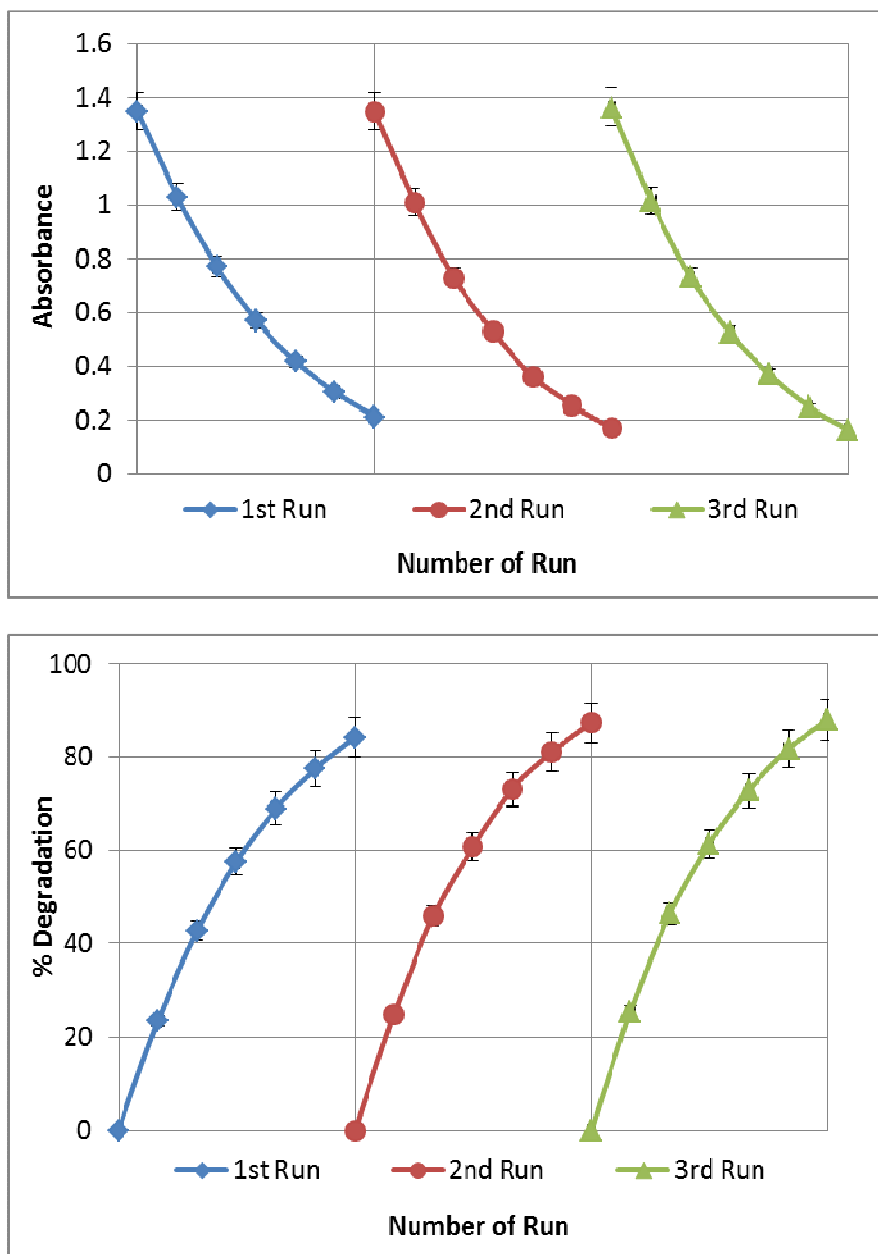


Figure 6.18: Repeatability analysis for TiO<sub>2</sub>/Fe<sub>3</sub>O<sub>4</sub> nanocomposites.

#### **6.4 Summary**

From the above results and discussion, it indicates that the preparation of the magnetic  $\text{TiO}_2/\text{Fe}_3\text{O}_4$  nanocomposites have been successfully achieved. Detail characteristics of the magnetic nanocomposites, such as loading amount of photocatalyst, appropriate doping of  $\text{Fe}_3\text{O}_4$  nanoparticle and sintering temperature have been performed to determine the optimum processing parameters. The optimum loading amount of the  $\text{TiO}_2/\text{Fe}_3\text{O}_4$  nanocomposites for highest degradation rate was 3.0 wt%. The appropriate ratio for the doping of  $\text{Fe}_3\text{O}_4$  into the  $\text{TiO}_2$  nanoparticle as well as the sintering temperature of the  $\text{TiO}_2/\text{Fe}_3\text{O}_4$  magnetic nanocomposite has also been obtained. The optimum amount for  $\text{Fe}_3\text{O}_4$  doped was 1 wt% with sintering temperature of 350 °C. The  $\text{TiO}_2/\text{Fe}_3\text{O}_4$  nanocomposites was also successfully retrieved and reused, without any significant changes on the photocatalytic capability.

## **CHAPTER 7**

### **Photodecomposition of Few Dyes by ZnO/Fe<sub>3</sub>O<sub>4</sub>**

#### **7.1 Introduction**

There have been various coloured chemical substances generated within the last few decades, 10,000 of which are industrially produced. On a global scale, over 0.7 million tons of organic synthetic dyes are manufactured each year mainly for use in textile, leather goods, industrial painting, food, plastics, cosmetics, and consumer electronic sectors. Considerable amounts are discarded into the wastewater during the process. Wastewater from industries is highly polluted because of most of the dyes that are used contain benzoic groups, which could give rise to carcinogenic degradation products due to e.g. microbial processes. But this is not all, the dye pollution generate many problems in the photosynthetic aquatic plants and algae because the dye absorbs most of the light the organisms need to survive (Das, Dey et al. 1995, Banat, Nigam et al. 1996).

Textile dyes and other industrial dyestuffs constitute one of the largest groups of organic compounds that represent an increasing environmental danger. About 10-20% of the total world production of dyes is lost during the synthesis, dyeing, printing and finishing process and is released in the textile effluents. It was estimated that about 615 tons of this toxic and

recalcitrant dyes being released into the environment and ecological system each day (Houas, Lachheb et al. 2001, Giwa, Nkeonye et al. 2012). The release of those coloured wastewaters into the environment is a critical source of non-aesthetic pollution and eutrophication and can originate dangerous by-products through oxidation, hydrolysis or other chemical reactions taking place in the wastewater phase (Bian, Tachikawa et al. 2012).

Therefore, decolourization and detoxification of organic dye effluents have taken an increasingly important environmental significance in recent years. Moreover, water recycling from the wastewater effluent has been recognised to be a strategic approach in water sustainability management to minimise the growing water element in a water-scarce environment (Ahmed, Rasul et al. 2010).

## **7.2 Background Study**

The amount of wastewater from the textile industries is abundance and it keeps on escalating with the effects of the growing demand for the textile products. The release of wastewater into the environment can be the reason for serious health and environmental problems because textile industries use many chemical compounds, including dyestuffs. The dyestuffs in wastewater and their breakdown products might have toxic and/or

mutagenic features to life (Weisburger 2002). Without any treatment, these dyes can be stable and remain in the environment (Hao, Kim et al. 2000).

Optimization procedure for the treatment of dye wastewater is an enormous task, made extremely complex by the thousands of dyestuffs currently commercially available. Dyes among the various classes (e.g., azo, anthraquinone) exhibit different chemical characteristics and, consequently, respond differently to treatments that focused at their particular classes. Industries group dyes into their chemical classes such as azo, anthraquinone, sulfur, indigoid, triphenylmethyl (trityl), and phthalocyanine derivatives (Forgacs, Cserhati et al. 2004). As discussed in the earlier chapter, the impact of the pollution into the environment could be removed, or reduced, from the wastewaters through three kinds of treatment techniques, such as chemical, physical and biological treatment techniques (Robinson, McMullan et al. 2001, Pearce, Lloyd et al. 2003).

Reactive dyes is a class of highly coloured organic substances and widely used in textile industry. It is also due to some advantages that this class of dyes have such as wide variety of colour shades, easy of application, good colour fastness and brilliant colour. Reactive dyes bind to their substrates by chemical reactions that form covalent bonds with reactive groups, such as OH, NH or SH in fibers such as cotton, nylon and wool (Lewis and Loan 2007). Synthetic dyes such as azo dyes, xanthene dyes and

anthraquinone dyes are not environmental friendly due to their toxicity to living organisms (Meyer 1981).

Azo dyes are the largest group of dyes with large industrial application. They stand for almost 70% of the textile dyestuffs produced by weight (Knackmuss 1996). Besides, azo dyes are cost-effective due to their synthesis ease and versatility (Saroj, Kumar et al. 2014). They are used in the colouring process of several textiles and leather products due to their variety in colour compared with natural dyes. Azo dyes contain at least one or more azo groups ( $-N=N-$ ) double bond with one or more aromatic systems (Wong and Yuen 1998). Azo dyes are classified into two subgroups according to number of their double bond as mono-azo and poly azo types for one and more double bond, respectively (Zollinger 1987). There are high amounts of azo dyes in the environment because of breakdown of azo bonds ( $R-N=N-R$ ) is quite difficult and they can be stable in acidic and alkaline conditions. They are resistant to high temperatures and light (Wong and Yuen 1996). In addition, their reductive degradation products, especially aromatic amines, are mutagenic (Chung, Stevens et al. 1992). Anthraquinone dyes represent the second most important class of textile dyes. They have a large range of colours. Anthraquinone dyes are used to colour cellulosic fabric, wool and polyamide fibres (Katsuda, Omura et al. 1997).

Dye wastewaters are extremely variable in composition, due to large number of dyes and other chemicals used in dyeing processes. Many researchers have placed tremendous attention towards textile wastewater treatment processes, not only due to their colour, but also on its toxicity of most of the raw materials used to synthesize dyes (e.g., certain aromatic amines used to produce azo dyes). In addition, textile dye wastewater is generally nutrient deficient which is needed for biological treatment, however, can be provided by mixing the dye wastewater with appropriate nutrient as required.

### **7.3 Results and Discussion**

In this experiment, 5 sample dyes, Reactive Red 120 (RR120), Disperse Blue 15 (DB15), Acid Brown 14 (AB14), Orange G (OG) and Acid Orange 7 (AO7), have been randomly picked for the study of the decomposition processes by the ZnO/Fe<sub>3</sub>O<sub>4</sub> nanocomposites materials. All dyes were subsequently decomposed, with different degradation rate, when the ZnO/Fe<sub>3</sub>O<sub>4</sub> nanocomposites material is added into the individual dye solutions.

### **7.3.1 Effect of Azo Functional Group on the Photodegradation Rate**

From Figure 7.1, it shows that the rate of degradation decreases with the decreased of the number of azo functional groups, from diazo (for RR120, DB15, AB14) to monoazo (for OG, AO7) dyes.

The results could be explained through the photocatalytic degradation study by Hu and his co-workers (2003b) on the triazine-containing azo dyes, Procion Red MX (MX-5B) and Reactive Brilliant Red K-2G, in aqueous suspension of TiO<sub>2</sub>. The complete decolorization for the MX-5B and K-2G dyes were recorded at 120 and 60 minutes of irradiation, respectively. They found that the decolorization and desulfuration for both dyes have taken place at almost the same rate simultaneously (Hu, Yu et al. 2003). The effectiveness of the degradation depends on the chemical structure and the substitute groups of the organic pollutants (Behnajady, Eskandarloo et al. 2011). This K-2G dye is adsorbed to TiO<sub>2</sub> surface through sulfonate group and the degradation took place *via* the  $h_{\nu B}^+$  and surface-bounded •OH radicals on the TiO<sub>2</sub> surface or near the interface of solid and solution (Li and Wang 2004).

Hu et al. (2003) reaffirmed that the oxidation of the azo group by the •OH radicals was taken placed, firstly, at the C–N single bond between the azo group and benzene or naphthalene ring, followed by the double bonds of the azo group (Hu, Yu et al. 2003). Therefore, with higher number of azo

group certainly contributes more C–N single bonds in the particular organic dyes. The number of C–N single bonds is counted as 12, 6, 4, 2 and 2 bonds for the RR120, DB15, AB14, OG and AO7 dyes, respectively. On the other hand, the number of sulfonate group for RR120, DB 15, AB14, OG and AO7 dyes are 6, 4, 2, 2 and 1, respectively. Since these two chemical processes going on simultaneously, they enhanced the decolourisation process and thus the results in Figure 7.1 was recorded. In the same year, Hu et al. (2003) has also reported very detail study on the degradation of the cationic blue X–GRL dye by the TiO<sub>2</sub>/SiO<sub>2</sub> photocatalyst (Hu, Tang et al. 2003).

On the other hand, although Abo-Farha (2010) reported that monoazo dye (AO10) was easily degraded as compared to the diazo dye (AR114) at their optimal conditions, which are different for each dye, such as H<sub>2</sub>O<sub>2</sub> dose and photocatalyst loading were recorded as 10 mM and 0.05 g/L and 50 mM and 0.15 g/L for AO10 and AR114, respectively. Nonetheless, at dye concentration of  $1.0 \times 10^{-4}$  M, the diazo dye (AR114) has higher degradation rate than the monoazo dye (AO10) (Abo-Farha 2010).

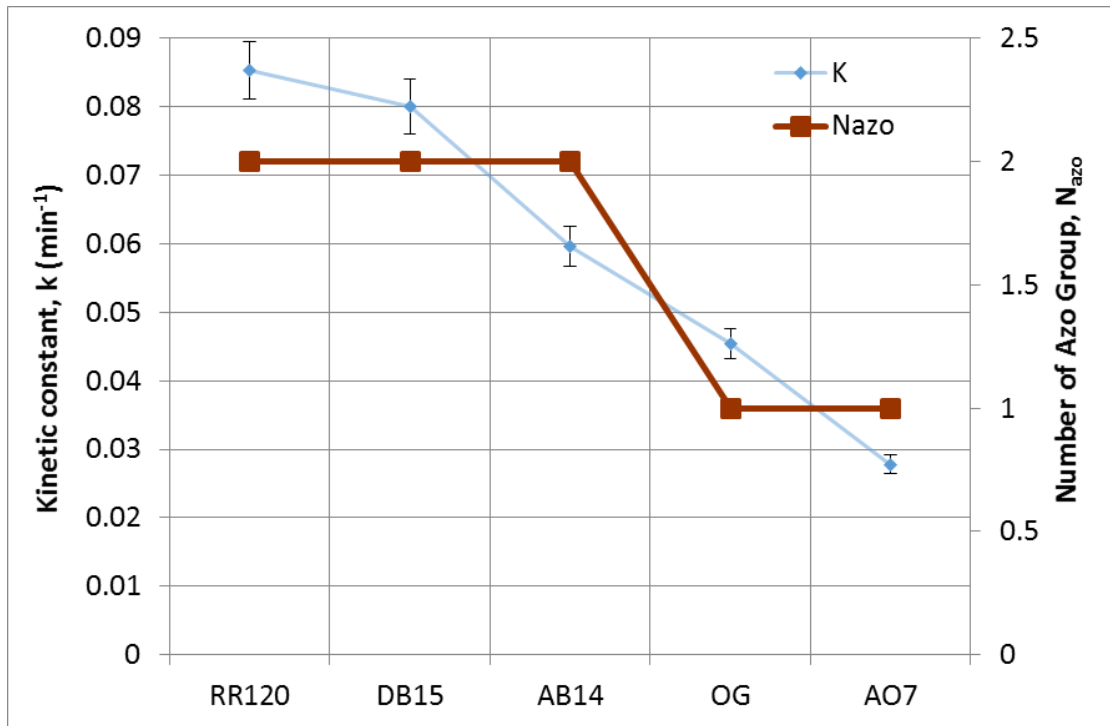


Figure 7.1 The kinetic constant and azo functional group of five dyes under decomposition of ZnO/Fe<sub>3</sub>O<sub>4</sub> composites nanoparticles.

### **7.3.2 Effect of Benzene Group on the Photodegradation Rate**

Figure 7.2 shows the kinetic constant in relation to the number of benzene functional group. The graph showed that the dyes degraded faster for dyes with higher number of benzene group. This result could be similarly explained from the point of the different structures and substituent groups possessed by those organic dyes. A study by Hu et al. (2006) on the degradation of four azo dyes (reactive red K-2G, reactive brilliant red X-3B, reactive red K-2BP, and reactive yellow KD-3G) in AgI/TiO<sub>2</sub> aqueous dispersions under visible light irradiation ( $\lambda = 420$  nm) could explain this result in details (Hu, Hu et al. 2006). The result they obtained from the FT-IR spectra and further confirmed by the GC-MS result, has strengthened and clearly identify the generation of reaction intermediates during the first 10 hrs and 30 hrs of the photodegradation of the organic dyes. They found that the broken of the azo bond and the benzene ring, as well as desulfuration occurred as when the decolourisation takes place.

Moreover, while phthalic acid was formed by the hydroxylation of naphthalene ring, glycerol and benzoic acid were still detectable from the solutions. As the measurement was made for the following irradiation duration, benzoic acid and phthalic acid were all oxidised into different aliphatic acids, such as 2-hydroxy-propanoic acid and succinic acid.

In addition, in another report by Hu et al. (2003) on the photodegradation of an azo dye, cationic blue X-GRL, solution with the suspension of  $\text{TiO}_2/\text{SiO}_2$  photocatalyst particles, could further clarify the above report (Hu, Tang et al. 2003). In this report, their characterization on the reaction solution by FT-IR during the first 2 hrs of irradiation has depicted a complete disappearance of the absorption band from the benzene ring and the C-N of aromatic amide when the colour has totally cleared. Therefore, the result from this experiment is fairly accommodates the earlier reported studies which the rate of degradation is directly proportional to the number of benzene group.

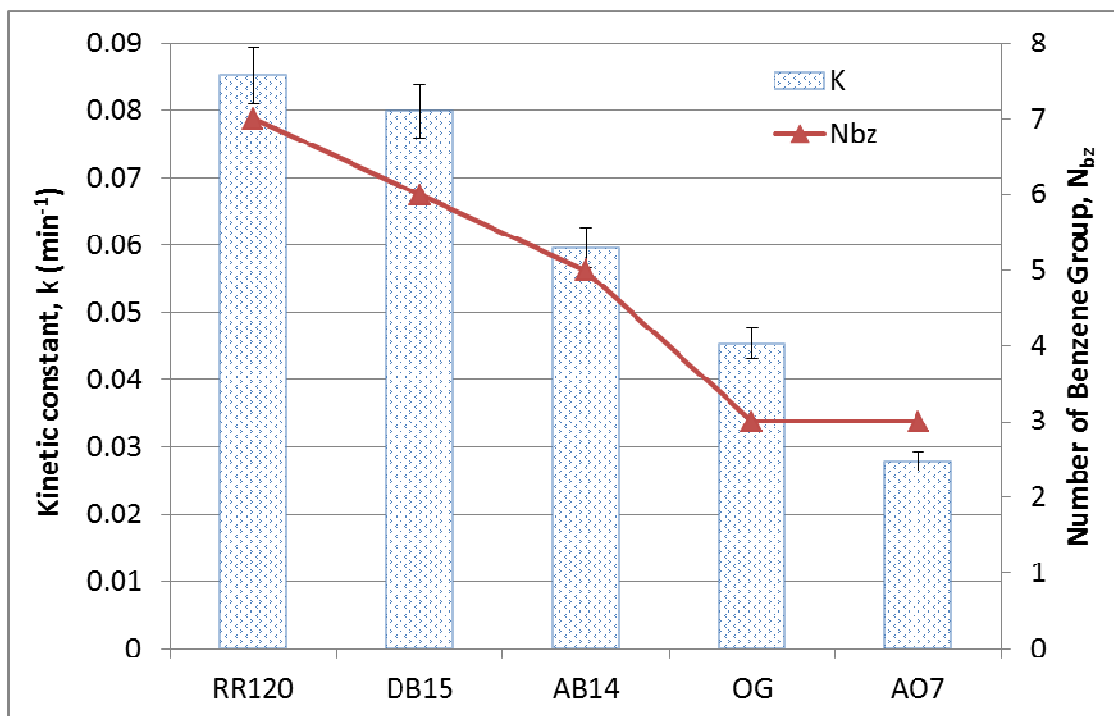


Figure 7.2 The kinetic constant and benzene functional group of five dyes under decomposition of  $\text{ZnO}/\text{Fe}_3\text{O}_4$  composites nanoparticles.

### **7.3.3 Effect of Molecular Mass on the Photodegradation Rate**

Figure 7.3 shows the change of the dyes molecular mass with their rate of degradation. The degradation rate decreased proportionally with the decreases of dyes molecular mass. A study was conducted by Ong and his group of researchers (2012) on the photocatalytic degradation of mono azo dyes, acid orange 7 and methyl orange, under solar light irradiation with TiO<sub>2</sub> as a photocatalyst (Ong, Min et al. 2012). They applied several operational parameters in the process to determine the degradation rate of the azo dyes. Their data fitted well with the pseudo-first-order kinetic derived from the Langmuir–Hinshelwood kinetic model. Their result showed that AO7 was degraded more rapidly than MO dye. This could be attributed to the different molecular structure of the azo dyes and the capability of the dyes to be adsorbed onto the TiO<sub>2</sub> surface (Ong, Min et al. 2012). In addition, AO7 has a higher molecular mass ( $M_{w,AO7} = 350.32$  g/mol) as compared to the MO ( $M_{w,MO} = 327.33$  g/mol) dye.

In this study, RR120 has higher molecular mass as compared to OG and AO7. Therefore, it has many molecular structures such as C-N single bonds and higher number of sulfonate group. Photocatalytic degradation process normally takes place at these functional groups, which indicates that the degradation took place by attacking these structures. Therefore the photodecomposition rate for RR120 was higher, due to the higher number of reaction sites available.

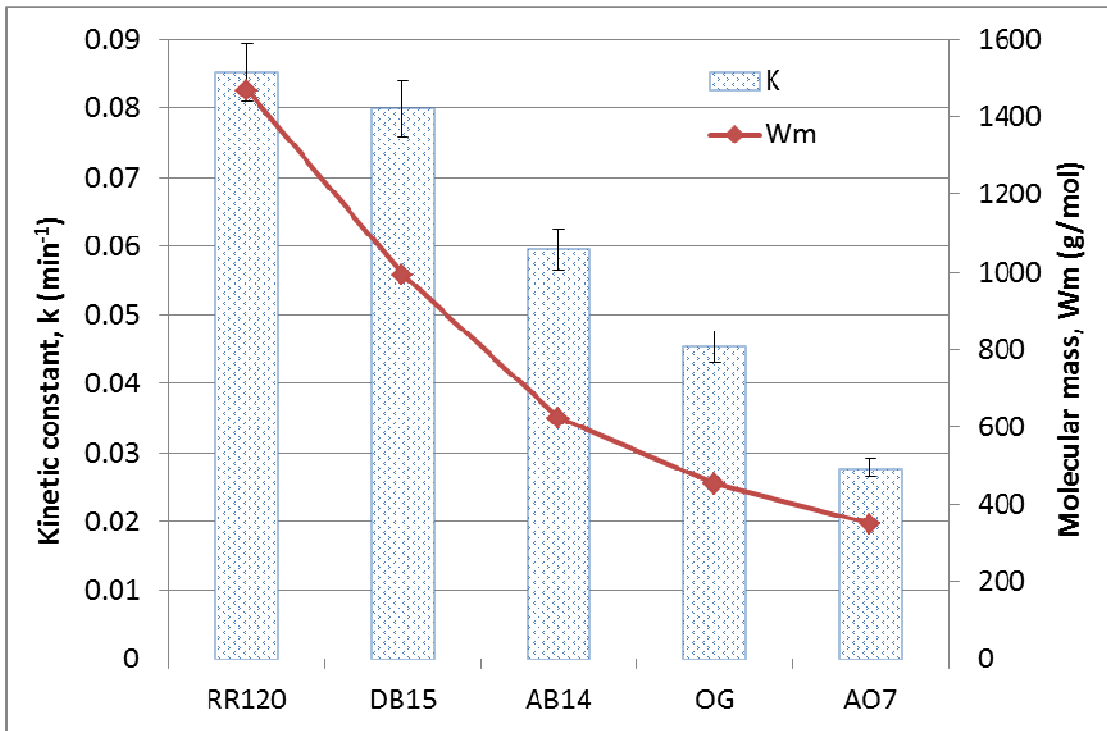


Figure 7.3 The kinetic constant and molecular mass of five dyes under decomposition of ZnO/Fe<sub>3</sub>O<sub>4</sub> composites nanoparticles.

### **7.3.4 Effect of Absorbance on the Photodegradation Rate**

Absorbance is the measure of the amount of light absorbed by a material (chemical substance). The basic principle is that each chemical compound absorbs or transmits light over a certain range of wavelength. This analysis is used because absorbance increases linearly with the increasing concentration of the absorbing compounds. As can be seen from Figure 7.4, the degradation rate decreased as the absorbance increases. Although the absorbance for AB14 and OG is seemingly very close, there is actually an increase in the absorbance between AB14 (1.3679) and OG (1.4202). Therefore, when the degradation rate decreased, there is an increase in the absorbance value, albeit is very minimal. The reason is unknown and recommended for future study.

The report by Hu and his co-workers (2003) on the photodegradation of Procion Red MX (MX-5B) and Reactive Brilliant Red K-2G (K-2G) dyes, with similar concentration of 100 mg/L, in aqueous suspension of TiO<sub>2</sub> (Hu, Yu et al. 2003). The molecular mass for MX-5B and K-2G is 615.33 and 876.077 g/mol, respectively. The absorbance for MX-5B (~0.78) is higher than the K-2G (~0.34) dye. Moreover, the K-2G dye was completely decolourised in just 1 hour whereas the MX-5B dye took 2 hours (Hu, Yu et al. 2003). This result was in agreement with the result obtained in this study, as shown in Figure 7.4. This clarify that the absorbance is inversely proportional to the rate of decolourisation, for the same concentration of dyes.

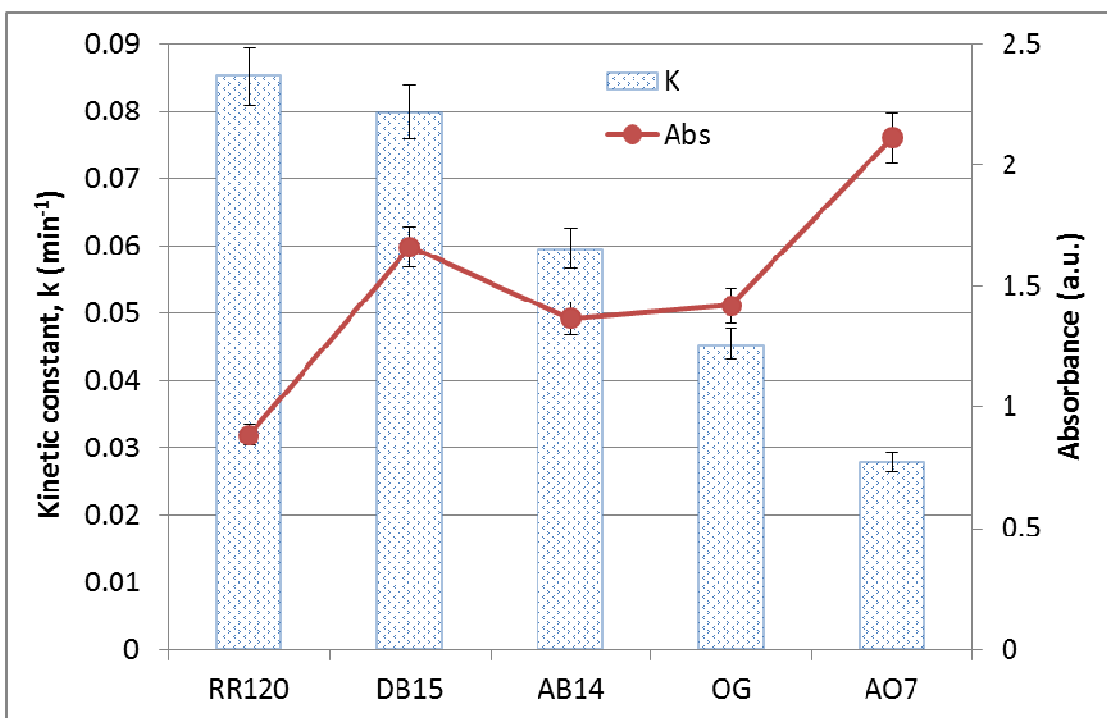


Figure 7.4 The kinetic constant and absorbance of five dyes under decomposition of ZnO/Fe<sub>3</sub>O<sub>4</sub> composites nanoparticles.

## 7.4 Summary

The study on 5 dyes, Reactive Red 120 (RR120), Disperse Blue 15 (DB15), Acid Brown 14 (AB14), Orange G (OG) and Acid Orange 7 (AO7), with the addition of ZnO/Fe<sub>3</sub>O<sub>4</sub> composites nanoparticles under UV light irradiation has been conducted. The results of this study can be concluded that the degradation rate of the organic dyes is directly proportional to the number of azo groups, the number of benzene groups, the molecular weight of the dyes and inversely proportional to the absorbance of the dyes' solution, as depicted in Figure 7.5.

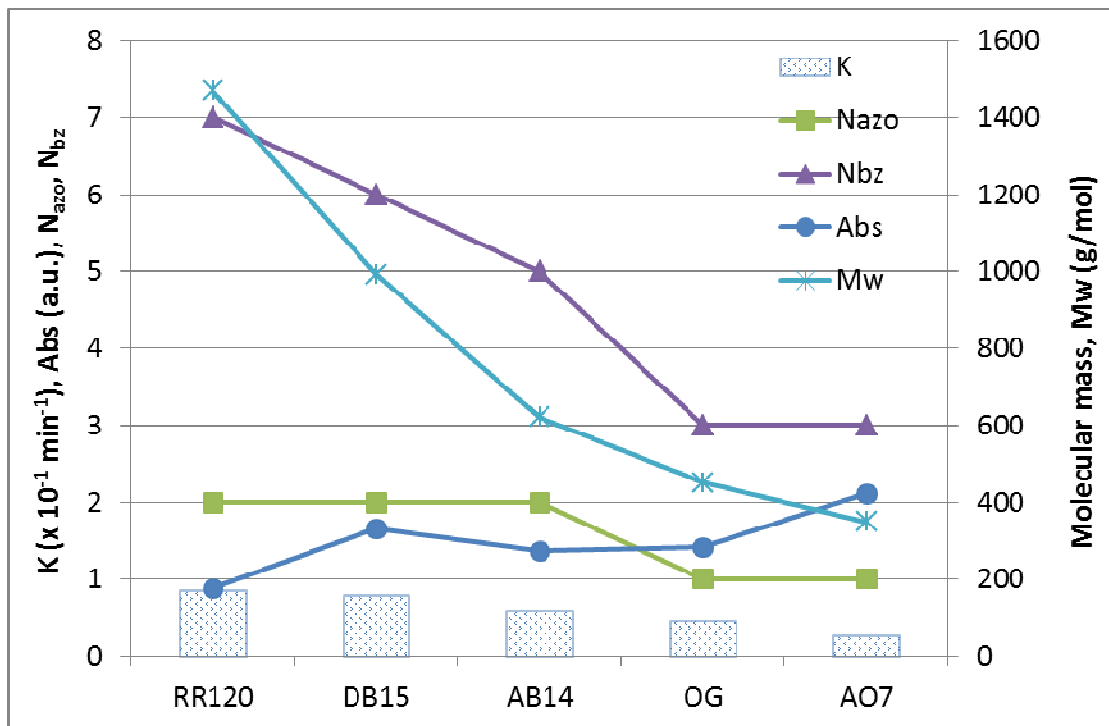


Figure 7.5 The kinetic constant of five dyes with various operational parameters under decomposition of ZnO/Fe<sub>3</sub>O<sub>4</sub> composites nanoparticles.

## **CHAPTER 8**

### **Conclusion and Proposition**

#### **8.1 Conclusion**

Current study is focusing on developing new magnetic photocatalytic nanocomposites through a simple, facile and cost-efficient preparation method. These nanocomposites would consist of dual functions which could significantly photodegrade organic contaminants and as well as separation of the nanocomposite through magnetic induction. During the process of realizing these nanocomposites materials, several aspects were monitored, such as the preparation, characterization and photocatalytic performance.

There were two novel nanocomposites have been prepared, which include ZnO/Fe<sub>3</sub>O<sub>4</sub> and TiO<sub>2</sub>/Fe<sub>3</sub>O<sub>4</sub> nanocomposite materials. ZnO and TiO<sub>2</sub> are chosen in this study due to their highly researched photocatalytic materials with excellent photocatalytic activity. Besides, these two oxides are nontoxic, structurally stable, low cost and widely available (Topkaya, Konyar et al. 2014). They are effective photocatalyst under UV light irradiation due to their quite similar and wide band gap of 3.2 eV at room temperature (Topkaya, Konyar et al. 2014). On the other hand, Fe<sub>3</sub>O<sub>4</sub> nanoparticles are used for its magnetic characteristic since it does not

contribute significant impact towards photocatalytic decomposition of organic contaminants (Singh, Barick et al. 2013).

The initial part of the study was performed by scrutinizing the physical characteristics and photocatalytic performance of the three oxides, i.e. ZnO, TiO<sub>2</sub> and Fe<sub>3</sub>O<sub>4</sub> nanoparticles. The ZnO nanoparticles consist of variation of shape from square like to elongated shapes. Its particles were well dispersed accompanied with some pores, and no agglomeration was observed. The particle size was measured within the range of 48 – 778 nm (32 – 381 nm for TEM). The XRD and EDX analysis confirmed the purity of ZnO in the form of wurtzite hexagonal crystal structure and that matched with the standard JCPDS card.

On the other hand, TiO<sub>2</sub> nanoparticles exist in the form of spherical shapes. It exists as a tetragonal crystal structure and its particle size was in the range of 32 – 175 nm (32 – 206 nm for TEM). In addition, Fe<sub>3</sub>O<sub>4</sub> nanoparticles appear as a pure cubic crystal structure with particle size in the range of 16 – 190 nm (23 – 134 nm for TEM). From the micrograph, Fe<sub>3</sub>O<sub>4</sub> also shows no agglomeration with well dispersed and high porosity nanoparticles.

These three nanoparticles were initially employed for the decomposition of the MB dye followed by PR and MO dyes. These three dyes were chosen as model dyes due to their different functional groups to

observe their photodegradability processes. Amongst these dyes, only MB is self-degradable, which means it was slowly degraded under the UV light with the absence of the photocatalyst, while this is not being observed for the other two dyes.

For the photocatalytic measurement, ZnO nanoparticles was found to be the better photocatalytic material as compared to TiO<sub>2</sub> and Fe<sub>3</sub>O<sub>4</sub>, whereas the weakest is the Fe<sub>3</sub>O<sub>4</sub> nanoparticles. The kinetic constants (and correlation coefficient) for the degradation of MB dye with concentration of 12.0 ppm, were 0.2221 (0.9913), 0.1012 (0.9861) and 0.0040 min<sup>-1</sup> (0.9904), for ZnO, TiO<sub>2</sub> and Fe<sub>3</sub>O<sub>4</sub> nanoparticles, respectively. On the other hand, the hardest dye to decompose was the MO dye, followed by PR and MB. It were recorded that the kinetic constants (and correlation coefficient) for 12.0 ppm concentration of MO dye, when decomposed with ZnO, TiO<sub>2</sub> and Fe<sub>3</sub>O<sub>4</sub> nanoparticles, were 0.0868 (0.9427), 0.0103 (0.9925) and 0.000030 min<sup>-1</sup> (0.1302), respectively. MO dye is the most recalcitrant organic material which possesses the azo functional group (-N=N-), whereas PR is a form of zwitterion (dipolar ion) cyclic group with sulfate and ketone group attached to it. It is a pH indicator that is frequently used in cell biology laboratories. On the other hand, MB is a heterocyclic aromatic chemical compound and a cationic thiazine dye.

For different initial concentration of dyes, it can be deduced that the percentage of degradation was higher for solution with lower concentration

for the same duration of irradiation, which means that the percentage degradation is inversely proportional to the concentration of the solution. In addition, the photodegradation rates were highly depending on the types of organic dyes and the amount of the nanocomposites photocatalyst loading.

The second part of this study is to fabricate ZnO/Fe<sub>3</sub>O<sub>4</sub> and TiO<sub>2</sub>/Fe<sub>3</sub>O<sub>4</sub> nanocomposites from the ZnO, TiO<sub>2</sub> and Fe<sub>3</sub>O<sub>4</sub> nanopowders. These nanocomposites photocatalysts were prepared through mechanical mixing method. The prepared nanocomposites were well mixed with no agglomeration and were homogeneous. Their average diameter could be recorded within the range of 94 – 259 nm, that is (162 ± 12) nm. It exists as mixed of pure wurtzite crystal of ZnO and cubic of Fe<sub>3</sub>O<sub>4</sub> and can be matched with the standard JCPDS pattern. Similarly, for the TiO<sub>2</sub>/Fe<sub>3</sub>O<sub>4</sub> nanocomposites, the XRD patterns show that the prepared nanocomposites are highly crystalline with both TiO<sub>2</sub> and Fe<sub>3</sub>O<sub>4</sub> crystalline structures co-existed in the spectrum. Their average diameter is recorded within the range of 44 – 171 nm, that is (86.2 ± 9.0) nm.

Through a measurement with VSM, both of the nanocomposites exhibit attractive magnetic characteristic. The nanocomposites were successfully retrieved by applying an external magnetic field. Each nanocomposites can be reused for the consecutive decomposition process. Based on the analysis, the nanocomposites were found to be reused for up to three consecutive treatments without huge drop in the photocatalytic performance. Only slight

deactivation throughout the three runs especially for the ZnO/Fe<sub>3</sub>O<sub>4</sub> nanocomposites photocatalyst. This may be due to the memory effect such as the earlier remnants that attached onto the surface of the nanocomposites and disturbed the stability of the reactive sites available for the photocatalytic process to take place.

The prepared ZnO/Fe<sub>3</sub>O<sub>4</sub> and TiO<sub>2</sub>/Fe<sub>3</sub>O<sub>4</sub> nanocomposites were employed for the decomposition of MB. The ZnO/Fe<sub>3</sub>O<sub>4</sub> nanocomposite photocatalyst has been successfully scrutinized by having the optimum loading of 9.0 wt%, 10 wt% of doped Fe<sub>3</sub>O<sub>4</sub> and 300 °C of sintering temperature. On the other hand, the optimum loading for TiO<sub>2</sub>/Fe<sub>3</sub>O<sub>4</sub> nanocomposites is found to be 3.0 wt%. TiO<sub>2</sub>/Fe<sub>3</sub>O<sub>4</sub> nanocomposites doped Fe<sub>3</sub>O<sub>4</sub> and sintering temperature is achieved at 1.0 wt% and 350 °C, respectively. The prepared nanocomposite was equally effective in degrading the organic dye as compared to the commercial materials.

In addition, the ZnO/Fe<sub>3</sub>O<sub>4</sub> nanocomposites photocatalyst has also been utilized to study the photodegradation of 5 different organic dyes, Reactive Red 120 (RR120), Disperse Blue 15 (DB15), Acid Brown 14 (AB14), Orange G (OG) and Acid Orange 7 (AO7) in order to evaluate the effect of number of azo groups, benzene groups, molecular mass and absorbance on the photodegradation efficiency. It is found that the degradation rate increases with the increased of the azo group. Similar observation was obtained for the photocatalytic efficiency with the benzene group which

shows higher degradation rate with the presence of higher numbers of benzene group in the organic dye molecule. Next, the analysis was scrutinised at the effect of the molecular mass on the photodegradation rate. It was found that the degradation rate increased when applied with higher molecular mass of organic dye. Moreover, when the effect of absorbance was studied, it shows an inverse relationship with the photodegradation rate, that is the photodegradation rate decreases with the increased of the absorbance.

## **8.2 Future Recommendation**

It is undeniable that this study has achieved a significantly new way to prepare magnetic photocatalytic nanocomposites with good photoreaction and magnetically separable. This novel finding would greatly contribute and assist for the technological treatment in the textile as well as other dyes related industries. However, there are still many routes for improvement and optimization to be realized as commercially applicable and reliable materials. Therefore, proper focus needs to be placed on the surface area optimization as well as the reactor design to facilitate the mass scale production of these nanocomposites materials.

First property that needs to focus is the surface area. Currently, the raw powder was commercially obtained, which was used without any

modification. Their surface area is comparatively smaller, that is 2.406 and 6.795 m<sup>2</sup>/g, for ZnO and TiO<sub>2</sub>, respectively. Therefore, to improve the total surface area of the raw materials, the preparation method, especially mixing of the semiconductor oxides need to be improved. One of the common methods, which is a typical solid state reaction method is by mixing and ground manually in an agate mortar to obtain fine powder. Using agate mortar would certainly results in a smaller particle size for the mixed powder. Then the mixture can be applied to any required calcined temperature as required to obtain the final nanocomposite powder.

On the other hand, to further improved the mixing process and particle size, which is size reduction, is through mechanical ball mixing, which is a commercial and practical ways of mixing powder. The ball milling process offers several benefits which include particle size reduction, mixing/blending, and particle shape changes. The common ball mill used is a planetary ball mill; a bowl sits on a grinding platform equipped with stainless steel spheres and rotates in a direction opposite to the direction of the base fixture. This action is a lot similar to the "teacup and saucer" rides commonly found in most amusement parks.

Moreover, instead of dry mixing, those semiconductor powders can also be mixed by applying the wet ball milling. A readily prepared of the mixed semiconductor powder is placed into a ball mill jar (~500 ml) which contained an appropriate solvent (like water, ethanol, methanol, etc.) and

ball mill. A certain powder to ball ratio needs to be chosen in achieving significant impact. Normally a 5 mm diameter zirconia balls and the zirconia jar were used as milling media. Generally, the milling process is performed for duration of 1 hour which already provides a good mixture. However, the milling process could be fixed at longer duration to obtain the required particle size. This is because as the milling period is longer, there will be more collision between the ball mill and the semiconductor powder which resulted in smaller particle size.

## **REFERENCE**

- Abo-Farha, S. A. (2010). Photocatalytic Degradation of Monoazo and Diazo Dyes in Wastewater on Nanometer-Sized TiO<sub>2</sub>. *Journal of American Science*, 6(11), 130-140.
- Abrahams, J., Davidson, R. S., & Morrison, C. L. (1985). Optimization of the photocatalytic properties of titanium dioxide. *Journal of Photochemistry & Photobiology, A: Chemistry*, 29(3-4), 353-361.
- Adachi, M., Jiu, J., Isoda, S., Mori, Y., & Uchida, F. (2008). Self-assembled nanoscale architecture of TiO<sub>2</sub> and application for dye-sensitized solar cells. *Nanotechnol. Sci. Appl.*, 1, 1-7.
- Ahmad, M., Hong, Z., Ahmed, E., Khalid, N. R., Elhissi, A., & Ahmad, W. (2013). Effect of fuel to oxidant molar ratio on the photocatalytic activity of ZnO nanopowders. *Ceramics International*, 39(3), 3007-3015. doi:10.1016/j.ceramint.2012.09.079
- Ahmed, L. M., Ivanova, I., Hussein, F. H., & Bahnemann, D. W. (2014). Role of Platinum Deposited on TiO<sub>2</sub> in Photocatalytic Methanol Oxidation and Dehydrogenation Reactions. *International Journal of Photoenergy*, 2014, 503516.
- Ahmed, S., Rasul, M. G., Martens, W. N., Brown, R., & Hashib, M. A. (2010). Heterogeneous photocatalytic degradation of phenols in wastewater: A review on current status and developments. *Desalination*, 261(1-2), 3-18. doi:10.1016/j.desal.2010.04.062
- Akimov, A. V., Neukirch, A. J., & Prezhdo, O. V. (2013). Theoretical insights into photoinduced charge transfer and catalysis at oxide interfaces. *Chem Rev*, 113(6), 4496-4565. doi:10.1021/cr3004899
- Akpan, U. G., & Hameed, B. H. (2009). Parameters affecting the photocatalytic degradation of dyes using TiO<sub>2</sub>-based photocatalysts: A review. *Journal of Hazardous Materials*, 170, 520-529.
- Al-Ekabi, H., & Mayo, P. D. (1985). Surface photochemistry: cadmium sulfide photoinduced cis-trans isomerization of olefins. *J. Phys. Chem. B*, 89(26), 5815-5821.
- Alamo-Nole, L., Bailon-Ruiz, S., Luna-Pineda, T., Perales-Perez, O., & Roman, F. R. (2013). Photocatalytic activity of quantum dot-magnetite nanocomposites to degrade organic dyes in the aqueous phase. *J. Mater. Chem. A*, 1, 5509-5516
- Amini, M., & Ashrafi, M. (2016). Photocatalytic degradation of some organic dyes under solar light irradiation using TiO<sub>2</sub> and ZnO nanoparticles. *Nano. Chem. Res.*, 1(1), 79-86.
- Ansari, S. A., Alam, F., Khan, A., Khan, W., Chaman, M., Muneer, M., & Naqvi, A. H. (2012). Influence of Cr Doping on the Microstructural, Optical and Photocatalytic Properties of ZnO Synthesized by Sol-Gel Method. *Current Nanoscience*, 8(4), 581-586. doi:10.2174/157341312801784195
- Assi, N., Mohammadi, A., Manuchehri, Q. S., & Walker, R. B. (2015). Synthesis and characterization of ZnO nanoparticle synthesized by a microwave-assisted combustion method and catalytic activity for the removal of ortho-nitrophenol. *Desalination and Water Treatment*, 54(7), 1939-1948.

- Augugliaro, V., Litter, M., Palmisano, L., & Soria, J. (2006). The combination of heterogeneous photocatalysis with chemical and physical operations: A tool for improving the photoprocess performance. *Journal of Photochemistry and Photobiology C: Photochemistry Reviews*, 7, 127–144.
- Babuponnusami, A., & Muthukumar, K. (2014). A review on Fenton and improvements to the Fenton process for wastewater treatment. *Journal of Environmental Chemical Engineering*, 2, 557–572.
- Bacsa, R. R., & Kiwi, J. (1998). Effect of rutile phase on the photocatalytic properties of nanocrystalline titania during the degradation of p-coumaric acid. *Applied Catalysis B: Environmental*, 16(1), 19-29.
- Baffoun, A., El Ghali, A., & Hachani, I. (2017). Decolorization Kinetics of Acid Azo Dye and Basic Thiazine Dye in Aqueous Solution by UV/H<sub>2</sub>O<sub>2</sub> and UV/Fenton: Effects of Operational Parameters. *Autex Research Journal*, 17(1), 85-94. doi:10.1515/aut-2016-0031
- Bahnemann, D. W. (1993). Ultrasmall Metal Oxide Particles: Preparation, Photophysical Characterization, and Photocatalytic Properties. *Israel Journal of Chemistry*, 33(1), 115–136. doi:10.1002/ijch.199300017
- Bakhsh, N., Khalid, F. A., & Hakeem, A. S. (2014). Effect of sintering temperature on densification and mechanical properties of pressureless sintered CNT-alumina nanocomposites. *IOP Conf. Series: Materials Science and Engineering*, 60, 012059.
- Banat, I. M., Nigam, P., Singh, D., & Marchant, R. (1996). Microbial decolorization of textile-dyecontaining effluents: A review. *Bioresource Technology*, 58(3), 217-227.
- Bansal, P., & Sud, D. (2011). Photodegradation of commercial dye, Procion Blue HERD from real textile wastewater using nanocatalysts. *Desalination*, 267(2-3), 244-249. doi:10.1016/j.desal.2010.09.034
- Baruah, S., & Dutta, J. (2009). Hydrothermal growth of ZnO nanostructures. *Science and Technology of Advanced Materials*, 10(1), 013001.
- Begum, T., Gogoi, P. K., & Bora, U. (2017). Photocatalytic degradation of crystal violet dye on the surface of Au doped TiO<sub>2</sub> nanoparticle. *Indian Journal of Chemical Technology*, 24(1), 97-101.
- Behnajady, M. A., Eskandarloo, H., Modirshahla, N., & Shokri, M. (2011). Influence of the chemical structure of organic pollutants on photocatalytic activity of TiO<sub>2</sub> nanoparticles: Kinetic analysis and evaluation of electrical energy per order (E<sub>EO</sub>). *Digest Journal of Nanomaterials and Biostructures*, 6(4), 1887-1895.
- Behnajady, M. A., Modirshahla, N., & Hamzavi, R. (2006). Kinetic study on photocatalytic degradation of C.I. Acid Yellow 23 by ZnO photocatalyst. *J Hazard Mater*, 133(1-3), 226-232. doi:10.1016/j.jhazmat.2005.10.022
- Beranek, R. (2011). (Photo)electrochemical Methods for the Determination of the Band Edge Positions of TiO<sub>2</sub>-Based Nanomaterials. *Advances in Physical Chemistry*, 2011, 786759.
- Beydoun, D., Amal, R., Low, G. K. C., & McEvoy, S. (2000). Novel photocatalyst: titania-coated magnetite. Activity and photodissolution. *J. Phys. Chem. B*, 104, 4387-4396.

- Bhukal, S., Shivali, & Singhal, S. (2014). Magnetically separable copper substituted cobalt–zinc nano-ferrite photocatalyst with enhanced photocatalytic activity. *Materials Science in Semiconductor Processing*, 26, 467-476. doi:10.1016/j.mssp.2014.05.023
- Bian, Z., Tachikawa, T., Kim, W., Choi, W., & Majima, T. (2012). Superior Electron Transport and Photocatalytic Abilities of Metal-Nanoparticle-Loaded TiO<sub>2</sub> Superstructures. *The Journal of Physical Chemistry C*, 116(48), 25444-25453. doi:10.1021/jp309683f
- Bridgwater, J. (2012). Mixing of powders and granular materials by mechanical means—A perspective. *Particuology*, 10(4), 397–427.
- Byrne, J. A., Eggins, B. R., Brown, N. M. D., McKinney, B., & Rouse, M. (1998). Immobilisation of TiO<sub>2</sub> powder for the treatment of polluted water. *Applied Catalysis B: Environmental*, 17(1-2), 25-36.
- Carabante, I., Grahn, M., Holmgren, A., Hedlund, J., & Kumpiene, J. (2009). Adsorption of As (V) on iron oxide nanoparticle films studied by in situ ATR–FTIR spectroscopy. *Colloids Surf A*, 346(1-3), 106-113.
- Casbeer, E., Sharma, V. K., & Li, X.-Z. (2012). Synthesis and photocatalytic activity of ferrites under visible light: A review. *Separation and Purification Technology*, 87, 1-14. doi:10.1016/j.seppur.2011.11.034
- Cassano, A. E., & Alfano, O. M. (2000). Reaction engineering of suspended solid heterogeneous photocatalytic reactors. *Catalysis Today*, 58(2-3), 167-197.
- Cesaro, A., Naddeo, V., & Belgiorno, V. (2013). Wastewater Treatment by Combination of Advanced Oxidation Processes and Conventional Biological Systems. *J. Bioremediation & Biodegradation*, 4(8), 1000208.
- Chamjangali, M. A., Bagherian, G., Javid, A., Boroumand, S., & Farzaneh, N. (2015). Synthesis of Ag-ZnO with multiple rods (multipods) morphology and its application in the simultaneous photocatalytic degradation of Methyl Orange and Methylene Blue. *Spectrochim Acta A Mol Biomol Spectrosc*, 150, 230-237.
- Chan, H. B. S., & Ellis, B. L. (2004). Carbon-encapsulated radioactive <sup>99m</sup>Tc nanoparticles. *Adv Mater*, 16, 144-149.
- Chatterjee, D., & Dasgupta, S. (2005). Visible light induced photocatalytic degradation of organic pollutants. *Journal of Photochemistry and Photobiology C: Photochemistry Reviews*, 6(2-3), 186-205.
- Chatterjee, D., & Mahata, A. (2001). Demineralization of organic pollutants on the dye modified TiO<sub>2</sub> semiconductor particulate system using visible light. *Applied Catalysis B: Environmental*, 33, 119–125.
- Chatzitakis, A., Berberidou, C., Paspaltsis, I., Kyriakou, G., Sklaviadis, T., & Poullos, I. (2008). Photocatalytic degradation and drug activity reduction of Chloramphenicol. *Water Res.*, 42(1-2), 386-394.
- Chen, D., & Ray, A. K. (1999). Photocatalytic kinetics of phenol and its derivatives over UV irradiated TiO<sub>2</sub>. *Applied Catalysis B: Environmental*, 23, 143–157.
- Chen, F., Xie, Y., Zhao, J., & Lu, G. (2001). Photocatalytic degradation of dyes on a magnetically separated photocatalyst under visible and UV irradiation. *Chemosphere*, 44, 1159-1168.

- Chen, J., Cen, J., Xu, X., & Li, X. (2015). The application of heterogeneous visible light photocatalysts in organic synthesis. *Catal. Sci. Technol.*, *6*(2), 349-362. doi:10.1039/c5cy01289a
- Chen, X., & Mao, S. S. (2007). Titanium Dioxide Nanomaterials: Synthesis, Properties, Modifications, and Applications. *Chem. Rev.*, *107*(7), 2891–2959.
- Cheng, X., Yu, X., Xing, Z., & Yang, L. (2016). Synthesis and characterization of N-doped TiO<sub>2</sub> and its enhanced visible-light photocatalytic activity. *Arabian Journal of Chemistry*, *9*, S1706-S1711.
- Chhabra, V., Pillai, V., Mishra, B. K., Morrone, A., & Shah, D. O. (1995). Synthesis, Characterization, and Properties of Microemulsion-Mediated Nanophase TiO<sub>2</sub> Particles. *Langmuir*, *11*(9), 3307–3311.
- Chiu, W. S., Khiew, P. S., Cloke, M., Isa, D., Tan, T. K., Radiman, S., . . . Lim, H. N. (2010). Photocatalytic study of two-dimensional ZnO nanopellets in the decomposition of methylene blue. *Chemical Engineering Journal*, *158*(2), 345-352. doi:10.1016/j.cej.2010.01.052
- Chong, M. N., Jin, B., Chow, C. W., & Saint, C. (2010). Recent developments in photocatalytic water treatment technology: a review. *Water Res*, *44*(10), 2997-3027. doi:10.1016/j.watres.2010.02.039
- Chowdhury, D., Paul, A., & Chattopadhyay, A. (2005). Photocatalytic polypyrrole-TiO<sub>2</sub>-nanoparticles composite thin film generated at the air-water interface. *Langmuir*, *21*(9), 4123-4128.
- Chung, K. T., Stevens, S. E., & Cerniglia, C. E. (1992). The reduction of Azo dyes by the intestinal microflora. *Critical Reviews in Microbiology*, *18*(3), 175-190.
- Collard, X., El Hajj, M., Su, B.-L., & Aprile, C. (2014). Synthesis of novel mesoporous ZnO/SiO<sub>2</sub> composites for the photodegradation of organic dyes. *Microporous and Mesoporous Materials*, *184*, 90-96. doi:10.1016/j.micromeso.2013.09.040
- Comparelli, R., Fanizza, E., Curri, M. L., Cozzoli, P. D., Mascolo, G., & Agostiano, A. (2005). UV-induced photocatalytic degradation of azo dyes by organic-capped ZnO nanocrystals immobilized onto substrates. *Applied Catalysis B: Environmental*, *60*(1-2), 1-11.
- Dalrymple, O. K., Yeh, D. H., & Troitz, M. A. (2007). Removing pharmaceuticals and endocrine-disrupting compounds from wastewater by photocatalysis. *Journal of Chemical Technology and Biotechnology*, *82*, 121-134.
- Dariani, R. S., Esmaili, A., Mortezaali, A., & Dehghanpour, S. (2016). Photocatalytic reaction and degradation of methylene blue on TiO<sub>2</sub> nano-sized particles. *Optik*, *127*, 7143-7154.
- Das, S. S., Dey, S., & Bhattacharyya, B. C. (1995). Dye decolorization in a column bioreactor using wood-degrading fungus *Phanerochaete chrysosporium*. *Indian Chem. Eng. Sect. A*, *37*, 176-180.
- Davis, A. P., & Huang, C. P. (1989). Removal of Phenols from Water by a Photocatalytic Oxidation Process. *Water Science and Technology*, *21*(6-7), 455-464.
- Deraz, N. M., & Alarifi, A. (2012). Structural, morphological and magnetic properties of nano-crystalline zinc substituted cobalt ferrite system. *Journal of Analytical and Applied Pyrolysis*, *94*, 41-47. doi:10.1016/j.jaap.2011.10.004
- DeRosa, M. C., & Crutchley, R. J. (2002). Photosensitized singlet oxygen and its applications. *Coordination Chemistry Reviews*, *233-234*, 351-371.

- Detle, C., Perez-Osorio, M. A., Kley, C. S., Punke, P., Patrick, C. E., Jacobson, P., . . . Kern, K. (2014). TiO<sub>2</sub> Anatase with a Bandgap in the Visible Region. *Nano Lett.*, *14*(11), 6533–6538. doi:10.1021/nl503131s
- Devi, L. G., & Kavitha, R. (2013). A review on non metal ion doped titania for the photocatalytic degradation of organic pollutants under UV/solar light: Role of photogenerated charge carrier dynamics in enhancing the activity. *Applied Catalysis B: Environmental*, *140-141*, 559-587. doi:10.1016/j.apcatb.2013.04.035
- Dewi, S. H., Sutanto, Fisli, A., & Wardiyati, S. (2016). Synthesis and Characterization of Magnetized Photocatalyst Fe<sub>3</sub>O<sub>4</sub>/SiO<sub>2</sub>/TiO<sub>2</sub> by Heteroagglomeration Method. *Journal of Physics: Conference Series*, *739*, 012113. doi:10.1088/1742-6596/739/1/012113
- Dindar, B., & İçli, S. (2001). Unusual photoreactivity of zinc oxide irradiated by concentrated sunlight. *Journal of Photochemistry and Photobiology A: Chemistry*, *140*(3), 263-268.
- Dozzi, M., & Selli, E. (2013). Specific Facets-Dominated Anatase TiO<sub>2</sub>: Fluorine-Mediated Synthesis and Photoactivity. *Catalysts*, *3*(2), 455-485. doi:10.3390/catal3020455
- Dozzi, M. V., Marzorati, S., Longhi, M., Coduri, M., Artiglia, L., & Selli, E. (2016). Photocatalytic activity of TiO<sub>2</sub>-WO<sub>3</sub> mixed oxides in relation to electron transfer efficiency. *Applied Catalysis B: Environmental*, *186*(5), 157-165.
- Dyk, A., & Heyns, A. (1998). Dispersion Stability and Photo-activity of Rutile (TiO<sub>2</sub>) Powders. *Journal of Colloid and Interface Science*, *206*, 381-391.
- El-Kemary, M., El-Shamy, H., & El-Mehasseb, I. (2010). Photocatalytic degradation of ciprofloxacin drug in water using ZnO nanoparticles. *Journal of Luminescence*, *130*(12), 2327-2331. doi:10.1016/j.jlumin.2010.07.013
- El-Sherik, A. M., & Erb, U. (1995). Synthesis of bulk nanocrystalline nickel by pulsed electrodeposition. *Journal of Materials Science*, *30*(22), 5743–5749. doi:<https://doi.org/10.1007/BF00356715>
- El Ghandoor, H., Zidan, H. M., Khalil, M. M. H., & Ismail, M. I. M. (2012). Synthesis and Some Physical Properties of Magnetite Nanoparticles. *Int. J. Electrochem. Sci.*, *7*, 5734 - 5745.
- Emeline, A. V., Zhang, X., Murakami, T., & Fujishima, A. (2012). Activity and selectivity of photocatalysts in photodegradation of phenols. *J Hazard Mater*, *211-212*, 154-160. doi:10.1016/j.jhazmat.2011.11.078
- Etacheri, V., Di Valentin, C., Schneider, J., Bahnemann, D., & Pillai, S. C. (2015). Visible-Light Activation of TiO<sub>2</sub> Photocatalysts: Advances in Theory and Experiments. *Journal of Photochemistry and Photobiology C: Photochemistry Reviews*, *25*, 1-29. doi:10.1016/j.jphotochemrev.2015.08.003
- Faisal, M., Ibrahim, A. A., Harraz, F. A., Bauzid, H., Al-Assiri, M. S., & Ismail, A. A. (2015). SnO<sub>2</sub> doped ZnO nanostructures for highly efficient photocatalyst. *Journal of Molecular Catalysis A: Chemical*, *397*, 19-25.
- Faisal, M., Khan, S. B., Rahman, M. M., Jamal, A., & Abdullah, M. M. (2012). Fabrication of ZnO nanoparticles based sensitive methanol sensor and efficient photocatalyst. *Applied Surface Science*, *258*(19), 7515-7522. doi:10.1016/j.apsusc.2012.04.075

- Fan, F.-L., Qin, Z., Bai, J., Rong, W.-D., Fan, F.-Y., Tian, W., . . . Zhao, L. (2012). Rapid removal of uranium from aqueous solutions using magnetic Fe<sub>3</sub>O<sub>4</sub>@SiO<sub>2</sub> composite particles. *Journal of Environmental Radioactivity*, *106*, 40-46.
- Farre, M., Gajda-Schranz, K., Kantiani, L., & Barcelo, D. (2009). Ecotoxicity and analysis of nanomaterials in the aquatic environment. *Anal Bioanal Chem*, *393*, 81-95.
- Feng, X., & Lou, X. (2015). The effect of surfactants-bound magnetite (Fe<sub>3</sub>O<sub>4</sub>) on the photocatalytic properties of the heterogeneous magnetic zinc oxides nanoparticles. *Separation and Purification Technology*, *147*, 266-275.
- Forgacs, E., Cserhati, T., & Oros, G. (2004). Removal of synthetic dyes from wastewater: a review. *Environment International*, *30*, 953-971.
- Fujii, H., Ohtaki, M., Eguchi, K., & Arai, H. (1997). Photocatalytic activities of CdS crystallites embedded in TiO<sub>2</sub> gel as a stable semiconducting matrix. *Journal of Materials Science Letters*, *16*(13), 1086–1088.
- Fujishima, A., Rao, T. N., & Tryk, D. A. (2000). Titanium dioxide photocatalysis. *Journal of Photochemistry and Photobiology C: Photochemistry Reviews*, *1*(1), 1-21.
- Gao, S., Jia, X., Yang, S., Li, Z., & Jiang, K. (2011). Hierarchical Ag/ZnO micro/nanostructure: Green synthesis and enhanced photocatalytic performance. *Journal of Solid State Chemistry*, *184*(4), 764-769. doi:10.1016/j.jssc.2011.01.025
- Gaya, U. I., & Abdullah, A. H. (2008). Heterogeneous photocatalytic degradation of organic contaminants over titanium dioxide: A review of fundamentals, progress and problems. *J. Photochem. Photobiol. C: Photochem. Rev.*, *9*, 1-12.
- Gennari, F. C., & Pasquevich, D. M. (1998). Kinetics of the anatase–rutile transformation in TiO<sub>2</sub> in the presence of Fe<sub>2</sub>O<sub>3</sub>. *Journal of Materials Science*, *33*(6), 1571–1578.
- Ghugal, S. G., Umare, S. S., & Sasikala, R. (2015). A stable, efficient and reusable CdS–SnO<sub>2</sub> heterostructured photocatalyst for the mineralization of Acid Violet 7 dye. *Applied Catalysis A: General*, *496*, 25-31.
- Girginova, P. I., Daniel-da-Silva, A. L., Lopes, C. B., Figueira, P., Otero, M., Amaral, V. S., . . . Trindade, T. (2010). Silica coated magnetite particles for magnetic removal of Hg<sup>2+</sup> from water. *Journal of Colloid and Interface Science*, *345*, 234–240.
- Giwa, A., Nkeonye, P. O., Bello, K. A., & Kolawole, E. G. (2012). Solar Photocatalytic Degradation of Reactive Yellow 81 and Reactive Violet 1 in Aqueous Solution Containing Semiconductor Oxides. *International Journal of Applied Science and Technology*, *2*(4), 90-105.
- Gogate, P. R., & Pandit, A. B. (2004). Sonophotocatalytic reactors for wastewater treatment: A critical review. *AIChE Journal*, *50*(5), 1051-1079. doi:10.1002/aic.10079
- Gopal, N. O., Lo, H.-H., Ke, T.-F., Lee, C.-H., Chou, C.-C., Wu, J.-D., . . . Ke, S.-C. (2012). Visible Light Active Phosphorus-Doped TiO<sub>2</sub> Nanoparticles: An EPR Evidence for the Enhanced Charge Separation. *J. Phys. Chem. C*, *116*(30), 16191–16197.

- Grabowska, E. (2016). Selected perovskite oxides: Characterization, preparation and photocatalytic properties—A review. *Applied Catalysis B: Environmental*, 186, 97–126.
- Grote, B. (2012). Application of Advanced Oxidation Processes (AOP) in Water Treatment. *37th Annual Qld Water Industry Operations Workshop*, 17-23.
- Guettaï, N., & Amar, H. A. (2005). Photocatalytic oxidation of methyl orange in presence of titanium dioxide in aqueous suspension. Part I: Parametric study. *Desalination*, 185(1-3), 427-437.
- Gupta, A., Saurava, J. R., & Bhattacharya, S. (2015). Solar light based degradation of organic pollutants using ZnO nanobrushes for water filtration. *RSC Adv.*, 5, 71472-71481.
- Hafez, H., Lan, Z., Li, Q., & Wu, J. (2010). High efficiency dye-sensitized solar cell based on novel TiO<sub>2</sub> nanorod/nanoparticle bilayer electrode. *Nanotechnol Sci Appl.*, 3, 45–51.
- Hakamada, M., Hirashima, F., & Mabuchi, M. (2012). Catalytic decoloration of methyl orange solution by nanoporous metals. *Catalysis Science & Technology*, 2(9), 1814. doi:10.1039/c2cy20218b
- Halmann, M. M. (1996). *Photodegradation of Water Pollutants*: CRC Press.
- Han, L., Wang, D., Cui, J., Chen, L., Jiang, T., & Lin, Y. (2012). Study on formaldehyde gas-sensing of In<sub>2</sub>O<sub>3</sub>-sensitized ZnO nanoflowers under visible light irradiation at room temperature. *Journal of Materials Chemistry*, 22(25), 12915. doi:10.1039/c2jm16105b
- Han, Z., Liao, L., Wu, Y., Pan, H., Shen, S., & Chen, J. (2012). Synthesis and photocatalytic application of oriented hierarchical ZnO flower-rod architectures. *J Hazard Mater*, 217-218, 100-106. doi:10.1016/j.jhazmat.2012.02.074
- Hao, O. J., Kim, H., & Chiang, P.-C. (2000). Decolorization of Wastewater. *Critical Reviews in Environmental Science and Technology*, 30(4), 449-505.
- Haque, M. M., Bahnemann, D., & Muneer, M. (2012). Photocatalytic Degradation of Organic Pollutants: Mechanisms and Kinetics. In D. T. Puzyn (Ed.), *Organic Pollutants Ten Years After the Stockholm Convention - Environmental and Analytical Update*: InTech.
- Haque, M. M., Muneer, M., & Bahnemann, D. W. (2006). Semiconductor-Mediated Photocatalyzed Degradation of a Herbicide Derivative, Chlorotoluron, in Aqueous Suspensions. *Environ. Sci. Technol.*, 40(15), 4765–4770.
- Hayat, K., Gondal, M. A., Khaled, M. M., Ahmed, S., & Shemsi, A. M. (2011). Nano ZnO synthesis by modified sol gel method and its application in heterogeneous photocatalytic removal of phenol from water. *Applied Catalysis A: General*, 393(1-2), 122-129. doi:10.1016/j.apcata.2010.11.032
- Heger, D., Jirkovsk, J., & Klan, P. (2005). Aggregation of Methylene Blue in Frozen Aqueous Solutions Studied by Absorption Spectroscopy. *J. Phys. Chem. A*, 109(30), 6702–6709.
- Herrmann, J.-M. (1999). Heterogeneous photocatalysis: fundamentals and applications to the removal of various types of aqueous pollutants. *Catalysis Today*, 53, 115–129.
- Herrmann, J.-M. (2005). Heterogeneous photocatalysis: state of the art and present applications In honor of Pr. R.L. Burwell Jr. (1912–2003), Former Head of

- Ipatieff Laboratories, Northwestern University, Evanston (Ill). *Topics in Catalysis*, 34(1-4), 49–65.
- Hilal, H. S., Al-Nour, G. Y. M., Zyoud, A., Helal, M. H., & Saadeddin, I. (2010). Pristine and supported ZnO-based catalysts for phenazopyridine degradation with direct solar light. *Solid State Sciences*, 12(4), 578-586. doi:10.1016/j.solidstatesciences.2010.01.008
- Hoffmann, M. R., Martin, S. T., Choi, W., & Bahnemann, D. W. (1995). Environmental Applications of Semiconductor Photocatalysis. *Chem. Rev.*, 95(1), 69-96.
- Hong, R. Y., Zhang, S. Z., Di, G. Q., Li, H. Z., Zheng, Y., Ding, J., & Wei, D. G. (2008). Preparation, characterization and application of Fe<sub>3</sub>O<sub>4</sub>/ZnO core/shell magnetic nanoparticles. *Materials Research Bulletin*, 43, 2457–2468. doi:10.1016/j.materresbull.2007.07.035
- Hosseini, S. M., Abdolhosseini Sarsari, I., Kameli, P., & Salamati, H. (2015). Effect of Ag doping on structural, optical, and photocatalytic properties of ZnO nanoparticles. *Journal of Alloys and Compounds*, 640, 408-415.
- Hou, X., Tian, Y., Zhang, X., Dou, S., Pan, L., Wang, W., . . . Zhao, J. (2015). Preparation and characterization of Fe<sub>3</sub>O<sub>4</sub>/SiO<sub>2</sub>/Bi<sub>2</sub>MoO<sub>6</sub> composite as magnetically separable photocatalyst. *Journal of Alloys and Compounds*, 638, 214-220.
- Houas, A., Lachheb, H., Ksibi, M., Elaloui, E., Guillard, C., & Herrmann, J.-M. (2001). Photocatalytic degradation pathway of methylene blue in water. *Applied Catalysis B: Environmental*, 31(2), 145-157.
- Hu, C., Hu, X., Wang, L., Qu, J., & Wang, A. (2006). Visible-Light-Induced Photocatalytic Degradation of Azodyes in Aqueous AgI/TiO<sub>2</sub> Dispersion. *Environ. Sci. Technol.*, 40(24), 7903–7907.
- Hu, C., Tang, Y., Yu, J. C., & Wong, P. K. (2003). Photocatalytic degradation of cationic blue X-GRL adsorbed on TiO<sub>2</sub>/SiO<sub>2</sub> photocatalyst. *Applied Catalysis B: Environmental*, 40(2), 131-140.
- Hu, C., Yu, J. C., Hao, Z., & Wong, P. K. (2003). Photocatalytic degradation of triazine-containing azo dyes in aqueous TiO<sub>2</sub> suspensions. *Applied Catalysis B: Environmental*, 42(1), 47-55.
- Hu, J., Chen, G., & Lo, I. (2005). Removal and recovery of Cr (VI) from wastewater by maghemite nanoparticles. *Water Res.*, 39(18), 4528-4536.
- Hunge, Y. M. (2017). Photoelectrocatalytic Degradation of Methylene Blue using Spray Deposited ZnO Thin Films under UV Illumination. *MOJ Polymer Science*, 1(4), 00020. doi:10.15406/mojps.2017.01.00020
- Ibhadon, A., & Fitzpatrick, P. (2013). Heterogeneous Photocatalysis: Recent Advances and Applications. *Catalysts*, 3(1), 189-218. doi:10.3390/catal3010189
- Iglesias-Jueza, A., Kubackaa, A., Colónb, G., & Fernández-García, M. (2013). Chapter 10 – Photocatalytic Nanooxides: The Case of TiO<sub>2</sub> and ZnO. In S. L. Suib (Ed.), *New and Future Developments in Catalysis: Catalysis by Nanoparticles* (pp. 245–266): Elsevier B.V.
- Ikeda, S., Abe, C., Torimoto, T., & Ohtani, B. (2003). Photochemical hydrogen evolution from aqueous triethanolamine solutions sensitized by binaphthol-modified titanium(IV) oxide under visible-light irradiation. *Journal of Photochemistry and Photobiology A: Chemistry*, 160(1-2), 61-67.

- Islam, S. Z., Nagpure, S., Kim, D. Y., & Rankin, S. E. (2017). Synthesis and Catalytic Applications of Non-Metal Doped Mesoporous Titania. *Inorganics*, 5(1), 15.
- Iwanski, P., Curran, J. S., Gissler, W., & Memming, R. (1981). The Photoelectrochemical Behavior of Ferric Oxide in the Presence of Redox Reagents. *J. Electrochem. Soc.*, 128(10), 2128-2133.
- Jagadish, C., & Pearton, S. (2006). *Zinc Oxide Bulk, Thin Films and Nanostructures*: Elsevier B.V.
- Janotti, A., & Van de Walle, C. G. (2009). Fundamentals of zinc oxide as a semiconductor. *Reports on Progress in Physics*, 72(12).
- Jia, X., Fan, H., Afzaal, M., Wu, X., & O'Brien, P. (2011). Solid state synthesis of tin-doped ZnO at room temperature: Characterization and its enhanced gas sensing and photocatalytic properties. *J Hazard Mater*, 193, 194-199.
- Jo, W.-K., & Tayade, R. J. (2014). New Generation Energy-Efficient Light Source for Photocatalysis: LEDs for Environmental Applications. *Ind. Eng. Chem. Res.*, 53(6), 2073–2084.
- Kanakaraju, D., Kockler, J., Motti, C. A., Glass, B. D., & Oelgemöller, M. (2015). Titanium dioxide/zeolite integrated photocatalytic adsorbents for the degradation of amoxicillin. *Applied Catalysis B: Environmental*, 166-167, 45-55.
- Kaneva, N. V., Dimitrov, D. T., & Dushkin, C. D. (2011). Effect of nickel doping on the photocatalytic activity of ZnO thin films under UV and visible light. *Applied Surface Science*, 257(18), 8113-8120. doi:10.1016/j.apsusc.2011.04.119
- Kannaiyan, D., Kim, E., Won, N., Kim, K. W., Jang, Y. H., Cha, M.-A., . . . Kim, D. H. (2010). On the synergistic coupling properties of composite CdS/TiO<sub>2</sub> nanoparticle arrays confined in nanopatterned hybrid thin films. *J. Mater. Chem.*, 20, 677-682.
- Kansal, S. K., Singh, M., & Sud, D. (2007). Studies on photodegradation of two commercial dyes in aqueous phase using different photocatalysts. *J. Hazard. Mater.*, 141, 581-540.
- Kato, S., Hirano, Y., Iwata, M., Sano, T., Takeuchi, K., & Matsuzawa, S. (2005). Photocatalytic degradation of gaseous sulfur compounds by silver-deposited titanium dioxide. *Applied Catalysis B: Environmental*, 57(2), 109-115.
- Katsuda, N., Omura, T., & Takagishi, T. (1997). Photodegradation of an anthraquinone type disperse dye on polyester, diacetate, and triacetate fibers, and in solution. *Dyes and Pigments*, 34(2), 147-157.
- Kaur, J., & Singhal, S. (2014). Facile synthesis of ZnO and transition metal doped ZnO nanoparticles for the photocatalytic degradation of Methyl Orange. *Ceramics International*, 40(5), 7417-7424. doi:10.1016/j.ceramint.2013.12.088
- Kaur, S., & Singh, V. (2007). TiO<sub>2</sub> mediated photocatalytic degradation studies of Reactive Red 198 by UV irradiation. *Journal of Hazardous Materials*, 141(1).
- Kelsall, R., Hamley, I., & Geoghegan, M. (2006). *Nanoscale Science and Technology*. West Sussex, England: John Wiley and Sons Ltd.
- Khayyat, S. A., Akhtar, M. S., & Umar, A. (2012). ZnO nanocapsules for photocatalytic degradation of thionine. *Materials Letters*, 81, 239-241. doi:10.1016/j.matlet.2012.04.039
- Kim, S.-E., Woo, J.-Y., Kang, S.-Y., Min, B. K., Lee, J. K., & Lee, S.-W. (2016). A facile general route for ternary Fe<sub>2</sub>O<sub>3</sub>@TiO<sub>2</sub>@nanometal (Au, Ag) composite as a

- high-performance and recyclable photocatalyst. *Journal of Industrial and Engineering Chemistry*, 43, 142–149.
- Kim, S., Hwang, S.-J., & Choi, W. (2005). Visible Light Active Platinum-Ion-Doped TiO<sub>2</sub> Photocatalyst. *J. Phys. Chem. B*, 109(51), 24260–24267.
- Knackmuss, H.-J. (1996). Basic knowledge and perspectives of bioelimination of xenobiotic compounds. *Journal of Biotechnology*, 51(3), 287-295.
- Koelsch, M., Cassaignon, S., Guillemoles, J. F., & Jolivet, J. P. (2002). Comparison of optical and electrochemical properties of anatase and brookite TiO synthesized by the sol-gel method. *Thin Solid Films*, 403–404, 312–319.
- Kołodziejczak-Radzimska, A., & Jesionowski, T. (2014). Zinc Oxide—From Synthesis to Application: A Review. *Materials*, 7(4), 2833-2881. doi:10.3390/ma7042833
- Kormann, C., Bahnemann, D. W., & Hoffmann, M. R. (1989). Environmental photochemistry: Is iron oxide (hematite) an active photocatalyst? A comparative study:  $\alpha$ -Fe<sub>2</sub>O<sub>3</sub>, ZnO, TiO<sub>2</sub>. *Journal of Photochemistry and Photobiology A: Chemistry*, 48(1), 161-169.
- Kositzki, M., Poulios, I., Samara, K., Tsatsaroni, E., & Darakas, E. (2007). Photocatalytic oxidation of Cibacron Yellow LS-R. *J. Hazard. Mater.*, 146(3), 680-685. doi:10.1016/j.jhazmat.2007.04.071
- Kuan, W.-H., & Chan, Y.-C. (2012). pH-dependent mechanisms of methylene blue reacting with tunneled manganese oxide pyrolusite. *Journal of Hazardous Materials*, 239-240, 152-159.
- Kumar, K. S., Van Swygenhoven, H., & Suresh, S. (2003). Mechanical behavior of nanocrystalline metals and alloys. *Acta Materialia*, 51, 5743–5774.
- Kumar, S., & Davis, A. P. (1997). HETEROGENEOUS PHOTOCATALYTIC OXIDATION OF NITROTOLUENES. *Water environment research*, 69(7), 1238-1245.
- Kusic, H., Koprivanac, N., & Bozic, A. L. (2013). Environmental aspects on the photodegradation of reactive triazine dyes in aqueous media. *Journal of Photochemistry and Photobiology A: Chemistry*, 252, 131-144. doi:10.1016/j.jphotochem.2012.11.018
- Lai, Y., Meng, M., & Yu, Y. (2010). One-step synthesis, characterizations and mechanistic study of nanosheets-constructed fluffy ZnO and Ag/ZnO spheres used for Rhodamine B photodegradation. *Applied Catalysis B: Environmental*, 100(3-4), 491-501.
- Lamba, R., Umar, A., Mehta, S. K., & Kansal, S. K. (2015). CeO<sub>2</sub>-ZnO Hexagonal Nanodisks: Efficient Material for the Degradation of Direct Blue 15 Dye and its simulated dye bath effluent under solar light. *Journal of Alloys and Compounds*, 620, 67-73.
- Lee, S. D., Nam, S.-H., Kim, M.-H., & Boo, J.-H. (2012). Synthesis and Photocatalytic Property of ZnO nanoparticles Prepared by Spray-Pyrolysis Method. *Physics Procedia*, 32, 320-326.
- Leghari, S. A. K., Sajjad, S., Chen, F., & Zhang, J. (2011). WO<sub>3</sub>/TiO<sub>2</sub> composite with morphology change via hydrothermal template-free route as an efficient visible light photocatalyst. *Chemical Engineering Journal*, 166(3), 906-915.
- Lewis, D., & Loan, T. (2007). Dyeing cotton with reactive dyes under neutral conditions. *Colouration Technology*, 123, 306-311.

- Li, W., & Wang, Y.-z. (2004). Photodegradation mechanism of two dyes: the influence of adsorption behavior on the novel TiO<sub>2</sub> particles. *Journal of Environmental Sciences*, 16(2), 328-331.
- Li, X., Guo, Z., & He, T. (2013). The doping mechanism of Cr into TiO<sub>2</sub> and its influence on the photocatalytic performance. *Phys. Chem. Chem. Phys.*, 15(46), 20037-20045.
- Li, X., Wang, G., Li, X., & Lu, D. (2004). Surface properties of polyaniline/nano-TiO<sub>2</sub> composites. *Applied Surface Science*, 229(1-4), 395-401.
- Libanori, R., Giraldi, T. R., Longo, E., Leite, E. R., & Ribeiro, C. (2009). Effect of TiO<sub>2</sub> surface modification in Rhodamine B photodegradation. *J Sol-Gel Sci Technol*, 49, 95-100.
- Linley, S., Liu, Y., Ptacek, C. J., Blowes, D. W., & Gu, F. X. (2014). Recyclable Graphene Oxide-Supported Titanium Dioxide Photocatalysts with Tunable Properties. *ACS Appl. Mater. Interfaces*, 6(7), 4658-4668.
- Linsebigler, A. L., Lu, G., & Yates, J. T. (1995). Photocatalysis on TiO<sub>2</sub> Surfaces: Principles, Mechanisms, and Selected Results. *Chem. Rev.*, 95(3), 735-758.
- Litter, M. I. (1999). Heterogeneous photocatalysis: Transition metal ions in photocatalytic systems. *Applied Catalysis B: Environmental*, 23(2-3), 89-114.
- Liu, G., Sun, C., Wang, L., Smith, S. C., Lu, G. Q., & Cheng, H.-M. (2011). Bandgap narrowing of titanium oxide nanosheets: homogeneous doping of molecular iodine for improved photoreactivity. *Journal of Materials Chemistry*, 21(38), 14672. doi:10.1039/c1jm11295c
- Liu, P., Zhang, P., Cao, D., & Xue, W. (2012). Preparation, characterization and photodegradation of methylene blue based on TiO<sub>2</sub> microparticles modified with thiophene substituents. *Chinese Science Bulletin*, 57(33), 4381-4386.
- Liu, R., Wang, P., Wang, X., Yu, H., & Yu, J. (2012). UV- and Visible-Light Photocatalytic Activity of Simultaneously Deposited and Doped Ag/Ag(I)-TiO<sub>2</sub> Photocatalyst. *J. Phys. Chem. C*, 116(33), 17721-17728.
- Liu, S., Chu, J., Guo, X., Ge, J., & Wu, H. (2015). Preparation of α-Fe<sub>2</sub>O<sub>3</sub>-TiO<sub>2</sub>/Fly Ash Cenospheres photocatalyst and its mechanism of photocatalytic degradation. *Colloids and Surfaces A: Physicochemical and Engineering Aspects*, 484, 434-440.
- Long, M., Cai, W., Chen, H., & Xu, J. (2007). Preparation, characterization and photocatalytic activity of visible light driven chlorine-doped TiO<sub>2</sub>. *Front. Chem. China*, 2(3), 278-282.
- López, F. A., Cebriano, T., Díaz, I. G., Fernández, P., Largo, O. R., & Fernández, A. L. (2017). Synthesis and microstructural properties of zinc oxide nanoparticles prepared by selective leaching of zinc from spent alkaline batteries using ammoniacal ammonium carbonate. *Journal of Cleaner Production*, 148, 795-803. doi:10.1016/j.jclepro.2017.02.031
- Lopez, J. A., Gonzalez, F., Bonilla, F. A., Zambrano, G., & Gomez, M. E. (2010). Synthesis and characterization of Fe<sub>3</sub>O<sub>4</sub> magnetite nanofluid. *Revista Latinoamericana de Metalurgia y Materiales*, 20(1), 60-66.
- Lu, C., Wu, Y., Mai, F., Chung, W., Wu, C., Lin, W., & Chen, C. (2009). Degradation efficiencies and mechanisms of the ZnO-mediated photocatalytic degradation of

- Basic Blue 11 under visible light irradiation. *Journal of Molecular Catalysis A: Chemical*, 310(1-2), 159-165.
- Lu, J., Yang, S., Ng, K. M., Su, C. H., Yeh, C. S., Wu, Y. N., & Shieh, D. B. (2006). Solid-state synthesis of monocrystalline iron oxide nanoparticles (MIONs) based ferrofluid suitable for magnetic resonance imaging (MRI) contrast application. *Nanotechnology*, 17(23), 5812-5820.
- Lu, J. G., Ye, Z. Z., Huang, J. Y., Zhu, L. P., Zhao, B. H., Wang, Z. L., & Fujita, S. (2006). ZnO quantum dots synthesized by a vapor phase transport process. *Applied Physics Letters*, 88, 063110. doi:10.1063/1.2172154
- Lu, X., Liu, Z. Z., Y., & Jiang, L. (2011). Sonochemical synthesis and photocatalytic property of zinc oxide nanoparticles doped with magnesium (II). *Materials Research Bulletin*, 46, 1638-1641.
- Lucas, M. S., & Peres, J. A. (2006). Decolorization of the azo dye Reactive Black 5 by Fenton and photo-Fenton oxidation. *Dyes and Pigments*, 71(3), 236-244.
- Luo, Q., Li, X., Wang, D., Wang, Y., & An, J. (2011). Photocatalytic activity of polypyrrole/TiO<sub>2</sub> nanocomposites under visible and UV light. *Journal of Materials Science*, 46(6), 1646-1654.
- Luttrell, T., Halpegamage, S., Tao, J., Kramer, A., Sutter, E., & Batzill, M. (2014). Why is anatase a better photocatalyst than rutile?--Model studies on epitaxial TiO<sub>2</sub> films. *Sci Rep*, 4, 4043. doi:10.1038/srep04043
- Mahalakshmi, M., Arabindoo, B., Palanichamy, M., & Murugesan, V. (2007). Photocatalytic degradation of carbofuran using semiconductor oxides. *Journal of Hazardous Materials*, 143(1-2), 240-245.
- Mahdavian, A. R., & Mirrahimi, M. A.-S. (2010). Efficient separation of heavy metal cations by anchoring polyacrylic acid on superparamagnetic magnetite nanoparticles through surface modification. *Chemical Engineering Journal*, 159, 264-271.
- Malato, S., Blanco, J., Campos, A., Caceres, J., Guillard, C., Herrmann, J. M., & Fernandez-Alba, A. R. (2003). Effect of operating parameters on the testing of new industrial titania catalysts at solar pilot plant scale. *Applied Catalysis B: Environmental*, 42(4), 349-357.
- Maliyekkal, S. M. M., Lisha, K. P., & Pradeep, T. (2010). A novel cellulose-manganese oxide hybrid material by in situ soft chemical. *J. Hazard. Mater.*, 181, 986-995.
- Matilainen, A., & Sillanpaa, M. (2010). Removal of natural organic matter from drinking water by advanced oxidation processes. *Chemosphere*, 80(4), 351-365. doi:10.1016/j.chemosphere.2010.04.067
- Mazzarino, I., Piccinini, P., & Spinelli, L. (1999). Degradation of organic pollutants in water by photochemical reactors. *Catalysis Today*, 48(1-4), 315-321.
- Mekasuwandumrong, O., Pawinrat, P., Praserttham, P., & Panpranot, J. (2010). Effects of synthesis conditions and annealing post-treatment on the photocatalytic activities of ZnO nanoparticles in the degradation of methylene blue dye. *Chemical Engineering Journal*, 164(1), 77-84. doi:10.1016/j.cej.2010.08.027
- Meyer, U. (1981). Biodegradation of synthetic organic colorants. In L. T., H. R., A. M. Cook, & J. Nuesh (Eds.), *Microbial degradation of xenobiotics and recalcitrant compounds*. London: Academic press.

- Mohamed, R. M., Mkhaliid, I. A., Baeissa, E. S., & Al-Rayyani, M. A. (2012). Photocatalytic Degradation of Methylene Blue by Fe/ZnO/SiO<sub>2</sub> Nanoparticles under Visiblelight. *Journal of Nanotechnology*, 2012, 1-5. doi:10.1155/2012/329082
- Mohammed Harshulkhan, S., Janaki, K., Velraj, G., Sakthi Ganapthy, R., & Nagarajan, M. (2016). Effect of Ag doping on structural, optical and photocatalytic activity of tungsten oxide (WO<sub>3</sub>) nanoparticles. *Journal of Materials Science: Materials in Electronics*, 27(5), 4744–4751.
- Mohseni, M. (2005). Gas phase trichloroethylene (TCE) photooxidation and byproduct formation: photolysis vs. titania/silica based photocatalysis. *Chemosphere*, 59, 335-342.
- Mozia, S., Tomaszewska, M., & Morawski, A. W. (2005). Photocatalytic degradation of azo-dye Acid Red 18. *Desalination*, 185, 449–456.
- Mrowetz, M., & Selli, E. (2006). Photocatalytic degradation of formic and benzoic acids and hydrogen peroxide evolution in TiO<sub>2</sub> and ZnO water suspensions. *Journal of Photochemistry & Photobiology, A: Chemistry*, 180(1-2), 15-22.
- Navarro, S., Fenoll, J., Vela, N., Ruiz, E., & Navarro, G. (2009). Photocatalytic degradation of eight pesticides in leaching water by use of ZnO under natural sunlight. *J Hazard Mater*, 172(2-3), 1303-1310. doi:10.1016/j.jhazmat.2009.07.137
- Nguyen, C., & Do, D. D. (1999). A New Method for the Characterization Of Porous Materials. *Langmuir*, 15(10), 3608–3615. doi:10.1021/la981140d
- Niemantsverdriet, J. W. (2007). *Spectroscopy in Catalysis: An Introduction* (3rd ed.). Weinheim: Wiley-VCH Verlag.
- Nogueira, A. E., Castro, I. A., Giroto, A. S., & Magriotis, Z. M. (2014). Heterogeneous Fenton-Like Catalytic Removal of Methylene Blue Dye in Water Using Magnetic Nanocomposite (MCM-41/Magnetite). *Journal of Catalysts*, 2014, 712067.
- Ong, S.-A., Min, O.-M., Ho, L.-N., & Wong, Y.-S. (2012). Comparative Study on Photocatalytic Degradation of Mono Azo Dye Acid Orange 7 and Methyl Orange under Solar Light Irradiation. *Water, air, and soil pollution*, 223(8), 5483-5493.
- Özgür, Ü., Alivov, Y. I., Liu, C., Teke, A., Reshchikov, M. A., Doğan, S., . . . Morkoç, H. (2005). A comprehensive review of ZnO materials and devices. *Journal of Applied Physics*, 98, 041301. doi:<http://dx.doi.org/10.1063/1.1992666>
- Padikkaparambil, S., Narayanan, B., Yaakob, Z., Viswanathan, S., & Tasirin, S. M. (2013). Au/TiO<sub>2</sub> Reusable Photocatalysts for Dye Degradation. *International Journal of Photoenergy*, 2013, 752605.
- Padmanabhan, P. V. A., Sreekumar, K. P., Thiyagarajan, T. K., Satpute, R. U., Bhanumurthy, K., Sengupta, P., . . . Warriier, K. G. K. (2006). Nano-crystalline titanium dioxide formed by reactive plasma synthesis. *Vacuum*, 80(11-12), 1252-1255.
- Palanivelu, K., Im, J. S., & Lee, Y.-S. (2007). Carbon Doping of TiO<sub>2</sub> for Visible Light Photo Catalysis - A review. *Carbon Science*, 8(3), 214-224.
- Palmer, M. A. (2010). Beyond Infrastructure. *Nature*, 467, 534-535.
- Pant, H. R., Park, C. H., Pant, B., Tijing, L. D., Kim, H. Y., & Kim, C. S. (2012). Synthesis, characterization, and photocatalytic properties of ZnO nano-flower

- containing TiO<sub>2</sub> NPs. *Ceramics International*, 38(4), 2943-2950. doi:10.1016/j.ceramint.2011.11.071
- Parks, G. A. (1965). The Isoelectric Points of Solid Oxides, Solid Hydroxides, and Aqueous Hydroxo Complex Systems. *Chem. Rev.*, 65(2), 177–198. doi:10.1021/cr60234a002
- Patchaiyappan, A., SaranSuja, S., & Devipriya, P. (2016). Recovery and reuse of TiO<sub>2</sub> photocatalyst from aqueous suspension using plant based coagulant - A green approach. *Korean Journal of Chemical Engineering*, 33(7), 2107–2113.
- Pearce, C. I., Lloyd, J. R., & Guthrie, J. T. (2003). The removal of colour from textile wastewater using whole bacterial cells: a review. *Dyes and Pigments*, 58(3), 179-196.
- Pirkanniemi, K., & Sillanpää, M. (2002). Heterogeneous water phase catalysis as an environmental application: a review. *Chemosphere*, 48, 1047-1060.
- Piscopo, A., Robert, D., & Weber, J. V. (2001). Influence of pH and chloride anion on the photocatalytic degradation of organic compounds Part I. Effect on the benzamide and para-hydroxybenzoic acid in TiO<sub>2</sub> aqueous solution. *Applied Catalysis B: Environmental*, 35, 117–124.
- Porter, A. L., & Youtie, J. (2009). How interdisciplinary is nanotechnology? *J Nanopart Res.*, 11(5), 1023–1041. doi:10.1007/s11051-009-9607-0
- Prabhu, S., Viswanathan, T., Jothivenkatachalam, K., & Jeganathan, K. (2014). Visible Light Photocatalytic Activity of CeO<sub>2</sub>-ZnO-TiO<sub>2</sub> Composites for the Degradation of Rhodamine B. *Indian Journal of Materials Science*, 2014, 536123.
- Qamar, M., Saquib, M., & Muneer, M. (2005). Photocatalytic degradation of two selected dye derivatives, chromotrope 2B and amido black 10B, in aqueous suspensions of titanium dioxide. *Dyes and Pigments*, 65(1), 1-9.
- Qiu, R., Song, L., Zhang, D., Mo, Y., Brewer, E., & Huang, X. (2008). Characterization of Conjugated Polymer Poly(fluorene-co-thiophene) and Its Application as Photosensitizer of TiO<sub>2</sub>. *International Journal of Photoenergy*, 2008, 164702.
- Rabindranathan, S., Devipriya, S., & Yesodharan, S. (2003). Photocatalytic degradation of phosphamidon on semiconductor oxides. *Journal of Hazardous Materials*, 102(2-3), 217-229.
- Rajendran, S., Mansoob Khan, M., Gracia, F., Qin, J., Gupta, V. K., & Arumainathan, S. (2016). Ce<sup>3+</sup>-ion-induced visible-light photocatalytic degradation and electrochemical activity of ZnO/CeO<sub>2</sub> nanocomposite. *Sci. Rep.*, 6, 31641. doi:10.1038/srep31641
- Ramezani, M., & Neitzert, T. (2012). Mechanical milling of aluminum powder using planetary ball milling process. *Journal of Achievements in Materials and Manufacturing Engineering*, 55(2), 790-798.
- Rattanakam, R., & Supothina, S. (2009). Visible-light-sensitive N-doped TiO<sub>2</sub> photocatalysts prepared by a mechanochemical method: effect of a nitrogen source. *Research on Chemical Intermediates*, 35(3), 263–269.
- Razeghi, M. (2009). *Fundamentals of Solid State Engineering* (3rd ed.). New York, USA: Springer US.
- Reddy, E. P., Davydov, L., & Smirniotis, P. (2003). TiO<sub>2</sub>-loaded zeolites and mesoporous materials in the sonophotocatalytic decomposition of aqueous organic pollutants: the role of the support. *Applied Catalysis B: Environmental*, 42, 1-11.

- Regulska, E., Brus, D. M., Rodziewicz, P., Sawicka, S., & Karpinska, J. (2016). Photocatalytic degradation of hazardous Food Yellow 13 in TiO<sub>2</sub> and ZnO aqueous and river water suspensions. *Catalysis Today*, 266, 72-81. doi:10.1016/j.cattod.2015.08.010
- Ren, R., Wen, Z., Cui, S., Hou, Y., Guo, X., & Chen, J. (2015). Controllable Synthesis and Tunable Photocatalytic Properties of Ti<sup>3+</sup>-doped TiO<sub>2</sub>. *Sci Rep*, 5. doi:10.1038/srep10714
- Rendina, G. (1971). *Experimental Methods in Modern Biochemistry*. Philadelphia: Saunders.
- Reynolds, D. C., Look, D. C., Jogai, B., & Collins, T. C. (2001). Polariton and free-exciton-like photoluminescence in ZnO. *Applied Physics Letters*, 79(23), 3794-3796. doi:10.1063/1.1412435
- Reza, K. M., Kurny, A., & Gulshan, F. (2015). Parameters affecting the photocatalytic degradation of dyes using TiO<sub>2</sub>: a review. *Applied Water Science*, 7(4), 1569–1578.
- Rizzo, L., Meric, S., Guida, M., Kassinos, D., & Belgiorno, V. (2009). Heterogenous photocatalytic degradation kinetics and detoxification of an urban wastewater treatment plant effluent contaminated with pharmaceuticals. *Water Research*, 43(16), 4070-4078.
- Robinson, T., McMullan, G., Marchant, R., & Nigam, P. (2001). Remediation of dyes in textile effluent: a critical review on current treatment technologies with a proposed alternative. *Bioresource Technology*, 77(3), 247-255.
- Saikia, L., Bhuyan, D., Saikia, M., Malakar, B., Dutta, D. K., & Sengupta, P. (2015). Photocatalytic performance of ZnO nanomaterials for self sensitized degradation of malachite green dye under solar light. *Applied Catalysis A: General*, 490, 42-49.
- Santos, L. M., Machado, W. A., França, M. D., Borges, K. A., Paniago, R. M., Patrocínio, A. O. T., & Machado, A. E. H. (2015). Structural characterization of Ag-doped TiO<sub>2</sub> with enhanced photocatalytic activity. *RSC Adv.*, 5(125), 103752-103759.
- Saravanan, R., Mansoob Khan, M., Gupta, V. K., Mosquera, E., Gracia, F., Narayanan, V., & Stephen, A. (2015). ZnO/Ag/CdO nanocomposite for visible light-induced photocatalytic degradation of industrial textile effluents. *Journal of Colloid and Interface Science*, 452, 126–133.
- Saravanan, R., Shankar, H., Prakash, T., Narayanan, V., & Stephen, A. (2011). ZnO/CdO composite nanorods for photocatalytic degradation of methylene blue under visible light. *Materials Chemistry and Physics*, 125(1-2), 277-280.
- Saroj, S., Kumar, K., Pareek, N., Prasad, R., & Singh, R. P. (2014). Biodegradation of azo dyes Acid Red 183, Direct Blue 15 and Direct Red 75 by the isolate *Penicillium oxalicum* SAR-3. *Chemosphere*, 107, 240-248.
- Sathishkumar, P., Sweena, R., Wu, J. J., & Anandan, S. (2011). Synthesis of CuO-ZnO nanophotocatalyst for visible light assisted degradation of a textile dye in aqueous solution. *Chemical Engineering Journal*, 171(1), 136-140. doi:10.1016/j.cej.2011.03.074
- Schmidt-Mende, L., & MacManus-Driscoll, J. L. (2007). ZnO – nanostructures, defects, and devices. *Materials Today*, 10(5).

- Schwarzenbach, R. P., Egli, T., Hofstetter, T. B., von Gunten, U., & Wehrli, B. (2010). Global Water Pollution and Human Health. *Annual Review of Environment and Resources*, 35(1), 109-136. doi:10.1146/annurev-environ-100809-125342
- Seriani, N., Pinilla, C., & Crespo, Y. (2015). Presence of Gap States at Cu/TiO<sub>2</sub> Anatase Surfaces: Consequences for the Photocatalytic Activity. *The Journal of Physical Chemistry C*, 119(12), 6696-6702. doi:10.1021/acs.jpcc.5b00846
- Serpone, N., Maruthamuthu, P., Pichat, P., Pelizzetti, E., & Hidaka, H. (1995). Exploiting the interparticle electron transfer process in the photocatalysed oxidation of phenol, 2-chlorophenol and pentachlorophenol: chemical evidence for electron and hole transfer between coupled semiconductors. *J. Photochem. Photobiol. A Chem.*, 85(3), 247-255.
- Shafaei, A., Nikazar, M., & Arami, M. (2010). Photocatalytic degradation of terephthalic acid using titania and zinc oxide photocatalysts: comparative study. *Desalination*, 252, 8-16. doi:10.1016/j.desal.2009.11.008
- Shen, T. F., Tang, J., Nie, Z. H., Wang, Y. D., Ren, Y., & Zuo, L. (2009). Preparation and application of magnetic Fe<sub>3</sub>O<sub>4</sub> nanoparticles for wastewater purification. *Separation and Purification Technology*, 68, 312-319.
- Shen, X., Liang, Y., Zhai, Y., & Ning, Z. (2013). Shape-controllable Synthesis of Ultrafine ZnO Powders of Different Morphologies. *Journal of Materials Science & Technology*, 29(1), 44-48. doi:10.1016/j.jmst.2012.11.004
- Sher Shah, M. S., Park, A. R., Zhang, K., Park, J. H., & Yoo, P. J. (2012). Green synthesis of biphasic TiO<sub>2</sub>-reduced graphene oxide nanocomposites with highly enhanced photocatalytic activity. *ACS Appl Mater Interfaces*, 4(8), 3893-3901. doi:10.1021/am301287m
- Shibata, T., Irie, H., Ohmori, M., Nakajima, A., Watanabe, T., & Hashimoto, K. (2004). Comparison of photochemical properties of brookite and anatase TiO<sub>2</sub> films. *Phys. Chem. Chem. Phys.*, 6, 1359-1362.
- Shifu, C., & Gengyu, C. (2005). Photocatalytic degradation of organophosphorus pesticides using floating photocatalyst TiO<sub>2</sub> · SiO<sub>2</sub>/beads by sunlight. *Solar Energy*, 79(1), 1-9.
- Shinde, S. S., Shinde, P. S., Bhosale, C. H., & Rajpure, K. Y. (2011). Zinc oxide mediated heterogeneous photocatalytic degradation of organic species under solar radiation. *J Photochem Photobiol B*, 104(3), 425-433. doi:10.1016/j.jphotobiol.2011.04.010
- Shrama, S. K., Saurakhiya, N., Barthwal, S., Kumar, R., & Sharma, A. (2014). Tuning of structural, optical, and magnetic properties of ultrathin and thin ZnO nanowire arrays for nano device applications. *Nanoscale Res Lett.*, 9(1), 122. doi:10.1186/1556-276X-9-122
- Silva, A. n. M. T., Nouli, E., Xekoukoulotakis, N. P., & Mantzavinos, D. (2007). Effect of key operating parameters on phenols degradation during H<sub>2</sub>O<sub>2</sub>-assisted TiO<sub>2</sub> photocatalytic treatment of simulated and actual olive mill wastewaters. *Applied Catalysis B: Environmental*, 73, 11-22.
- Singh, S., Barick, K. C., & Bahadur, D. (2013). Fe<sub>3</sub>O<sub>4</sub> embedded ZnO nanocomposites for the removal of toxic metal ions, organic dyes and bacterial pathogens. *Journal of Materials Chemistry A*, 1(10), 3325. doi:10.1039/c2ta01045c

- Singh, S., Seth, R., Tabe, S., & Yang, P. (2015). Oxidation of Emerging Contaminants during Pilot-Scale Ozonation of Secondary Treated Municipal Effluent. *Ozone: Science & Engineering*, 37(4), 323-329.
- Singh, S. C., Zeng, H., Guo, C., Gopal, R., & Cai, W. (2012). Introduction of Materials and Architectures at the Nanoscale. In S. C. Singh, H. Zeng, C. Guo, & W. Cai (Eds.), *Nanomaterials: Processing and Characterization with Lasers*: Wiley-VCH Publication.
- Sirtori, C., Altvater, P. K., de Freitas, A. M., & Peralta-Zamora, P. G. (2006). Degradation of aqueous solutions of camphor by heterogeneous photocatalysis. *Journal of Hazardous Materials*, 129(1-3), 110-115.
- Sochacka, J. (2015). Application of phenol red as a marker ligand for bilirubin binding site at subdomain IIA on human serum albumin. *Journal of Photochemistry and Photobiology B: Biology*, 151, 89-99.
- Song, L., Qiu, R., Mo, Y., Zhang, D., Wei, H., & Xiong, Y. (2007). Photodegradation of phenol in a polymer-modified TiO<sub>2</sub> semiconductor particulate system under the irradiation of visible light. *Catalysis Communications*, 8, 429-433.
- Song, S., Hong, F., He, Z., Wang, H., Xu, X., & Chen, J. (2011). Influence of zirconium doping on the activities of zirconium and iodine co-doped titanium dioxide in the decolorization of methyl orange under visible light irradiation. *Applied Surface Science*, 257, 10101-10108.
- Spasiano, D., Marotta, R., Malato, S., Fernandez-Ibañez, P., & Di Somma, I. (2015). Solar photocatalysis: Materials, reactors, some commercial, and pre-industrialized applications. A comprehensive approach. *Applied Catalysis B: Environmental*, 170-171, 90-123.
- Su, T.-L., Chiou, C.-S., & Chen, H.-W. (2012). Preparation, Photocatalytic Activity, and Recovery of Magnetic Photocatalyst for Decomposition of Benzoic Acid. *International Journal of Photoenergy*, 2012, 1-8. doi:10.1155/2012/909678
- Subash, B., Krishnakumar, B., Pandiyan, V., Swaminathan, M., & Shanthi, M. (2012). An efficient nanostructured Ag<sub>2</sub>S-ZnO for degradation of Acid Black 1 dye under day light illumination. *Separation and Purification Technology*, 96, 204-213. doi:10.1016/j.seppur.2012.06.002
- Sugiyana, D., Handajani, M., Kardena, E., & Notodarmojo, S. (2014). Photocatalytic Degradation of Textile Wastewater Containing Reactive Black 5 Azo Dye by Using Immobilized TiO<sub>2</sub> Nanofiber-Nanoparticle Composite catalyst on Glass Plates. *Journal of JSCE*, 2, 69-76.
- Surender, G. D., Fotou, G. P., & Pratsinis, S. E. (1998). Titania-based aqueous phase photocatalytic remediation processes: strategies for enhancement of quantum efficiency. *Trends in Chemical Engineering*, 4, 145 - 159.
- Talebian, N., & Nilforoushan, M. R. (2010). Comparative study of the structural, optical and photocatalytic properties of semiconductor metal oxides toward degradation of methylene blue. *Thin Solid Films*, 518(8), 2210-2215.
- Tan, Y. N., Wong, C. L., & Mohamed, A. R. (2011). An Overview on the Photocatalytic Activity of Nano-Doped-TiO<sub>2</sub> in the Degradation of Organic Pollutants. *ISRN Materials Science*, 2011, 261219.

- Tanaka, K., Capule, M. F. V., & Hisanaga, T. (1991). Effect of crystallinity of TiO<sub>2</sub> on its photocatalytic action. *Chemical Physics Letters*, 187(1), 73-76. doi:10.1016/0009-2614(91)90486-S
- Tayade, R. J., Natarajan, T. S., & Bajaj, H. C. (2009). Photocatalytic Degradation of Methylene Blue Dye Using Ultraviolet Light Emitting Diodes. *Ind. Eng. Chem. Res.*, 48(23), 10262–10267. doi:10.1021/ie9012437
- Topkaya, E., Konyar, M., Yatmaz, H. C., & Ozturk, K. (2014). Pure ZnO and composite ZnO/TiO<sub>2</sub> catalyst plates: A comparative study for the degradation of azo dye, pesticide and antibiotic in aqueous solutions. *Journal of Colloid and Interface Science*, 430, 6-11.
- Tudose, I. V., & Sucheai, M. (2016). ZnO for photocatalytic air purification applications. *IOP Conf. Series: Materials Science and Engineering*, 133, 012040. doi:10.1088/1757-899X/133/1/012040
- Turchi, C. S., & Ollis, D. F. (1990). Photocatalytic degradation of organic water contaminants: Mechanisms involving hydroxyl radical attack. *Journal of Catalysis*, 122(1), 178-192.
- Uddin, M. T., Nicolas, Y., Olivier, C., Toupance, T., Servant, L., Müller, M. M., . . . Jaegermann, W. (2012). Nanostructured SnO<sub>2</sub>-ZnO Heterojunction Photocatalysts Showing Enhanced Photocatalytic Activity for the Degradation of Organic Dyes. *Inorg. Chem.*, 51(14), 7764–7773.
- Velmurugan, R., & Swaminathan, M. (2011). An efficient nanostructured ZnO for dye sensitized degradation of Reactive Red 120 dye under solar light. *Solar Energy Materials and Solar Cells*, 95(3), 942-950. doi:10.1016/j.solmat.2010.11.029
- Velusamy, P., & Lakshmi, G. (2017). Enhanced photocatalytic performance of (ZnO/CeO<sub>2</sub>)-β-CD system for the effective decolorization of Rhodamine B under UV light irradiation. *Applied Water Science*, 1–12.
- Venkatachalam, N., Palanichamy, M., & Murugesan, V. (2007). Sol-gel preparation and characterization of alkaline earth metal doped nano TiO<sub>2</sub>: Efficient photocatalytic degradation of 4-chlorophenol. *Journal of Molecular Catalysis A: Chemical*, 273(1-2), 177-185.
- Wang, C., Guo, Y., Yang, Y., Chu, S., Zhou, C., Wang, Y., & Zou, Z. (2014). Sulfur-Doped Polyimide Photocatalyst with Enhanced Photocatalytic Activity under Visible Light Irradiation. *ACS Appl. Mater. Interfaces*, 6(6), 4321–4328.
- Wang, J., Yang, J., Li, X., Wang, D., Wei, B., Song, H., . . . Fu, S. (2016). Preparation and photocatalytic properties of magnetically reusable Fe<sub>3</sub>O<sub>4</sub>@ZnO core/shell nanoparticles. *Physica E: Low-dimensional Systems and Nanostructures*, 75, 66-71.
- Wang, M., Ioccozia, J., Sun, L., Lin, C., & Lin, Z. (2014). Inorganic-modified semiconductor TiO<sub>2</sub> nanotube arrays for photocatalysis. *Energy Environ. Sci.*, 7, 2182-2202.
- Wang, P., Ming, T., Wang, X., & Yu, H. (2012). Selective-adsorption Removal of Methyl Orange (MO) by CTAB-assisted AgBr Powder. *Journal of Wuhan University of Technology-Mater. Sci. Ed.*, 27(4), 675-678.
- Wang, S. Q., Liu, Q. L., & Zhu, A. M. (2011). Preparation of multisensitive poly (N-isopropylacrylamide-co-acrylic acid)/TiO<sub>2</sub> composites for degradation of methyl orange. *European Polymer Journal*, 47(5), 1168-1175.

- Wang, X., Zhai, B., Yang, M., Han, W., & Shao, X. (2013). ZrO<sub>2</sub>/CeO<sub>2</sub> nanocomposite: Two step synthesis, microstructure, and visible-light photocatalytic activity. *Materials Letters*, *112*(90-93).
- Wang, Y. (2000). Solar photocatalytic degradation of eight commercial dyes in TiO<sub>2</sub> suspension. *Water Research*, *34*(3), 990-994. doi:[https://doi.org/10.1016/S0043-1354\(99\)00210-9](https://doi.org/10.1016/S0043-1354(99)00210-9)
- Wang, Z. L. (2004). Zinc oxide nanostructures: growth, properties and applications. *J. Phys.: Condens. Matter*, *16*, R829–R858. doi:10.1088/0953-8984/16/25/R01
- Weisburger, J. H. (2002). Comments on the history and importance of aromatic and heterocyclic amines in public health. *Mutation Research/Fundamental and Molecular Mechanisms of Mutagenesis*, *506-507*, 9–20.
- White, B. R., Stackhouse, B. T., & Holcombe, J. A. (2009). Magnetic  $\gamma$ -Fe<sub>2</sub>O<sub>3</sub> nanoparticles coated with poly-L-cysteine for chelation of As(III), Cu(II), Cd(II), Ni(II), Pb(II) and Zn(II). *J Hazard Mater*, *161*(2-3), 848-853.
- Wong, & Yuen. (1996). Metabolism of azo dyes by lactobacillus casei TISTR 1500 and effects of various factors on decolorization.
- Wong, P. K., & Yuen, P. Y. (1998). Decolorisation and Biodegradation of N, N-dimethyl-p-phenylenediamine by Klebsiella pneumoniae RS-13 and Acetobacter liquefaciens. S-I. *Applied Microbiology*, *85*, 87-99.
- Wu, C., & Huang, Q. (2010). Synthesis of Na doped ZnO nanowires and their photocatalytic properties. *J Luminescence*, *130*, 2136-2141. doi:10.1016/j.jlumin.2010.06.007
- Wu, C., Shen, L., Zhang, Y.-C., & Huang, Q. (2011). Solvothermal synthesis of Cr-doped ZnO nanowires with visible light-driven photocatalytic activity. *Materials Letters*, *65*(12), 1794-1796. doi:10.1016/j.matlet.2011.03.070
- Wu, W., Gao, S., Tu, W., Chen, J., & Zhang, P. (2010). Intensified photocatalytic degradation of nitrobenzene by Pickering emulsion of ZnO nanoparticles. *Particuology*, *8*, 453–457.
- Xia, J., Wang, A., Liu, X., & Su, Z. (2011). Preparation and characterization of bifunctional, Fe<sub>3</sub>O<sub>4</sub>/ZnO nanocomposites and their use as photocatalysts. *Applied Surface Science*, *257*(23), 9724-9732. doi:10.1016/j.apsusc.2011.05.114
- Xia, Y., Wang, J., Chen, R., Zhou, D., & Xiang, L. (2016). A Review on the Fabrication of Hierarchical ZnO Nanostructures for Photocatalysis Application. *Crystals*, *6*, 148. doi:10.3390/cryst6110148
- Xiang, Q., Yu, J., & Jaroniec, M. (2012). Graphene-based semiconductor photocatalysts. *Chem Soc Rev.*, *41*(2), 782-796.
- Xiang, Q., Yua, J., & Wong, P. K. (2011). Quantitative characterization of hydroxyl radicals produced by various photocatalysts. *Journal of Colloid and Interface Science*, *357*(1), 163-167.
- Xie, J., Wang, H., Duan, M., & Zhang, L. (2011). Synthesis and photocatalysis properties of ZnO structures with different morphologies via hydrothermal method. *Applied Surface Science*, *257*(15), 6358-6363. doi:10.1016/j.apsusc.2011.01.105
- Xu, N., Shi, Z., Fan, Y., Dong, J., Shi, J., & Hu, M. Z.-C. (1999). Effects of Particle Size of TiO<sub>2</sub> on Photocatalytic Degradation of Methylene Blue in Aqueous Suspensions. *Ind. Eng. Chem. Res.*, *38*(2), 373–379.

- Xu, S., Gu, L., Wu, K., Yang, H., Song, Y., Jiang, L., & Dan, Y. (2012). The influence of the oxidation degree of poly(3-hexylthiophene) on the photocatalytic activity of poly(3-hexylthiophene)/TiO<sub>2</sub> composites. *Solar Energy Materials and Solar Cells*, *96*, 286-291.
- Xu, T., Zhang, L., Cheng, H., & Zhu, Y. (2011). Significantly enhanced photocatalytic performance of ZnO via graphene hybridization and the mechanism study. *Applied Catalysis B: Environmental*, *101*(3-4), 382-387. doi:10.1016/j.apcatb.2010.10.007
- Xu, X. R., Li, H. B., & Gu, J. D. (2006). Simultaneous decontamination of hexavalent chromium and methyl tert-butyl ether by UV/TiO<sub>2</sub> process. *Chemosphere*, *63*(2), 254-260.
- Xu, Y., & Schoonen, M. A. A. (2000). The absolute energy positions of conduction and valence bands of selected semiconducting minerals. *American Mineralogist*, *85*, 543-556.
- Yagub, M. T., Sen, T. K., Afroze, S., & Ang, H. M. (2014). Dye and its removal from aqueous solution by adsorption: a review. *Adv Colloid Interface Sci*, *209*, 172-184. doi:10.1016/j.cis.2014.04.002
- Yang, C., Wu, J., & Hou, Y. (2011). Fe<sub>3</sub>O<sub>4</sub> nanostructures: synthesis, growth mechanism, properties and applications. *Chem. Commun.*, *47*, 5130-5141.
- Yang, H. G., & Zeng, H. C. (2004). Preparation of Hollow Anatase TiO<sub>2</sub> Nanospheres via Ostwald Ripening. *J. Phys. Chem. B*, *108*(11), 3492-3495. doi:10.1021/jp0377782
- Yang, M. Q., Zhang, N., Pagliaro, M., & Xu, Y. J. (2014). Artificial photosynthesis over graphene-semiconductor composites. Are we getting better? *Chem Soc Rev.*, *43*(24), 8240-8254.
- Yang, Y., Xu, L., Su, C., Che, J., Sun, W., & Gao, H. (2014). Electrospun ZnO/Bi<sub>2</sub>O<sub>3</sub> Nanofibers with Enhanced Photocatalytic Activity. *Journal of Nanomaterials*, *2014*, 130539.
- Yassitepe, E., Yatmaz, H. C., Öztürk, C., Öztürk, K., & Duran, C. (2008). Photocatalytic efficiency of ZnO plates in degradation of azo dye solutions. *Journal of Photochemistry and Photobiology A: Chemistry*, *198*(1), 1-6. doi:10.1016/j.jphotochem.2008.02.007
- Yoshimura, N. (2007). *Vacuum Technology: Practice for Scientific Instruments*. Berlin Heidelberg: Springer Science & Business Media.
- Yu, W., Li, X., Gao, X., & Wu, F. (2005). Large-Scale Synthesis and Microstructure of SnO<sub>2</sub> Nanowires Coated with Quantum-Sized ZnO Nanocrystals on a Mesh Substrate. *J. Phys. Chem. B*, *109*(36), 17078-17081. doi:10.1021/jp0526905
- Zangeneh, H., Zinatizadeh, A. A. L., Habibi, M., Akia, M., & Isa, M. H. (2015). Photocatalytic Oxidation of Organic Dyes and Pollutants in Wastewater Using Different Modified Titanium Dioxide: A Comparative Review. *Journal of Industrial and Engineering Chemistry*, *26*, 1-36.
- Zhan, Y., Zhou, X., Fu, B., & Zhen, Y. (2011). Catalytic Wet Peroxide Oxidation of Azo Dye (Direct Blue 15) Using Solvothermally Synthesized Copper Hydroxide Nitrate as Catalyst. *J Hazard Mater*, *187*, 348-354.

- Zhang, L., Feng, C., Chen, Z., Liu, L., Jiang, K., Li, Q., & Fan, S. (2008). Superaligned Carbon Nanotube Grid for High Resolution Transmission Electron Microscopy of Nanomaterials. *Nano Lett.*, 8(8), 2564–2569. doi:10.1021/nl8012727
- Zhang, X., Qin, J., Xue, Y., Yu, P., Zhang, B., Wang, L., & Liu, R. (2014). Effect of aspect ratio and surface defects on the photocatalytic activity of ZnO nanorods. *Scientific Reports*, 4, 4596
- Zhang, Z., Wang, C.-C., Zakaria, R., & Ying, J. Y. (1998). Role of Particle Size in Nanocrystalline TiO<sub>2</sub>-Based Photocatalysts. *J. Phys. Chem. B*, 102(52), 10871–10878.
- Zhu, G., Hojamberdiev, M., Katsumata, K.-i., Cai, X., Matsushita, N., Okada, K., . . . Zhou, J. (2013). Heterostructured Fe<sub>3</sub>O<sub>4</sub>/Bi<sub>2</sub>O<sub>2</sub>CO<sub>3</sub> photocatalyst: Synthesis, characterization and application in recyclable photodegradation of organic dyes under visible light irradiation. *Materials Chemistry and Physics*, 142(1), 95-105. doi:10.1016/j.matchemphys.2013.06.046
- Zhu, J., Wei, S., Zhang, L., Mao, Y., Ryu, J., Haldolaarachchige, N., . . . Guo, Z. (2011). Electrical and dielectric properties of polyaniline–Al<sub>2</sub>O<sub>3</sub> nanocomposites derived from various Al<sub>2</sub>O<sub>3</sub> nanostructures. *J. Mater. Chem.*, 21, 3952-3959 doi:10.1039/C0JM03908J
- Zollinger, H. (1987). *Color Chemistry- Syntheses, properties and application of organic dyes pigment*. New York: VCH.
- Zuo, R., Du, G., Zhang, W., Liu, L., Liu, Y., Mei, L., & Li, Z. (2014). Photocatalytic Degradation of Methylene Blue Using TiO<sub>2</sub> Impregnated Diatomite. *Advances in Materials Science and Engineering*, 2014, 170148. doi:10.1155/2014/170148